Mobility and Reactivity of Sulfate Green Rust and Sulfidized Nanoscale Zerovalent Iron for *In-Situ* Remediation of Chromium Contaminated Sites

Zur Erlangung des akademischen Grades eines

DOKTORS DER NATURWISSENSCHAFTEN

von der KIT-Fakultät für

Bauingenieur-, Geo- und Umweltwissenschaften

des Karlsruher Instituts für Technologie (KIT)

genehmigte

DISSERTATION

von

M.Sc. Flavia Digiacomo

aus Ragusa (Italien)

Tag der mündlichen Prüfung:

05.02.2021

Referent:	Prof. Dr. Thomas Neumann
Korreferentin:	Prof. Dr. Dominique J. Tobler
Korreferent:	Prof. Dr. Jochen Kolb
Berater:	Dr. Thomas Held

Karlsruhe 2021

Erklärung

Hiermit erkläre ich, dass ich die vorliegende Dissertation selbständig verfasst und keine anderen als die angegebenen Hilfsmittel benutzt habe. Die Stellen der Arbeit, welche anderen Quellen im Wortlaut oder dem Sinn nach entnommen wurden, sind durch Zitation kenntlich gemacht. Dies gilt auch für bildliche Darstellungen, Tabellen sowie für Quellen aus dem Internet.

Karlsruhe, den 08.12.2020   Flavia Digiacomo

Acknowledgment

This work would not have been possible without the support of many people, near and far. I would like to take this opportunity to express my gratitude to all those people who have supported me in any way.

Foremost, I would like to express my gratitude to my supervisor **Thomas Neumann** for providing me the opportunity to work on this challenging subject and supporting me. I am grateful to **Dominique Tobler** for her valuable guidance and feedback throughout this project and for taking the responsibility to act as external supervisor. I want to thank **Jochen Kolb** for his support during my stay at the Institute of Applied Geosciences (AGW), Karlsruhe Institute of Technology (KIT), and for his willingness to act as co-referent. Many thanks to **Thomas Held**, from Arcadis Germany GmbH, for acting as advisor and sharing his knowledge on this topic.

I would like to thank all the members of the Department of Geochemistry and Economic Geology (EGG), at AGW-KIT, for supporting me during the thesis. I especially want to thank **Ralf Wachter** for keeping alive the glovebox and always finding a solution to any technical problems in the lab. Many thanks to **Elisabeth Eiche**, **Gesine Preuß**, **Chantalle Kotschenreuther**, **Beate Oetzel** and **Andrea Friedrich** for their help. Moreover, I would like to thank **Andrew Thomas**, **Hongyan Wang**, **Jingwei Yang**, **Andre Wilhelms** and **Jonas Bauer** for the valuable discussions on how to survive during our PhD years.

I would also like to thank all the people from external institutes who have contributed to the analytical part of this work: **Johannes Lützenkirchen** and **Teba Gil-Díaz** from the Institute for Nuclear Waste Disposal (KIT- INE), **Jonas Kaltenbach** from the Institute of Functional Interfaces (KIT- IFG), **Gisela Guthausen** and **Nicolas Schork** from the Institute of Institute of Mechanical Process Engineering and Mechanics (KIT-MVM), **Liane Benning** and **Jeffrey Perez** from the Interface Geochemistry research group (GFZ, Potsdam). Moreover, I would like to express my gratitude to the staff members of the NanoGeoScience Group (University of Copenhagen) for the productive and pleasant time I had during my visits. Special thanks to **Marcel Ceccato** for the opportunity to discuss my work.

Many thanks to all the members of the **Metal-Aid project** for the fruitful discussions concerning the scientific and technical aspects of developing a successful remediation technology. I am grateful to **Clare Desplats** for her valuable support and advice. Special thanks to **Virginia Alonso de Linaje, Marco Mangayayam**, **Adrian Schiefler** and **Weichao Sun** for the nice moments that we have shared over the past few years.

Abstract

Groundwater contamination is one of the most challenging global environmental problems, as it threatens the water supply of humans and wildlife. All over the world, the quality of groundwater deteriorates considerably due to anthropogenic pollution (e.g., by industrial and agricultural activities, domestic and urban waste, industrial spills etc.) that occurs at the land surface and spreads easily into the subsurface. Amongst many contaminants commonly found in soils and groundwater, chromium (Cr) represents a serious threat, as its hexavalent form (Cr(VI)) is known to be carcinogenic and it is widely used in many industrial sectors. Nowadays many efforts are undertaken to reduce and prevent soil contamination and a wide range of remedial strategies have been developed to decontaminate polluted sites. Nevertheless, there is still a great need for innovative, non-disruptive and cost-effective technologies for *in-situ* remediation. The big advantage of *in-situ* compared to *ex-situ* approaches is the immobilization of contaminants directly underground, for example through the implementation of a permeable reactive zone/barrier obtained by introducing a reactant material into the subsoil. However, for a successful remediation, the material must remain reactive long enough to reduce the contaminant concentration below the remediation targets. Furthermore, in case of injection-based strategies, the transportability of the reactant through the aquifer must be guaranteed and is as important as its reactivity. The aim of this work is to contribute to a better understanding of the reactivity and transport behavior of two promising iron-bearing nanomaterials, sulfate green rust (GR_{SO4}) and sulfidized nano zerovalent iron (S-nZVI), in order to develop environmental-friendly and successful *in-situ* clean-up strategies. Therefore, laboratory experiments were designed to assess the effectiveness of GR_{SO4} and S-nZVI in immobilizing Cr(VI) in simulated permeable reactive barriers (PRBs) as well as to evaluate their suitability as injectable reactant materials.

The first part of the thesis investigates the geochemical processes occurring during Cr(VI) immobilization by GR_{SO4} and S-nZVI. By the combination of batch experiments with column studies, reactivity of both reactants in porous media (quartz sand) was investigated at static and dynamic conditions. Immobilization of Cr(VI) observed in these systems is mainly interpreted as a reduction of Cr(VI) to Cr(III). Additionally, under specific conditions adsorption of Cr(VI) on newly formed Fe(III)-hydroxides can play a role. Comparison of results from batch experiments with and without quartz sand, demonstrate that the presence of a porous medium does not hinder the immobilization processes. However, the column studies prove that the reactivity of GR_{SO4} and S-nZVI is exhausted much faster in dynamic conditions compared to the static batch experiments. This earlier exhaustion is explained by the constant Cr(VI) influx that keeps the reaction rates on the reactant particle surfaces high, which in turn induces faster surface passivation. Moreover, the results from different sets of

column tests at various conditions indicate that acidic conditions and a lower flow velocity of the contaminated water body through the reactive medium yield to higher Cr(VI) immobilization. These outcomes highlight the importance of conducting reactivity column studies for scaling up lab-scale applications to field scale. Furthermore, the comparison of the effectiveness of the two materials shows a significantly better performance of GR_{SO4} compared to S-nZVI, although a higher amount of reducing iron equivalents is present in S-nZVI. This can be explained by the fact that reduction of Cr(VI) by GR_{SO4} occurs not only at the particle surface but also in its interlayers, providing more reactive sites compared to the core-shell structure of S-nZVI. Moreover, S-nZVI particles tend to form larger aggregates more easily due to magnetic attraction, resulting in a less available reactive surface than assumed.

The second part of this thesis focuses on the transport behavior of GR_{SO4} and S-nZVI in model substrate (i.e., quartz sand), with the aim to evaluate their use as injectable particles and to identify the factors that influence their mobility. To answer these research questions, particle characterization analyses were performed in combination with transport column experiments. The results show the neglectable mobility of the tested GR_{SO4}, in contrast to the higher transport potential of S-nZVI when properly modified with the anionic stabilizer sodium carboxymethyl cellulose (CMC). Specifically, the results show that GR_{SO4} does not migrate through the voids of the porous medium mainly due to its crystal size and hexagonal shape that result in the clogging of the pores. Moreover, the attraction between the positive surface charge of GR and the negatively charged quartz sand particles leads to unfavorable conditions for particle mobility. On the other hand, S-nZVI that is modified with CMC after the synthesis (post-grafting method) exhibits better transportability than bare S-nZVI and its counterpart modified with CMC during nZVI synthesis (pre-grafting method). Although the post-grafting method yields to slightly bigger particle sizes, it provides electrosteric (combination of steric and electrostatic) forces that counterbalance the attractive forces between particles. This limits the formation of bigger and heavier aggregates and thus favors particle migration through the voids of the matrix. Overall, S-nZVI mobility through the packed bed columns is strictly dependent on the particle colloidal stability and on the effectiveness of the surface modification approach. The results of the on-line monitored column experiments indicate that greater particle mobility is achieved with higher injection flow velocity, lower particle concentration and higher CMC concentration. The results obtained by magnetic resonance imaging (MRI) show that it is possible to follow the particle movement trough the quartz sand matrix, evaluate the kinetics of particle migration, identify preferential flow paths and reconstruct the spatial distribution of the particles.

In conclusion, this thesis shows the better suitability of GR_{SO4} in immobilizing Cr(VI) in PRB applications and the higher transport potential of S-nZVI for injection-based *in-situ* technologies. The outcomes contribute to broaden the knowledge on the behavior of these iron-bearing materials as

reactants for groundwater remediation and confirm that it is worthwhile to conduct further studies on their field scale application.

Kurzfassung

Die Verunreinigung von Grundwasser durch Schadstoffe ist eines der größten globalen Umweltprobleme, da es vielerorts die Wasserversorgung von Menschen und Tieren bedroht. Überall auf der Welt verschlechtert sich die Qualität des Grundwassers aufgrund anthropogener Umweltverschmutzungen (z.B. durch industrielle und landwirtschaftliche Aktivitäten, Haus- und Siedlungsabfälle, Industrieabwässer usw.), die oft zuerst an der Erdoberfläche auftreten und sich anschließend in den Untergrund ausbreiten. Unter den vielen Schadstoffen, die häufig in Böden und im Grundwasser zu finden sind, stellt Chrom (Cr) eine ernsthafte Bedrohung dar, da es in seiner sechswertigen Form (Cr(VI)) nachweislich stark gesundheitsgefährdend ist und in zahlreichen Industriezweigen Anwendung findet. Gegenwärtig werden viele Anstrengungen unternommen, die Kontamination von Böden und Grundwasserressourcen zu reduzieren bzw. zu verhindern und es wurde eine Vielzahl von Sanierungsstrategien entwickelt, um verunreinigte Standorte zu dekontaminieren. Dennoch besteht nach wie vor ein großer Bedarf an innovativen, disruptionsarmen und kostengünstigen Technologien für die *in-situ* Sanierung von Altlasten. Der große Vorteil von *in-situ* gegenüber *ex-situ* Sanierungsverfahren ist die Immobilisierung von Schadstoffen direkt im Untergrund, zum Beispiel durch die Implementierung einer durchlässigen reaktiven Zone/Barriere, welche durch das Einbringen eines reaktiven Materials (Reaktant) in den Untergrund erzeugt wird. Für eine erfolgreiche Sanierung muss dieses Material jedoch lange genug reaktiv bleiben, um die Schadstoffkonzentration unter die angestrebten Sanierungsziele zu senken. Darüber hinaus muss im Falle von Injektionsstrategien die Transportfähigkeit des Reaktanten innerhalb des Grundwasserleiters gewährleistet sein und ist daher ebenso bedeutsam wie seine Reaktivität.

Ziel dieser Arbeit ist es, zu einem besseren Verständnis der Reaktivität und des Transportverhaltens von zwei vielversprechenden Nanomaterialien auf Eisenbasis, Grüner Rost Sulfat (GR$_{SO4}$) und sulfidiertes nullwertiges Nano-Eisen (S-nZVI), beizutragen, um umweltschonende und effiziente *in-situ* Sanierungsstrategien zu entwickeln. Aus diesem Grund wurden Laborexperimente konzipiert und durchgeführt, um die Wirksamkeit von GR$_{SO4}$ und S-nZVI zur Immobilisierung von Cr(VI) in simulierten permeablen reaktiven Barrieren (PRBs) zu bewerten und ihre Eignung als injizierbare reaktive Nanomaterialien zu evaluieren.

Der erste Teil der Arbeit untersucht die geochemischen Prozesse, die während der Cr(VI)-Immobilisierung durch GR$_{SO4}$ und S-nZVI auftreten. Durch die Kombination von Batch-Experimenten mit Säulenversuchen wurde die Reaktivität beider Reaktanten in porösen Medien (Quarzsand) unter statischen und dynamischen Bedingungen untersucht. Die in beiden Systemen beobachtete Immobilisierung von Cr(VI) wird in erster Linie als eine Reduktion von Cr(VI) zu Cr(III)

interpretiert. Zusätzlich kann unter bestimmten Bedingungen die Adsorption von Cr(VI) an neu gebildeten Fe(III)-Hydroxiden eine Rolle spielen. Der Vergleich der Ergebnisse von Batch-Experimenten mit und ohne Quarzsand zeigt, dass die Anwesenheit des porösen Mediums die Immobilisierungsprozesse nicht beeinträchtigt. Die Säulenversuche beweisen jedoch, dass die Reaktivität von GR_{SO4} und S-nZVI unter dynamischen Bedingungen im Vergleich zu den statischen Batch-Experimenten erheblich schneller erschöpft wird. Diese früher eintretende Erschöpfung erklärt sich durch den konstanten Cr(VI)-Zufluss, der die Reaktionsraten auf den Oberflächen der reaktiven Nanomaterialen auf einem konstant hohen Niveau hält, was wiederum eine schnellere Oberflächenpassivierung induziert. Darüber hinaus deuten die Ergebnisse aus verschiedener Versuchsreihen von Säulenexperimenten unter variierenden Bedingungen darauf hin, dass saure pH-Bedingungen und eine geringere Strömungsgeschwindigkeit des kontaminierten Wasserkörpers durch das reaktive Medium zu einer höheren Cr(VI)-Immobilisierung führen. Diese Ergebnisse machen deutlich, wie wichtig die Durchführung umfangreicher reaktiver Säulenversuche ist, bevor im Labor getestete Applikationen auf den Feldmaßstab hochskaliert werden. Darüber hinaus zeigt der Vergleich der beiden Materialien eine deutlich bessere Wirksamkeit von GR_{SO4} im Vergleich zu S-nZVI, obwohl im Falle von S-nZVI eine höhere Menge an reduzierenden Eisenäquivalenten vorhanden ist. Dies lässt sich durch die Tatsache erklären, dass die Reduktion von Cr(VI) durch GR_{SO4} nicht nur an der Partikeloberfläche, sondern auch in den Zwischenschichten stattfindet, so dass im Vergleich zur Core-Shell-Struktur von S-nZVI trotz geringerer Menge an Eisenäquivalenten mehr funktionelle Stellen vorhanden sind. Darüber hinaus neigen S-nZVI-Partikel dazu, aufgrund ihrer magnetischen Anziehung größere Aggregate zu bilden, was zu einer Verringerung der verfügbaren reaktiven Oberfläche führt.

Der zweite Teil dieser Arbeit befasst sich mit dem Transportverhalten von GR_{SO4} und S-nZVI in einem Modellsubstrat (Quarzsand), mit dem Ziel, ihre Verwendung als injizierbare Partikel zu bewerten und die Faktoren zu identifizieren, die ihre Mobilität beeinflussen. Um diese Forschungsfragen zu beantworten, wurden Analysen zur Partikelcharakterisierung in Kombination mit Säulenexperimenten zum Transportverhalten durchgeführt. Die Ergebnisse zeigen die vernachlässigbare Mobilität des getesteten GR_{SO4}, im Vergleich zu dem höheren Transportpotential von S-nZVI nach entsprechender Modifikation mit dem anionischen Stabilisator Natriumcarboxymethylcellulose (CMC). Die Ergebnisse zeigen insbesondere, dass GR_{SO4} nicht durch die Hohlräume des porösen Mediums migriert, was hauptsächlich auf seine Korngröße und hexagonale Form zurückzuführen ist, die zum Verstopfen der Poren führen. Darüber hinaus führt die Anziehung zwischen der positiven Oberflächenladung von GR und den negativ geladenen Sandpartikeln zu ungünstigen Bedingungen für die Partikelmobilität. Demgegenüber weist S-nZVI, das nach der Synthese mit CMC modifiziert wird (post-grafting Methode), eine bessere Transportfähigkeit auf als reiner S-nZVI und sein entsprechendes Pendant, das während der nZVI-Synthese mit CMC modifiziert wurde (pre-grafting Methode). Obwohl die post-grafting Methode zu etwas größeren Partikelgrößen führt, bewirkt sie höhere elektrosterische Kräfte

(Kombination von sterischen und elektrostatischen Kräften), die die Anziehungskräfte zwischen den Partikeln ausgleichen. Dies begrenzt die Bildung von größeren und schwereren Aggregaten und begünstigt so die Partikelmigration durch die Hohlräume der Matrix. Insgesamt ist die Mobilität von S-nZVI innerhalb des porösen Mediums stark abhängig von der kolloidalen Stabilität der Partikel und der Wirksamkeit der Oberflächenmodifikation. Die Ergebnisse der online überwachten Säulenversuche deuten darauf hin, dass sich Partikelmobilität durch eine höhere Injektionsflussgeschwindigkeit, eine geringere Partikelkonzentration und höhere CMC-Konzentrationen grundsätzlich verbessert. Die Ergebnisse der Magnetresonanztomographie (MRT) zeigen, dass es möglich ist, die Bewegung der Partikel durch die Quarzsandmatrix zu verfolgen, die Kinetik der Partikelmigration zu bewerten, bevorzugte Strömungswege zu identifizieren und die räumliche Verteilung der Partikel zu rekonstruieren.

Zusammenfassend zeigt diese Arbeit die bessere Eignung von GR_{SO4} zur Immobilisierung von Cr(VI) in PRB-Anwendungen und das höhere Transportpotential von S-nZVI für injektionsbasierte in-situ Technologien. Die Ergebnisse tragen dazu bei, das Wissen über das Verhalten dieser eisenhaltigen Nanomaterialien als Reaktanten für die Grundwassersanierung zu erweitern und bestätigen, dass es sich lohnt, weitere Studien zu ihrer Anwendung im Feldmaßstab durchzuführen.

Table of Contents

List of Figures

List of Figures

List of Tables

Abbreviations

A	Ampere
Å	Angstrom
Abs	Absorption at a specific distance
Abs_0	Absorption at time zero
AC	Activated Carbon
AGW	Institute of Applied Geosciences
ATSDR	Agency for Toxic Substances and Disease Registry
B_0	Static External Magnetic Field (T or $kg/s^2 \cdot A$)
BTC	Breakthrough Curve
BTEX	Benzene, Toluene, Ethylbenzene, Xylenes
cis-DCE	cis-Dichloroethylene
C	Particle concentration at a specific distance (kg/L or mM)
C_0	Inlet Particle Concentration (kg/L or Mm)
CMC	Sodium Carboxymethyl Cellulose
Cr	Chromium
Cr(III)	Hexavalent Chromium
Cr(VI)	Trivalent Chromium
cVOC	Chlorinated Volatile Organic Compound
δ	Density (kg/m^3)
D	Dispersion Coefficient
d	Interlayer Distance (Å)
Da	Dalton
d_c	Diameter of the matrix/collector diameter (m)
d_p	Diameter of the reactant particles (m)
D&G	Drain-and-Gate
DLVO	Derjaguin, Landau, Verwey, Overbeek
DNAPL	Dense Non-Aqueous Phase
ECHA	European Chemicals Agency
EC-PRB	Efficiently Controllable Permeable Reactive Barrier
EDL	Electrostatic Double Layer
EEA	European Environment Agency
EGG	Geochemistry and Economic Geology
ELS	Electrophoretic Light Scattering
ENP	Engineered Nanoparticle

Abbreviations

ESEM	Environmental Scanning Electron Microscope
F&G	Funnel-and-Gate
GAC	Granular Activated Carbon
γ	Share Rate (s^{-1})
γ_g	Gyromagnetic Ratio ($s^{-1} \cdot T^{-1}$)
GIF	Gatan Imaging Filter
GMS	Gatan Microscopy Suite
GR	Green Rust
GR_{SO4}	Sulfate Green Rust
Hz	Hertz (s^{-1})
ICP-OES	Inductively Coupled Plasma Optical Emission Spectrometry
IMA	International Mineralogical Association
ISCO	*In-Situ* Chemical Oxidation
ISCR	*In-Situ* Chemical Reduction
ITRC	Interstate Technology and Regulatory Council
JRC	Joint Research Centre
k	kilo
KIT	Karlsruhe Institute of Technology
LERA	Laboratory of Environmental and Raw Materials Analysis
LLNL	Lawrence Livermore National Laboratory
LNAPL	Light Non-Aqueous Phase
LOD	Limit of Detection
LOQ	Limits of Quantification
MCL	Maximum Contaminant Level
μ	Magnetic Moment ($A \cdot m^2$)
min	Minute
ms	milliseconds
MRI	Magnetic Resonance Imaging
MRT	Magnetic Resonance Tomography
MW	Molecular Weight (kg/mol)
n	Porosity (%)
NA	Natural Attenuation
NMR	Nuclear Resonance Magnetic
NPL	National Priorities List
NRD	Natural Reductant Demand
nZVI	Nanoscale Zerovalent Iron
ω_0	Lamor Frequency (mHz)
P	Angular Momentum (T or $kg \cdot m^2/s$)

PAH	Polycyclic Aromatic Hydrocarbons
PCB	Polychlorinated Biphenyl
PCE	Tetrachloroethylene
P&T	Pump-and-Treat
pH	Power of Hydrogen
PP	Polypropylene
ppm	Parts per Million
ppb	Parts per Billion
PRB	Permeable Reactive Barrier
PVC	Polyvinyl Chloride
px	Pixel
pzc	Point of Zero Charge
RARE	Rapid Acquisition with Relaxation Enhancement
REACH	Registration, Evaluation, Authorization and Restriction of Chemicals
SEM	Scanning Electron Microscope
s	Second
S-nZVI	Sulfidized Nanoscale Zerovalent Iron
SVHCs	Substances of Very High Concern
T	Time (s)
T	Tesla
TEM	Transmission Electron Microscopy
T&G	Trench-and-Gate
TCA	Trhichloroacetic Acid
TCE	Trichloroethylene
US EPA	United States Environmental Protection Agency
UV-Vis	Ultraviolet and Visible
V	Volume (m^3)
v	Velocity (m/sec)
VC	Vinylchloride
v_s	Settling Velocity (m/sec)
WHO	World Health Organization
wt	weight
x	Cuvette height (m)
XG	Xanthan Gum
XRD	X-Ray Diffraction
ζ	Zeta Potential (Mv)

1 Introduction and Objective of the Study

The past century has witnessed a significant environmental deterioration worldwide due to the extremely high rates of population growth, urbanization and industrialization, which have generated an increasing number of contaminated sites (European Commission - JRC, 2014; Pal et al., 2014; Jan et al., 2015). Common contaminants include organic compounds such as pesticides, petroleum hydrocarbons, chlorinated hydrocarbons, and inorganic species such as toxic metal(loids) and radioactive wastes (US EPA, 2006; Wuana and Okieimen, 2011; European Commission - JRC, 2014). Many of these pollutants are highly toxic and in some cases even carcinogenic (Wilbur et al., 2012; Jan et al., 2015). According to the recent European Commission's Joint Research Centre (JRC) Technical Report about the status of local soils contamination, there are around 2.8 million potentially contaminated sites in Europe (Pérez and Rodríguez Eugenio, 2018). At the end of 2016, around 694,000 sites (260,000 of them in Germany) have been registered where polluting activities took or are taking place, with an increment of 76,000 new sites compared to 2014. Most of the contaminated sites occur in highly developed areas, agricultural areas and industrial zones; but in many cases, it is hard to accurately identify the specific pollution source (e.g., industries, farms, highways etc.) (Mateo-Sagasta et al., 2017; Pérez and Rodríguez Eugenio, 2018; US EPA, 2018). Over the past decades, numerous regulations have been enacted (i.e., strict regulations for the disposal of toxic, implementation of recycling) to lower and prevent land contamination (ITRC, 2005). Concomitantly, several different remedial strategies have been used to clean-up contaminated sites (US EPA, 1996; Smith et al., 2003; Birke et al., 2006). Nevertheless, about 90 % of the registered sites are still polluted (Pérez and Rodríguez Eugenio, 2018). Compared to soil remediation, which generally is very challenging and often expensive, groundwater remediation is made more difficult by the "dynamic" nature of the environment (National Research Council, 1994b; Naidu et al., 2014). Heterogeneity of the subsurface environment strongly affects contaminant distribution (e.g., preferential flows, downward migration), which makes groundwater decontamination one of the most challenging environmental problems (US EPA, 2018). The majority of the widely used groundwater remedial strategies have not fully succeeded due to technologically limitations or environmental constrains (Travis and Doty, 1990; National Research Council, 1994c).

Among the wide range of remediation strategies, a distinction must be made between those that treat the "source zone" and those that treat "contaminated plume" (National Research Council, 1994b; US EPA, 2008a). Most of the technologies used to treat contaminated source media involve the physical extraction and treatment and/or disposal to a suitable facility off site, thus they are named *ex-situ* technologies (US EPA, 1997). The original site is then filled with uncontaminated material. If the

pollutant exists only in soil, the soil is excavated. Meanwhile, if contamination has reached the groundwater, it is pumped with wells and both the polluted soil and water are removed (US EPA, 1996; US EPA, 1997). Some examples of *ex-situ* technologies are steam flushing, conductive heating, air sparging, electrical resistance heating, dig-and-pump, pump-and-treat (P&T) (US EPA, 1990). The biggest drawbacks of these technologies are interference with the activities and infrastructures present above ground, the need of large storage and treatment areas, the use of working with heavy excavation equipment, and exposure to highly contaminated materials (US EPA, 1999a). They are also generally costly and require very long treatment times (~ 50-100 years) (US EPA, 1989a; US EPA, 2001). However, although they are extremely expensive and land disruptive, they are still often the first choice.

Given those disadvantages, the search for innovative, cost-effective and environmental-friendly strategies is critical. Thus, *in-situ* approaches are good alternatives to these highly disruptive extraction-based strategies (US EPA, 1998; Gavaskar, 1999; Thiruvenkatachari et al., 2008). An *in-situ* approach generally aims to transform or degrade the compound of concern into a less toxic phase directly underground (US EPA, 1998; Gavaskar, 1999). Depending on the extent and location of contamination, different *in-situ* clean-up technologies have recently been optimized (Thiruvenkatachari et al., 2008; Mueller et al., 2012). Over the past decades, *in-situ* chemical reduction (ISCR) performed via introduction of reducing agents (e.g., sodium dithionite, zerovalent iron (ZVI)) has been shown to be a promising strategy to treat the source zones of contaminants without disturbance to the soil structure (US EPA, 1998; Crane and Scott, 2012; Mueller et al., 2012). In general, there are two ways to bring the reducing agent in contact with the contaminated area: direct injection, or construction of a permeable reactive barrier (PRB) (Tratnyek and Johnson, 2006; Crane and Scott, 2012). Injection of mobile reactive particles is mostly employed to treat source contaminated areas (Crane and Scott, 2012). However, it is not suitable for decontamination of contaminant plumes, due to the heterogeneous distribution and different aquifer characteristics along the groundwater flow direction. PRBs, on the other hand, are installed in the subsurface to intercept and treat the contaminated plume avoiding any displacement above land or water body extraction (US EPA, 1998; Thiruvenkatachari et al., 2008).

One of the most common material used for ISCR is nanosized zerovalent iron (nZVI), due to its high reactivity (Kate Bronstein, 2005; Mueller et al., 2012). However, it has been shown that reactions between nZVI and natural reducible water constituents are responsible for surface passivation, which leads to a fast decrease in particle longevity and contaminant reactivity (Lim and Zhu, 2008; Sarathy et al., 2008). Recently, modification of nZVI surface via sulfidation (i.e., by reducing sulfur compounds) has emerged as a new approach to avoid reaction with water (anaerobic corrosion) (Han and Yan, 2016; Fan et al., 2017). This approach enhances the selectivity and degradation rate for contaminants such as trichloroethylene (TCE) (Kim et al., 2013; Rajajayavel and Ghoshal, 2015) or hexavalent chromium, Cr(VI) (Gong et al., 2017; Li et al., 2018). Therefore, sulfidized-nZVI (S-nZVI) is considered a highly promising reactant for ISCR in contaminated groundwater. Aside from S-nZVI, there are also natural

reactant materials such as green rust (GR) that have drawn the attention of researchers due to their physicochemical properties. GR is a natural occurring Fe(II)-Fe(III) layered double hydroxides (LDHs) that often forms in suboxic/anoxic, Fe^{2+}-rich environments (Refait et al., 1998; Trolard et al., 1997). Due to its structural and chemical properties, GR has shown high potential for the remediation of organic and inorganic contaminants (Bhave and Shejwalkar, 2018; Latta et al., 2015; Skovbjerg et al., 2006). In addition, GR is quite easy and inexpensive to produce.

To date, very little is known about:

- stability, reactivity and mobility of S-nZVI and GR when they are in contact with porous matrix,
- the reactivity of S-nZVI and GR under dynamic conditions,
- the optimal conditions enhancing the removal performances as well as the hindering factors causing a fast depletion.

Answering those questions will help shaping their application as *in-situ* reductants.

One aim of this PhD thesis is to assess and compare the performances of S-nZVI and GR for Cr(VI) removal, which is one of the world's most critical metals (Wuana and Okieimen, 2011). Hexavalent chromium was chosen as the main target contaminant because of its high environmental relevance as it is widely used in many industrial applications (e.g., tanning, dyes and paint productions, wood preservatives, metallurgy, electroplating), but it is also a highly toxic and carcinogenic metal (Gad, 1989; Wilbur et al., 2012; Lunk, 2015). So far, very little is known about GR and S-nZVI reactivity in sand matrices, whether in batch or column set-ups but such information is critically needed to evaluate the potential use of GR as alternative reductant material to ZVI in *in-situ* subsurface treatment applications. In this context, batch systems have been investigated under anoxic conditions and reactivity sand-bed column experiments were performed to better understand the role of operating parameters such as linear flow rates, inlet Cr(VI) concentrations and pH conditions. In the end, a conceptual model has been developed to understand the optimal geochemical conditions for a successful *in-situ* Cr(VI) remedial strategy based on each reactant.

However, before upscaling a remediation strategy that is efficient to remove a specific contaminant, it is necessary to address uncertainties, including how to effectively introduce these particles in the subsurface environment. To successfully clean-up contaminated source areas, the transportability of the reductant material is a key factor. Additionally, this research is focused on the study of the transport properties of the two reactants at lab scale, focusing on the parameters that influence their stability and longevity as injected into an anoxic model aquifer material. To achieve this, transport column experiments with representative homogenous porous media were designed and performed to assess the mobility behavior of the tested reactants. The overall aim of the thesis is the comparison of reactivity (versus Cr(VI)) and transportability of GR and S-nZVI regarding to their use as reactants in *in-situ* remediation technologies.

2 Groundwater Contamination: A Global Environmental Issue

As a consequence of the increased urbanization and global industrialization, undesirable chemical elements (organic and inorganic compounds) have spread into air, water and soil (European Commission - JRC, 2014; Pal et al., 2014). To date, most of these substances have been categorized as pollutants (Sharma and Bhattacharya, 2017). Inorganic and organic pollutants derive from a wide range of sources and represent one of the major threats to natural ecosystems, endangering the health of many species including humans (Brown et al., 1984; US EPA, 2006).

Typical examples of single water contamination sources, referred as "point sources pollution", are related to anthropogenic activities such as industrial manufacturing, (oil) refining, mining and ore processing, as well as improper (often illegal) waste disposal and accidents involving hazardous materials (Wuana and Okieimen, 2011; Sharma and Bhattacharya, 2017). Moreover, many industrial sectors use a large number of emerging contaminants such as artificial sweeteners, flame retardants (e.g., polybrominated diphenyl ethers) (Pal et al., 2014), unregulated chemicals and substances such as heavy metals, rare earth metals, brominated and chlorinated organics and inorganics for commercial use that will significantly elevate the level of environmental pollutants within the next thirty years (Kuppusamy et al., 2016). According to Daughton (2004), approximately 27 % of the unregulated chemical pollutants, which are estimated to be 22,000, is commercially available and only 0.03 % is addressed by the current regulations. Additionally, "non-point sources pollution" deriving from diffuse sources such as pesticides used in agriculture or storm water runoff from land into waterways, can also cause severe water pollution (Thiruvenkatachari et al., 2008; Mateo-Sagasta et al., 2017). Unfortunately, non-point sources are very challenging to deal with due to their hardly traceable origin (National Research Council, 1994b). Furthermore, harmful substances, which are released into the air, eventually settle down and can accumulate in water resources. Given the serious threat posed by both organic and inorganic contaminants, many institutions such as the World Health Organization (WHO), the European Environment Agency (EEA) and the United States Environmental Protection Agency (US EPA) have been working for many years to address environmental issues and create a cleaner global environment by establishing environmental regulations/laws and defining threshold limits. Nevertheless, the number of contaminated sites continues to increase. In Europe, there are 2.8 million potentially contaminated sites, of which more than 650,000 have already been identified (Pérez and Rodríguez Eugenio, 2018). Approximately 90 % of the registered sites need to be remediated. In the USA as 2020, there were 1,335 Superfund sites on the National Priorities List (NPL) that require a long-term response to clean-up hazardous material contaminations (US EPA, 2020).

2.1 Nature of Contamination

Inorganic contaminants include anions (e.g., fluoride, chloride, nitrate, phosphate, sulfate, and cyanide) and (heavy) metals (arsenic (As), lead (Pb), chromium (Cr), copper (Cu), uranium (U), iron (Fe), nickel (Ni), zinc (Zn), cadmium (Cd), mercury (Hg), manganese (Mn), molybdenum (Mo), selenium (Se), vanadium (V)) (US EPA, 2006; Geurts et al., 2009; Wuana and Okieimen, 2011). Although some anions and metals are required in small doses by organisms for specific catalytic functions, they are toxic in excess and may cause severe damage depending on the length of exposure (US EPA, 2006; Jan et al., 2015). Unlike many chlorinated volatile organic carbons (cVOCs) like chlorinated ethenes (tetrachloroethylene (PCE), trichloroethylene (TCE), cis-dichloroethylene (cis-DCE) and vinylchloride (VC)), which in a reductive environment can be partially or totally converted to harmless substances (e.g, halogen-free ethane, ethene and chloride) (Matheson, 1994; Liu et al., 2005; Tobiszewski and Namieśnik, 2012), inorganic contaminants cannot be broken down into harmless elements or compounds, nor do they undergo chemical or microbial degradation (Kirpichtchikova et al., 2006). Overall, (heavy) metals such as Pb, Cr, As, Zn, Cd, Cu, Hg and Ni are the most found (in order of abundance) at contaminated sites (Wuana and Okieimen, 2011). Some of these metals can undergo redox reactions to form solid precipitates with groundwater constituents, while those that are not susceptible to redox reactions may be removed by adsorption, precipitation or co-precipitation on mineral surfaces. Therefore, clean-up strategies for inorganics are based on many different methods and processes like physical separation and recycling, sequential extraction, physical encapsulation/stabilization, vitrification, phytoremediation or transformation of them into non-toxic forms through complexation with organics or by changing their speciation (Mulligan and Gibbs, 2001).

The range of toxicity to human health depends on the chemical form of the heavy metal. Till the 1990s, some heavy metals with a generally lower toxicity were often left on-site due to their low bioavailability, allowing natural biological, chemical and physical processes to treat groundwater contaminants; often without a constructed treatment system used in combination. This approach is called "natural attenuation" (NA) and the likelihood of success was later rated as moderate or low (Gerth et al., 2001). In general, NA effectiveness has being debated critically (MacDonald, 2000).

2.2 Groundwater Remediation Techniques

2.2.1 Conventional Techniques: *Ex-Situ* Treatments

Over the past fifty years, several technologies have been used in pilot- and field-scale applications in order to remove toxic compounds from the subsurface. *Ex-situ* (above ground) technologies are the most used although they are land disruptive, generally expensive and very lengthy in reaching the remedial goals. They require the extraction of contaminated groundwater through wells and its subsequent treatment and/or disposal off-site (US EPA, 1996).

2.2.1.1 Pump-and-Treat

Pump-and-treat (P&T) system is the one of the oldest and most widespread technology employed for groundwater decontamination worldwide. P&T is a hydraulic containment method, which aims to stop contaminant propagation from the contaminated source area (US EPA, 1996). To meet this goal, P&T requires the extraction of groundwater and its on-site treatment above ground. Once treated, it can either be reinjected underground or disposed of off-site (US EPA, 1996; US EPA, 1999c). In the latter case, the extracted groundwater is replaced with clean water coming from nearby reservoirs. Occasionally, the extracted groundwater is directly discharged into a surface water body (e.g., stream) without prior treatment (US EPA, 1999c). This is possible when the contaminant concentration in the extracted water does not exceed surface water standards. Most P&T systems cause some mixing of clean and contaminated ground water during extraction, which leads to an increasing volume of water that needs to be extracted. The extraction design (e.g., location, numbers and spacing of extraction wells, drilling method and pumping rate), the *ex-situ* treatment process (e.g., the specific water treatment system, single or multiple clean-up method, need of holding tanks) as well as the discharge location (on-site water body, subsurface or off-site) are strongly dependent not only on the local hydro-geochemical and contaminant conditions, but also on the infrastructure. Particularly in urban areas, the installation and operation of a P&T system can be very difficult.

Until 1992, P&T was the predominant technology for addressing groundwater contamination (Kate Bronstein, 2005; Karn et al., 2009). Although it is still a well-accepted approach, it is often not applicable and may not suitable for many remedial scenarios due to specific on-site hydrogeological and contaminant properties (Voudrias, 2001). Unfavorable conditions include: low hydraulic conductivities ($< 10^{-7}$ cm/s) and/or low-permeability formations (e.g., clays and silts), heterogeneous geological conditions (e.g., stratified silt-sand-clay-gravel aquifers) or, in case of organic contaminants, the presence of significant volumes of light and/or dense non-aqueous phase liquids (NAPL) trapped on top or below the water table (US EPA, 1990). Often, contaminant concentration in groundwater treated with P&T can undergo two phenomena, namely *"rebound"* and *"tailing"*, which are often responsible for ineffectiveness of the remedial technology (Figure 2-1) (US EPA, 1994; US EPA, 1996). "Rebound" occurs when due to the extraction of groundwater at multiple extraction wells (pumping at the same time and at different depths) the water table depresses too quickly, leaving residual contaminants in the soil. Once the treatment is shut down and the groundwater level returns to its normal level, the leftover contaminants dissolve again and reach nearly pre-pumping concentrations (US EPA, 1996). "Tailing" refers to the progressively slower rate of decline in dissolved contaminant concentration while P&T is still operating (US EPA, 1996). It is the asymptotic decrease of contaminant concentration in water that is removed in the clean-up process. Due to tailing, it is necessary to pump greater volumes and for a longer period of time to achieve a specific clean-up target and it has been

shown that in the long run the contaminant concentration will often return to the pre-pumping level (Voudrias, 2001).

In 1989, the US EPA surveyed 19 operating P&T sites and published that at none of these sites the aquifer had been restored to drinking water standards (US EPA, 1989a; US EPA, 1989b; US EPA, 1989c). This was confirmed in a more extensive study made by the National Research Council (National Research Council, 1994a) that showed that 90 % of 77 investigated P&T sites had not attained remediation goals. Travis and Doty (1990) conducted an extensive survey of P&T operations in the USA and revealed that it is impossible to reduce dissolved contaminant compounds below drinking water standards in less than 50-100 years. Typically, an initial drop in the contaminant concentration by a factor of 2-10 was experienced, followed by a levelling with no further decline. The authors heavily criticized P&T systems because of the extensive groundwater pumping and the required treatment of large water volumes over long time periods, emphasizing the ineffectiveness of the method in achieving clean-up goals in short times. Generally, the duration required for remediation increases with the total contaminant amount and the size of the source area. In general, P&T is more effective for plume containment than aquifer restoration (Doty and Travis, 1991).

According to a survey conducted in the USA in 2001, only 2 of the 32 groundwater remediation sites investigated had achieved the defined remediation goals with an average capital cost of $ 4.9 million (US EPA, 2001). As a result, the number of public sites in the USA remediated by P&T decreased from an average of 80 % before 1992 to less than 20 % in the period 2001-2005 (Karn et al., 2009).
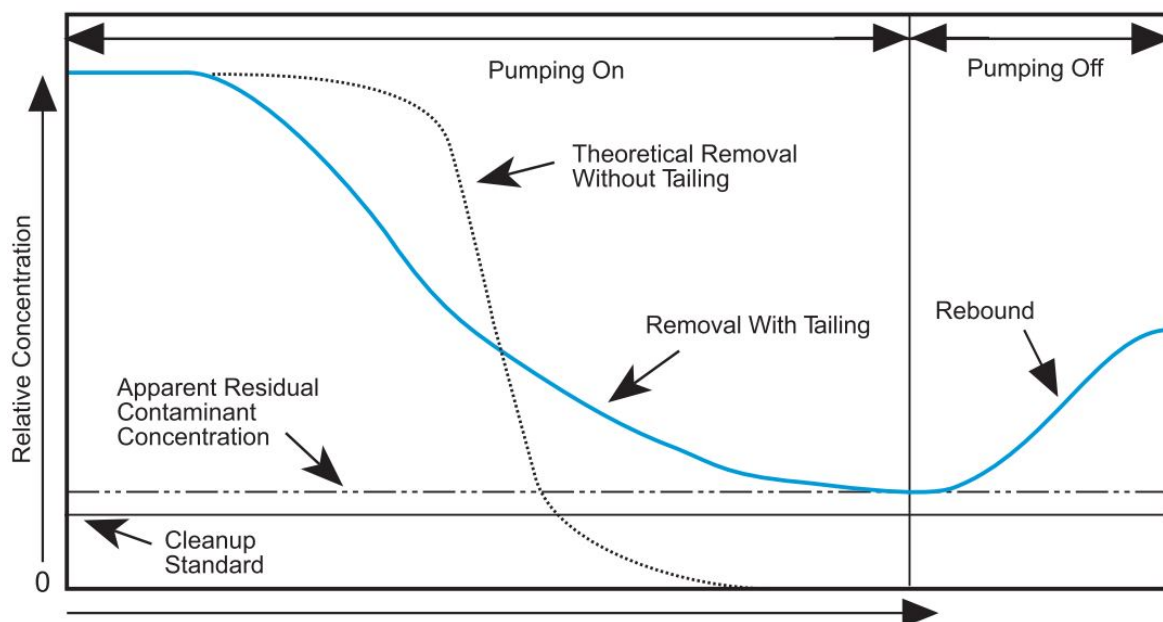
Figure 2-1   Graph of contaminant concentration versus pumping duration or volume showing tailing and rebound effects (US EPA, 1996).

Other major disadvantages of P&T facilities are the large amount of waste generated during water treatment (contaminated sludges or filters) as well as the risk of a possible contaminant leakage into deeper soil beds. To prevent leakage, P&T applications should be combined with measures of isolation and/or removal of the source of contamination, measures that significantly increase operating and maintenance costs (Voudrias, 2001). Another drawback is the continuous high energy consumption required for: pumping water from the extraction wells, operating water treatment, maintenance and long-term monitoring. Moreover, as P&T operations are shut down, dissolved contamination plumes often form again (Starr and Cherry, 1994).

2.2.2 *In-Situ* Treatments: Permeable Reactive Zones

Over the last two decades, innovative *in-situ* (below-ground) technologies such as bioremediation, chemical oxidation, multiphase extraction, natural attenuation, have drawn attention of researchers, experts and stakeholders. The most promising, effective and environmentally acceptable alternative to conventional *ex-situ* approaches is the permeable reactive barrier (PRB) technology (Gu et al., 1999; Puls et al., 1999; Gavaskar et al., 2005). A PRB technology was originally defined by the US EPA as (US EPA, 1998):

> *"An emplacement of reactive materials in the subsurface designed to intercept a*
> *contaminant plume, provide a flow path through the reactive media, and*
> *transform the contaminant(s) into environmentally acceptable forms to attain*
> *remediation concentration goals down gradient of the barrier."*

The clean-up goal is to lower the contaminant concentration to a level equal to or lower than a permitted limit value based on toxicity studies and defined by environmental agencies such as the US EPA or the EEA. PRB measures are meant to be non-disruptive, environmentally sustainable and cost-effective. Unlike the *ex-situ* technologies, PRB installations passively remove the contaminants (physically, chemically or biologically) in the underground without any additional treatment, thereby avoiding the dislocation of soil or groundwater, reducing the risk of exposure to the polluted material and allowing the use of the aboveground infrastructures (US EPA, 1998; Faisal et al., 2018). Furthermore, PRB systems do not produce waste waters that need to be disposed or treated and there is no risk of potential cross media contaminations as the contaminants are not brought to the surface (US EPA, 1999a). Moreover, after installation, the property can be re-used for other purposes.

PRBs have been used since the 1970s. Firstly, the goal was to intervene at sites polluted by acid mine drainage. In the earlier stages, the most common used reactive material was limestone ($CaCO_3$), a natural and cheap raw material (Faisal et al., 2018). In the following two decades, PRB technology represented only an alternative for the commonly used *ex-situ* clean-up strategies if these were not applicable. In 1990, Reynolds and his group from the University of Waterloo (Ontario, Canada)

published the first paper on the reductive dehalogenation of halogenated hydrocarbons by certain well casing materials, including granular iron (also known as zerovalent iron or ZVI) (Reynolds et al., 1990). After this publication, the use of ZVI for environmental issues was extensively researched, as it was readily and inexpensively available and due to its promising effectiveness in removing chlorinated organic compounds from groundwater (Reynolds et al., 1990; O'Hannesin and Gillham, 1998). However, the first field applications of ZVI have not received particular attention. In 1994, the first pilot-scale PRB system using ZVI was built at the Canadian Forces Base Borden site in Ontario to treat groundwater polluted by chlorinated ethylenes; while the first full-scale commercial application was installed at the Intersil Semiconductor Site in Sunnyvale, California. Two years later, a full-scale continuous wall PRB (46 m long, 7.3 m deep, and 0.6 m wide) was installed to treat a combined inorganic (chromate and sulfate) and organic (volatile chlorinated organic compounds such as TCE, cis-DCE, and VC) plume at the USCG Facility in Elizabeth City (North Carolina) (Wilkin et al., 2014).

In lights of these first promising applications, in the period between 1993 and 2001, many PRBs have been installed across the United States and Canada to treat a wide range of contaminants, including organic contaminants and (heavy) metals. In June 2002, the US EPA declared that: *"PRBs are no longer perceived as an innovative remediation technology but are rapidly maturing and may be considered as a standard remediation technology"* (US EPA, 2002a). In 2004, of the more than 200 PRBs in use around the world, 120 (90 in the US) were based on zerovalent iron, while the rest was using other reactive materials such as organic carbon, wood waste and by-products from pulp and paper manufacturing, zeolite, apatite and phosphate-based adsorbents as well as amorphous ferric oxyhydroxides (ITRC, 2005).

2.2.2.1 Reactive Zone Design

PRBs can be replaceable, semi-permanent, or permanent units within the flow path of a contaminant plume (Faisal et al., 2018). They are best applied to shallow, unconfined aquifer systems in unconsolidated deposits. A PRB must be placed down gradient from the edge of the plume and perpendicularly oriented to the groundwater flow to maximize contaminant interception (Gavaskar, 1999; Puls et al., 1999). As the plume passes through the PRB, contaminants are either transformed into less harmful compounds or trapped by the reactant material. Based on the method used for the allocation of the reactant, many methods have been optimized for decontamination (Kate Bronstein, 2005).

A PRB must be designed to provide adequate residence times (contact time between the contaminants and the reactive medium) so that the physicochemical interaction processes can take place (US EPA, 1998). The thickness (b) of the barrier is determined by the groundwater velocity (v) and the residence time (t) required (Gavaskar, 1999):

$$\mathbf{b = vt} \qquad\qquad \textbf{Equation 2-1}$$

It is worth noting that v is the velocity through the reactive wall and not the velocity in the aquifer and depends on the relative porosities and hydraulic conductivities of both the aquifer and the reactive barrier. In case of extremely fast-moving groundwater, the thickness and the width of the barrier must be designed accordingly. On the other hand, extremely slow-moving or stationary groundwater may hinder the contact between the contaminants and the reactive medium. Generally, most contaminated sites are likely between these two extremes (Gavaskar, 1999).

It is important that the reactive materials remain in place and active for the intended life cycle of the PRB, meaning that no material wash-out or passivation should occur. A decrease in effectiveness would be counterproductive for the remedial aim and economically disadvantageous. Permeable reactive zone technologies fall into two general categories:

1. Wall strategies:
   - continuous walls systems where the reactive medium is placed in an excavated area (trench) (Figure 2-2a)
   - funnel-and-gate (F&G) systems in which impermeable walls direct the groundwater flow through smaller cells/gates of reactive material (Gavaskar, 1999).
2. Injection strategies where reducing agents (e.g., sodium dithionite), organic substrates (e.g., vegetable oil and nutrients) or reactive nanoparticles are injected directly into the subsurface (Figure 2-2).

The depth of the installation is the main factor that drives the selection of a particular construction design for permeable barriers. The PRB installations require some degree of excavation, which limits the operating depth to maximum 20 m (Thiruvenkatachari et al., 2008).
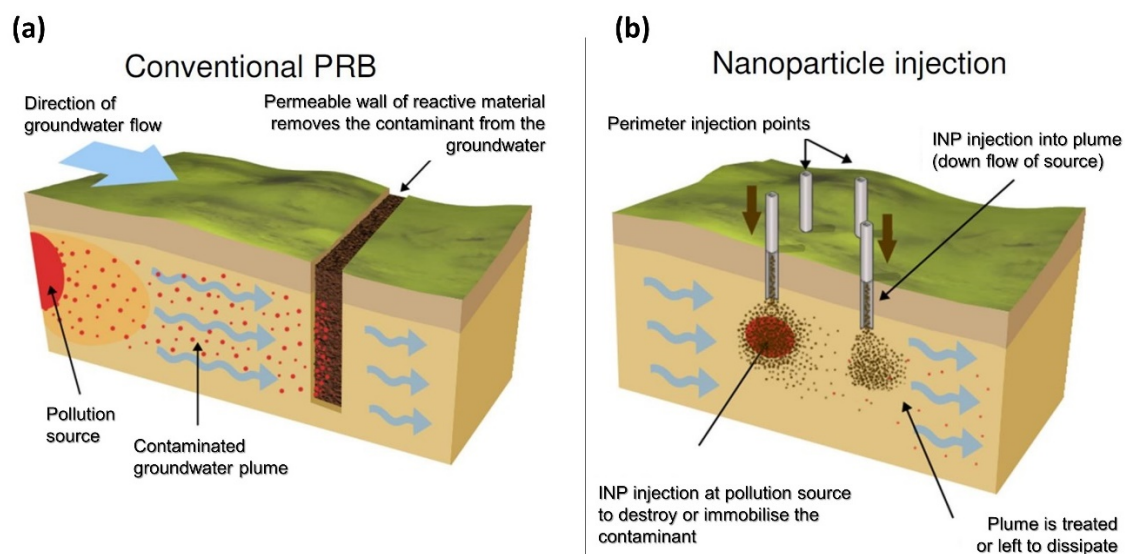
Figure 2-2 **(a) Conventional PRB (continuous wall or trench) configuration and (b) nanoparticle injection (Crane and Scott, 2012).**

i   Continuous walls

Continuous wall (or trench) PRBs consist of a treatment zone created by excavating an area isolated by walls, and refilling it with a porous reactive medium (e.g., granular/nanosized iron, pyrite, apatite, zeolites, reducing agents etc.), which is selected based on the reaction rate of the contaminant to be treated (US EPA, 1998; Kate Bronstein, 2005; Faisal et al., 2018). The walls or trenches must be more or as permeable as the surrounding aquifer material (US EPA, 1998). The width of the trench depends on the characteristics of the site (Figure 2-3a and Figure 2-3c). This approach is limited to shallow applications (depths of 10 m or less) (Henderson and Demond, 2007). A main disadvantage of this method is the cost of building the trench.

ii   Funnel-and-gate

The funnel-and-gate (F&G) configuration consists of impermeable sides like sheet pilings or slurry walls with low hydraulic conductivity that are installed in a saturated aquifer to deviate contaminated plume through one or more permeable reactive gates (Figure 2-3b and Figure 2-3d) (Starr and Cherry, 1994). The concept was mentioned by McMurtry and Elton in 1985, while the term was introduced in by Starr and Cherry in 1994. This technology suits to shallow aquifers (< 15 m below surface) and can be deployed slightly deeper than continuous trench systems (Yabusaki et al., 2001). The width of a F&G barrier system depends on the relative hydraulic conductivities of the reactive gates and the surrounding aquifer (Gavaskar, 1999). Generally, the groundwater velocity through the gate is several times higher than the natural velocity, while the ratio of the length of the funnel to the length of the gate is usually less than six (ITRC, 2005). Construction cost of a F&G barrier is higher than of a continuous wall system (Thiruvenkatachari et al., 2008). However, the F&G configuration requires less reactive media and is therefore usually chosen when a costly reactive material is employed (Thiruvenkatachari et al., 2008). Additionally, F&G systems are intended to function with little or no maintenance for long periods. Figure 2-3 shows a schematic configuration of both trench/wall and F&G configuration.
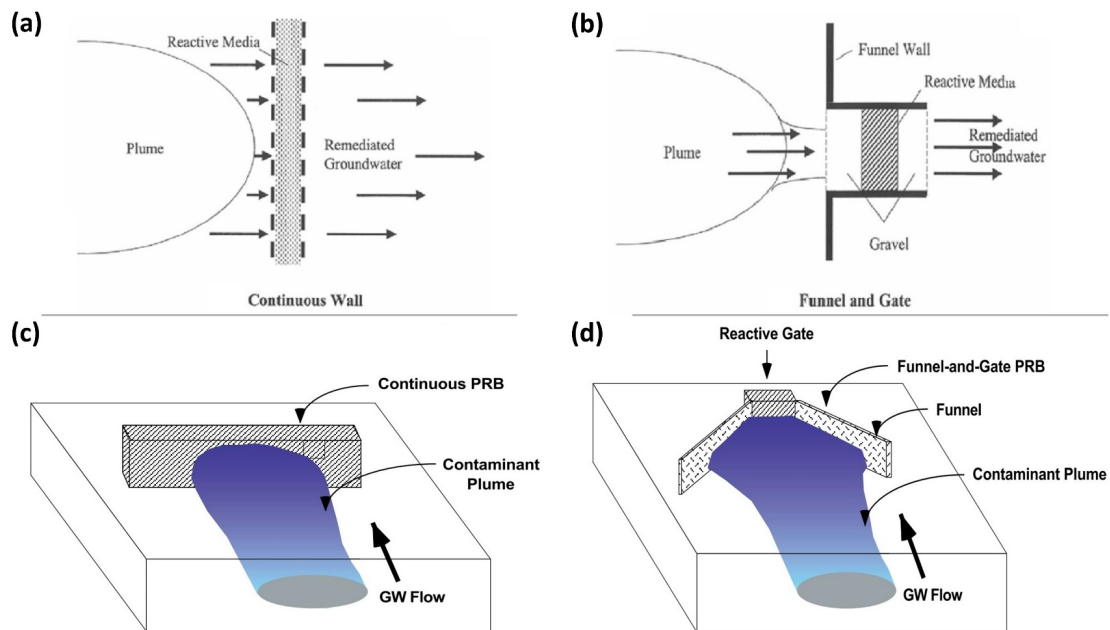
Figure 2-3 **Plume capture by (a, c) a continuous trench/wall PRB system and by a (b, d) funnel-and-gate PRB system (US EPA, 1998; ITRC, 2005).**

Furthermore, new PRB designs have been developed, such as drain-and-gate (D&G) or trench-and-gate (T&G) systems, where the groundwater is directed toward a reactor chamber equipped with inserted reactors and filter pipes instead of cut-off walls; or "Efficiently Controllable" PRBs (EC-PRBs), where the groundwater flow is directed and controlled by drainage, pipes, or even by active pumping (Birke and Burmeier, 2014).

iii   Injection strategy

If site conditions do not allow the application of traditional barrier systems, for example due to the impracticability of digging a trench (e.g., presence of existing infrastructures), a "reactive permeable zone" can also be created by drilling a series of injection wells or boreholes and injecting reactive or adsorptive substances into the subsurface (Figure 2-4a). In case of injection of reactive particles that are characterized by little or no mobility, the resulting treatment zone consists of overlapping layers of reactive particles adsorbed to the grains of a porous medium formed by sequential injections (Figure 2-4b) (Crane and Scott, 2012). Alternatively, if the reactive nanoparticles are sufficiently mobile, they are injected upstream of the contamination source, as they can migrate directly to the polluted zones (Tratnyek and Johnson, 2006) (Figure 2-4c).
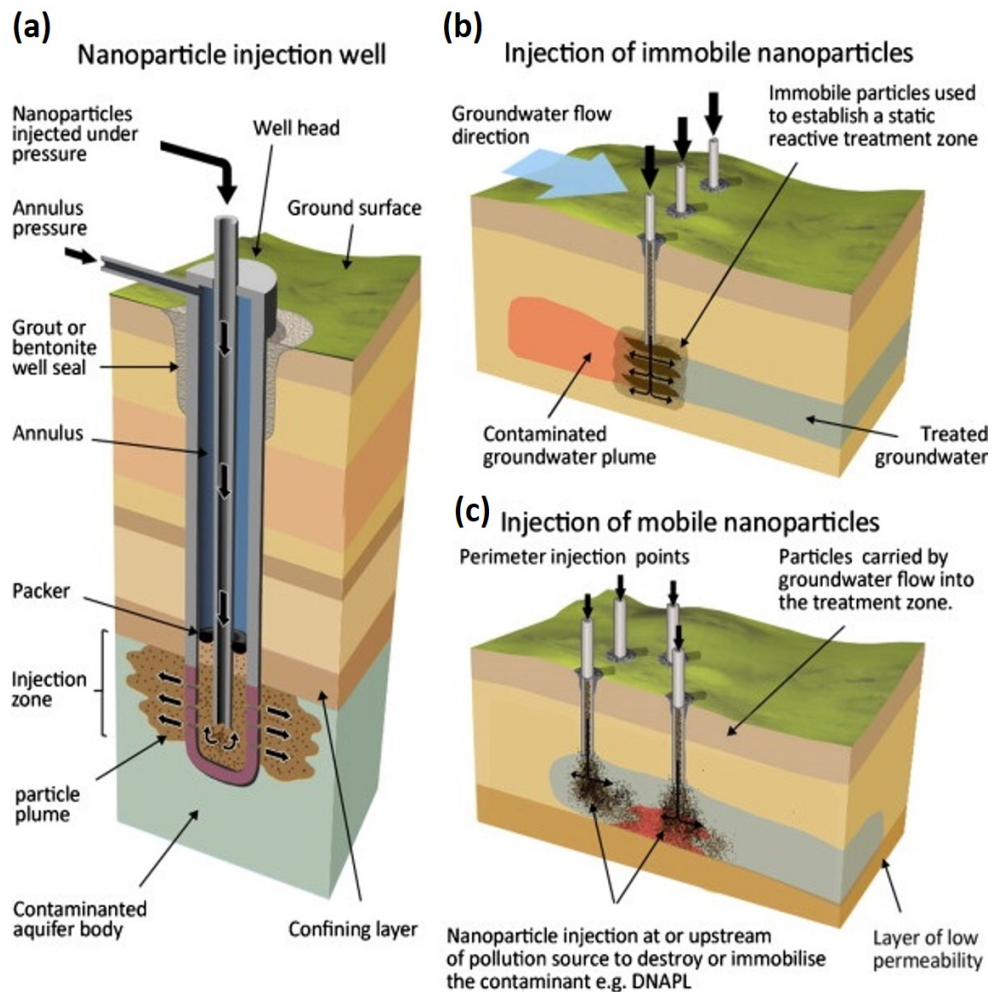
Figure 2-4 **(a) Scheme of a nanoparticle injection well and of the injection technology using (b) immobile and (c) mobile nanoparticles (Crane and Scott, 2012).**

Injection can be made via sonic push or sonic drilling through proper wells (US EPA, 1998; Crane and Scott, 2012; Mueller et al., 2012). In case of highly consolidated layers, hydraulic and/or pneumatic fracturing injection methods are chosen to facilitate the particle migration through the near-field soil pores (US EPA, 1998). Injection is suitable to reach deep contaminated aquifers that otherwise could not be treated with trenched or F&G-PRB configurations. The distribution and amount of injection wells depend on the local geological and geochemical conditions of a contaminated site rather than on the location of the contaminant zone (Crane and Scott, 2012). Injection methods have been used also for shallower applications to treat either plumes or contaminant source zones (Crane and Scott, 2012; Vermeul et al., 2014). Moreover, injection wells and the permeable walls can also be installed in combination. Effectiveness and longevity of injection-based PRB systems mainly depend on the sufficient and uniform distribution of the reactive material through the soil pore spaces.

Overall, in Europe, the F&G, D&G and EC-PRBs solutions are now common, while in North America are widely used the conventional continuous wall and reactive injection zones (Birke et al., 2006; Birke and Burmeier, 2014).

2.2.2.2 Reactive Media and Treatment Processes

While the remediation goal for organic compounds is to break them down into innocuous molecules and elements, the goal for inorganic contaminants is to change their chemical speciation via interaction processes, which result in their immobilization or degradation. Specifically, the principal reactions occurring in a PRB are based on one or a combination of the following biophysicochemical processes (Kate Bronstein, 2005).

In case of organic pollutants:

- abiotic reductive/oxidative degradation
- retardation and biodegradation
- sorption

In case of inorganic pollutants:

- abiotic reduction
- biotic reduction/oxidation
- chemical precipitation
- sorption or ion exchange.

Among the reactive materials often used in PRB measures (Table 2-1), zerovalent iron (ZVI) traditionally plays a central role (Birke et al., 2002; Henderson and Demond, 2007). ZVI particles are available in different sizes (granular, micro- or nanosized) and can be used either separately or in combination (Birke et al., 2006). However, recently nanoscale ZVI (nZVI) is getting the most attention due to its higher specific surface area and thus higher reactivity (Gillham and O'Hannesin, 1994; Roberts et al., 1996; Wang and Zhang, 1997). To date, nZVI is the most widely used reactive nanomaterials to clean-up soil and groundwater (Karn et al., 2009). While 40 % of the US remediation projects are carried out with bimetallic nZVI (nZVI combined with a metal catalyst such as Ni, Pd, Pt, Cu, Ag), in Europe, only regular nZVI is used due to the concerns regarding the toxicity for organisms (Mueller et al., 2012). Furthermore, other types of Fe^0-based materials have been used and tested in PRBs, some examples are: iron foams and pellets obtained combining aluminosilicates and iron and via a high-temperature process; "sponge iron" prepared by high-temperature reduction of iron ore; granular combinations of iron and solid degradable carbon materials; iron particulates and powders prepared using re-melted iron scrap materials (ITRC, 2005; Birke et al., 2006).

Table 2-1 **Reactive materials used in PRBs for metals and radionuclides treatment (US EPA, 1998; Kate Bronstein, 2005).**

Reactive Materials	Geochemical Process
Activated Carbon	Adsorption
Amorphous Ferric Oxyhydroxide	Adsorption
Basic Oxygen Furnace Slag (BOFS)	Sorption
Ion exchange resins	Adsorption
Limestone	Precipitation
Apatite	Precipitation
Sodium Dithionite	Reduction & Precipitation
Sulfate Reducing Bacteria	Microbial degradation
Zeolites	Adsorption
ZVI	Reduction & Precipitation
Sand/Gravel beds + nutrients + oxygen	Promotes microbial degradation

2.2.2.3 Examples of PRB Applications

The PRB concept and technology were mainly initiated and developed in North America. Therefore, the research carried out to develop and optimize such technologies was initially mainly aimed for the remediation of critical pollutants regulated by the American and Canadian legislation. However, after two early projects in Ireland in 1994-1995 and a full-scale application performed in Germany in 1998, European projects and research have started to play a role in the development of PRB (Birke et al., 2006). The reports made by the US EPA (2005, 2002, 1999) summarize information about PRB case studies for groundwater remediation in the United States, Canada, and selected locations abroad.

i   Metallic iron-based PRBs

Metallic iron, also known as ZVI, has been used for many years in PRBs at sites contaminated with organic substances (e.g., chlorinated hydrocarbons, alkanes, aromatics) (Tratnyek and Johnson, 2006). Moreover, ZVI can also immobilize inorganic compounds like Cr, As, Ni, Pb, U, SO_4^{2-}, NO_3^- and PO_4^{3-} (Astrup et al., 2000; Morrison et al., 2001; Alowitz and Scherer, 2002; Xenidis et al., 2002). According to a survey made in USA in 2002, 45 % of 124 evaluated PRB projects were ZVI-based (Xenidis et al., 2002). Besides the installations at the Canadian Forces Base in Borden in Ontario, at the Intersil Semiconductor Site in Sunnyvale in California and at the US Coast Guard (USCG) Support Center in North Carolina (mentioned at the beginning of Chapter 2.2.2.), the PRB at the Savannah River Superfund Site (South California) is a good example of how continuous research and increasing knowledge of clean-up applications lead to better and more effective remedial solutions. Indeed, the PRB at this Superfund Site was originally limestone-based (used to raise the pH to allow precipitation of the metals) and then replaced with a permeable wall made of 760 tons of iron filings recycled from the automotive industry. Later, a mixture of iron filings and starch-like material was injected under high

pressure via 22 wells creating fractures in the rocks, which were filled by the mixture (Kate Bronstein, 2005; Faisal et al., 2018).

In Europe, the first PRB was installed in 1995 at an operational industrial site in Belfast (Northern Ireland) and ZVI was used as reactive material (Birke and Burmeier, 2014). The area was used to manufacture electronic components; therefore it was highly contaminated by chlorinated compounds (mainly TCE). Some groundwater samples were used at the EnviroMetal Technologies Inc. (Waterloo, Canada) for column treatability studies, and the results were used to plan the field application (Thomas et al., 1995). In 1995, a F&G PRB with an innovative design was installed at Monkstown (Ireland) to treat TCE and monitored consistently for the first 10 years (Phillips et al., 2010). In 1999, a ZVI-based F&G PRB was erected in Vapokon (Denmark) for cVOCs (mainly TCA, TCE, and PCE) degradation (Birke and Burmeier, 2014). Other examples of ZVI-based PRBs are in Willisau, Switzerland for Cr(VI) contamination (2004) and in Horice, Czech Republic (2009), to treat PCE, TCE, and cis-DCE. In Germany, ZVI-based PRBs were erected in: Rheine (1998), Bernau (2001), Bitterfeld (1999, combination of ZVI and GAC), Edenkoben, (1998 and 2001), Bornheim (Mueller et al., 2012). The type of ZVI exclusively employed in German PRBs are "Gotthart-Maier", "iron sponge" (ReSponge®), and "Hartgussstrahlmittel" (Birke et al., 2006; Birke and Burmeier, 2014).

Detailed information about the characteristics and performances of PRB installations together with other selected PRB (not only ZVI-based) sites in Germany are listed in Table A-1 (Appendix).

ii Activated carbon

Activated carbon (AC)-based PRBs are chosen in case of clean-up based on sorption reaction. In Germany, in Denkendorf (2001), Karlsruhe (2000-2001) and Offenbach (2007) have been erected AC-based PRBs for adsorption of chlorinated volatile organic carbons (cVOCs) and polycyclic aromatic hydrocarbons (PAHs). In Denkendorf, a 6 m deep D&G full scale PRB was installed to treat cVOCs (e.g., TCE, PCE, cis-DCE) (Birke et al., 2002; Birke and Burmeier, 2014). The PRB in Karlsruhe, an example of full-scale F&G system (240 m long and 17 m deep funnel with eight gates) equipped with granular activated carbon (GAC), was installed at the former manufactured gas plant site for long-term remediation of groundwater contaminated by PAHs, benzene, toluene, ethylbenzene, xylenes (BTEX) and vinylchloride (Schad et al., 2000; Birke et al., 2002; Birke and Burmeier, 2014). Despite the initial malfunctioning, PAH concentrations have reached the remediation target value at all monitoring wells leading to a clean-up efficacy of the entire system close to 100 %. The pilot scale PRB in Offenbach was designed for the removal of tar oil pollutants from contaminated groundwater at an abandoned tar factory site (Birke and Burmeier, 2014).

iii Dithionite

A permeable reactive zone can be created by injecting dithionite (e.g., sodium dithionite) in liquid form in a contaminated aquifer to create a reduced treatment zone formed by reducing the ferric iron, which

is present in ferric hydroxides in the sediments, to ferrous iron (Fruchter et al., 2000). Dithionite, which is a strong reducing agent, acts either as reductant for redox sensitive metals (e.g., Cr, U and Th) or precipitant for the degradation of hydrocarbons (Fruchter, 2002; Zachara et al., 2004). A pilot test using sodium dithionite as reducing additive has been made at the Cr-contaminated site at Hanford Site (Washington), while a full-scale treatment was carried out in 2001 at the US Coast Guard (USCG) Support Center in Elizabeth City (North Carolina), at the same contaminated site previously treated with a ZVI-based PRB strategy (Malone, 2004).

2.2.2.4 Longevity, Sustainability and Costs of PRBs

One of the main factors influencing the choice for or against a specific remedial approach is the longevity of the method. The longevity of a PRB is based on how long it can treat groundwater to design remediation goals, maintaining its hydraulic permeability and reactivity in the years following installation (Henderson and Demond, 2007). That means how long can the groundwater quality be maintained at the remediation level by treatment with the reactive barrier. In the years 1994-2004, many lab scale investigations reported on potential effects and scenarios that might affect the longevity of PRBs. Results from column studies highlighted how high flow rates and high concentration of minerals like carbonate or bicarbonate in the matrix can cause mineral precipitation, which adversely affects the permeability of the system (Kamolpornwijit et al., 2003; Klausen et al., 2003). Wilkin et al. (2003) showed that in terms of long-term operating systems, secondary mineral precipitation mainly causes reduction of porosity (by occupying pore space and blocking flow), permeability and reactivity of the barrier, while Morrison (2003) demonstrated that hydraulic conductivity decreases as quickly as the porosity decreases. Li et al. (2005) reviewed nine ZVI-based PRBs installed in carbonate-rich alluvial aquifer and reported the types and quantities of secondary minerals formed, showing that the most common minerals are calcite, aragonite, siderite, magnetite, goethite, hematite, lepidocrocite, green rust, ferrous hydroxide, ferrous sulfide and marcasite. Furthermore, they reported that the porosity reduction ranges from 0.0007 % to 0.03 % per year and depends on *in-situ* geochemistry as well as flow condition. Specifically, they concluded that the reduction in porosity is greatest near the entry surface and then decreases with distance into the PRB.

After the ITRC guidance was published in 2005, many other lab-studies have contributed to fill the lack of information related to the long-term operation of PRB systems. Unfortunately, there have been only a few field monitoring studies and in most cases the data is not accessible to the public because these PRBs have been installed at private sites. Furthermore, it is worth mentioning that long-term monitoring information about newer and emerging PRB installations (e.g., injection of ZVI slurry) is not yet available. However, statistical and numerical modelling studies help in simulating long-term PRB performances. In most cases, the published studies predicted that secondary mineral precipitation may decrease barrier porosity, hence adversely affecting the PRB longevity (Yabusaki et al., 2001; Mayer et al., 2002; Li et al., 2006). However, field monitoring results often did not match previous modelling

predictions, as many critical parameters such as saturation indices, dissolved oxygen concentrations, or total dissolved solids are not easily predictable. For example, Gavaskar et al. (2005) demonstrated that the PRB at Moffett Field in Mountain View (California) continued to significantly degrade target contaminants (cVOCs) after 8 years of operation, with no evidence of a decrease in hydraulic performance, contradicting the predictions based on the numerical model of Yabusaki et al. (2001). Another example of how far model predictions and the actual situation in the field can diverge is the PRB at Elisabeth City Coast Guard Station (North Carolina). Mayer et al. (2002) performed reactive transport modelling studies and reported that secondary mineral precipitation will decrease barrier porosity and reactivity in the long-term. Recently, Wilkin et al. (2014) evaluated the long-term performance of this PRB and showed that it kept removing the target contaminants (Cr(VI) and TCE) from the groundwater even fifteen years after installation and, in the case of Cr(VI), the reactive performance exceeded the lifetime of the contaminant plume. In general, parameters such as Eh conditions, influent pH, and influent concentrations of alkalinity are considered trustful predictors for modelling and predicting long-term PRB performance (Henderson and Demond, 2007).

In the design phase of a remediation system, in addition to focusing on pollutant reactions, it is essential to consider the potential environmental impact on other media and to include factors such as air emissions of pollutants, water and land resource consumption, waste generation and energy use (Higgins and Olson, 2009). With its Best Management Practices (BMPs) Program, the US EPA defined "sustainable practices" as *"clean-up processes that minimize the environmental and energy footprint of actions taken during a project life"* (2008). Given that PRB systems require very low (almost negligible) water and energy consumptions, and that the reactants are recycled or waste products, PRB technologies are widely considered to be environmentally sustainable practices (Phillips, 2009). With respect to water use footprint, a PRB can be considered 100 % green, since it does not remove any water. Generally, PRBs are the second most sustainable groundwater remediation techniques after monitored natural attenuation (NA), whereas excavation is the "least green" practice (Figure 2-5) (ITRC, 2008; ITRC, 2011). Moreover, PRBs are considered particularly sustainable if used for more than ten years (ITRC, 2011).
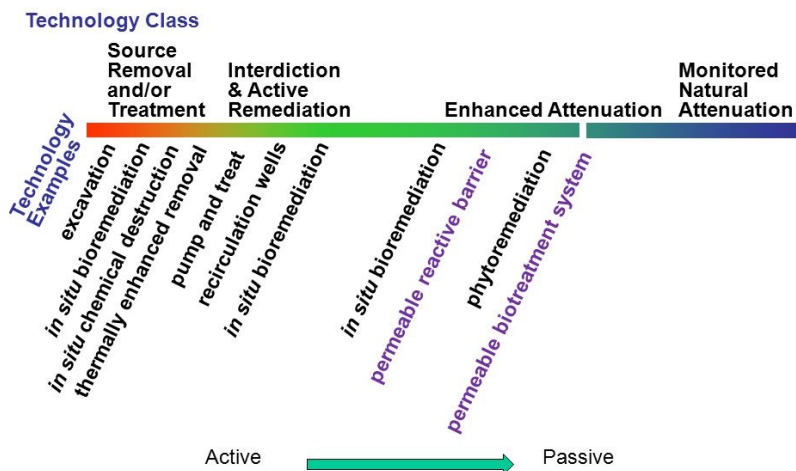
Figure 2-5   **Remediation technologies ranging from least environmentally friendly (excavation) to most "green" approaches (ITRC, 2011).**

Higgins and Olson (2009) compared and modelled the life-cycle environmental impacts (time scale of 30 years) of a ZVI-based PRB system and a P&T system. To assess the environmental impact, they considered the following categories: global warming, acidification, human health, eutrophication, ozone depletion and smog formation. For the PRB, the authors showed significant reductions in acidification, eutrophication and ozone depletion as well as a significant lower impact on human health (Figure 2-6). Moreover, they found that the environmental impact of P&T is related to the high energy demand during operation, while the environmental impact of PRBs is mostly (> 80 %) the result of material production and energy consumption during construction.
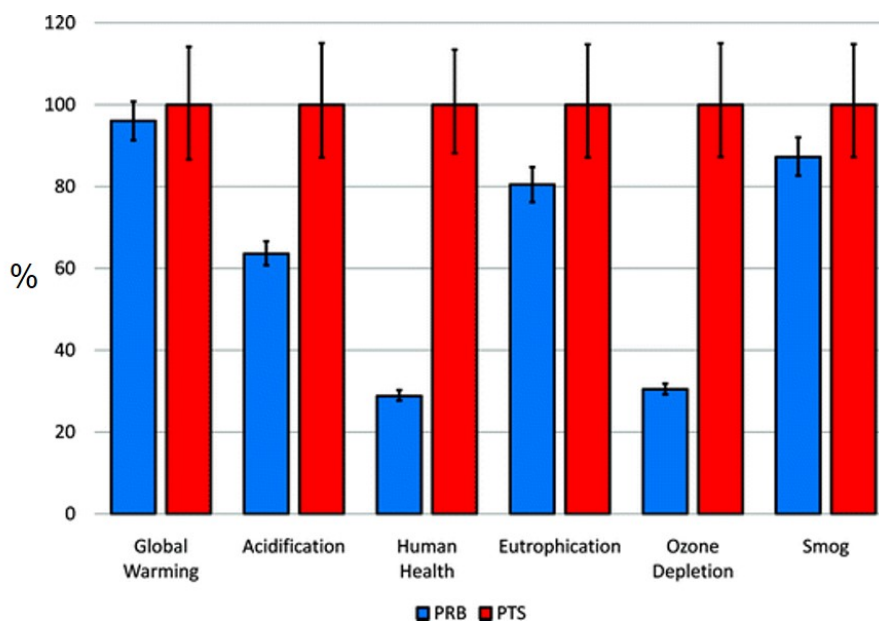
Figure 2-6   **Comparison between the environmental impacts of PRB and P&T systems. The results were normalized by the greatest value in each impact category (Higgins and Olson, 2009).**

Overall, PRB systems offer significant economic advantages over *ex-situ* approaches such as P&T. According to a survey made from the US EPA in (2001), the average annual costs of a PRB application is equal to $ 730,000 (calculation based on 16 sites), which is circa 6.7 times lower than a P&T system ($ 4.9 million), with investment costs (calculated according to the surface area of the barrier) between 180 and 3,500 €/m^2. Even though the initial investment costs are higher than for P&T, PRBs require less energy for maintenance and thus lower costs for long-term operation (Puls et al., 1999). Thereby, after a few years, the costs of a PRB system can be much lower than for a P&T system (Birke et al., 2006).

3 Innovative Engineered Nanoparticles: Promising *In-Situ* Reactants

The effectiveness and longevity of *in-situ* remediation techniques are highly dependent on the materials used as reactive media (ITRC, 2005; Kate Bronstein, 2005). The reactant must be manufactured or modified (in case of natural material) so that it can be placed within the contaminated plume or injected near the source of the contaminant zone. For a successful remedial approach, the reactant should retain its hydraulic characteristics and stay reactive long enough to reduce the contaminant concentration below the clean-up goals (Henderson and Demond, 2007). Additionally, in case of injectable materials, the transportability through the porous media is as important as the reactivity. Moreover, a crucial factor in this context is also the toxicity of the reactant material to the organisms present in the soil. Due to greater concerns about toxicity, regulations on the use of certain materials are currently stricter in Europe than in the USA (Mueller et al., 2012).

Over the last two decades, a large variety of reactants (e.g., limestone, apatite, zeolites, ZVI) has been extensively studied and tested at the laboratory scale and, in many cases, at the field scale (Chapter 2.2.2) (US EPA, 1998; ITRC, 2005; Kate Bronstein, 2005). The outcomes of these investigations and long-term performance monitoring studies in PRB applications have shown the many advantages, but also the drawbacks of these materials. Given the environmental relevance of this issue in light of the urgent global need to develop effective decontamination strategies, intensive research is being conducted to optimize already existing reactants and to develop and design innovative, easy-to-produce, environmentally-friendly and cost-effective reactive materials for *in-situ* remediation applications.

These innovative, newly developed reactant materials are nowadays often referred to as "*engineered nanoparticles* (ENPs)" and defined as: *"Particles, in an unconsolidated state or as an aggregate or agglomerate, where more than 50 % of the particles have one or more external dimensions in the range of size 1-100 nm"* (Cornelis et al., 2014).

This chapter describes the chemical, physical, and mineralogical properties of two emerging iron-bearing reactants:

- green rust (GR)
- sulfidized nanoscale zerovalent iron (S-nZVI)

Both reactants have shown high potential for the removal of harmful compounds and for their application *in-situ* in the field (Randall et al., 2001; Bond and Fendorf, 2003; Jönsson and Sherman, 2008; Y. Wang et al., 2010; Q. Wang et al., 2010; Latta et al., 2015; Fan et al., 2016a; Li et al., 2018).

For a successful *in-situ* application (Figure 3-1), however, it is necessary to understand the behavior of these reactants once they are introduced, either placed or injected, into a porous medium.
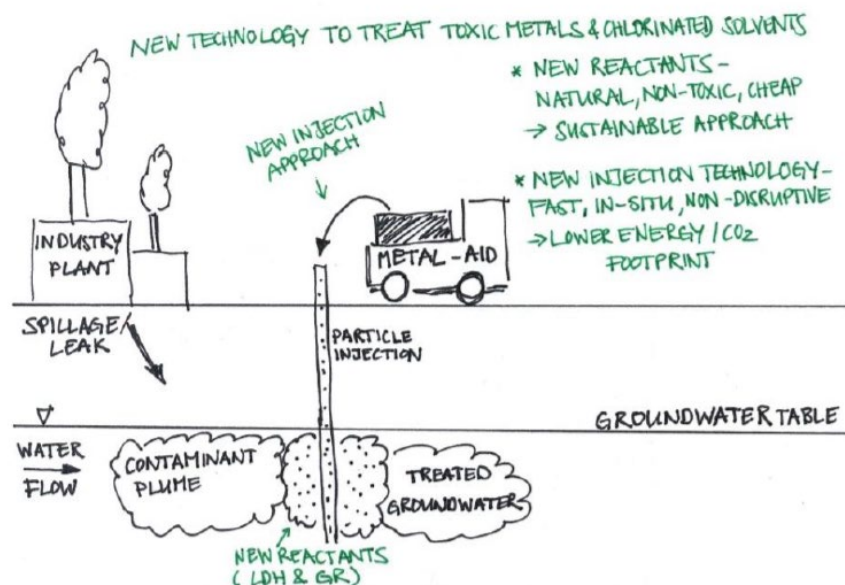
Figure 3-1 **Schematic representation of the application of sulfidized nanoscale zerovalent iron (S-nZVI) or green rust (GR) in an *in-situ* remediation system (Metal-Aid, 2016).**

3.1 Green Rusts: Fe(II)-Fe(III) Layered Double Hydroxides

Iron (Fe) is the 4th most abundant element in Earth's crust (5.6 wt %), after oxygen (O, 46.4 wt %), silicon (Si, 28.2 wt %) and aluminum (Al, 8.2 wt %), (Taylor, 1964). Si and Al form together with O, silicates and aluminates, while Fe in the presence of O, and/or OH, forms either oxides, hydroxides, or oxide-hydroxides, which are here referred as *iron oxides*. Near the surface of Earth's crust, Fe mostly exists as Fe(III) oxides, due to the presence of oxygen. Based on the iron oxidation state, *iron oxides* can be divided into three different groups: (i) ferrous oxides containing exclusively divalent Fe(II) (Fe(II)O and Fe(II)(OH)$_2$); (ii) ferric oxides containing only trivalent Fe(III) (including e.g., ferrihydrite, goethite (α-FeOOH), hematite (α-Fe$_2$O$_3$), lepidocrocite (γ-FeOOH)); and (iii) mixed-valent iron oxides containing both Fe(III) and Fe(II) in their crystal structure (including the minerals magnetite (γ-Fe$_3$O$_4$) and green rust) (Cornell and Schwertmann, 2003).

Green rust (GR) is a particular type of layered double hydroxide (LDH), which contains only iron (both ferrous and ferric) as a cation (M) in brucite-type layers (e.g., the [Fe(II)-Fe(III) LDH]). GR formation requires specific geochemical conditions that allow the co-presence of both Fe(II) and Fe(III) (Feitknecht and Keller, 1950; Trolard et al., 2007). In 1935, Girard and Chaudron observed the precipitation of a metastable green oxide that transformed into lepidocrocite by aerial oxidation and named it ''hydrated magnetite''. The term "green rust", was mentioned for the first time in a Ph.D. dissertation by Keller in 1948 and derives from the typical bluish-green color of the material. This color

is caused by the presence of mixed-valent Fe(II)-Fe(III) species, but turns into ochre once exposed to the air (Trolard et al., 1997). Later, Bernal et al. (1959) and Feitknecht and Keller (1950) synthesized similar compounds and used the same name. In 1969, GR was observed for the first time as a corrosion product of steel water pipes in water drain (Guilbaud et al., 2013).

3.1.1 Occurrence

Although GR is not considered a rare mineral phase, its natural occurrence is limited to certain environments. At the interface between oxic and anoxic zones, where both Fe(II) and Fe(III) can coexist, mixed-valent compounds such as GR can form (Trolard et al., 1997). Since its first natural identification in 1969, GR has been recognized as common mineral in suboxic and anoxic, Fe(II)-rich soils, sediments, hydromorphic soil, lacustrine waters and groundwater (Abdelmoula et al., 1998; Génin et al., 1998; Zegeye et al., 2012). In 1996, a soil sample was identified (via Mössbauer and Raman spectroscopies) as the natural homologous to GR (Trolard et al., 1997). It was found in a hydromorphic soil in the forest of Fougères (Brittany, France) and for this reason it was named "fougerite" (Figure 3-2) (Trolard et al., 1997). Fougerite has been approved as a mineral by the International Mineralogical Association (IMA) with the identification number 2003-057.

Figure 3-2 **Soil profile containing fougerite with blue-greenish color pattern. The sample was collected by the IUSS Working Group WRB in Fougères (France) in 2006 (Trolard et al., 2007).**

Recently, new occurrences of natural GR were found: in an ochreous deposit at an abandoned coal mine site in South Wales Coalfield, UK, (Bearcock et al., 2006); in groundwater from a chalk aquifer and from bore holes drilled into granite walls in an underground tunnel in Denmark (Christiansen et al., 2009b); in the Fe(II)-rich stratified (oxic/anoxic) lake Matano, Indonesia (Zegeye et al., 2012); in CO_2-rich soils on a mofette field in Czech Republic (Rennert et al., 2012); in uranium-polluted mine drainages, at the transition zone between anoxic subsurface and the oxic surface in Thuringia, Germany (Johnson et al., 2014). GR can form abiotically by partial oxidation of $Fe(OH)_2$ (Refait et al., 1998;

Génin et al., 2006) and by the interaction of dissolved ferrous iron with ferric oxides (Géhin et al. 2002; Ruby et al. 2003; Usman et al. 2012). It can also form biotically in association with microbial communities (Pantke et al., 2012) or by partial bacterial reduction of various iron oxides such as ferrihydrite (Kukkadapu et al., 2004), lepidocrocite and hydrous ferric oxide (Ona-Nguema et al., 2002; O'Loughlin et al., 2007; Jorand et al., 2013). GR is stable at pH > 6 but unstable at highly alkaline pH and under oxidizing conditions (Génin et al., 1998). Refait et al. (2001) showed that the Fe content within GR layers in soils is between 2 and 4 %. GR oxidizes very quickly after exposure to air; hence, the characterization of natural samples is very difficult. However, many studies have been conducted on synthetic GRs (Génin et al., 1998; Refait et al., 2003; Génin et al., 2006; Ruby et al., 2006a). Besides its natural occurrence, GR is frequently observed as a corrosion product of steel in oxygen-limited settings (Génin et al., 1998; Santana Rodríguez et al., 2002) and metallic iron in permeable reactive barriers containing Fe^0 (Gu et al., 1999; Roh et al., 2000; Yin et al., 2015).

3.1.2 Structure and Composition

GR belongs to the sjögrenite–pyroaurite mineral class and is the redox-active subfamily of LDHs. The GR structure consists of brucite-like mixed Fe(II)/Fe(III) tri-octahedral, positively charged hydroxide layers, which alternate with hydrated, negatively charged interlayers containing planar (e.g., CO_3^{2-} and Cl^-) or tetrahedral (e.g., SO_4^{2-}) anions (Feitknecht and Keller, 1950; Bernal et al., 1959), and occasionally cations (Christiansen et al., 2009b). The hydroxide layers are composed of $[Fe(OH)_6]^{2+}$ octahedra, in which Fe(II) ions are partially replaced by Fe(III) ions (Figure 3-3).
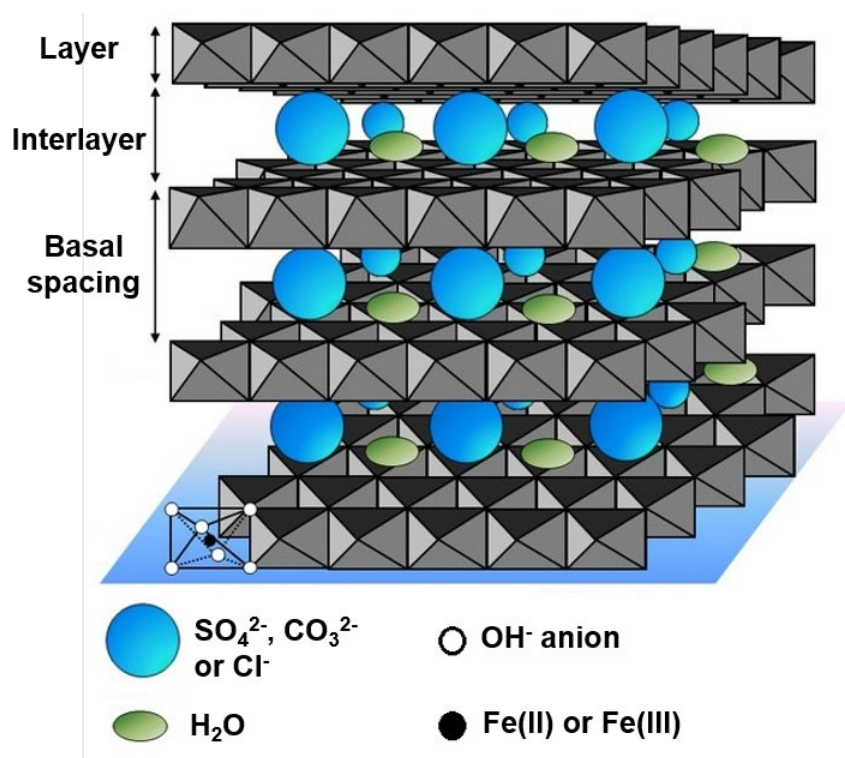
Figure 3-3   **Schematic representation of the green rust (GR) structure (modified after Bi et al., 2014).**

The general formula was established to be the following:

$$\left[\mathbf{Fe(II)}_{(2/3+y)}\mathbf{Fe(III)}_{(1/3-y)}\mathbf{(OH)_2}\right]^{(1/3-y)+} \cdot \left[(1/3 - y/n)\mathbf{A^{n-}} \cdot (m/n)\mathbf{H_2O}\right]^{(1/3-y)}$$

where $0 < y < \sim 1/12$, A^{n-} represents the intercalated anion (mainly SO_4^2, CO_3^{2-} or Cl^-) and m is the number of intercalated water molecules (Génin et al., 2001).

The ratio of Fe(II)/Fe(III) ranges between 0.5-0.66 in natural GR minerals and 0.25-0.33 in laboratory-synthesized GR (Khan and O'Hare, 2002). In laboratory, this ratio can be obtained either by mixing ferrous and ferric hydroxides, or oxidation of ferrous compounds or reduction of ferric compounds. It was shown that GR with a higher Fe(II)/Fe(III) ratio and incorporated monovalent anions is more reactive in the reduction of contaminants such as nitrate (Hansen et al., 2001).

The charge of the positively charged hydroxide layers is balanced by intermediate layers consisting of different types of anions, which derive from the nature of the related solution (Drissi et al., 1995; Génin et al., 1998). The occurrence of specific anions in the crystal structure defines two distinct types of GR, which were distinguished by their X-ray diffraction (XRD) patterns as green rust 1 (GR1) and green rust 2 (GR2) (Refait et al., 1998; Loyaux-Lawniczak et al., 2000; Ruby et al., 2003):

- GR1 forms with planar or spherical anions (e.g., carbonate, chloride, oxalate) and presents a trigonal structure and a rhombohedral unit cell (Figure 3-4a); in this group, layers are separated by only one layer of water molecules, and the sequence of stacking of OH planes along the c-axis is: AcBiBaCjCbAkA… (three-layer repeat), where *A-C*, designate OH^- planes, *a-c* metal cation layers and *i-k* intercalated layers (Génin et al., 2001).
- GR2 forms with tetrahedral anions (e.g., sulfate and selenite) and presents a hexagonal unit cell (Figure 3-4b); in this group, layers are separated by two layers of water molecules and the sequence of OH$^-$ planes is: AcBijA (single-layer repeat) (Simon et al., 2003).
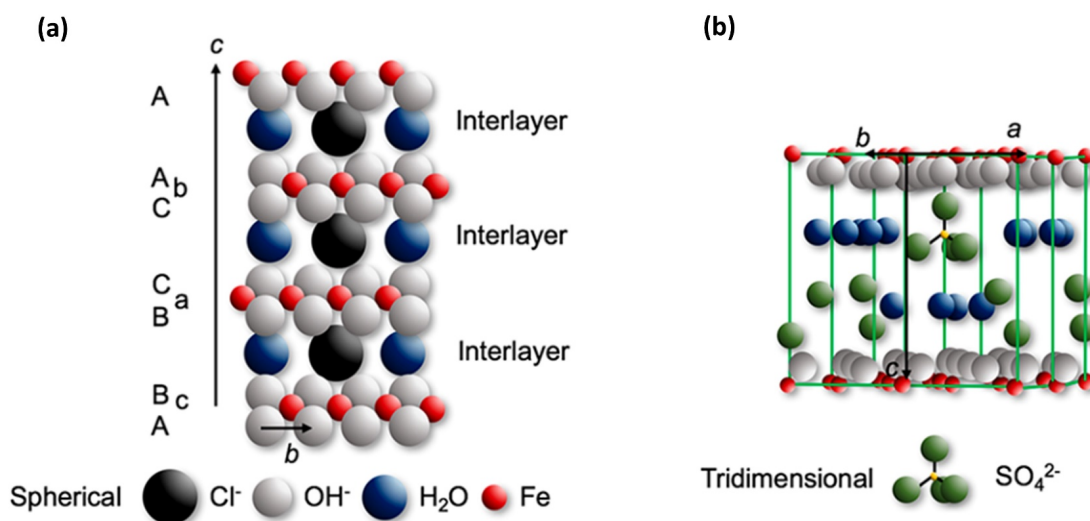
Figure 3-4   Crystal structure of green rusts: (a) GR1 (GRCl$^-$) and (b) GR2 (GRSO$_4^{2-}$) (Usman et al., 2018).

Due to the different number of interlayers (anions and water molecules) and the nature of the interlayer anion, GR1 and GR2 have different interplanar distances between two hydroxide layers in the stack sequence along the *c*-axis (Trolard et al., 2007). These distances are reflected in the most intense reflection (*d*) in the low 2-theta range of XRD diffractograms. Hence, these reflections are diagnostic to distinguish between the different GR types. Particularly, as shown in Figure 3-5**Fehler! Verweisquelle konnte nicht gefunden werden.**, the position of the most intense (003) reflection peak of $GR(CO_3^{2-})$ is situated at a much lower angle than the (0001) peak of $GR(SO_4^{2-})$ (Ruby et al., 2010). Trolard et al. (2007) showed via XRD characterization that GR1 (system trigonal, space group R$\bar{3}$1m) presents d_{003} at 7.5-8 Å ($\sim$ 7.6 Å for $GR(CO_3^{2-})$ and $\sim$ 7.9 Å for $GR(Cl^-)$), whilst GR2 (system trigonal, space group P$\bar{3}$m) presents d_{001} at 11.0-11.6 Å. Since iron hydroxide layers are about 2 Å thick, the interlayer distance is about 6 Å in GR1 and 9 Å GR2 (Drits and Bookin, 2001).
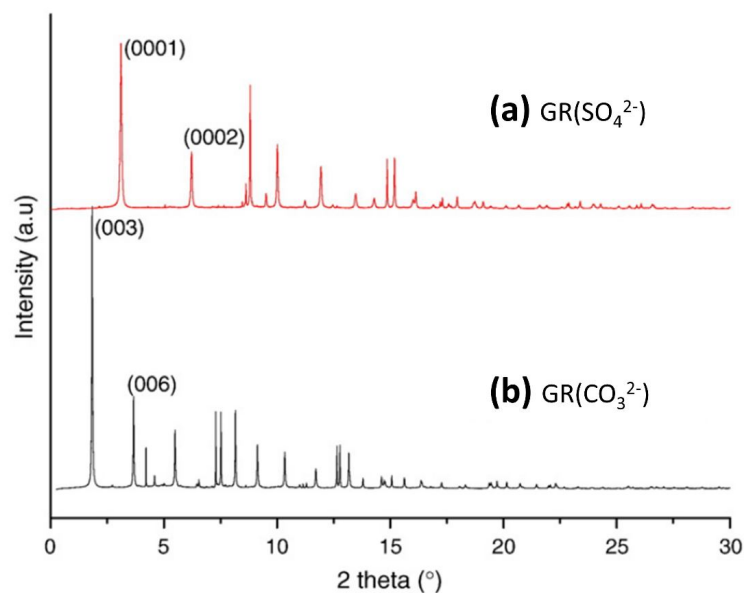
Figure 3-5   X-ray diffraction patterns of (a) hydroxyl-sulfate green rust, GR(SO_4^{2-}), and (b) hydroxyl-carbonate green rust, GR(CO_3^{2-}) (Ruby et al., 2010).

GR structure and composition have been extensively documented in literature (Refait et al., 1998; Génin et al., 2001; Ruby et al., 2003; Simon et al., 2003). Generally, the most common GR types are hydroxyl-sulfate GR, $GR(SO_4^{2-})$, hydroxyl-carbonate GR, $GR(CO_3^{2-})$, and hydroxyl-chloride GR, $GR(Cl^-)$. In fresh water, where (bi)carbonate is abundant, $GR(CO_3^{2-})$ is the most likely GR type to form (Christiansen et al., 2009a). Whereas, when the dissolved concentrations of SO_4^{2-} or Cl^- are much higher than CO_3^{2-} (i.e., corrosion of iron in seawater), respectively $GR(SO_4^{2-})$ and $GR(Cl^-)$ is favored. Their chemical formula, space groups, cell parameters, and interlayer distances are summarized in Table 3-1 (*a* and *c* are the cell parameters values and *d* corresponds to the interlayer distance). Compared to GR1, the basal *d*- spacing of $GR(SO_4^{2-})$ is larger because it contains a double layer of oriented sulfate anions and water molecules. Additionally, other anions such as selenite (Refait et al., 2000), oxalate

(Bourdoiseau et al., 2012) and C9-C14 linear alkyl carboxylates (Ayala-Luis et al., 2010) can be intercalated in the GR structure. In case of incorporation of large organic anions in the GR structure, diffractograms will show higher d-spacing values. For example, the incorporation of bulky alkyl anions results in a d-spacing equal to 42 Å (Ayala-Luis et al., 2010).

Table 3-1   **Crystallographic data of GR(SO$_4^{2-}$), GR(CO$_3^{2-}$) and GR(Cl$^-$); *a* and *c* are the cell parameters values and *d* corresponds to the interlayer distance (Usman et al., 2018).**

Type of GR	GR(SO$_4^{2-}$)	GR(CO$_3^{2-}$)	GR(Cl$^-$)
Chemical Formula	Fe(II)$_4$Fe(III)$_2$(OH)$_{12}$SO$_4\cdot$8H$_2$O	Fe(II)$_4$Fe(III)$_2$(OH)$_{12}$CO$_3\cdot$3H$_2$O	Fe(II)$_3$Fe(III)(OH)$_8$Cl$\cdot\sim$1.5H$_2$O
Space group	P$\overline{3}$m1	R$\overline{3}$m	R$\overline{3}$m
a (Å)	5.50683 (Ruby et al., 2010)-5.5524 (Simon et al., 2003)	3.1759 (Aissa et al., 2006; Ruby et al., 2010)	3.19 (Refait et al., 1998)
c (Å)	10.9664 (Ruby et al., 2010)-11.011 (Simon et al., 2003)	22.7123 (Aissa et al., 2006; Ruby et al., 2010)	23.85 (Refait et al., 1998)
d (Å)	11.011	7.57	7.95

Water molecules and anions (or occasionally cations) present in the interlayer space are weakly bonded allowing exchange of molecules with the bulk solution, including oxidants. Compared to magnetite (the other mixed-valent Fe oxide, which presents a cubic and closely packed structure), GR has higher amounts of available Fe(II) and interlayers that allow the exchange of big molecules (Skovbjerg et al., 2006) and higher amount of available Fe(II). Furthermore, it has been shown that GR stability is enhanced by replacing some iron ions in the cationic layer with other cations such as Mg(II), Al(III) and Zn(II) (Ruby et al., 2008).

3.1.3 Morphology

Previous scanning electron microscopy (SEM) and transmission electron microscopy (TEM) measures on synthetic GR, provided information about GR crystal sizes and morphology. Figure 3-6 shows the typical pseudo-hexagonal GR prisms, which are typically found as very thin nano-sized platelets. Generally, GR prisms reach a lateral size in the micrometer range, however, the crystal size can decrease rapidly when divalent or trivalent cations substitute the iron ions (Ruby et al., 2010). Ruby et al. (2010) obtained a decrease of the lateral crystal size to $\sim$ 10 nm after they substituted half of the Fe(III) ions by Al(III) in GR(SO$_4^2$).
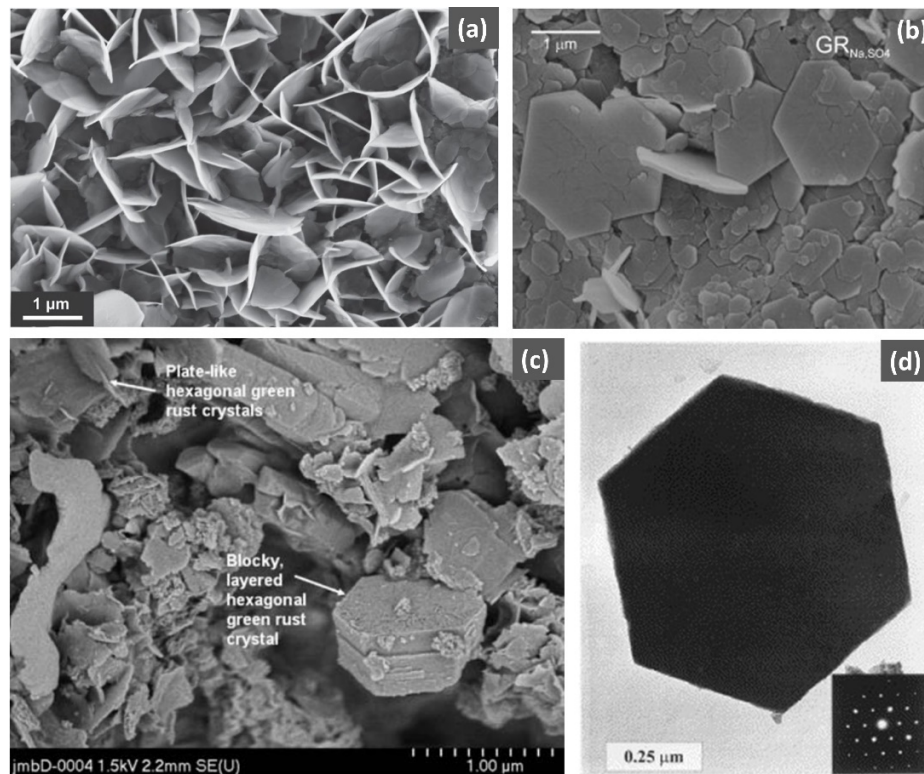
Figure 3-6   SEM and TEM images of GR samples with hexagonal plate-like particle morphologies. (a) GR(SO_4^{2-}) formed at pH 8.5 (Ahmed et al., 2010), (b) GR(NaSO$_4^{2-}$) (Christiansen et al., 2009b) and (c) blocky and plate-like hexagonal crystals (Bearcock et al., 2006); (d) TEM image of GR(CO_3^{2-}) (Legrand et al., 2001).

3.2 Sulfidized Nano Zerovalent Iron (S-nZVI)

Sulfidized nano zerovalent iron (S-nZVI) is obtained via "sulfidation" (or "sulphidation") of nano zerovalent iron (nZVI). The sulfidation method consists in the exposure of a material to sulfur compounds (primarily sodium sulfide and sodium dithionite) of various oxidation states (Fan et al., 2013; Rajajayavel and Ghoshal, 2015). The need of sulfidation as treatment method for nZVI is related to the fact that, although nZVI is widely used as *in-situ* reductant to remove contaminants in subsurface environments (e.g., chlorinated solvents, heavy metals and organic dyes), it is characterized by short persistence in the environment due to natural reductant demand (NRD) (Fan et al., 2016b). Indeed, once nZVI is introduced into an environmental system, the metallic iron (Fe^0) quickly reacts with water (e.g., anaerobic corrosion), dissolved oxygen and/or other natural reducible species commonly present in the subsurface (e.g., nitrate) (Fan et al., 2016b).

These reactions take place also in controlled conditions. Fe^0 corrodes and generates Fe(II) and H_2 as follows:

$$Fe^0 + 2H^+ \rightarrow Fe^{2+} + H_2 \text{ (g)} \qquad \text{Equation 3-1}$$

leading to a quick loss of reducing capacity and surface passivation by formation of an oxidized iron (hydr)oxide shell (Figure 3-7) (Phenrat et al., 2008; Sarathy et al., 2008; Fan et al., 2016a). The reducing

capacity (in mole) is the quantity of reducing equivalents (e.g., electrons) that are available for NRD and contaminant reduction. The theoretical maximum reducing capacity of S-nZVI is three times the amount of Fe^0 in moles, as Fe(III) is the highest oxidation state expected in the subsurface (Fan et al., 2016b).

By modifying the nZVI surfaces via sulfidation treatment, by reacting nZVI with either sodium sulfide or sodium dithionite, some of these negative side effects can be limited (Fan et al., 2013), which leads to increased longevity and can improve selectivity towards target contaminants such as cVOCs (Rajajayavel and Ghoshal, 2015; Fan et al., 2016a; Fan et al., 2017; Mangayayam et al., 2019a) and chromate (Gong et al., 2017; Li et al., 2018). At first, sulfidation was considered only as an *in-situ* and/or natural biogeochemical process when nZVI was applied in sulfate-rich groundwater systems (Fan et al., 2017). Recently, this method became an emerging treatment used to modify any metal-based materials with strong affinities for sulfide.

3.2.1 Structure and Composition

S-nZVI consists of an iron core (Fe^0) covered with a sulfide layer (FeS) (Figure 3-7), which results from the reaction between Fe^0 and sulfur agents (e.g., dithionite, elemental sulfur, sodium sulfide). The FeS layer protects Fe^0 from further corrosion and inhibits H_2 evolution (Rajajayavel and Ghoshal, 2015). Specifically, in presence of sodium sulfide (Na_2S), the aqueous sulfide (HS^-) gets adsorbed onto the Fe^0 surface (replacing previously adsorbed OH^-) and then reacts with the Fe(II) that is generated by corrosion of Fe^0, leading to formation of FeS onto the surface of Fe^0 (Fan et al., 2013; Rajajayavel and Ghoshal, 2015), as follows:

$$\mathbf{Fe(II) + HS^- \rightarrow FeS + H^+} \hspace{3cm} \textbf{Equation 3-2}$$

During sulfidation by Na_2S only a small amount of Fe^0 is used to form FeS, while the rest remains available for contaminants reduction. Conversely, dithionite converts a majority of the nZVI to FeS, consuming much of the reducing capacity originally provided by the Fe^0 (Fan et al., 2016a). The thin FeS layer not only limits the interactions between the Fe^0 atoms and the water molecules but also enables electron transfer from the Fe^0 core to the surface for effective reduction at the FeS surface sites. FeS is a very conductive compound and a strong reductant for a number of contaminants, including chlorinated solvents (Y. T. He et al., 2010; Gong et al., 2016; Gu et al., 2017).
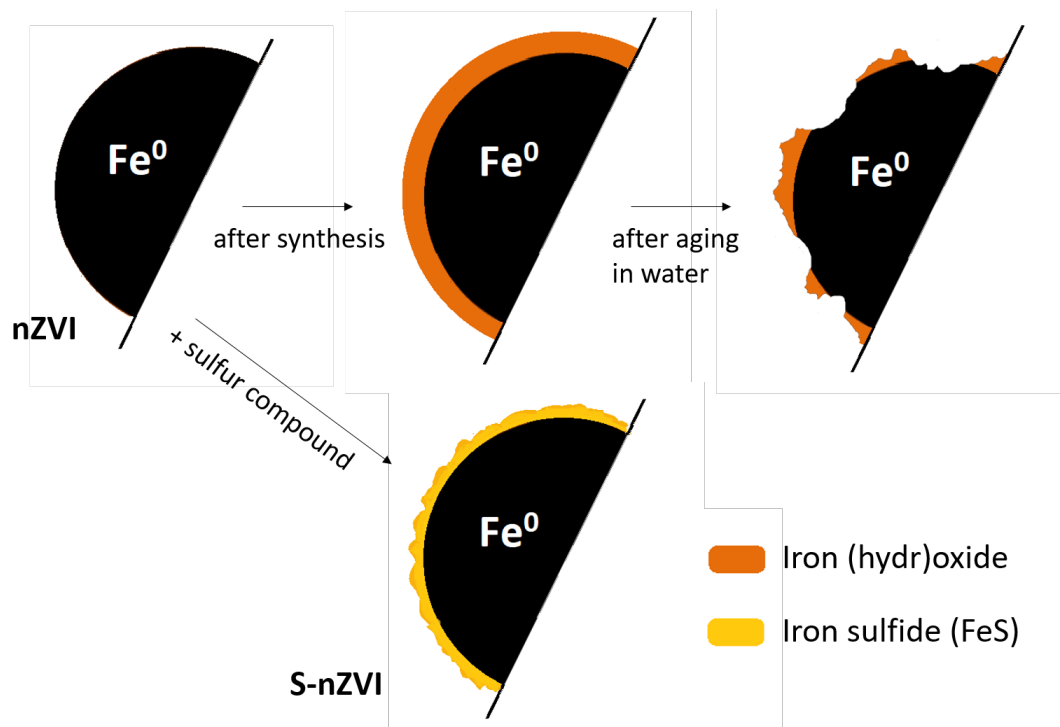
Figure 3-7 **Structure of nZVI in absence and in presence of a sulfur compound. The sulfur compound leads to the formation of the FeS layer around Fe⁰, forming S-nZVI.**

FeS is mostly present as amorphous or nanocrystalline mackinawite, which is a metastable iron sulfide mineral phase (Fan et al., 2013; Gong et al., 2017). Longer reaction times or presence of excess of aqueous sulfide can lead to transformation of the FeS layer into crystalline mackinawite or the more stable sulfide phases pyrite (FeS_2) and/or greigite (Fe_3S_4) (Fan et al., 2017). Furthermore, FeS has been shown to be effective in immobilizing metals and metalloids via a combination of adsorption and co-precipitation (Morse and Arakaki, 1993; Wharton et al., 2000). It also mediates reductive transformation of halogenated organic pollutants (Jeong and Hayes, 2003). Kim et al. (2011) argued that the S-nZVI reactivity is enhanced thanks to the efficient electron transfer of the FeS, which has metallic-like properties, while according to Han and Yan (2016) it is due to the interaction by FeS of atomic hydrogen on the surface, which can react with the contaminants. In general, different hypotheses might be related to the different synthesis procedures used to produce S-nZVI.

At present, there are three main procedures to synthesize S-nZVI: (i) one-pot (or aqueous-aqueous) method, also known as "pre-synthesis" approach, using sodium dithionite as a sulfur precursor (Kim et al., 2011); (ii) mechanical ball-milling (or "solid-solid" method) of solid sulfur and iron-based precursors (Gu et al., 2017); and (iii) "post-synthesis" (or "aqueous-solid") approach, using dissolved sulfur species such as sodium dithionite, sodium sulfide or sodium thiosulfate (Rajajayavel and Ghoshal, 2015). Fan et al. (2017) provides an overview of the different synthesis protocols, showing some of the compositional differences of the various S-nZVI types and how variables such as S/Fe ratio,

sulfidation process and duration, and used sulfur compound affect the structure and morphology of sulfidized materials (Table 3-2).

Table 3-2   **Sulfidation methods (i.e., aqueous-solid, aqueous-aqueous, solid-solid and gas-solid processes) for iron-based materials (Fan et al., 2017).**

Sulfidation agent (S valence)	Sulfidized material	Sulfidation conditions
sulfate SO_4^{2-} (+VI)	granular ZVI, FeO_x	aqueous-solid (microbial)
sulfur dioxide SO_2 (+IV)	nZVI	gas-solid
dithionite $S_2O_4^{2-}$ (+III)	nZVI	aqueous-aqueous, aqueous-solid
thiosulfate $S_2O_3^{2-}$ (+II)	nZVI, FeO_x	aqueous-solid, aqueous-aqueous
elemental sulfur S^0 (0)	mZVI	solid-solid
sulfide, bisulfide and polysulfides S^{2-} (-II)	nZVI , mZVI, FeO_x	aqueous-solid
thioacetamide $H_3CC(=S)NH_2$ (-II)	nZVI	aqueous-solid

3.2.2 Morphology

S-nZVI is defined as nanomaterial because its dimension ranges between 1 and 100 nm. It is characterized by small particle sizes and large surface areas (Figure 3-8). Like nZVI (O'Carroll et al., 2013b), S-nZVI has a spherical shape, consisting of a core and a shell. S-nZVI is characterized by a sulfide layer of ~5 nm (Mangayayam et al., 2019b).
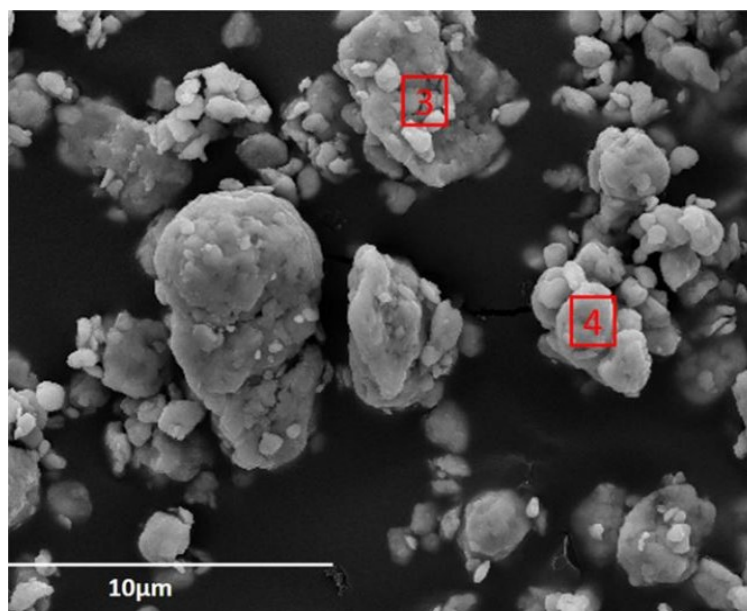
Figure 3-8   **Sulfidized microscale ZVI synthesized by ball milling ZVI with elemental sulfur (Gu et al., 2017).**
The authors determined the atomic ratio of S/Fe at two randomly selected spots (points 3 and 4) and resulted equal to 0.104.

3.3 Application of GR and S-nZVI for Groundwater Remediation

GR has recently received increasing attention due to its high reactivity with a wide range of inorganic substances and its ability to immobilize them. These properties make GR a promising reactant for environmental-friendly clean-up strategies. Latta et al. (2015) presented a comprehensive literature survey, which highlighted that GR can interact with at least 35 elements through 4 pathways (Figure 3-9). These interaction mechanisms are: (i) adsorption of redox-stable oxyanions (e.g., phosphate, arsenate (Randall et al., 2001, Jönsson and Sherman, 2008) and arsenite (Y. Wang et al., 2010) onto the external GR surface; (ii) interlayer incorporation of anions (e.g., sulfate, sulfite, chloride, carbonate or selenite) and monovalent cations; (iii) incorporation of divalent and trivalent metals into the octahedral sheets of GR; and (iv) redox transformations of oxyanions. Interaction via redox transformation concerns among others the redox-sensitive oxyanions chromate (Loyaux-Lawniczak et al., 2000; Williams and Scherer, 2001; Bond and Fendorf, 2003; Skovbjerg et al., 2006; Thomas et al., 2018), selenate and selenite (Börsig et al., 2018), nitrate and nitrite (Hansen et al., 1994; Hansen et al., 2001), as well as a large number of radionuclides (e.g., U(VI), Np(V), Tc(VII)), Cu(II), Hg(II) (O'Loughlin et al., 2003; Latta et al., 2015). Moreover, it should be mentioned that several elements can interact with GR in more than just one way, depending on the particular conditions.
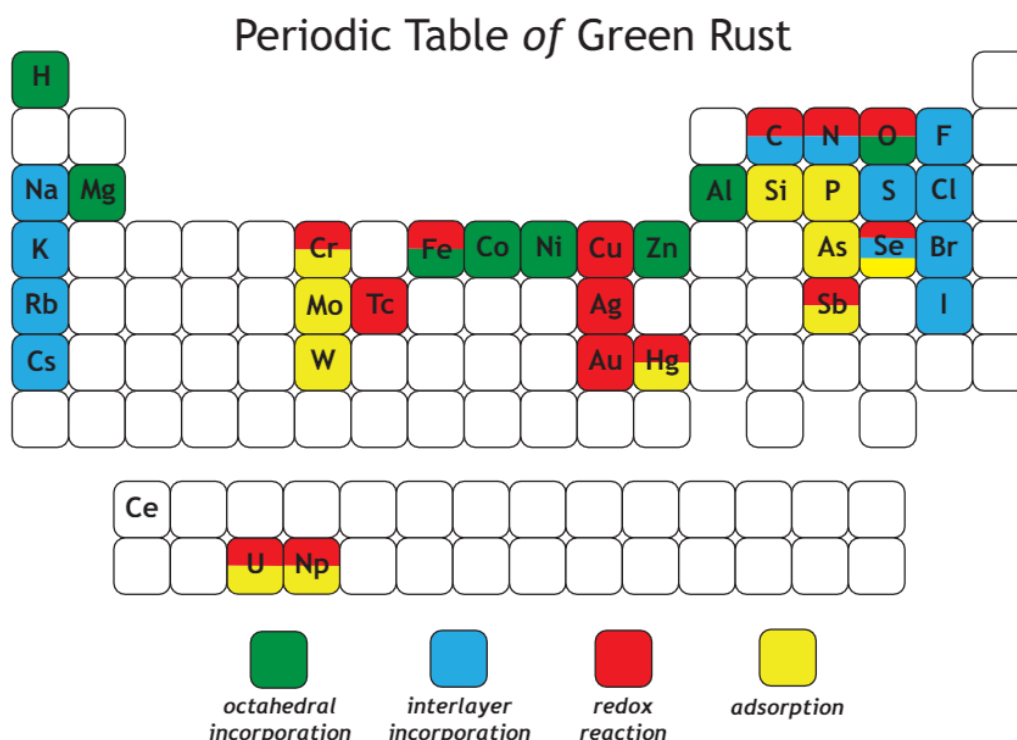
Figure 3-9 **Periodic table illustrating the various interactions between green rust and 35 different elements (Latta et al., 2015).**

Due to its high content of ferrous iron in the GR structure, which can oxidize to ferric iron while reducing critical compounds, most of remediation studies dealing with GR have focused on reduction processes (O'Loughlin et al., 2003; Legrand et al., 2004). Abiotic reductive transformation processes play a key role in the fate, mobility and toxicity of redox-sensitive contaminants, both in natural and engineered systems. Such reactions lead to less toxic, often less mobile and more bioavailable species that are more easily degradable than the parent compound. However, this interaction leads to the oxidation of GR into ferric solid phases (e.g., lepidocrocite, goethite) (Loyaux-Lawniczak et al., 2000; Williams and Scherer, 2001; Skovbjerg et al., 2006). The oxidation of Fe(II) into Fe(III) occurs within a few minutes of exposition to air. Reduction rates of GR increase linearly as a function of the Fe(II) contents (Lee and Batchelor, 2003). In case of reduction of Cr(VI) by GR, the reaction exhibits pseudo-first order rate coefficients and the rate of contaminant reduction is proportional to the surface area concentration of GR (Williams and Scherer, 2001; Bond and Fendorf, 2003). Compared to aqueous Fe(II), structural Fe(II) or Fe(III) complexes with oxygen ligands within the GR structure are more reactive (Williams and Scherer, 2001), making GR a more promising reductant material than dissolved ferrous iron. Moreover, Fe and OH^- are weakly bonded, making the GR structure loose and allowing exchange of ions with the bulk.

Contrary to inorganic compounds, only few studies are available on the mechanism and extent of removal of organic contaminants by GR. In particular, GR has been suggested to be effective as reducing agent for chlorinated solvent pollutants such as tetra-, tri and dichloroethylenes (PCE, TCE and cis-DCE) or chlorinated hydrocarbons (Lee and Batchelor, 2002; Liang et al., 2009; Liang and Butler, 2010; Han et al., 2012; Jeong et al., 2013). However, those few studies have reported contrasting results, most likely due to different GR synthesis techniques. Recently, Mangayayam et al. (2018) investigated the reaction of four different GR types (with different interlayer and hydroxide sheet modification) with three different chlorinated ethenes, showing contradictory results to the previous literature. Even after 10 months, there was no evidence of significant reduction of the chlorinated ethenes. In 2006, GR was suggested to be employed as material for reduction based remediation technologies for the first time (Ruby et al., 2006b). However, so far neither field- nor pilot-scale implementations with GR as reductant material have been realized.

In contrast to GR, sulfidized nZVI (S-nZVI), has greater visibility in the remediation market due to its strong similarity to nZVI and attracts the attention of stakeholders and researchers more easily than GR. This is related to the fact that the use of the non-sulfidized zerovalent iron form (ZVI) is a proven method for remediation of chlorinated volatile organic compounds (e.g., PCE and TCE), but also heavy metals (particularly chromium and uranium), via reduction to less harmful daughter products (Alowitz and Scherer, 2002; Zhang, 2003; Liu et al., 2005; Gheju, 2011). Both micro- and nanosized ZVI have been used in a large number of applications in the USA and recently also in Europe (F. He et al., 2010; Johnson et al., 2013; Chowdhury et al., 2015). However, due to the above-mentioned limitations, many

researchers paid attention to enhance the efficiency of ZVI using various methods (e.g., increasing the surface area, modifying the surface with surfactants or polymers etc.) (He and Zhao, 2007; F. He et al., 2010). Pilot or field applications with innovative S-nZVI are still in progress. Although S-nZVI shares many properties with non-sulfidized nZVI (e.g., nanosized, spherical and magnetic particle, core-shell structure), prior to any remedial applications, it is necessary to evaluate the parameters that might jeopardize its reactivity against the target contaminant and its mobility into the subsurface.

It is important to note that for both iron-based materials (GR and S-nZVI), the synthesis procedure plays a key role for the effectiveness of the reductant, affecting their removal efficiency or transport potential (Skovbjerg et al., 2006; Kim et al., 2011; Fan et al., 2017). Therefore, experiments at the laboratory scale are required to evaluate the best conditions for a successful, and in the best case also cost-effective, field-scale application.

3.4 Behavior of Nanoparticles in Porous Media

A high reactivity of ENPs alone is not enough to ensure an effective *in-situ* remediation. In case of injection-based strategies, the injected particles should be sufficiently mobile in the subsurface to be transported over considerable distances around the injection point, in order to be distributed throughout the contaminated area. Therefore, it is essential to know the transport behavior of ENPs in porous media and to understand the factors that influence/improve their mobility.

3.4.1 Factors Influencing Particle Transport

Recently, Wang et al. (2016) and Liu et al. (2019) published two comprehensive reviews about the most important factors that influence ENP transport behavior. Overall, transport and retention of ENPs are related to their physicochemical properties such as surface charge, size, shape or particle concentration. Some of the most important information is listed below.

i   Particle surface charge

Due to the strong Van der Waals attractions, ENPs have a strong tendency to aggregate, which can limit their scope of application (Wang et al., 2016). Moreover, as quartz sand grains normally carry negative charges (Jada et al., 2006; Bradford et al., 2013), ENPs with positive surface charge get easily adsorbed to the surface of the minerals present in soils or sediments (e.g., quartz, silicates or clays) due to electrostatic forces. On the other hand, negatively charged ENPs generally have a higher mobility due to the dominant electrostatic repulsion forces between the particles and the quartz sand grains (Bayat et al., 2015). The coating of ENPs with a surfactant or biopolymers (e.g., guar gum, starch, carboxymethyl cellulose) is used to improve the ENPs stability in aqueous solutions (He et al., 2009; Tiraferri and Sethi, 2009; Gastone et al., 2014b). The coating causes higher negative surface charges of the particles, providing electrostatic double layer (EDL) repulsions between the ENPs themselves (inhibiting

aggregation) and between the ENPs and the minerals present in the soil (inhibited attachment) (Phenrat et al., 2008; Saleh and Kim, 2008; Tiraferri et al., 2008). Moreover, it can also increase the steric repulsions, enhancing the overall colloidal stability (Wang et al., 2016).

ii   Particle size

Particle size has a strong influence on the transport of ENPs in porous media. According to the Derjaguin-Landau-Verwey-Overbeek (DLVO) theory and the colloid filtration theory, the decrease of particle size yields to an increased probability of collision between particles and porous media (because of enhanced Brownian movement), resulting in a higher chance of attachment to the collector (i.e., higher retention). This behavior was observed in many studies (C. Wang et al., 2012; O'Carroll et al., 2013a). Conversely, in other studies, the opposite trend was observed, i.e., larger particles are less mobile (Tufenkji and Elimelech, 2004; Pelley and Tufenkji, 2008; Phenrat et al., 2009b; Hu et al., 2017). In this case, the high deposition rate of large ENPs was ascribed to the heterogeneity in the surface charge (May and Li, 2013) or to physical straining (see Chapter 3.4.2) as a major contributing mechanism (Y. Wang et al., 2012). It was hypothesized that there could be an optimal particle size and that particle transport is reduced when the particle size is below or above this value (Liu et al., 2019). Overall, there are discrepancies in the literature about the size effect on the transport of ENPs in porous media, mainly because of the simultaneous impact of other factors such as physical straining, surface charge heterogeneity, particle shape, surface roughness and their mutual influence (Wang et al., 2016).

iii   Particle shape

It has been shown that particle shape plays also an important role for the transport behavior of ENPs (Xu et al., 2008; Liu et al., 2010; Seymour et al., 2013). In general, rod-shaped ENPs with high aspect ratios and plate-like particles, aggregate easily and get entrapped within pores, resulting in lower mobility; while spherical ENPs are usually more mobile (Seymour et al., 2013). However, the literature regarding the impact of particle shape is still limited and further investigations are needed.

iv   Particle concentration

Previous studies have shown that ENP behavior in porous media is concentration-dependent, but often with inconsistent conclusions (Phenrat et al., 2009a; Raychoudhury et al., 2010; Raychoudhury et al., 2012; Kasel et al., 2013; Rahman et al., 2013). However, due to different experimental conditions (e.g., use of different measurement units for particle concentrations like mg/L or particles/mL) it is not possible to directly compare these studies.

Some studies have demonstrated that higher ENP concentrations lead to more particle-particle collisions and thus to higher particle aggregation. This effect is responsible for lower particle mobility and higher retention in the porous media caused by gravitational sedimentation or straining (Phenrat et al., 2009a; Raychoudhury et al., 2010; Raychoudhury et al., 2012). It has also been shown that increased particle concentrations may trigger the occurrence of either blocking or ripening effects. In the former case, the

available attachment sites on the porous media surface are occupied more quickly, resulting in enhanced mobility (Kasel et al., 2013; Liang et al., 2013; Iqbal et al., 2017). By contrast, in the case of ripening, higher particle concentration is responsible for increasing amounts of attachment sites due to the newly attached particles, leading to higher ENP retention (Saberinasr et al., 2016).

3.4.2 Particle Transport Mechanisms

A variety of physical, chemical or physical-chemical processes affect the transport behavior of colloid-sized particles in saturated porous media (Tosco et al., 2014). The main mechanisms associated to ENP mobility in porous media are advection, dispersion, straining, adsorption, blocking, ripening, and aggregation (Figure 3-10), described in detail in the recent review by Liu et al. (2019).
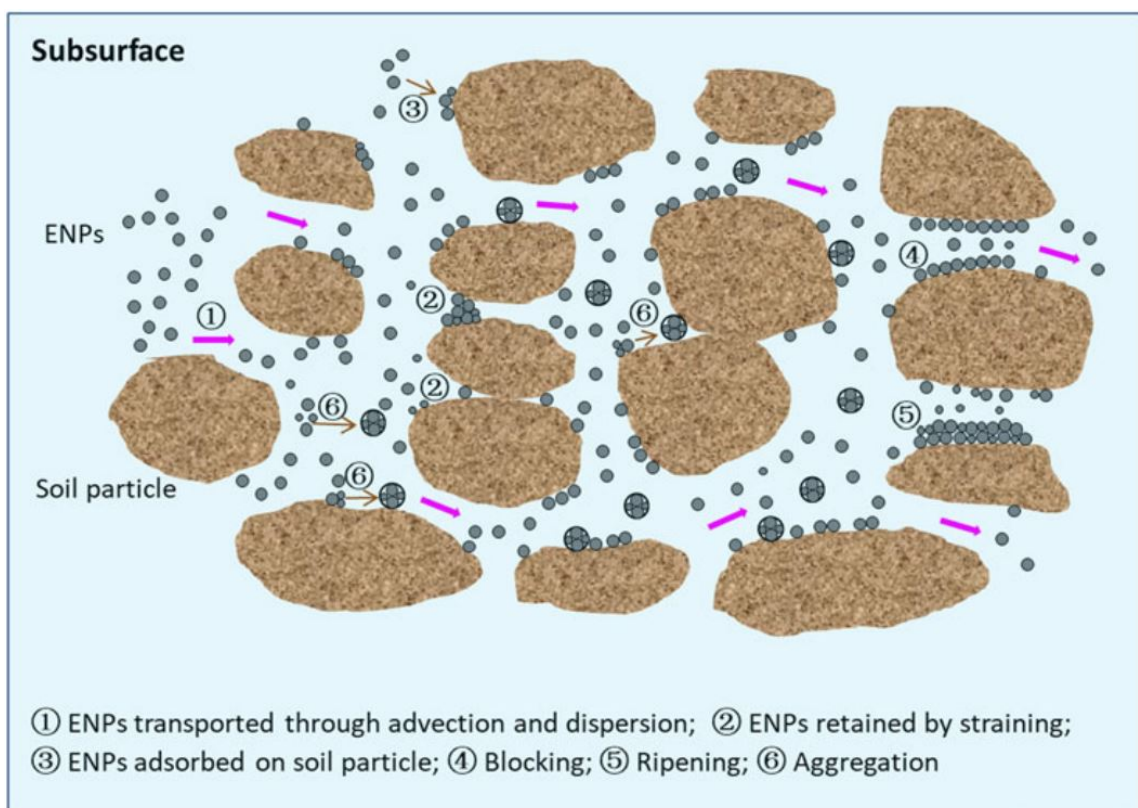
Figure 3-10   Schematic representation of the main transport and retention mechanisms of ENPs in porous media (Liu et al., 2019).

i   Advection and hydrodynamic dispersion

In general, particle size and flow velocity significantly impact advection and dispersion. Advection is a process by which the particles are transported by the water flow (Zhong et al., 2017), whilst hydrodynamic dispersion includes mechanical dispersion and diffusion. Mechanical dispersion is a process of spreading particles perpendicular to and parallel with the direction of water flow and it is caused by heterogeneity of porous media and pore structure, which in turn cause variation in direction and velocity of water flow at pore scale (Mehmani and Balhoff, 2015). Diffusion is a process by which

the particles move from a region of high particle concentration to a region of low particles concentration due to the Brownian motion (Zhong et al., 2017). It has been shown that diffusion plays a significant role as transport mechanism of ENPs in case of very compact and fine porous media or for ENPs with sizes of less than 1 μm (Auset and Keller, 2004; He et al., 2009; Phenrat et al., 2010).

ii Straining

Straining is a physical process responsible for deposition of particles on the porous medium (Figure 3-10) (Tosco et al., 2014). It is a process that causes trapping of particles in the pore throats and voids that are narrower than the size of the ENPs and too small to allow the passage of particles (Porubcan and Xu, 2011). This is due to the fact that even for ideal spherical and uniform grains and nanoparticles, the pores have an angular shape due to the existence of narrow gaps at the contact angle of the spheres, which are not ideal flow channels (Babakhani et al., 2017).

The rate of straining within saturated porous media depends on the particle size and shape, the ratio of particle diameter to sand-grain diameter, the shape and surface roughness of the solid matrix, pore-scale hydrodynamics and the pore water chemistry (Bradford et al., 2003; Auset and Keller, 2004; Tufenkji et al., 2004). Moreover, at higher concentrations, the smaller pores and dead-end pores are filled up with particles more quickly, reducing the areas available for particle transport, while larger pores act as preferential pathways allowing faster particle mobility (Raychoudhury et al., 2010). Straining can be grouped in surface straining, wedging, and bridging (Bradford and Torkzaban, 2008; Babakhani et al., 2017). Surface straining occurs in the case of high particle concentration and refers to a scenario where many particles arrive simultaneously at an opening area and clog it. Wedging is a process by which particles are trapped at two boundaries of porous media without interference of particles, while bridging is due to accumulation of particles at a pore constriction (Dong et al., 2015).

iii Adsorption

Adsorption processes can be responsible for ENP retention due to interfacial forces between the particles (adsorbate) and porous media surfaces (adsorbent) (Figure 3-10). Two groups of forces are involved in adsorption processes: (i) dipole and hydration forces, which are also called short-range forces as they are relevant only within 5 nm distance from the surface of the adsorbent and (ii) electric double-layer (attractive or repulsive) and van der Waals attraction forces (Liu et al., 2019). The forces of the second group are also called long-range forces as they can affect the adsorbate behavior in the range of 100 nm around the adsorbent.

According to the DLVO theory, which has been widely used to interpret the adsorption mechanism of particles on the solid surface of porous media, particles can adhere either reversibly or irreversibly to the solid surface (Derjaguin and Landau, 1941). ENPs are usually adsorbed by the porous media via irreversible processes due to the presence of strong and multiple adsorption mechanisms between the ENPs and the surfaces of the porous medium. In such cases, detachment of adsorbed particles is possible

only if a significant perturbation (either physical or chemical) takes place (Babakhani et al., 2017). Conversely, if the particle bond with porous medium surfaces is not sufficiently strong to be maintained permanently, particles are reversible adsorbed and thereby they can be easily subjected to detachment.

iv   Blocking

Blocking effects can occur due to the repulsive particle-particle interactions that hinder further deposition of particles on previously deposited particles. Thus, the subsequent attachment of particles is limited (Ko and Elimelech, 2000). The blocking phenomenon is the result of the decrease of the deposition rate over time, which occurs simultaneously with the increase of adsorbed particles (Figure 3-10). Usually, blocking effects result in an arising plateau of the breakthrough curve (BTC), i.e., plot of normalized concentration as function of pore volumes or time (Saiers et al., 1994; Babakhani et al., 2017).

v   Ripening

In contrast to blocking, ripening is a phenomenon that describes an increasing rate of particle attachment rate over time due to high particle-particle interaction processes (Bradford and Torkzaban, 2008). In this case, particle-particle interactions are stronger than particle-surface interactions and the attached particles act as additional collectors for the attachment of subsequent particles entering the porous media, leading to multi-layer accumulation of particles on the surface of the porous medium (Figure 3-10). Unlike blocking, where the presence of a layer of attached ENPs does not significantly affect the pore flow, ripening leads to clogging of the pore space and therefore to a continuous decrease of porosity and permeability (Tosco and Sethi, 2010). The ripening phenomenon usually gives a descending plateau of the BTC (Babakhani et al., 2017).

vi   Aggregation

Aggregation is one of the key factors influencing the mobility of ENPs in subsurface porous media (Liu et al., 2019). Aggregation involves collisions among particles, either caused by the Brownian motion of particles or by fluid flow that causes shear stress. However, it has been shown that by modifying the ENP surface with surfactants or polymers, the colloidal stability of ENPs in aqueous dispersions and consequently also their transport behavior can be enhanced (He et al., 2007; Phenrat et al., 2008; Phenrat et al., 2009a; F. He et al., 2010; Raychoudhury et al., 2010; Sakulchaicharoen et al., 2010; Cirtiu et al., 2011; Kocur et al., 2013).

4 Chromium as Target Contaminant

4.1 Chromium in the Environment

Chromium was named after the Greek word *"chroma"* that means color. It is a hard metal with a blue shade, which produces a wide array of colored solutions and many colored compounds. Small amounts of chromium are responsible for the green color of emerald, serpentine and chrome mica as well as for the red color of ruby. Chromium was firstly discovered in its metallic form in 1797 by the French chemist Louis-Nicolas Vauquelin and isolated one year later from an orangish-red, lead mineral, which nowadays is known as crocoite ($PbCrO_4$) (Lunk, 2015). Vauquelin successfully isolated chromium from crocoite after dissolving, precipitating and filtering out the lead. Since the 1800s, chromium was commonly used in paints and tanning salts, while nowadays, it is mainly used in the metal and steel industry, especially in the production of alloys and stainless steel, due to its anti-corrosive properties.

4.1.1 Physical Properties

In the periodic table, chromium (Cr) is in the group of the transition metals (Group 6, Period 4) between vanadium and manganese. Its atomic number is 24, the atomic mass is 51.9961 u and the electron configuration is $[Ar]3d^54s^1$ (Meija et al., 2016). Chromium is the first element in the 3d series where the 3d electrons start to enter the inert electron core of the atom. This configuration causes these electrons to contribute less to metallic bonding, hence the melting and boiling points (1907 ºC and 2671 ºC) as well as the enthalpy of atomization are lower than those of the preceding element (1910 ºC and 3407 ºC melting and boiling points of vanadium) (PubChem, 2020). Elemental chromium crystallizes in two forms: body-centred cubic (alpha) and hexagonal close-packed (beta). It is the third hardest element behind carbon (diamond) and boron with a hardness of 8.5 on the Mohs scale of mineral hardness (Samsonov, 1968).

Cr, in its elemental form, can display different magnetic properties. At room temperature and below, Cr is antiferromagnetic, while at temperatures above 38 ºC it is paramagnetic (weakly attracted to a magnet) (Fawcett, 1988). Cr compounds (e.g., chromium dioxide) are instead ferromagnetic. The isotopes of chromium are in the range from ^{42}Cr to ^{67}Cr. Specifically, naturally occurring chromium is composed of the radioisotope ^{50}Cr (4.35 %, half-life of $> 1.3 \cdot 10^{18}$ years) and three stable isotopes: ^{52}Cr (83.789 %), ^{53}Cr (9.501 %), ^{54}Cr (2.365 %) (Audi et al., 2003). Moreover, there are 22 synthetic radioisotopes, of which ^{51}Cr is the most stable (half-life of 27.7 days) and ^{66}Cr is the least stable (half-life of 10 ms); most of the remaining radioisotopes have a half-life shorter than 24 hours (Audi et al., 2003).

4.1.2 Chemical Properties

Chromium exhibits multiple oxidation states from -4 to +6. The most common oxidation states are +3 and +6, with the +3 state being energetically the most stable. Although the states +1, +2, +4 and +5 are generally rare, a few stable chromium compounds with this oxidation numbers do exist. Some examples are: $K_3[Cr(CN)_5NO]$ (+1), $CrCl_2$ (+2), K_2CrF_6 (+4) and K_3CrO_4 (+5). Chromium compounds with an oxidation number of zero or negative states (-4 to -1) are very rare and negligible for natural systems. In water, chromium ions are usually octahedrally coordinated with water molecules, forming hydrates. The solubility, reactivity, mobility and bioavailability of chromium compounds largely depend on their oxidation state, which in turn is strongly related to the prevailing pH and redox conditions.

Trivalent chromium, Cr(III), is the most stable form of chromium. Cr(III) tends to form octahedral complexes, such as Cr(III) oxide, Cr(III) chloride, Cr(III) nitrate and Cr(III) acetate. Cr(III) oxide (Cr_2O_3) is the ninth most abundant chemical in the Earth's crust (0.18 wt %) and occurs as the mineral eskolaite (Heiserman, 1992). C_2O_3 is the thermodynamically favored Cr species over a large pH range under reducing conditions, while dissolved Cr^{3+} is dominant only at strongly acidic conditions, as shown in the Eh-pH diagram (Figure 4-1a) and in the stability and distribution diagrams of Cr as a function of pH (Figure 4-1b).
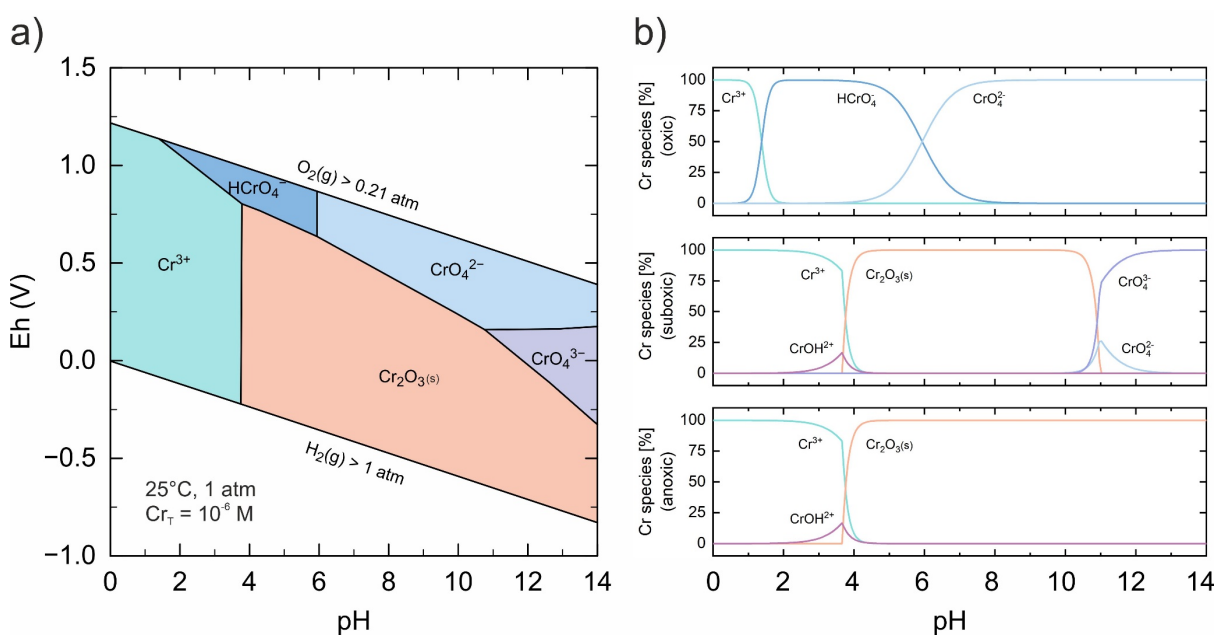
Figure 4-1 **(a) Eh-pH diagram for the system $Cr-H_2O$ at 25°C and 1 atm; Cr_{total}: 10^{-6} M. (b) Stability and distribution of Cr species as a function of pH.**
Diagrams were calculated with PHREEQC (USGS) using the Lawrence Livermore National Laboratory (_LLNL_) database.

At acidic and near neutral groundwater pH values, positively charged and mainly insoluble Cr(III) species like $Cr(OH)^{2+}$ or $Cr(OH)_2^+$ are the thermodynamically favored Cr species (Figure A-1). Furthermore, at circum-neutral pH (6.5-8.5), Cr(III) has a strong affinity to particle surfaces and tends

to form insoluble hydroxide and oxide compounds with metals, such as lead and especially iron (e.g., chromite) (Figure A-2). Thus, under most natural conditions, Cr(III) is typically barely soluble and scarcely mobile. However, in the presence of very strong oxidants, Cr(III) can oxide to Cr(VI) (Tadesse et al., 2006).

Hexavalent chromium, Cr(VI), is a strongly oxidizing agent. Compared to Cr(III), Cr(VI) is more soluble and mobile (Ertani et al., 2017). Depending on the pH values, Cr(VI) occurs in oxic aqueous solutions as different oxyanion species (Figure 4-1). In near-neutral and alkaline solutions, the thermodynamically most common form of Cr(VI) is the monochromate oxyanion, CrO_4^{2-} (Figure 4-2a). In acidic solutions ($\sim$ pH 2-6), protonation of CrO_4^{2-} results in the formation of the hydrogen monochromate anion ($HCrO_4^-$), which can transform (by a condensation reaction) to the stable dichromate anion ($Cr_2O_7^{2-}$) at high Cr concentrations (Figure 4-2b) (Lunk, 2015).
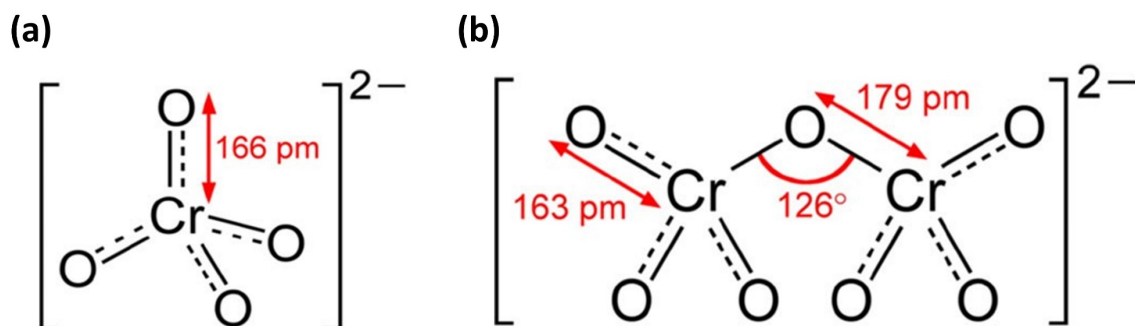
Figure 4-2   **(a) Monochromate anion and (b) dichromate anion (Lunk, 2015).**

Thermodynamic calculations reveal that Cr(VI) is the dominant from under oxic conditions, whereas Cr(III) predominates under suboxic and anoxic conditions (Figure 4-1b). However, both forms have been detected simultaneously in estuarine water, seawater and suboxic groundwater (Kleber and Helz, 1992; Mugo and Orians, 1993). Despite the strong adsorption affinity of Cr(VI) oxyanions for protonated mineral surfaces (typical for iron and aluminum oxides), they are generally mobile in most soil and subsurface systems (Zachara et al., 1987). This is due to the limited sorption capacity of negatively charged soil and sediment minerals (e.g., quartz, silicates or clays) for anionic species (Deng and Bai, 2004). Under certain conditions, Cr(VI) can be reduced to the less soluble and less mobile Cr(III), while oxidants present in soil (e.g., dissolved oxygen and MnO_2) can oxidize Cr(III) to Cr(VI) (Fendorf and Zasoski, 1992). However, oxidation of Cr(III) by dissolved oxygen has been found to be insignificant when compared to MnO_2 (Rai et al., 1989).

4.1.3 Occurrence

Chromium is the 7th most abundant element in the Earth and the 21st most abundant element in the Earth's crust with a concentration above 200 mg/kg (Oze et al., 2004). Cr concentrations in soil vary widely depending on the natural composition of the parent rocks and sediments. Cr is present in granitic,

basaltic and ultramafic rocks with an average concentration of about 10, 200 and 2400 mg/kg, respectively (Oze et al., 2004; Izbicki et al., 2015; Ertani et al., 2017). Natural occurrence of Cr in alkaline, oxic groundwater as Cr(VI), has been reported since the mid-1970s, and it is commonly associated to the presence of ultramafic rocks (mainly ophiolitic serpentinites) and serpentinite soils (Oze et al., 2004). Moreover, both surface and subsurface environments are often exposed to Cr pollution deriving from anthropogenic activities. Indeed, Cr-bearing wastes are often disposed on land or discharged into ponds, lakes or rivers. Migration of Cr through the vadose zone can lead to the contamination of nearby groundwater resources. Overall, the chemical speciation of Cr in an environmental system depends on the primary Cr source as well as on the local geochemical conditions (Seaman et al., 1999).

Cr is commonly found and mined in the minerals chromite ($FeCr_2O_4$) (Figure 4-3a) and magnesiochromite ($MgCr_2O_4$) (Figure 4-3b), which are found in mafic or ultramafic rocks (Lunk, 2015; Ertani et al., 2017). Economically used metallic chromium is obtained by heating the chromite ore in presence of air with a mixture of calcium carbonate and sodium carbonate; Cr is oxidized to chromate, which dissolves via leaching at elevated temperatures and leaves the insoluble iron oxide. The chromate is then converted by sulfuric acid into dichromate, which is converted to Cr_2O_3 by reduction with carbon, and, at the end, reduced via an aluminothermic reaction to Cr. For the production of ferrochromium, the chromite ore is reduced in electric arc furnaces or in smaller smelters using aluminum or silicon (Lunk, 2015).
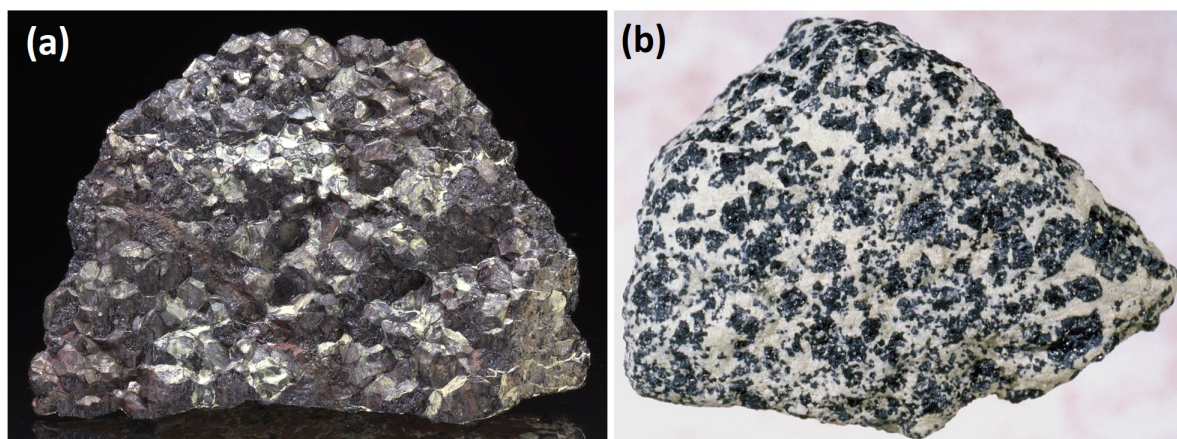
Figure 4-3   **Samples of: (a) chromite ($FeCr_2O_4$) from Zimbabwe (Weinrich, 2014) and (b) Magnesiochromite ($MgCr_2O_4$) from Japan (JGW, 2008).**

In 2019, chromium reserves have been estimated to 570 million metric tons, while the global mine production amounted to 44 million metric tons (US Geological Survey, 2020). South Africa has the second largest reserves worldwide and is the largest chromium producing country in the world with 17 million tons annual mine production, followed by Turkey (10 million tons), Kazakhstan (6.7 million tons) and India (4.1 million tons) (US Geological Survey, 2020). Deposits of elemental chromium exist

but are rare; one example is the Lucky Pipe in Russia, while it is less rare to find Cr in the form of the mineral eskolaite (Cr_2O_3).

Dissolved Cr in water is present in trivalent, Cr(III), or hexavalent, Cr(VI), form, depending on the hydro-chemical conditions (Rai et al., 1989). In seawater Cr(VI) accounts for 75-95 % of the total dissolved Cr (Sirinawin et al., 2000). Cr concentrations in freshwater ranges between 0.1 and 117 µg/L, in seawater it varies from 0 to 0.5 µg/L (Pawlisz et al., 1997). Due to anthropogenic pollution, Cr concentrations in water bodies can be much higher. For example in 1988, the Cr contents in the River Rhine and in the River Elbe ranged between 5-20 and 10-40 µg/L, respectively (Weijden and Middelburg, 1989) (Lenntech, 2020).

4.1.4 Applications

Chromium metal is employed worldwide in amounts of around 20,000 tons per year (Mitra et al., 2010). Metallurgy and electroplating are the sectors with the largest volume uses of chromium (Lunk, 2015). Chromium compounds are mainly used in alloys such as stainless steel, in chrome plating (e.g., decorative electroplating), in metal ceramics and metallurgy to impart high-corrosion resistance, hardness and a shiny finish as well as wood preservatives to protect wood decay from wood attacking insects). Furthermore, Cr is used as catalyst for processing hydrocarbons, in pigments, dyes and paints, to produce synthetic rubies or in the tanning of leather (90 % of all leather is tanned using chromium compounds) (Lunk, 2015). Moreover, chromium is present in a large amount of synthetic, every-day life items. Hence, chromium may be present in domestic waste, which may spread easily to the environment through waste incineration.

4.2 Chromium Toxicity and Epidemiology

The environmental risk deriving from Cr depends on its chemical speciation and its environmental mobility (Rai et al., 1989). Particularly, the toxicological risk is connected to the carcinogenic properties of the anionic Cr(VI), which is worldwide recognized as a toxic and potentially harmful element, while Cr(III) is highly insoluble and generally considered non-toxic (Gad, 1989; Richard A, 1997). Most of the hexavalent compounds (e.g., chromic acid, chromates, chlorochromates) that are used in several industrial sectors for various purposes are toxic and several of them can be carcinogenic if inhaled or ingested (Sedman et al., 2006). Skin contact with Cr(VI) compounds can provoke dermatitis, skin allergies, dermal corrosion or dermal necrosis (Gad, 1989).

Because Cr(III) can be oxidized to Cr(VI) under certain conditions (e.g., presence of strong oxidants), the US EPA does not distinguish between the trivalent and hexavalent Cr (Tadesse et al., 2006). Therefore, US EPA and WHO had set the permissible limits for drinking water (corresponding to the maximum contaminant level, MCL) for total chromium at 50 µg/l (Baral and Engelken, 2002) and the tolerance limit for Cr(VI) discharge into inland surface waters at 100 µg/L. However, Cr has been found

in groundwater at industrial sites in concentrations that exceed the MCL. In the nuclear waste plume at Hanford site, UK, Cr(VI) concentration ranged from 4.7 to 5 mg/L (Poston et al., 2002; Petersen et al., 2009), while the Cr contents in a contaminated groundwater plume at the US Coast Guard Support Center, Elizabeth City, North Carolina reached 26 mg/L (e.g., Lai and Lo, 2008).

Chromate contaminations of surface waters, soils, vadose zones and groundwater is a topical and serious threat. Since 2010, in the European Economic Area (EEA), the use of Cr(VI) compounds has been restricted, and in some cases banned (ECHA, 2010). In the last two years, nine more Cr-based substances were included in the Authorization List SVHCs (substances of very high concern) of REACH (registration, evaluation, authorization and restriction of chemicals) (ECHA, 2010). In the USA, as of 2019, Cr(VI) is the 17th substance in the priority list of 25 hazardous substances that pose the greatest potential threat to human health due to their known or suspected toxicity, frequency and human exposure at Superfund sites (ATSDR, 2020).

4.3 Cr(VI) Removal Methods

Over the last years, several methods have been developed to remove toxic Cr(VI) from water, including redox precipitation (Zhou and Korenaga, 1993); adsorption on various available adsorbents (Sharma and Forster, 1994; Calace et al., 2002; Han et al., 2006; Bhattacharya et al., 2008; Gupta et al., 2011; Shen et al., 2012; Jung et al., 2013; Nag et al., 2016; Yao et al., 2016), membrane separation (Chakravarti et al., 1995; Hasan et al., 2009) as well as anion exchange and extraction, using anionic and non-ionic surfactants, alkaline extractants and phosphate buffers (Pagilla and Canter, 1999). Compared to the other methods, adsorption presents significant economic and environmental advantages such as low cost, availability and simplicity of operation. However, Cr(VI) remediation methods based on adsorption suffer from certain drawbacks such as poor selectivity, limited adsorption efficiency at low ion concentrations as well as regeneration and recovery of sorbents. Particularly, poor selectivity represents the principal difficulty in the removal of Cr(VI) species by adsorption processes.

Overall, to date, removal techniques based on reduction of Cr(VI) to the non-toxic Cr(III) has shown to be the most effective strategy in lowering the Cr(VI) content in groundwater below the maximum acceptable toxicity limits (Fruchter, 2002; Malone, 2004; Kate Bronstein, 2005).

4.3.1 Reduction

Reduction of Cr(VI) to Cr(III) leads to the conversion from highly soluble, toxic and mobile hexavalent forms into the less soluble, less toxic and immobile trivalent forms of Cr. Indeed, the two most stable oxidation states of chromium, Cr(VI) and Cr(III), present a significantly different mobility, bioavailability and toxicity (Rai et al., 1989; Wilbur et al., 2012; Ertani et al., 2017). Cr(VI) compounds such as chromate (CrO_4^{2-}), dichromate ($Cr_2O_7^{2-}$) and hydrogen chromate ($HCrO_4^-$) are the most toxic

forms and some are considered carcinogenic (Wilbur et al., 2012; Ertani et al., 2017). Reduction to Cr(III) results in the precipitation and thus immobilization of these Cr(VI) species as either amorphous or partially crystalline Cr(III)-Fe(III) substituted phases (Eary and Rai, 1988; Powell et al., 1995; Peterson et al., 1997; Loyaux-Lawniczak et al., 2001). Although manganese oxides present in soils and sediments are generally able to re-oxidize Cr(III) to Cr(VI), re-oxidation does not easily take place under conditions encountered in most natural groundwater environments and is furthermore limited by the effects of surface alteration (Fendorf and Zasoski, 1992).

In water, sediments and soils, reduction of Cr(VI) to Cr(III) can be induced by naturally occurring reductants such as sulfides or organic acids. However, those reactions are extremely slow and the rate decreases as the pH increases (Sedlak and Chan, 1997). The ability of iron as Fe^0 and Fe(II) to reduce redox sensitive elements has been demonstrated at both laboratory scale and in field tests (Puls et al., 1999). On this basis, iron compounds have also been used as permeable reactive redox barrier in *in-situ* treatment applications installed downstream of Cr(VI) plumes (Powell et al., 1995; Blowes et al., 1997; Pratt et al., 1997). Additionally, reducing synthetic agents (e.g., dithionite) were injected in the subsurface to reduce naturally occurring Fe(III)-bearing mineral phases and obtain the reactive ferrous iron state (Istok et al., 1999; Fruchter et al., 2000; Malone, 2004).

4.3.1.1 Reduction by Ferrous Iron

Ferrous ion, Fe(II), is one of the most important natural reductants of Cr(VI) and it is relatively abundant in suboxic/anoxic soils. Divalent iron is released by the weathering of Fe(II)-bearing minerals or can derive from reductive dissolution of insoluble ferric compounds and silicates under reducing condition (Eary and Rai, 1989).

Under oxic conditions, Fe(II) rapidly reduces Cr(VI) at pH between 6 and 9 (Eary and Rai, 1988). However, the presence of oxygen leads to rapid depletion of Fe(II) and formation of Fe(III)-bearing species. In absence of oxygen, the reduction rate of Cr(VI) by Fe(II) is strongly dependent on the pH of the solution: it increases with decreasing pH under acidic conditions and increases with increasing pH under neutral and basic conditions (Buerge and Hug, 1997; Sedlak and Chan, 1997).

The stoichiometric redox reaction to reduce Cr(VI) to Cr(III) by Fe(II) involves three successive one-equivalent electron (e^-) transfer steps, meaning that it requires three equivalents of Fe(II) (Eary and Rai, 1988; Buerge and Hug, 1997; Sedlak and Chan, 1997).

The oxidation-reduction (redox) reaction is:

$$\mathbf{Cr^{VI} + 3e^- \rightarrow Cr^{III}} \quad \text{(reduction)} \qquad \qquad \textbf{Equation 4-1}$$

$$\mathbf{3Fe^{II} \rightarrow 3Fe^{III} + 3e^-} \quad \text{(oxidation)} \qquad \qquad \textbf{Equation 4-2}$$
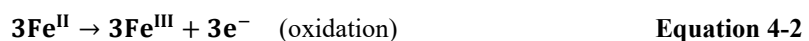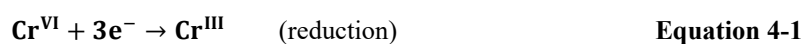
Since the molecular weights of Fe and Cr are approximately the same (respectively 55.8 and 52 u), the stoichiometric weight ratio is also close to 3 to 1. In soil and sediment systems, the redox reaction

between Cr(VI) and Fe(II) is thermodynamically favored, dependent on pH, temperature and concentration of Fe(II), and takes place in a period of minutes to months (Sedlak and Chan, 1997). The reaction can be written as follows:

$$Cr^{VI}{}_{aq} + 3Fe^{II}{}_{s} \rightarrow 3Fe^{III}{}_{s} + Cr^{III}{}_{s} \qquad \text{Equation 4-3}$$

Fe(II) reacts with Cr(VI) and promotes its reduction to Cr(III), while Fe(II) is oxidized to Fe(III), creating insoluble ferric (hydr)oxide phases [Fe(OH)$_3$]. Cr(III) is precipitated either as (hydr)oxide or as mixed Cr(III)-Fe(III) oxides.

In case of the reduction of Cr(VI) as CrO$_4{}^{2-}$ by Fe(II) in form of Fe(II)(OH)$_2$, a possible redox-reaction resulting in the precipitation of Cr(III) hydroxide and formation of Fe(OH)$_3$ would look as follows:
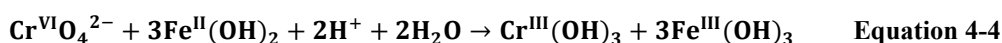
$$Cr^{VI}O_4{}^{2-} + 3Fe^{II}(OH)_2 + 2H^+ + 2H_2O \rightarrow Cr^{III}(OH)_3 + 3Fe^{III}(OH)_3 \qquad \text{Equation 4-4}$$

It is important to note that the Fe and Cr reactants and products involved in this equation can vary greatly depending on the source materials and hydro-chemical conditions, thus this reaction should be considered only as an example of a possible redox reactions between Fe(II) and Cr(VI).

It has been proven that Fe(II) bound to surface of ferric oxide minerals significantly enhances the reduction rate of Cr(VI), showing higher reactivity than aqueous Fe(II) in solution (Buerge and Hug, 1999). Reactive Fe(II) can form on the surface of iron minerals such as ferrous sulfide (FeS), pyrite (FeS$_2$), siderite (FeCO$_3$), ferric (hydr)oxides such as goethite (α-FeOOH), lepidocrocite (γ-FeOOH), or hematite (α-Fe$_2$O$_3$) and reduced ferruginous clay minerals or mixed valent Fe(II)/Fe(III) mineral phases such as magnetite (Fe$_3$O$_4$) and green rust (Elsner et al., 2004). Elsner et al. (2004) showed that reaction rates of surface-bound Fe(II) are strongly dependent on the chemical composition of the iron-bearing minerals. Moreover, the reactivity of Fe(II) bound to different mineral phases is different due to their different crystallography and surface structures. For example, compared to the pure Fe(III) minerals, mixed valent Fe(II)/Fe(III)-minerals contain reactive Fe(II) in their mineral structure, which can significantly increase the reactivity (Elsner et al., 2004).

4.3.1.2 Reduction by Zerovalent Iron

Fe^0-bearing materials (e.g., ZVI) can remove a wide range of organic and inorganic compounds from the aqueous phase, including Cr(VI) (Gould, 1982; Astrup et al., 2000; Alowitz and Scherer, 2002; Franco et al., 2009). The stoichiometric redox reaction to reduce Cr(VI) to Cr(III) by Fe^0 proceeds by two simultaneous processes, where Fe^0 is directly oxidized to Fe(III), as following:

$$Fe^0 + Cr^{VI} \rightarrow Fe^{III} + Cr^{III} \qquad \text{Equation 4-5}$$

Unlike the reduction of Cr(VI) by Fe(II), where the process results in the consumption of 3 mol of Fe per mol of Cr(VI) reduced, the process represented by the Equation 4-5 results in the consumption of 1 mol of Fe per mol of Cr(VI) reduced. Hence, the stoichiometric weight ratio is 1 to 1. Reduction of

Cr(VI) as CrO_4^{2-} by ZVI and subsequent precipitation of Cr(III) hydroxide and formation of Fe(III) hydroxide would look as follows:
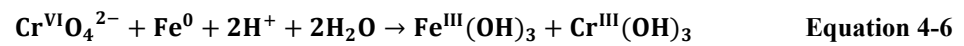
$$Cr^{VI}O_4^{2-} + Fe^0 + 2H^+ + 2H_2O \rightarrow Fe^{III}(OH)_3 + Cr^{III}(OH)_3 \qquad \textbf{Equation 4-6}$$

It is important to note that the Fe and Cr reactants and products involved in this equation can vary greatly depending on the source materials and hydro-chemical conditions, thus this reaction should be considered only as an example of a possible redox reactions between Fe^0 and Cr(VI).

5 Materials and Analytical Methods

GR$_{SO4}$ and S-nZVI were investigated in two independent experimental studies that were based on the two main topics and research questions of this thesis as they were specified in Chapter 1. These two topics concern:

1. reactivity of GR$_{SO4}$ and S-nZVI against Cr(VI) in sandy porous media under dynamic conditions
2. transport behavior of GR$_{SO4}$ and S-nZVI inside a porous medium.

Both studies were generally based on column experiments. However, depending on whether reactivity or transport was investigated, two different experimental column set-ups were designed. Experimental conditions and more detailed information on the specific set-up of the reactivity and transport studies are therefore described in Chapter 6 and Chapter 7, respectively.

5.1 Materials

The following commercially available chemicals were used in this study: sodium carboxylmethyl cellulose, CMC (MW = 250 kDa, Sigma-Aldrich), xanthan gum, XG (Carl Roth), sodium borohydride (NaBH$_4$, 99 %, Sigma-Aldrich), ferric sulfate hydrate (Fe$_2$(SO$_4$)$_3$, Sigma-Aldrich), ferrous sulfate heptahydrate (FeSO$_4\cdot$7H$_2$O, Sigma-Aldrich), ferrous chloride tetrahydrate (FeCl$_2\cdot$4H$_2$O, Sigma-Aldrich), acetic acid (Sigma-Aldrich), sodium acetate anhydrous (> 99 % Sigma-Aldrich), sodium nitrate (NaNO$_3$ > 99 %, Carl Roth), sodium sulfide nonahydrate (Na$_2$S, > 98 %, Strem Chemichals Inc.), hydrochloric acid (HCl, 37 %, Sigma-Aldrich), sodium hydroxide (NaOH, Sigma Aldrich). Furthermore, quartz sand of different grain sizes was used for the experiments: 0.1-0.3 mm (Chemsolute®, Th. Geyer), 0.4-0.8 mm and 0.6-1.3 mm (Carl Roth Germany); the details on the chemical composition and specification are listed in Table A- 2 and Table A- 3. Solutions were made of de-ionized Millipore Milli-Q water (18.2 MΩ cm). In order to prevent metal contamination, all glassware used for the experiments was acid washed and kept overnight in a 10 % v/v HCl solution prior to each use.

Initially a newly developed prototype of a column reactor was intended to be used for the column experiments (Figure A-3). However, due to the presence of dead volumes at the bottom and at the top of the reactor, operational difficulties were experienced. Although the bottom/top units of this column prototype were designed *ad hoc* to ensure a homogeneous flow distribution, it was observed during the transport experiments that these parts entrap the injected reactants and alter their distribution within the column. These effects resulted to be even higher in case of experiments carried out in horizontal manner.

In addition, the dead volumes are responsible for the dilution of the inlet/outlet solution, which may affect the outcomes of both reactivity and transport column tests. Therefore, it was decided to use a different type of column reactor for the experiments.

The column reactors used to carry out the experiments of this study were prepared from conical centrifuge tubes superclear (VWR, 15 ml), made of polypropylene (PP) and with diameter and length of 1.4 cm and 11 cm, respectively (Figure A-4). Although the physical dimensions of columns are not standardized (in literature column dimensions vary considerably), it is recommended to use a reasonable length/diameter ratio (Banzhaf and Hebig, 2016). For example, a short column with a too large diameter (relative to its length) may prevent homogeneous flow within the sediment; on the other hand, preferential flow may occur in long columns with small diameters. The columns used for this study has a length/diameter ratio equal to approximately 8. Moreover, as the tubes are transparent, they allow visual control during the eperiments. At the bottom and at the top of the reactor, a small layer of coarse sand (d_c = 0.6-1.3 mm) was placed to ensure homogeneous flow distribution. Each centrifuge tube was equipped with an inlet and outlet tubing made of polyvinyl chloride (PVC) and with an internal diameter of 1.52 mm. A peristaltic pump (Ismatec IPC) was used to provide uniform flow also at low flow rates.

5.1.1 Quartz Sand

Quartz (SiO_2) is one of the major constituent of Earth's crust (66-70 wt % in the upper continental crust) and is generally concentrated in the sand and silt fractions of soils, where its abundance reflects its chemical stability and resistance to weathering (Rudnick, 2010; Southard et al., 2014). Quartz is a crystalline mineral composed of silicon and oxygen atoms, which are linked in a continuous framework of silicon-oxygen tetrahedra, $[SiO_4]^{4-}$, with each oxygen being shared by two tetrahedra, resulting in the overall chemical formula of SiO_2. Quartz exists in two forms, the normal α-quartz and the high-temperature β-quartz, which crystallize in the trigonal crystal system and hexagonal system respectively. It is characterized by a high hardness (hardness of 7 on the Mohs scale), which leads to a high chemical stability and high resistance to weathering and erosion.

Because of its characteristics, quartz sand is commonly used as a model substrate for the experimental simulation of aquifers. In this study, the reactivity and transport experiments were carried out using sea sand purified by acid and calcined as matrix material (collector) with grain dimeters (d_c) of 0.1-0.3 mm (Figure 5-1) or 0.4-0.8 mm (Figure 5-2).
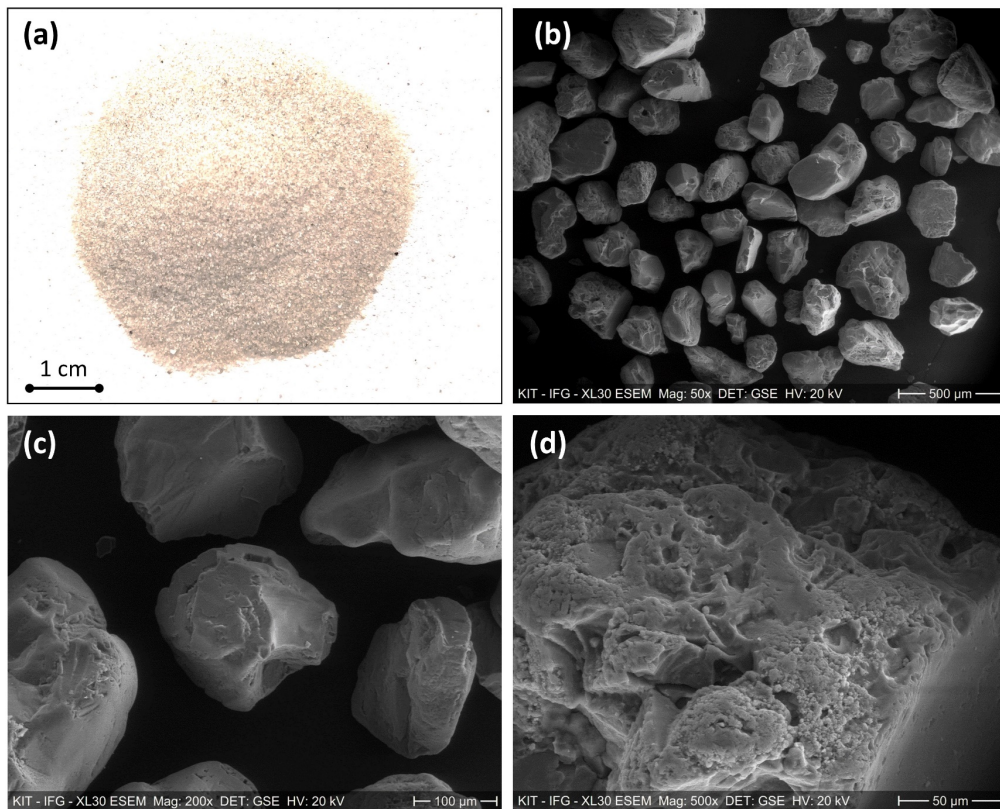
Figure 5-1 **(a) Photo and (b-d) ESEM images of quartz sand (Chemsolute®, Th. Geyer) with crystal size in the range of 0.1-0.3 mm.**
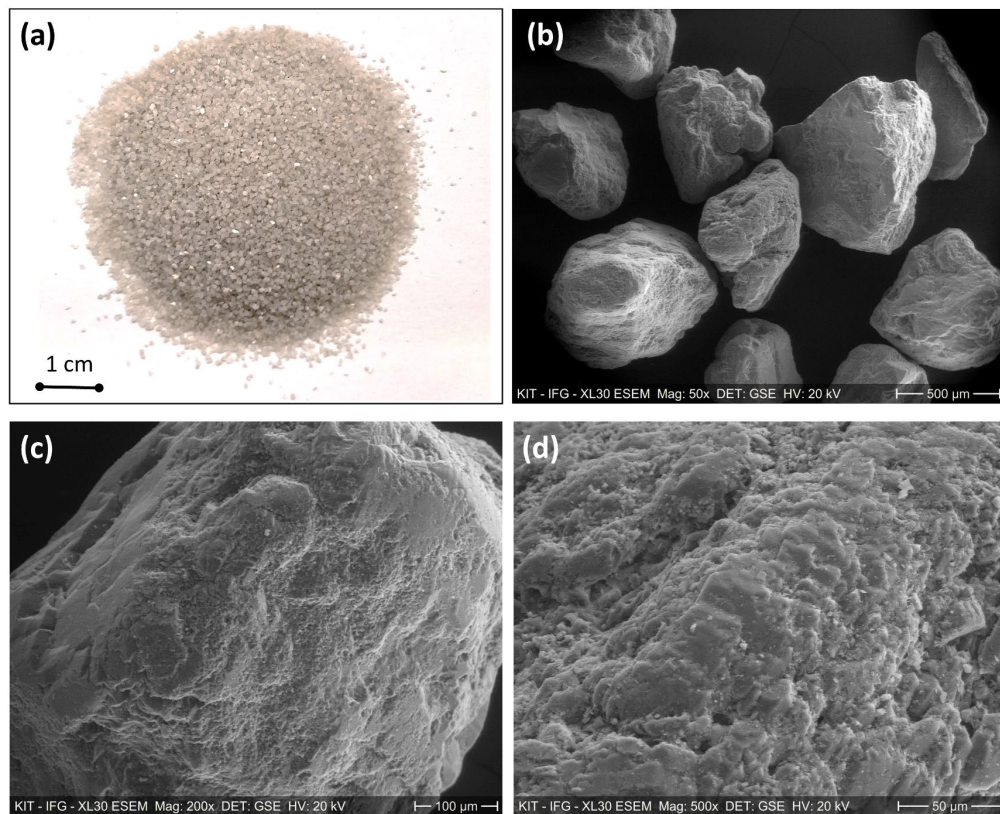
Figure 5-2 **(a) Photo and (b-d) ESEM images of quartz sand (Carl Roth Germany) with crystal size in the range of 0.4-0.8 mm.**

5.1.2 Sulfate Green Rust and Sulfidized Nano Zerovalent Iron

GR_{SO4} and S-nZVI were synthesized in the Laboratory of Environmental and Raw Materials Analysis (LERA), Department of Geochemistry and Economic Geology (EGG), Institute of Applied Geosciences (AGW), Karlsruhe Institute of Technology (KIT). Due to their oxygen sensitivity, the syntheses procedures, the storage of the samples until they were further processed or analyzed and all the experiments, if not mentioned otherwise, were carried out inside an anoxic glovebox P[Box] Compact Glove Box, from Jacomex (Dagneux, France) filled with argon atmosphere. The glovebox maintains a strict < 3 ppm oxygen atmosphere through argon that reacts with a reactor equipped with a copper catalyst to remove residual oxygen. The chemicals, the required glassware and utensils were transferred into the glovebox before each experiment by using a lock chamber. To avoid oxygen being introduced into the glove box, the lock chamber was subjected to a 4-time flushing cycle that includes evacuation of oxygen via a vacuum pump and intake of oxygen-fee argon atmosphere. The Milli-Q water was deoxygenated for at least 1 hour prior to its transfer to the glovebox. The degassing process was carried out by the injection of nitrogen.

5.1.2.1 Synthesis of Sulfate Green Rust

GR_{SO4} ($Fe(II)_4Fe(III)_2(OH)_{12}SO_4 \cdot 8H_2O$) was synthesized after the co-precipitation method described in the study by Thomas et al. (2018) as follows: 40 mL of a 33 mM $Fe_2(SO_4)_3$ solution were slowly titrated (1 mL/min, Ismatec IPC peristaltic pump) to 20 mL of 67 mM $FeSO_4 \cdot 7H_2O$ inside a polypropylene beaker under constant stirring (300 rpm) inside the glovebox. The solution pH was maintained at approximately 7.0 using dropwise addition of 1 M NaOH. Following titration, the green rust suspension was stirred for 24 hours and then stored at room temperature inside the glovebox until use (maximum of 5 days) (Figure 5-3a).

5.1.2.2 Synthesis of Sulfidized Nano Zerovalent Iron

S-nZVI was synthesized following the procedure reported by Mangayayam et al. (2019). First, nanoscale zerovalent iron (nZVI) was synthesized by titrating 71.6 mL of 0.25 M $FeCl_2 \cdot 4H_2O$ solution with 35.8 mL of 1 M $NaBH_4$ at a rate of 5 mL/min using a peristaltic pump. The resulting solution was mechanically stirred for 15 minutes before separating the formed nZVI particles using a strong magnet. The separated nZVI was re-suspended in 120.4 mL of 0.2 M acetate buffer (pH 5.7) inside a 160 mL serum bottle, crimp sealed and sonicated for 15 minutes. Thereafter, 4.2 mL of 1 M Na_2S was added to the suspension, sonicated for another 5 minutes and then placed on an orbital shaker (180 rpm) for 3 hours. Afterwards, the particles were washed thrice with degassed 96 % ethanol (Figure 5-3b). With this synthesis method a total amount of approximately 1 g S-nZVI could be produced. S-nZVI was used shortly after synthesis. For solid characterization, S-nZVI particles were dried under anoxic conditions (in Ar atmosphere).
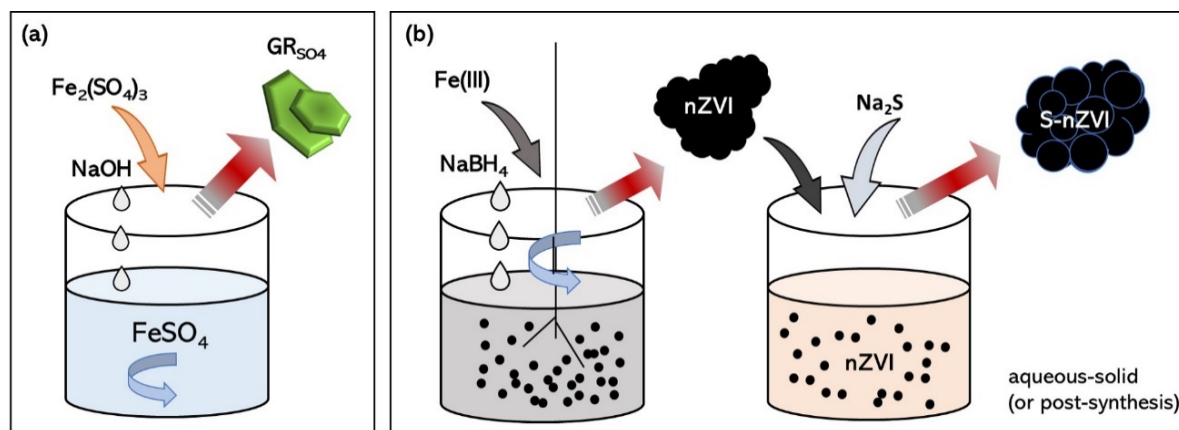
Figure 5-3 Schematic representation of the procedures used for the synthesis of (a) GR$_{SO4}$ via the co-precipitation method and (b) S-nZVI via the post-synthesis method.

5.2 Analytical Methods

5.2.1 X-Ray Diffractometry (XRD)

X-ray diffractometry (XRD) was used to carry out mineralogical characterization of the solid samples immediately after their synthesis. A Bruker D8 Diffractometer (Karlsruhe, Germany) in the Laboratory of LERA, Department of EGG (AGW, KIT) was used for these analyses. The diffractograms were recorded with Cu-Kα ($\lambda = 1.5418$ Å) radiation at 40 kV and 40 mA in the Bragg-Brentano (θ-θ) geometry. The LynxEye detector scanned at 2θ values between 2° and 72°, with a step size of 0.02 and dwell time of 1 s per step. The detector window had an opening of 2° and the nickel filter, divergence stop and Soller stop were at 0.5 mm, 0.6 mm and 2.5°. With regard to the detection limit of the XRD analysis, it can be assumed that, on the basis of the mainly investigated single-phase systems and the expected mineral content known in advance, the detection limit is in the range of about 1-2 wt %. Data evaluation was carried out with the software DIFFRAC.SUITE EVA (version 13) from Bruker AXS. Peak identification was made using the "American Mineralogist Crystal Structure" database.

5.2.2 Scanning Electron Microscopy (SEM)

Scanning electron microscopy (SEM) was used to investigate morphology, surface topography and composition of the S-nZVI particles. SEM images were acquired in the Potsdam Imaging and Spectral Analysis (PISA) Facility at GFZ German Research Centre for Geosciences (Potsdam, Germany). Preparation of the sample was carried out inside an anaerobic chamber (97 % N$_2$, 3 % H$_2$, Coy Laboratory Products, Inc.). The samples were re-suspended in 2 mL deoxygenated water and ultra-sonicated for 5 min. Approximately 50 µl of the re-suspended samples were drop-casted onto an aluminum SEM stub and allowed to dry overnight. The stubs were put inside an anaerobic jar (AnaeroJar^{TM} Oxoid^{TM}, Thermo Fisher Scientific) to minimize oxidation during rapid transfer to the SEM. The stubs were quickly loaded into vacuum sputter coater (BAL-TEC MED 020, Leica

Microsystems) and were coated with carbon (~20 nm) to avoid charging effects during imaging. SEM images were acquired using a ZEISS Ultra Plus FE-SEM operated in high vacuum mode at an acceleration voltage of 2 kV with 20 μm aperture size using an InLens secondary electron detector. Elemental analyses of the samples were performed at 15 kV with 120 μm aperture size in point and shoot mode using a Thermo Scientific Ultra Dry Energy Dispersive Spectrometry (EDS) detector.

5.2.3 Environmental Scanning Electron Microscopy (ESEM)

Environmental scanning electron microscopy (ESEM) was used to investigate morphology and surface topography of GR_{SO4}. ESEM images were acquired in the laboratory of the Institute of Functional Interfaces (IFG) at KIT. After synthesis or the reactivity experiments with Cr(VI), the GR_{SO4} particles have been allowed to dry inside the anaerobic chamber and then stored in tightly sealed containers for transportation. The samples were quickly placed on a holder with conductive double-sided tape (Leit-Tabs, Plano GmbH) and immediately coated with a mixture of gold (80 %) and palladium (20 %) (MED 020, BAL-TEC) in order to achieve a better contrast and less charge effects during imaging. ESEM images were obtained on a Philips XL 30 FEG environmental scanning electron microscope operated at acceleration voltages of 10 kV and 20kV at high vacuum ($5.4 \cdot 10^{-6}$ mbar, SE-Detector) and in a water vapor atmosphere of 1 Torr (GSE Detector).

5.2.4 Transmission Electron Microscopy (TEM)

Transmission electron microscopy (TEM) was used to investigate crystal structure, morphology and particle size of the synthesized S-nZVI materials. TEM images were acquired at the PISA Facility at GFZ Potsdam. TEM samples were prepared by drop-casting the suspension sample onto amorphous holey carbon-coated copper grid, which was then loaded into a single tilt TEM holder and sealed for rapid transfer (< 30 s) into the TEM. Preparation of the sample grids was carried out inside an anaerobic chamber. The samples were re-suspended in 10 mL deoxygenated 96 % ethanol and ultra-sonicated for 5 min. Approximately 50 μl of re-suspended sample was drop-casted onto a grid on top of a cellulose acetate filter paper, and the sample was allowed to dry for ca. 5 minutes. The TEM grid was loaded onto a TEM grid box holder and transported to the TEM room. The grid was loaded onto a single tilt TEM holder and loaded onto the TEM instrument. The TEM images, electron dispersive X-ray (EDX) spectra and elemental maps were acquired using an FEI Tecnai G20 F20 X-Twin FEG S/TEM operated at 200 kV and equipped with a Gatan imaging filter (GIF) Tridiem™, a Fischione high angle annular dark field (HAADF) detector and an EDAX X-ray analyzer. The mean particle diameter (d_p) was estimated by manually measuring the diameters of 250 particles using Gatan Microscopy Suite® (GMS) version 2.3.

5.2.5 Electrophoretic Mobility Measurements (EPM)

Electrophoretic mobility was used to measure zeta potential of S-nZVI particles. The analyses were performed in the laboratory of the Institute for Nuclear Waste Disposal (INE) at KIT, using a NanoBrook ZetaPlus zeta-potential analyser (Brookhaven Instruments Corporation) with Phase Analysis Light Scattering (PALS) technique and a gold electrode (S/N Au-110), based on doppler velocimetry (electrophoretic light scattering or ELS). Via applying an electric field generated between the walls of the electrode, the charged particles acquire a terminal velocity proportional to the applied field. The frequency of the scattered light is a function of particle velocity due to the Doppler shift. Electrophoretic mobility is then determined from the known applied electric field (V/cm) and the measured particle velocity (μm/s). Zeta potential (mV) is then calculated using Smoluchowski, Hückel or Henry's equations, depending on the particle size and ionic strength of the suspensions.

5.2.6 Spectrophotometric Analysis

Spectrophotometric analyses were used in case of chromium reactivity studies as well as for the nanoparticle transport experiments. For reactivity column experiments (Chapter 6), two independent UV-Vis methods were employed to analyze the concentrations of hexavalent chromium, Cr(VI), in the effluent samples. On the other hand, for the transport studies (Chapter 7), spectrophotometric analysis was used for turbidity measurements in order to determine particle concentrations.

5.2.6.1 Cr(VI) Measurements

The concentrations of hexavalent chromium, Cr(VI), of the reactivity column experiments were determined by using two different UV-Vis spectrophotometric approaches: (i) manual collection of the samples and UV-Vis analysis via colorimetric method and (ii) on-line measurements using an UV-Vis flow through cell (Figure 5-4).

i   Manual collection of the samples and UV-Vis analysis via colorimetric method

The manually collected column effluent samples were analyzed using the 1,5-diphenylcarbazide colorimetric method (Environmental Protection Agency, EPA Method 7196A). For the colorimetric method, 0.5 mL of 1,5-diphenylcarbazide reagent (0.5 g 1,5-diphenylcarbazide in 100 mL acetone) and 25 mL of 0.01 M HCl solution were used to prepare the samples for analysis. Pink color developed after approximately 15 min and absorbance was measured immediately at 540 nm using a 5 cm optical glass cell with a Perkin-Elmer Lambda 2S UV-Vis spectrophotometer (Waltham, MA, USA), calibrated using a four-point calibration curve. The limits of detection (LOD) and quantification (LOQ), which are defined as the lowest analyte concentration that can be reliably detected and quantified, are equal to 0.1 and 0.2 mg/L, respectively.
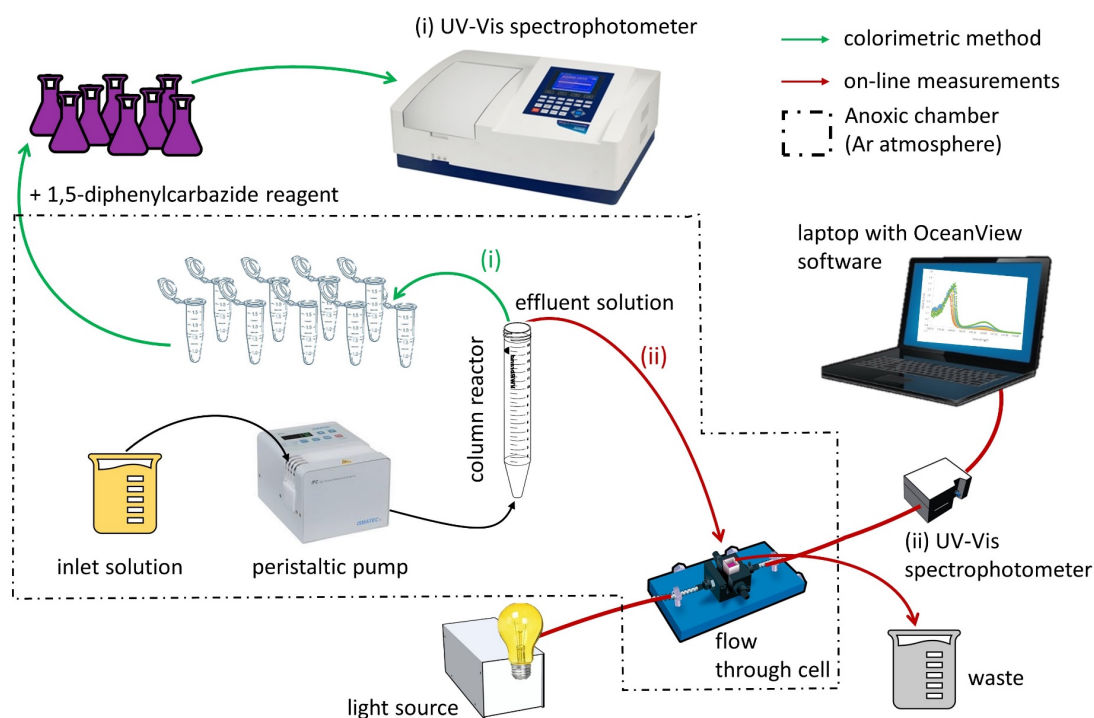
Figure 5-4 **Schematic representation of the two spectrophotometric procedures used to analyze chromate concentrations in column effluent samples.**
The effluent solution was (i) manually collected or (ii) on-line monitored.

ii   On-line measurements using an UV-Vis flow through cell

On-line measurements (at resolution < 1 s) using a UV-Vis flow through cell (2 mm path length, Hellma, Germany) connected with an UV-Vis spectrophotometer (STS-UV-L-50-400-SMA, 190-600 nm, Ocean Optics). Aqueous solutions of hexavalent chromium (without any complexing agents) absorb light in the ultraviolet and violet regions of the spectrum but wavelength-specific absorbance varies with solution pH and hence also on the Cr(VI) speciation (Buerge and Hug, 1997; Fournier-Salaün and Salaün, 2007). Initial calibrations showed that Cr(VI) concentration correlates linearly with absorbance at wavelengths of 274.3 and 371.3 nm at solution pH 7.0 and 9.5, and at wavelengths of 257 and 345 nm at pH 4.5 (Figure 5-5a and Figure 5-5b). Figure 5-5c and Figure 5-5d show the calibration curves used for Cr(VI) aqueous solution (0.125-2 mM or 6.5-104 mg/L) at pH 7.0. Those observations are in agreement with the study by Fournier-Salaün and Salaün (2007), where the authors reported that the absorption spectrum presents two maxima at 275 nm and at 371 nm in alkaline media and at 257 nm and at 349 nm in acid media. The LOD and LOQ for chromate analysis were determined to be respectively 0.01 and 0.05 mM (0.5 and 2.6 mg/L).
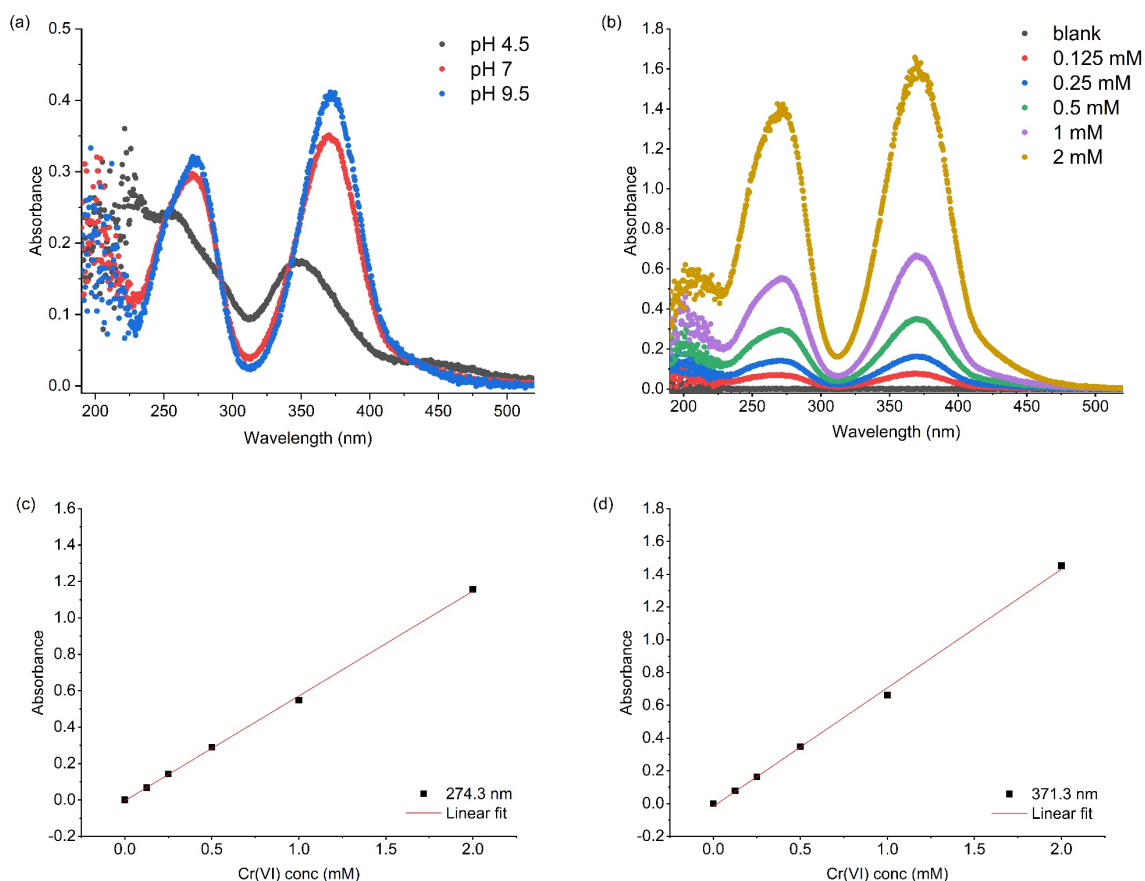
Figure 5-5   Calibrations of UV-Vis for Cr(VI) measurements.
(a) Effect of the pH (4.5, 7.0 and 9.5) of a Cr(VI) solution on UV-Vis absorption spectra; (b)
UV-Vis spectra of Cr(VI) solutions of varying concentrations (0.125-2 mM) at pH 7.0, used to
set the calibration curves for absorbance at wavelength of (c) 274.3 nm with R^2 = 0.999 and
(d) 371.3 nm with R^2 = 0.998.

The colorimetric approach is the most common method used for Cr(VI) determination. However, the on-line method allowed the acquisition of more accurate Cr(VI) measurements at a much higher temporal resolution compared to the colorimetric method. Furthermore, it enabled the monitoring of pH changes that may occur during Cr(VI) injection.

5.2.6.2 Turbidity Measurements of Particle Suspensions

The physical stability of S-nZVI particles in suspension and the particle concentration in the column effluent samples were determined via turbidity measurements using time-resolved absorbance measurements with a UV-Vis spectrophotometer (STS-UV-L-50-400-SMA, 190-600 nm, Ocean Optics) inside the anoxic chamber at room temperature (as shown in Figure 5-4, second procedure). Similar to previous studies (He et al., 2007; Cirtiu et al., 2011), this procedure was used to perform the transport experiments. Absorbance spectra at different concentrations were obtained to verify linear correlation between absorbance and particle concentration (Figure 5-6c and Figure 5-6d). The tested nanoparticles absorb light in the entire UV-Vis range, without showing any peak (Figure 5-6a and Figure 5-6b), thus the range between 500 and 520 nm was used to determine how the absorbance is

affected by the particle concentration. The absorbance data were collected over time. The LOD and LOQ are equal to 0.02 and 0.03 g/L.
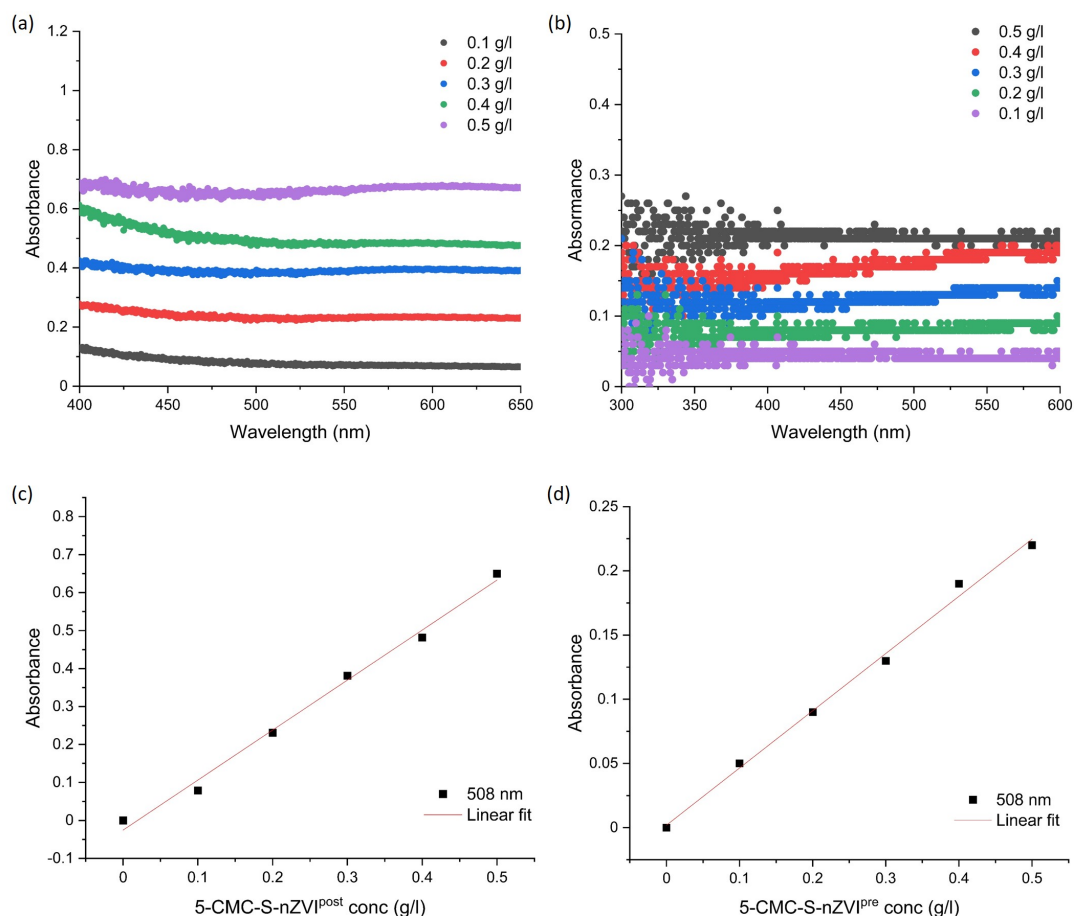
Figure 5-6   Calibrations of UV-Vis for measuring S-nZVI particle concentration.
UV-Vis absorption spectra of (a) 5-CMC-S-nZVI^{post} and (b) 5-CMC-S-nZVI^{pre} of varying concentrations (0.1-0.5 g/L) as well as the respective calibration curves established in the range from 500-520 nm with (c) R^2 = 0.992 and (d) R^2 = 0.993.

5.2.7 Inductively Coupled Plasma Optical Emission Spectrometry (ICP-OES)

Total chromium and iron concentration in solutions from manually collected samples were determined by inductively coupled plasma optical emission spectrometry (ICP-OES, Varian 715ES) in the in the Laboratory of LERA, Department of EGG (AGW, KIT). Total iron and chromium were analyzed at wavelength of 259.94 nm and 267.72 nm, respectively. The samples and standards were diluted with various volumes of 1 % HNO$_3$ depending on the element concentration required. For iron and chromium, the single-element ICP-Standard ROTI®STAR from Carl Roth with a Fe and Cr stock solutions of 1000 mg/L was used for the preparation of the calibration standards. For quality control purposes, selected standards were regularly re-measured as samples within each measurement series in order to detect analytical drifts. The LOD and LOQ for chromium are 0.08 and 0.23 mg/L, while they are equal to 0.06 and 0.18 mg/L for iron.

5.2.8 Magnetic Resonance Imaging (MRI)

5.2.8.1 Measurement Method and Conditions

Magnetic resonance imaging (MRI) is a non-invasive, *in-situ* technique mostly used in medical and biological sciences, which has recently proven its suitability in contaminant hydrology and environmental research. In this study, magnetic resonance imaging (MRI) was employed to visualize the iron nanoparticles during injection within a sandy porous matrix and to quantify the kinetics of their transport. For the experiments of this work, a Bruker Avance HD III, 200 MHz SWB magnet equipped with gradients for imaging (Bruker BioSpin GmbH, Karlsruhe, Germany; Larmor frequency of 200 MHz) was used with a magnetic field strength B_0 of 4.7 T (kg/s^2·A) and a vertical bore of 150 mm using a ^{1}H-NMR birdcage (25 mm inner diameter). The studies were conducted at the Institute of Mechanical Process Engineering and Mechanics (MVM) at KIT. Measurements were performed using the "rapid acquisition with relaxation enhancement" (RARE) pulse sequence (Table A-6) and MRI data were processed with the software ParaVision® 4.0 (Bruker BioSpin GmbH, Karlsruhe, Germany) and with a self-written MATLAB® (version R2017b, Matlab Works Inc., Ismaning, Germany) script. Detailed information about the experimental set-up and evaluation of the measurements are in Chapter 7.2.4.2.

5.2.8.2 Basic Principles of NMR/MRI

MRI method is based on nuclear magnetic resonance (NMR), whose physical principle is based on the nuclear magnetism of atomic nuclei. Among others, nuclei such as hydrogen ^{1}H, carbon ^{13}C, nitrogen ^{15}N or phosphorus ^{31}P are suitable for NMR measurements as they show a nuclear spin > 0. Detailed descriptions of MRI are provided in several textbooks (Callaghan, 1993; Blümich, 2000), here are described some basic knowledge.

In this work, ^{1}H was used for the measurements, which is the mostly common NMR-active nucleus used due to its high physical sensitivity and high presence in organic and inorganic systems. Outside a magnetic field, the magnetic moments of the ^{1}H are randomly distributed (Figure 5-7a). As soon as they are exposed to an external magnetic field (B_0), the nuclear magnetic moments interact with the external field and start to align either parallel or antiparallel to the external field (Figure 5-7b), as the nuclear spins can take only two discrete energy levels (spin quantum number of +1/2 and -1/2). ^{1}H atoms energetically favor to align parallel to the outer magnetic field, hence this energetic level is more frequently occupied. The nuclei and resulting macroscopic magnetization, described with a vector, precess around B_0 with a speed defined by the Larmor frequency (ω_0), given by the Larmor equation:

$$\omega_0 = \gamma_g \cdot B_0 \qquad \text{Equation 5-1}$$

where B_0 (T or kg/s^2·A) is the external magnetic field and γ_g (s^{-1}·T^{-1}) is the gyromagnetic ratio of the atom defined as follows:

$$\gamma_g = \frac{\mu}{P} \qquad \text{Equation 5-2}$$

where μ (A·m^2) is the magnetic moment and P (kg·m^2/s) is the angular momentum of a magnetic core.
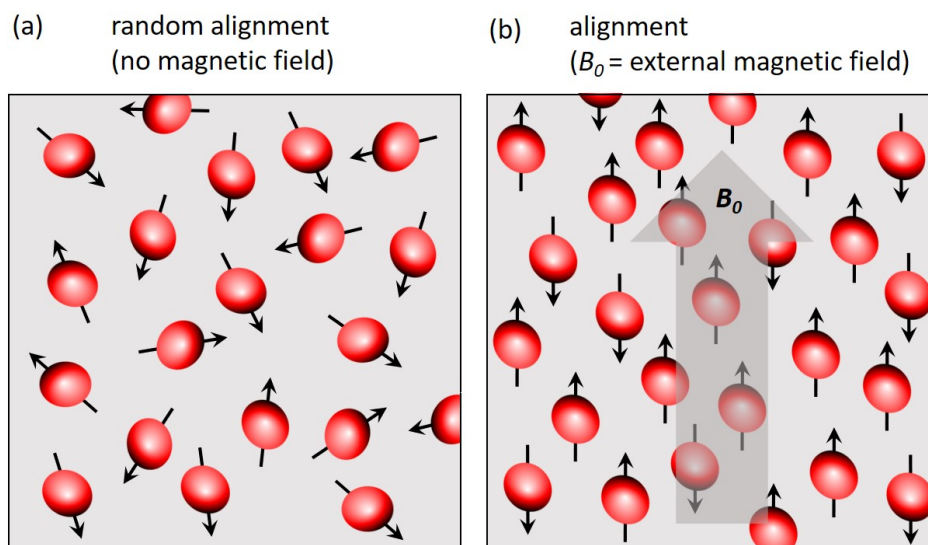
Figure 5-7 **Alignment of ^{1}H nuclei without (a) and with (b) an external magnetic field (B_0).**

During the NMR measurements, the energy from the radio frequency pulse leads the energy levels out of thermodynamic equilibrium (this state is called "excitation"). Immediately after excitation, the energy levels start to return into their hydrodynamic equilibrium (this state is called "relaxation"). The transition from the lowest to the highest energy levels (excitation) and vice versa (relaxation) occurs by emission or absorption of electromagnetic radiation with the Larmor frequency ω_0. Magnetization undergoes relaxation until it returns to zero. Relaxation phenomena (longitudinal and transverse) are responsible for the generation of the image contrast in MRI.

5.2.9 PHREEQC

PHREEQC stands for PH REdox EQuilibrium. It is a widely used geochemical modelling software written in C++ language for simulating a variety of chemical reactions in natural water-based systems or lab experiments. Calculations are made using designated thermodynamic databases that include a wide range of aqueous compounds and mineral phases. PHREEQC allows the calculation of speciation distribution, saturation indices of minerals, mixing of solution, kinetics of mineral reactions, reaction path modelling, inverse modelling and surface complex formation etc. (Postma and Appelo, 2000; Mao et al., 2004). It can be used also for advective/dispersive one-dimensional transport processes, involving reversible reactions (such as aqueous, mineral, gas, solid-solutions, surface-complexation) and irreversible reactions (such as mixing of solutions, temperature changes, kinetically controlled reactions). In the present study, PHREEQC was used to calculate the occurrence and frequency of aqueous chromium species and solid phases under different pH and Eh conditions.

6 Reactivity of Sulfate Green Rust and Sulfidized Nanoscale Zerovalent Iron in Sand Media: Application for Chromate Immobilization

Most parts of this study were published in *Geochemical Transactions* as:

DIGIACOMO, F.; TOBLER, D.J.; HELD, T.; NEUMANN, T. (2020). Immobilization of Cr(VI) by sulphate green rust and sulphidized nanoscale zerovalent iron in sand media: batch and column studies. *Geochem. Trans*. **21**, 1-12

Available at: 10.1186/s12932-020-00073-9

6.1 Introduction

Chromium (Cr) is one of the most common heavy metals found in the biosphere and a key micronutrient, but it is also a frequent contaminant in soils and groundwater worldwide, due to the uncontrolled release of Cr contaminated waters from various industries (e.g., wood treatment, electroplating operations, leather tanning or metal plating solutions) (Izbicki et al., 2015; Lunk, 2015; Ertani et al., 2017). Chromium mainly exists in two oxidation states under near surface conditions: the trivalent form, Cr(III), and the hexavalent form, Cr(VI). Cr(III) is highly insoluble, generally nontoxic (Richard A, 1997) and thus of low concern. Moreover, Cr(III) species (i.e., $Cr(OH)^{2+}$, or $Cr(OH)_2^+$) are positively charged at acidic and near neutral groundwater pHs, meaning they are easily adsorbed onto negatively charged soil particles (Deng and Bai, 2004), such as quartz grains and clay minerals. In contrast, the dominant Cr(VI) species at pH > 7 is chromate (CrO_4^{2-}), whilst at pH values between 2 and 7, Cr(VI) may be present as dichromate ($Cr_2O_7^{2}$) and hydrogen chromate ($HCrO_4^-$). These negatively charged Cr(VI) oxyanions act as strong oxidants, are highly soluble (i.e., the dominant species in industry waste spills), are known to be highly toxic, mutagenic and carcinogenic and thus pose severe threats to ecosystems and human health (Gad, 1989; Sedman et al., 2006). In many countries, it is therefore a key mandate to clean-up Cr contaminated sites.

An efficient way to clean-up Cr(VI) contaminated waters is by reaction with reductant materials, which most often consist of sulfur and/or iron bearing materials, e.g., sodium dithionite, iron sulfides, dissolved Fe(II) (Eary and Rai, 1988; Fendorf and Li, 1996; Pettine et al., 1998), magnetite (Peterson

et al., 1996), and zerovalent iron (ZVI) (Powell et al., 1995; Blowes et al., 1997; Astrup et al., 2000). In this process, Cr(VI) is quickly reduced to Cr(III), which leads to instant immobilization as insoluble Cr(III) phases (e.g., Cr(OH)$_3$ or Cr-bearing iron oxyhydroxides) due to their low solubility (Rai et al., 1987).

Pump-and-treat (P&T) is a common *ex-situ* method to clean up groundwater contaminants (US EPA, 1990; US EPA, 1996). In this approach, groundwater is extracted and treated above ground prior to discharge. The extraction design (number and location of extraction wells) and the treatment system (i.e., need of a holding tank, single or multiple clean-up method) are strongly dependent on the local hydro-geochemical conditions, which can make installation and running thereof difficult, particularly in urban areas. Moreover, pump-and-treat facilities have to deal with large amounts of wastes produced as a result of treatment (i.e., Cr(III) bearing sludge or Cr(III) plugged filters) and treatment times are very long (e.g., 50-100 years); thus, clean-up goals are often difficult to reach with pump-and-treat (US EPA, 2001). Faster and less disruptive clean-up is obtained by *in-situ* treatment via emplacement of reactants in the subsurface to create permeable reactive barriers (PRBs) or zones, where contaminants are degraded and/or immobilized, often under reducing conditions (Kate Bronstein, 2005; Faisal et al., 2018).

Nanoscale ZVI (nZVI) is frequently applied for the *in-situ* treatment of subsurface Cr(VI) contamination, however, it is non-selective and reacts rapidly with water and other oxidants, which leads to a rapid loss of reactivity (Liu and Lowry, 2006; Phenrat et al., 2008; Sarathy et al., 2008). Sulfidation of nZVI has recently emerged as a new approach to counterbalance some of these disadvantages, whereby an FeS shell is created around the metallic iron core, to protect the core from anoxic corrosion and rapid loss of reducing equivalents (Fan et al., 2016a; Fan et al., 2017). Sulfidized-nZVI (S-nZVI) has shown to be more reactive with Cr(VI) compared to non-sulfidized nZVI, both in anoxic (Gong et al., 2017) and oxic systems (Li et al., 2018). However, there are also materials such as green rusts (GRs) which are equally, if not more reactive with Cr(VI), representing a promising alternative to nZVI. GRs are natural occurring Fe(II), Fe(III) layered double hydroxides (LDHs) that often form in suboxic/anoxic, Fe^{2+}-rich environments (Trolard et al., 1997; Refait et al., 1998). GRs have been increasingly investigated over the past 20 years due to their high reactivity with Cr(VI) (Loyaux-Lawniczak et al., 2000; Williams and Scherer, 2001; Bond and Fendorf, 2003; Skovbjerg et al., 2006; Thomas et al., 2018), as well as many other contaminants, including NO$_2^-$ (Hansen et al., 1994), NO$_3^-$ (Hansen et al., 2001), Se(IV) and Se(VI) (Myneni et al., 2011; Börsig et al., 2018), U(VI) (O'Loughlin et al., 2003), tetra- and trichloromethane (Erbs et al., 1999) and nitroaromatic compounds (Boparai et al., 2010; Wu et al., 2013).

GR materials consist of positively charged Fe(II)/Fe(III) hydroxide layers, that sandwich negatively charged, hydrated interlayers containing anions (e.g., SO$_4^{2-}$, CO$_3^{2-}$ and Cl$^-$) (Feitknecht and Keller, 1950; Bernal et al., 1959) and occasionally cations (Christiansen et al., 2009b). Besides its natural occurrence,

GR is frequently observed as a corrosion product of steel in O$_2$-limited settings (Santana Rodríguez et al., 2002) and metallic iron in PRBs (Gu et al., 1999; Roh et al., 2000; Yin et al., 2015). Of all GR types, sulfate-bearing green rust (GR$_{SO4}$) is the most commonly used GR material in Cr(VI) reduction studies, most likely due to its ease of synthesis and because CrO$_4^{2-}$ and SO$_4^{2-}$ anions have similar tetrahedral structure and charge which allows CrO$_4^{2-}$ to diffuse into the GR$_{SO4}$ interlayer (Génin et al., 2001; Simon et al., 2003). Several batch studies have determined Cr(VI) reduction rates by GR$_{SO4}$ and combined these with the characterization of the oxidation end-products to determine reaction kinetics and the fate of the formed Cr(III) (Loyaux-Lawniczak et al., 2000; Williams and Scherer, 2001; Bond and Fendorf, 2003; Skovbjerg et al., 2006; Thomas et al., 2018). All these studies have demonstrated that reduction rates are extremely fast, with most Cr(VI) reduced within the first 10 min of the reaction. However, the type of oxidation product can vary depending on the applied Cr(VI)/Fe(II) ratio (Thomas et al., 2018), the presence of aqueous Fe(II) (Skovbjerg et al., 2006), GR type (Loyaux-Lawniczak et al., 2000; Loyaux-Lawniczak et al., 2001; Williams and Scherer, 2001; Bond and Fendorf, 2003; Legrand et al., 2004) as well as GR synthesis and preparation protocols (e.g., fresh, washed and/or aged GR) (Skovbjerg et al., 2006). These batch studies have provided key information on GR-Cr(VI) interactions and these certainly help towards prediction of GR effectiveness in Cr(VI) wastewater tanks (e.g., P&T facilities). However, observations from batch solution studies give little insight into behavior in porous subsurface environments as would be needed to predict GR effectiveness in PRBs. In this study, GR will be exposed to dynamic flow conditions and steady Cr(VI) concentrations, while it may also interact with surrounding grain surfaces. So far, no study has looked at GR reactivity with Cr(VI) in sand matrices, whether in batch nor column systems but such information is critically needed to evaluate the potential use of GR as alternative reductant material to ZVI/S-nZVI in *in-situ* subsurface treatment applications such as PRBs.

In this chapter, Cr(VI) immobilization by GR$_{SO4}$ under dynamic flow conditions inside packed sand columns was assessed. Specifically, the impact of flow rate, inlet Cr(VI) concentration, and pH conditions on Cr(VI) removal efficiency were tested by evaluation of breakthrough curves. In addition, Cr(VI) reduction by GR$_{SO4}$ was examined in batch sand experiments (static conditions) for comparison of removal efficiencies to experiments under dynamic flow. Lastly, a few representative batch and column experiments were also performed with S-nZVI, for direct comparison of reductive capacity to GR$_{SO4}$. Moreover, in addition to the application of GR as engineered reactant, it is worth emphasizing the potential of naturally occurring GR materials for Cr(VI) removal in contaminated subsurface environments.

6.2 Experimental Section

6.2.1 Reactivity Batch Studies

GR$_{SO4}$ and S-nZVI were freshly synthesized prior to each experiment as detailed described in Chapter 5.1.2. The immobilization capacity and kinetics of Cr(VI) by GR$_{SO4}$ and S-nZVI was studied in batch reactors with quartz sand (size range: 0.1-0.3 mm, density: 2.66 g/m^3, purchased in acid washed, dry state from Chemsolute®, Th. Geyer) for later comparison to flow experiments in sand columns. The following procedures were used to prepare the samples:

i. GR$_{SO4}$ slurry (1 mL of 72.4 mM Fe(II)$_{tot}$, pH 7.0) was mixed with 23 g quartz sand and 5 mL Milli-Q water inside 50 mL centrifuge tubes, and then spiked with 30 mL of separately prepared Cr(VI) stock solutions, produced by dissolving defined quantities of K$_2$Cr$_2$O$_7$ in Milli-Q water, to yield final Cr(VI) contents of 7.5, 15.1 and 30.0 µmol, and Cr(VI)/Fe(II)$_{tot}$ molar ratios of 0.1, 0.21 and 0.41. Note that at Cr(VI)/Fe(II)$_{tot}$ ratios < 0.33, Fe(II)$_{tot}$ will be in excess, i.e., all Cr(VI) can theoretically be reduced to Cr(III) by oxidation of Fe(II)$_{tot}$ to Fe(III), while at ratios > 0.33, Cr(VI) will be in excess (i.e., there are insufficient reducing equivalents for full Cr(VI) reduction).

ii. Following S-nZVI synthesis and drying under vacuum, the S-nZVI slurry (for mixing with the sand) was prepared as follows: approximately 43.5 mg dry S-nZVI were weighed into a glass vial, amended with 100 mL Milli-Q water, then crimped sealed for sonication outside the anaerobic chamber. After, 6 mL of this suspension were mixed with the sand. As for GR$_{SO4}$ experiments, the S-nZVI content was kept constant in all experiments. Assuming that Fe^0 core of S-nZVI represents around 73 % of the total volume, the amount of Fe^0 in batch reactors is equal to 38 µmol (calculations in Chapter 6.3.1.3). In the reaction with Cr(VI), Fe^0 gets oxidized to Fe(II) and then Fe(III) (Manning et al., 2007; Gong et al., 2017), thus each Fe^0 atom donates 3 electrons. As such, S-nZVI batch (and column) experiments theoretically have ~ 2.4 times the amount of reducing equivalents compared to GR$_{SO4}$ experiments.

The prepared batch reactions were shaken on an orbital shaker at 300 rpm at room temperature (~ 25 °C). To assess the decrease in Cr(VI) with time, two tubes were removed at regular sampling times, centrifuged and the supernatant filtered (0.2 µm syringe filter, Chromafil, Carl Roth Germany) for analysis of dissolved Cr(VI) using the 1,5-diphenylcarbazide colorimetric method (details in Chapter 5.2.6.1) Attempts of solid characterization of the reaction products of GR$_{SO4}$ with dissolved Cr(VI) of the sand batch experiments were not successful due to the low ratio of reactant/sand and the impossibility to separate the reactant particles from the quartz sand. Therefore, two sand-free batch experiment with only GR$_{SO4}$ and Cr(VI) at pH 7.0 and 4.5 (Cr(VI)/Fe(II)$_{tot}$ = 0.21) were set up to get sufficient material for XRD analysis of final GR$_{SO4}$ oxidation products. The pH was adjusted to the desired value and the reaction vessels were stirred for 24 hours. During this time, pH was checked

regularly and if necessary readjusted. Samples were then centrifuged and filtered with 0.2 μm syringe filter, the effluent was analyzed for Cr(VI) content while the solid samples were analyzed via XRD.

6.2.2 Reactivity Column Studies

Column experiments (diameter x length = 1.4 cm x 11 cm) were carried out to investigate the effect of initial Cr(VI) concentration (0.125-1 mM), flow rate (0.25, 1 and 3 mL/min) and solution pH (4.5, 7.0 and 9.5; adjusted by adding 1 M HCl or 1 M NaOH) on Cr(VI) removal by GR$_{SO4}$ in porous media. These Cr(VI) concentrations are representative of conditions found at Cr(VI) contaminated sites. For example, Cr(VI) concentrations in a waste plume at the Hanford site, Washington (USA) range from 0.090 to 0.96 mM (Poston et al., 2002; Petersen et al., 2009), and reached around 0.5 mM in a contaminated groundwater plume at the US Coast Guard Support Center, Elizabeth City, North Carolina (Lai and Lo, 2008). Note that the chosen flow rates yield pore water velocities (calculated from the breakthrough curves of the tracer test, Eqn. 1) that are generally higher than groundwater velocities in field PRBs (up to 2.2 m/day) (Klausen et al., 2003). However, such rates are technically hard to achieve in the laboratory. Also, if these materials are used for treatment either via injection or by installing a funnel-and-gate PRB, then rates will be closer to what it was tested here. PRBs with a funnel-and-gate configuration consist of two impermeable walls that direct the contaminated groundwater towards the reactive area (gate) (Kate Bronstein, 2005). In this scenario, the groundwater passing through the gate, will have a much higher velocity than the natural flow velocity (ITRC, 2005).

6.2.2.1 Experimental Set-Up

Column experiments were set-up identically for all the tested reactants and monitored using the same sampling procedures. The schematic diagram of the column set-up is shown in Figure 6-1. The columns (diameter x length = 1.4 cm x 11 cm) were wet-packed with a homogeneous GR$_{SO4}$/S-nZVI-sand slurry, prepared the same way as for batch experiments (except the addition of Cr(VI) solutions). The in- and out-let areas were amended with coarse sand (~ 80 mg, size range: 0.6-1.3 mm, Carl Roth Germany) to ensure plug flow and prevent loss of small sand grains. To determine the hydrodynamic properties of the column (i.e., dispersivity) and the corresponding linear flow velocities (Klausen et al., 2003; Zakari et al., 2016), a non-reactive tracer solution (0.4 M NaNO$_3$) was injected into one column containing quartz sand only. To avoid the formation of trapped air bubbles within the column, the column was constantly tapped during wet packing. Preliminary Magnetic Resonance Imaging (MRI) images of the water-saturated sand column show the suitability of this method for the preparation of the column, which provide homogeneous packed columns without any bubbles of air or empty spaces (Figure A-5). It was assumed that the presence of the reactant did not alter the hydrodynamic properties within the column owing to the very low reactant/sand ratio (about 1/2500). The columns were oriented vertically with upward flow to avoid channeling due to gravity. Before any injection, approximately 5 pore volumes of deoxygenated Milli-Q water were pumped through the column (Ismatec IPC peristaltic

pump) to displace any trapped gas bubbles and to obtain steady-state flow conditions. For all Cr(VI) experiments, chromate solutions were injected until full breakthrough was observed. As a control experiment to measure any potential Cr(VI) sorption to sand grains and/or the column walls, one column was packed with quartz sand only (no added GR_{SO4}/S-nZVI) and then flushed with a 0.5 mM Cr(VI) solution, using a flow rate of 1 mL/min.
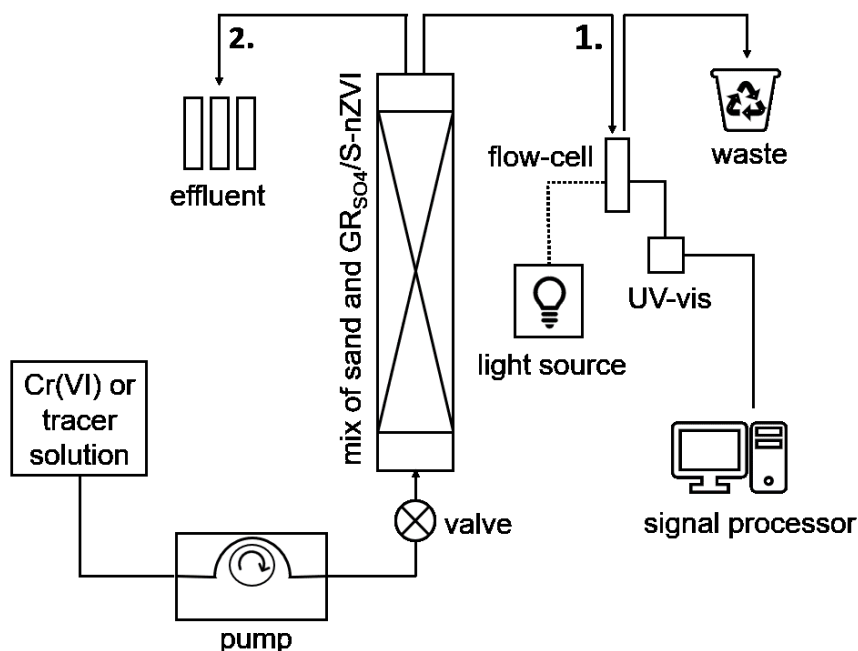
Figure 6-1 **Experimental set-up used for measuring breakthrough curves under strictly anoxic conditions.**
(1.) on-line measurements by solution absorbance using a UV-Vis flow through cell connected to an UV-Vis spectrophotometer; (2.) manual collection to determine Cr(VI) via the 1,5-diphenylcarbazide colorimetric method, and Cr_{tot} and Fe_{tot} via ICP-OES.

The chromium and nitrate concentrations in the outlet were monitored on-line by solution absorbance using an UV-Vis flow through cell (2 mm path length, Hellma, Germany) connected to an UV-Vis spectrophotometer (Ocean Optics). Periodically, samples were also manually collected to measure total Cr, Cr(VI) and total Fe concentrations to check for any mobile Cr(III) and any released Fe. Total Cr and Fe were determined by ICP-OES, while Cr(VI) concentrations were determined using the 1,5-diphenylcarbazide colorimetric method (Environmental Protection Agency colorimetric method, EPA Method 7196A) (details in Chapter 5.2.6 and 5.2.7). All experimental conditions were tested in duplicate at room temperature (~ 25 °C), with each replicate column experiment conducted on a different day and using a different reactant synthesis batch. This ensured that the observed differences accounted for slight variations in sand column texture and GR synthesis and confirmed reproducibility. Replica of experiments and analysis were carried out also in the laboratory of the NanoGeoScience Group, Chemistry Department, University of Copenhagen (Denmark), confirming reproducibility. For the graphs of the breakthrough curves, the mean values of these duplicated were plotted.

6.2.2.2 Theoretical Background

Packed-sand column experiment is a very important tool that reveals fundamental information about the removal efficiency of a reactant versus a contaminant. The column experiments are performed in order to study how the content of specific compound changes within a specific substrate (Banzhaf and Hebig, 2016). In this study, the substrate consists of a mixture of quartz sand (model substance to simulate aquifer material) and a reactant. Unlike batch experiments, during which the monitored contaminant concentration decreases while the removal process takes place and all processes are monitored until equilibrium is achieved, in columns the reactant is in contact with a constant amount of "fresh" contaminant that continuously enters the system (Andersson et al., 2012). During a column experiment, at the begenning of the injection the immobilization process takes place near the inlet of the column, where the solid reactant is in contact with the highest concentration (C_0) of contaminant, and it propagates through the column over time (Figure 6-2). The sum of these processes, which are often the result of dynamic and non-equilibrium processes, are reflected on the conservative breakthrough curves (BTCs) (Banzhaf and Hebig, 2016).
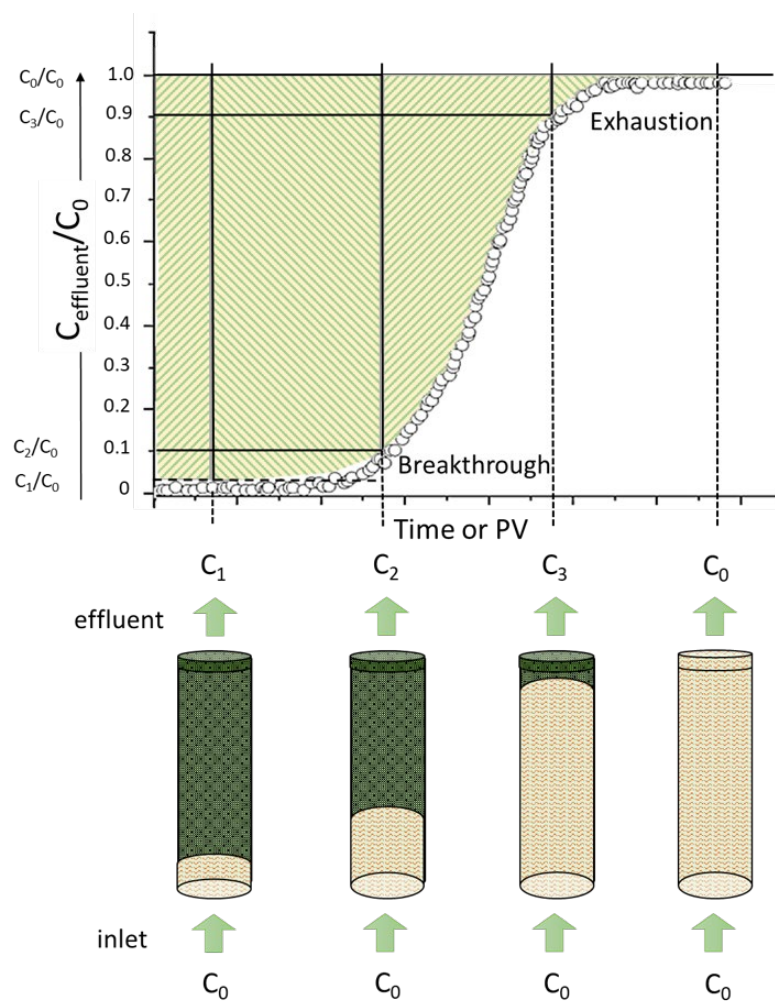
Figure 6-2 **Representation of a breakthrough curve obtained during Cr(VI) reduction (modified after Gupta et al. 2016).**

The BTC analysis is the common procedure to evaluate overall column performance. BTCs are plots of the normalized concentration (C/C_0) as a function of time or eluted pore volume (PV). A typical BTC presents an S-profile, while the different shape and steepness of each breakthrough curve give an estimation of the bed efficiency with respect to the feed concentration and the flow rate (Gupta et al., 1997; Aksu et al., 2002). The breakthrough point is fixed arbitrary at values very close to zero (Gupta et al., 1997), while the exhaustion point is usually fixed at a C value between 90 % and 95 % of C_0.

6.2.2.3 Fitting Breakthrough Curves

i   Determination of hydrodynamic properties

Sodium nitrate (NaNO$_3$) was used as non-reactive solute for tracer tests to determine the values of porosity (n), pore water velocity (v) and longitudinal dispersion coefficients (D). NaNO$_3$ concentration was determined via spectrophotometric measurements at wavelength of 240 nm. The porosity (n), which is usually expressed as a percentage between 0 and 100 %, can be calculated as follows:

$$n = \frac{V_v}{V_{tot}} \qquad\qquad \text{Equation 6-1}$$

where V_v (m^3) is the volume of interconnected network of pore channels over the total volume, V_{tot} (m^3). The amount of empty spaces that is connected contributes to the fluid (i.e., water) movement. The values of the pore water velocity (v) (mm/min) and longitudinal dispersion coefficients (D) can be calculated from the breakthrough measured for the non-reactive tracer as follows (Zakari et al., 2016):

$$v = \frac{L}{t_{0.5}} \qquad\qquad \text{Equation 6-2}$$

$$D = \frac{v^2}{8t_{0.5}}(t_{0.84} - t_{0.16})^2 \qquad\qquad \text{Equation 6-3}$$

where L is the length of the column, and $t_{0.16}$, $t_{0.5}$ and $t_{0.84}$ correspond to the time at which C/C_0 is equal to 0.16, 0.5 and 0.84.

ii   Determination of Cr(VI) removal capacity

In this study, the breakthrough point was fixed at 5% of C_0 and GR$_{SO4}$ and S-nZVI were assumed to be exhausted when the effluent Cr(VI) concentration reaches 90% of C_0.

The total injected volume, V_{inj} (ml), and total injected Cr(VI) mass (q$_{total}$, µmol and mg) are calculated as follows (Aksu and Gönen, 2004):

$$V_{inj} = Qt_{0.9} \qquad\qquad \text{Equation 6-4}$$

$$q_{total} = \frac{C_0 V_{inj}}{1000} \qquad\qquad \text{Equation 6-5}$$

where Q is the volumetric flow rate (mL/min) and $t_{0.9}$ is the time at $C/C_0 = 0.9$.

The quantity of Cr(VI) immobilized within the column ($Cr(VI)_q$; μmol and mg) can be calculated by integrating the area (A) beneath the breakthrough curve obtained by plotting C_0 - C as function of time within the limits of t_0 and $t_{0.9}$ as follows:

$$\mathbf{Cr(VI)_q} = \frac{QA}{1000} = \frac{Q}{1000} \int_{t0}^{t=t_{0.9}} (C_0 - C)\, dt \qquad \textbf{Equation 6-6}$$

where t_0 marks the point where 1 PV of Cr(VI) solution has passed through the column and after subtracting the delay time due to the length of the inlet tubes.

The absolute *Cr(VI) removal* (mg/g) was calculated based on the amount of reductant, i.e., GR ($9.1 \cdot 10^{-3}$ g) and S-nZVI ($2.6 \cdot 10^{-3}$ g), added to batch and column experiment:

$$\mathbf{Cr(VI)\ removal} = \frac{Cr(VI)_q}{reductant\ mass} \qquad \textbf{Equation 6-7}$$

The *Cr(VI) removal efficiency (%)* was calculated relative to the amount of available reducing equivalents *(RE)* by the added reductants, i.e., GR_{SO4} (= $[Fe(II)_s]$) and S-nZVI (= 3 x $[Fe^0]_s$):

$$\mathbf{Cr(VI)\ removal\ efficiency}\ (\%) = \frac{Cr(VI)_q}{RE} \qquad \textbf{Equation 6-8}$$

RE factor reflects the number of electrons needed to reduce Cr(VI) to Cr(III), which is equal to 1 in the case of GR_{SO4} (from Fe(II) to Fe(III)) and equal to 3 in the case of S-nZVI (from Fe^0 to Fe(III)).

6.3 Results and Discussions

6.3.1 Characterization of the Synthesized Materials

6.3.1.1 Solid Characterization

Figure 6-3 shows the XRD spectra of the freshly synthesized GR$_{SO4}$ (with a small amount of goethite) and S-nZVI.
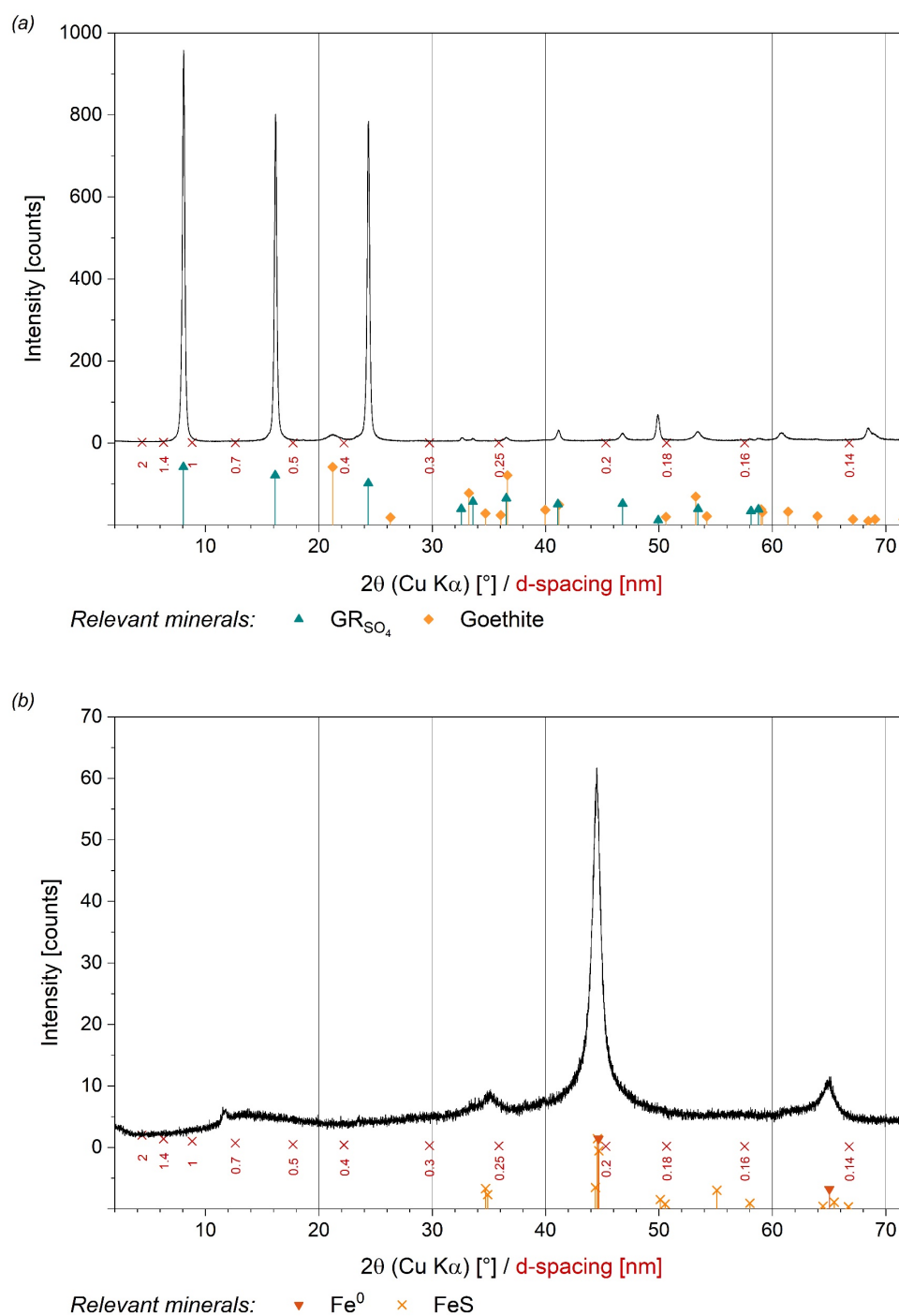
Figure 6-3   XRD patterns (Cu-Kα) of freshly synthesized and glycerol-coated a) GR$_{SO4}$ (PDF# 13-0092) and (b) S-nZVI (Fe^0: PDF# 06-0696 and FeS: PDF# 89-6268).

Prior to solid characterization, the material suspensions were vacuum filtered (Whatman 0.2 μm nylon membrane filter) and amended with glycerol to prevent oxidation during XRD analysis (Williams and Scherer, 2001; Bocher et al., 2004; Guilbaud et al., 2013). Data were collected at 2θ values between 2° and 72°, with a step size of 0.02 and dwell time of 1 s per step. XRD patterns were analyzed with the EVA 100 software.

6.3.1.2 Calculation of Fe(II) Content and GR$_{SO4}$ Mass

To determine the total and dissolved iron content, [Fe$_{tot}$] and [Fe$_d$], of the GR suspension used for the batch and column experiments, acid digestions of the GR suspension and its supernatant (obtained by filtering through 0.2 μm syringe filter) were performed. Samples were then analyzed via Inductively Coupled Plasma Optical Emission Spectrometry (ICP-OES; Varian 715ES) at $\lambda = 259.940$ nm, measuring:

$$[\mathbf{Fe_{tot}}] = \mathbf{95.7 \; mmol/L}$$

$$[\mathbf{Fe_d}] = \mathbf{25.7 \; mmol/L}$$

Thus, the concentration of Fe in the solid, [Fe$_s$] (e.g., GR particles), is:

$$[\mathbf{Fe_s}] = [\mathbf{Fe_{tot} - Fe_d}] = \mathbf{70 \; mmol/L} \qquad \textbf{Equation 6-9}$$

It was then assumed that:

1. Fe(II)/Fe(III) ratio in GR$_{SO4}$ is 2
2. total dissolved Fe ([Fe$_d$]) is mainly consisting of dissolved Fe(II) (the solubility of Fe(III) is very low at circum-neutral pH) (Eisele and Gabby, 2014).

Based on this, the concentration of Fe(II) in the solid ([Fe(II)$_s$]), and total Fe(II) in the GR$_{SO4}$ suspension ([Fe(II)$_{tot}$]) can be calculated as follows:

$$[\mathbf{Fe(II)_s}] = [\mathbf{Fe_s}] \times \tfrac{2}{3} = \mathbf{46.7 \; mmol/L} \qquad \textbf{Equation 6-10}$$

$$[\mathbf{Fe(II)_{tot}}] = (\mathbf{Fe_d + Fe(II)_s}) \; \mathbf{mmol/L} = \mathbf{72.4 \; mmol/L} \qquad \textbf{Equation 6-11}$$

The mass of GR$_{SO4}$, m(GR$_{SO4}$)$_{susp}$, in the synthesized 60 mL suspension (V) can be calculated as follows (based on GR$_{SO4}$ formula: Fe(II)$_4$Fe(III)$_2$(OH)$_{12}$SO$_4$•8H$_2$O, with molar mass, M(GR$_{SO4}$) = 780 g/mol (Simon et al., 2003):

$$\mathbf{m(GR_{SO4})_{60ml}} = \left(\frac{\mathbf{[Fe(II)_s] \times V_{60ml}}}{\mathbf{4}} \right) \times \mathbf{M(GR_{GRSO4})} = \mathbf{0.546 \; g} \qquad \textbf{Equation 6-12}$$

For each experiment 1 mL GR suspension was employed, i.e., 9.1 mg of GR$_{SO4}$, that contain 72.4 μmol Fe(II)$_{tot}$, of which 46.7 μmol is Fe(II)$_s$ and 25.7 μmol is Fe(II)$_d$.

6.3.1.3 Determination of Mass and Volume of Fe^0 Core and FeS Shell in S-nZVI

S-nZVI was assumed to be spherical, with an average radius of 50 nm and a FeS shell thickness of 5 nm (based on TEM images, Figure 7-7). Hence, the radius of the iron core (Fe^0) is 45 nm. The relative volume % of the Fe^0 core (*%V$_{Fe0}$*) and the FeS shell (*%V$_{FeS}$*) were calculated as follows:

$$\frac{V_{Fe0}}{V_{SnZVI}} = \frac{(r_{Fe0})^3}{(r_{SnZVI})^3} = 0.73; \ \%V_{Fe0} = 0.73 \ \& \ \%V_{FeS} = 0.27 \qquad \textbf{Equation 6-13}$$

2.6 mg of S-nZVI (*m$_{tot-SnZVI}$*) was used for each experiment. Assuming the densities of Fe^0 and FeS are as follows:

$$\delta_{Fe0} = 7.87 \ \text{g/cm}^3$$

$$\delta_{FeS} = 4.84 \ \text{g/cm}^3$$

the average density of S-nZVI (*δ$_{SnZVI}$*) and the total added S-nZVI volume (*V$_{tot-SnZVI}$*) were calculated as follows:

$$\delta_{SnZVI} = (\%V_{Fe0} \cdot \delta_{Fe0} + \%V_{FeS} \cdot \delta_{FeS}) = 7.05 \ \text{g/cm}^3 \qquad \textbf{Equation 6-14}$$

$$V_{tot-SnZVI} = \frac{m_{tot-SnZVI}}{\delta_{S-nZVI}} = 0.00037 \text{cm}^3 \qquad \textbf{Equation 6-15}$$

Hence, the total added Fe^0 volume, *V$_{tot-Fe0}$*, the Fe^0 mass, *m$_{tot-Fe0}$*, and the Fe^0 molar mass, *n$_{tot-Fe0}$*, are:

$$V_{tot-Fe0} = (\%V_{Fe0} \cdot V_{tot-SnZVI}) \ \text{mm}^3 = 2.7 \cdot 10^{-4} \ \text{cm}^3 \qquad \textbf{Equation 6-16}$$

$$m_{tot-Fe0} = (V_{tot-Fe0} \cdot \delta_{Fe0}) = 2.12 \cdot 10^{-3} \text{g} = 2.12 \ \text{mg} \qquad \textbf{Equation 6-17}$$

$$n_{tot-Fe0} = \frac{m_{tot-Fe0}}{M(Fe)} = 3.80 \cdot 10^{-5} \text{mol} = 38 \ \mu\text{mol} \qquad \textbf{Equation 6-18}$$

6.3.2 GR$_{SO4}$ Batch Studies

The removal of Cr(VI) by GR$_{SO4}$ in anoxic batch sand experiments is shown in Figure 6-4. A control experiment with sand and Cr(VI) only (no added GR$_{SO4}$) showed that Cr(VI) sorption to grain surfaces or the sample tube was negligible, thus any monitored decrease in Cr(VI) with time is due to removal by the added GR$_{SO4}$. Under all tested Cr(VI) concentrations, removal rates were very fast with about > 96 % of the initially added Cr(VI) removed already after 5 min, with little more Cr(VI) immobilized thereafter. Concomitantly, the pH decreased from 7.0 to 5.2 ± 0.3. This pH decrease can be explained by the reduction of Cr(VI) by the aqueous Fe(II) present in the added GR slurry (about 35.5 % of Fe(II)$_{tot}$), followed by the formation of Fe(III)-hydroxides as previously observed (Eary and Rai, 1988; Thomas et al., 2018).
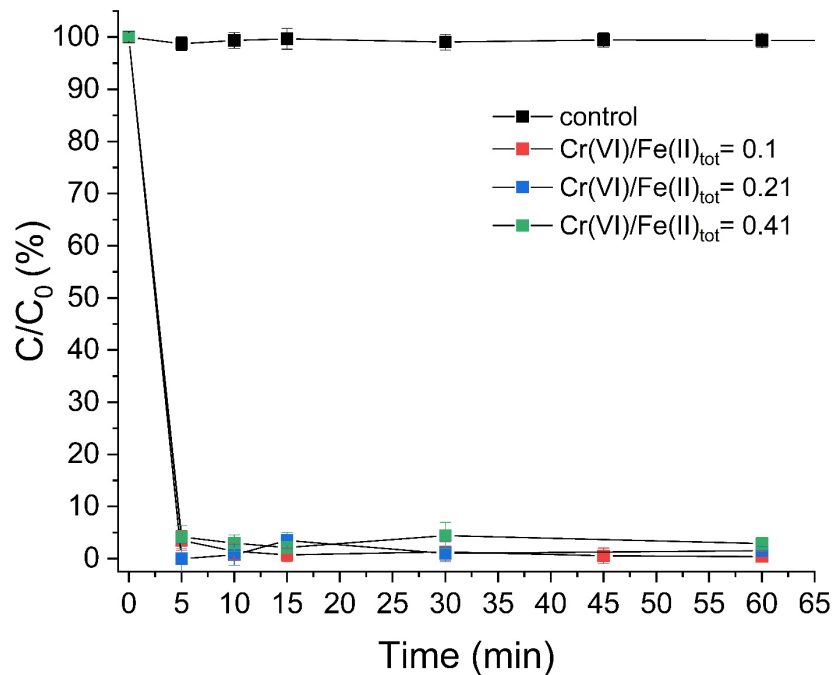
Figure 6-4   **Cr(VI) immobilization efficiency by GR_{SO4} in batch sand experiments at variable Cr(VI)/Fe(II) ratio and constant green rust concentration.**
Control reaction with sand only (no added green rust) is also shown.

Overall, these fast Cr(VI) removal rates match well with the removal rate observed in previous sand-free batch experiment (Eary and Rai, 1988; Thomas et al., 2018), indicating that the sand matrix had little effect on Cr(VI) immobilization by GR_{SO4}. XRD analyses of reaction products in the sand-free experiment after 24 hours showed that most of the initial GR_{SO4} phase oxidized to goethite (α-FeOOH) (Figure 6-5).

Relevant minerals: ▲ GR_{SO_4} ◆ Goethite
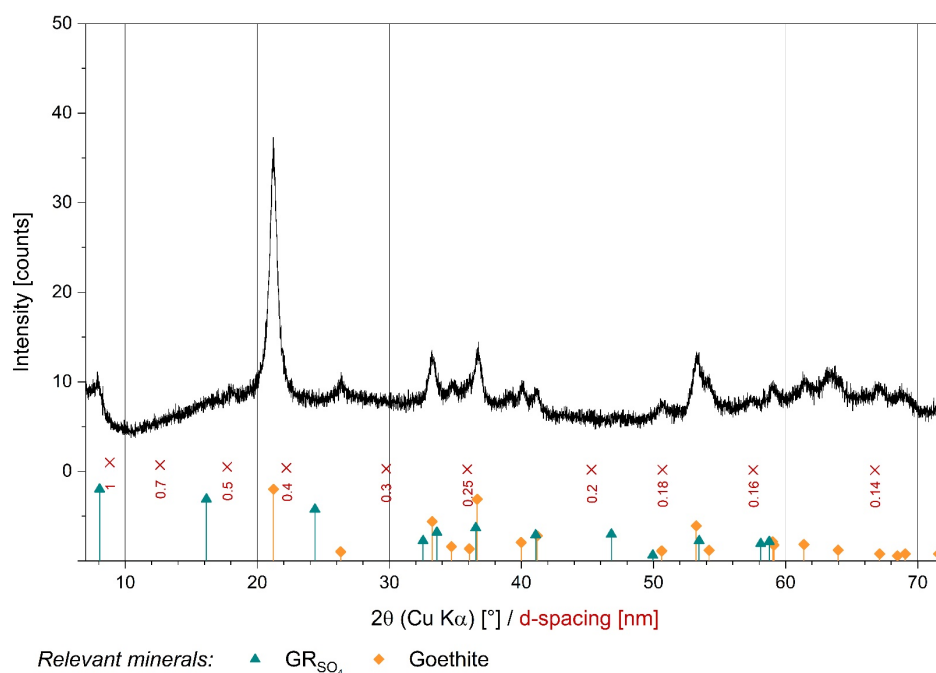
Figure 6-5   **XRD pattern (Cu-Kα) of the oxidation products of GR_{SO4} after reaction with Cr(VI) solution (pH 7.0), showing peaks of goethite (α-FeOOH, PDF# 29-0713) and GR_{SO4}.**

Note that these reactions were performed under strict anoxic conditions, thus the observed oxidation of GR_{SO4} is consistent with Cr(VI) removal by reduction to Cr(III), as shown by the calculated Eh-pH diagram in Figure 6-6. The fact that some GR remained after 24 h reaction is because there was an excess in Fe(II)$_{tot}$, i.e., reducing equivalents, in this experiment. Overall, these observations are in agreement with previous GR_{SO4}-Cr(VI) batch reactivity studies where Cr(III)-bearing goethite was identified as the primary oxidation product (Thomas et al., 2018). It is likely that some of the Cr(III) precipitated as amorphous Cr,Fe-phase, as observed in some studies with X-ray absorption spectroscopy (Skovbjerg et al., 2006), but this could not be resolved with the XRD used here.
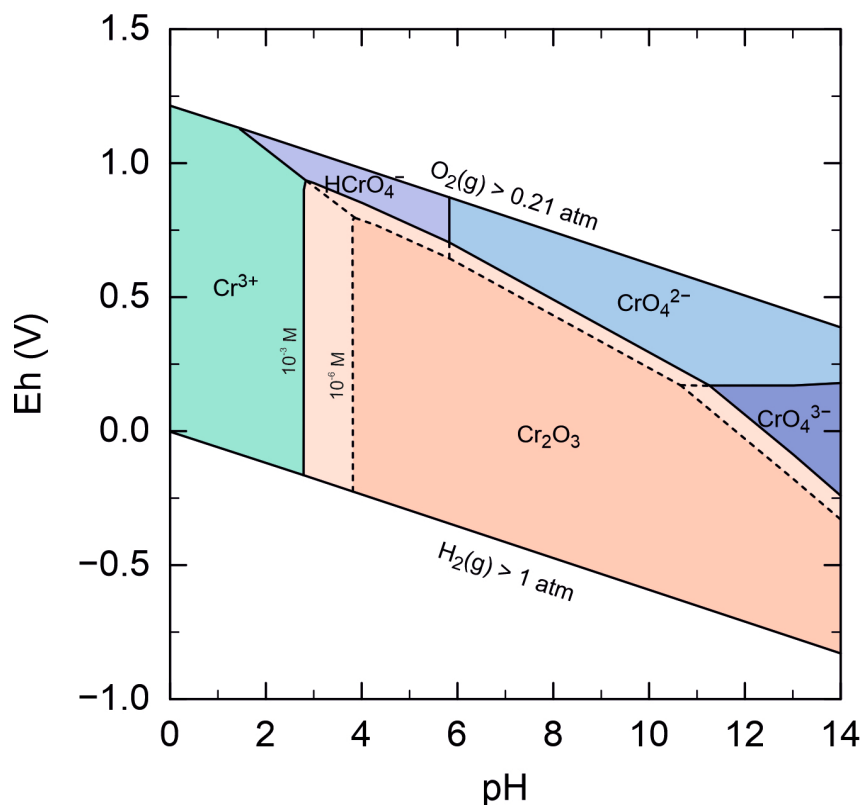
Figure 6-6   **Eh-pH diagram for chromium based on experimental chromium concentration (10^{-3} M). Dashed line is based on lower concentrations (10^{-6} M). Calculations were made using PHREEQC (USGS).**

In terms of Cr(VI) removal efficiencies relative to the added GR_{SO4} reducing equivalents, at the two lower tested Cr(VI) concentrations, where Fe(II)$_{tot}$ was in excess (i.e., more reducing equivalents present than needed; Cr(VI)/Fe(II)$_{tot}$ < 0.33), complete Cr(VI) removal was achieved within less than an hour of reaction. However, at the highest Cr(VI) concentration, where Cr(VI) was in excess (i.e., Cr(VI)/Fe(II)$_{tot}$ > 0.33), 97 % of the added Cr(VI) was immobilized. While incomplete removal was indeed expected for that experiment, because of insufficient reducing equivalents, it was actually 15 % higher than the expected immobilization capacity based on reduction only. This may be due to additional Cr(VI) removal by Cr(VI) adsorption onto the newly formed goethite particles, which is

favored at the neutral pH studied here (i.e., below goethite zero point of charge of 9.1), as observed previously (Zachara et al., 1987; Abdel-Samad and Watson, 1997; Ajouyed et al., 2010).

Indeed, adsorption affinity increases with decreasing pH below the point of zero charge (pzc) of the adsorbent (Zachara et al., 1987; Rai et al., 1989). Goethite is ubiquitous, the most stable iron oxide in soil environments and is a major adsorbent in many soils (Grossl et al., 1997). It has been shown that adsorption affinity is diminished as solution pH increases, as ionic strength decreases and by the presence of other competing anionic constituents (e.g., H_4SiO_4, CO_2, SO_4^{2-}, PO^{3-}) and cations (e.g., Ca^+ and Mg^+), which leads to higher CrO_4^{2-} mobility (Zachara et al., 1987; Ajouyed et al., 2010; Veselská et al., 2016). Ajouyed et al. (2010) showed that maximum Cr(VI) adsorption occurred when pH was ≤ 3 for goethite and that Cr(VI) adsorption to goethite (and hematite) is ascribed to an inner-sphere surface complexation.

6.3.3 GR_{SO4} Column Studies

The breakthrough curves for the tracer ($NaNO_3$) as a function of differing injection flow rate (0.25, 1 and 3 mL/min) are shown in Figure 6-7a. Under all conditions, the nitrate recovery was 100 % demonstrating that it did not adsorb to the quartz sand grains in the column, and that collisions between nitrate and sand grains were elastic. The pore volume and the porosity of the column were calculated to be 7.5 mL and 44 %, respectively. From these data, the linear flow velocity (v) and longitudinal dispersion coefficient (D) were calculated yielding $8.72 \cdot 10^{-5}$, $3.48 \cdot 10^{-4}$ and $10.5 \cdot 10^{-4}$ m/s (7.5, 30 and 90 m/day) and $1.81 \cdot 10^{-3}$, $7.24 \cdot 10^{-3}$ and $2.17 \cdot 10^{-2}$ cm^2/s, respectively, at the three different flow rates (i.e., 0.25, 1 and 3 mL/min). In turn, this meant that the residence times were 30, 7.5 and 2.5 min.
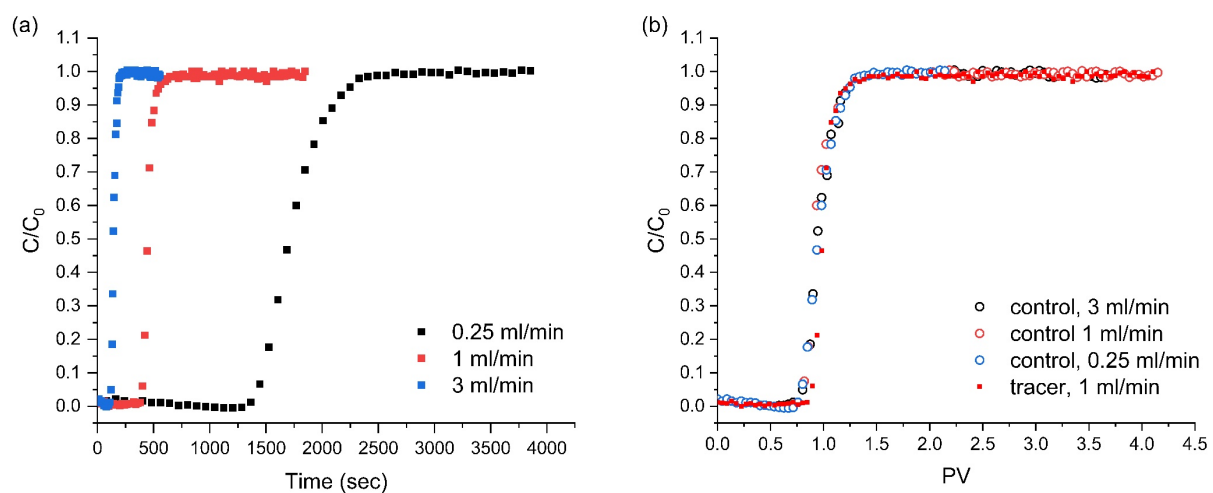
Figure 6-7 **BTCs of tracer and control tests, as function of time and/or pore volume.**
(a) BTCs (as a function of time) obtained by injecting 0.4 M $NaNO_3$ at 0.25, 1 and 3 mL/min.
(b) Comparison of BTCs (as a function of pore volume) obtained by injecting 0.5 mM Cr(VI) solution (control) at 0.25, 1 and 3 mL/min and 0.4 M $NaNO_3$ solution (tracer) at 1 mL/min. All BTCs show no delay in breakthrough, i.e., are typical of non-reactive solutes.

Similar to the tracer experiments, control columns without added GR_{SO4} showed that all injected Cr(VI) (5 pore volumes of 0.5 mM) was retrieved at the outlet, i.e., no Cr(VI) adsorbed to the surfaces of the quartz sand grains (Figure 6-7b). This is also explained by the fact that both quartz sand and Cr(VI) species carry a net negative electric charge, thus repulsive electrostatic interactions will inhibit sorption processes between these compounds (Silva et al., 2008).

Moreover, analyses of the manually collected effluent samples of experimental columns by the colorimetric method (EPA Method 7196A) (total Cr(VI)) and ICP-OES (total Cr) matched the values measured using *in-situ* spectrophotometry, reaffirming the suitability of the later method for experimental columns (Figure 6-8). Also, the total Cr was equal to total Cr(VI) in the effluent of GR_{SO4} amended columns, which reaffirmed that the effluent contained no detectable Cr(III) species. Thus, any Cr(III) formed during reduction by GR_{SO4} must have become immobilized within the column (onto the surface of particles) by co-precipitation with the forming Fe(III) oxyhydroxides. It is worth noting that column experiments were not affected by significant pH changes during Cr(VI) injection, thus inlet and effluent pH values were identical.
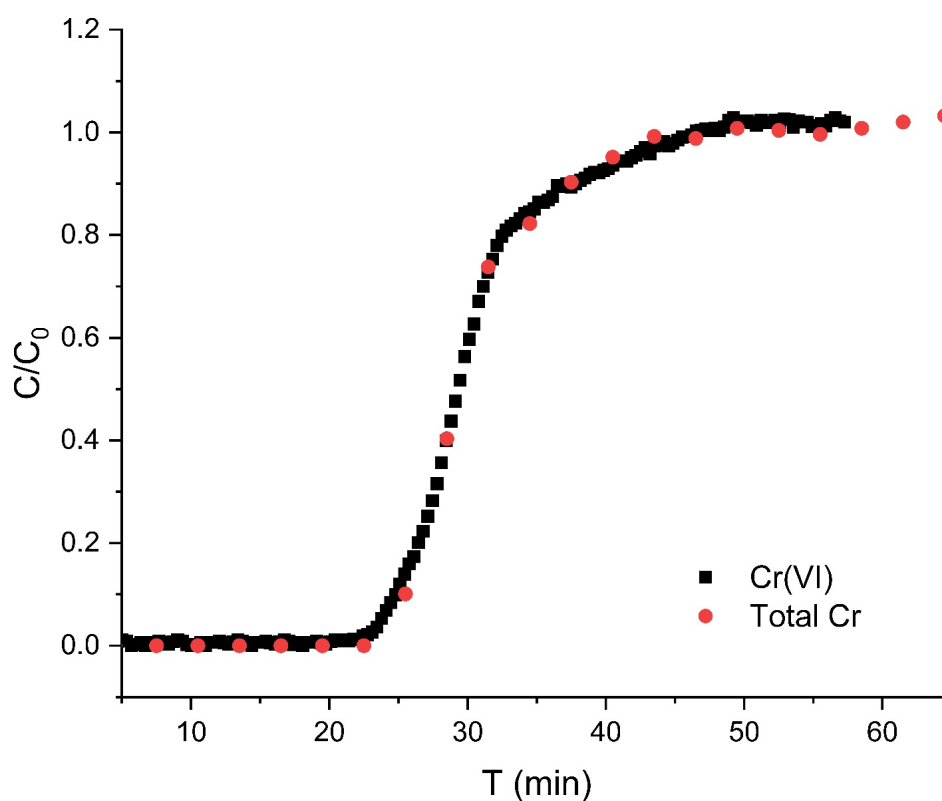
Figure 6-8 **Comparison of BTCs obtained by measuring effluent Cr(VI) concentrations using the on-line UV-Vis set-up (black squares) and by determining total Cr concentrations via ICP-OES in the manually collected samples (red circles).**
The test conditions were identical with $[Cr(VI)_0]$ = 0.5 mM, pH = 7.0 and flow rate = 1 mL/min. The fact that the two BTCs overlap demonstrates that Cr(VI) is the only Cr species detected in the effluent. Thus, any Cr(III) forming due to reduction is immobilized within the sand column.

Lastly, the aqueous Fe(II) that was initially present in the added GR slurry (~ 25 µmol) was mostly flushed out during the Milli-Q water rinse (5 pore volumes) performed before each experiment (Figure 6-9), thus the only reductant present within the columns was the added GR_{SO4} ([Fe(II)s] ~ 46.7 µmol).
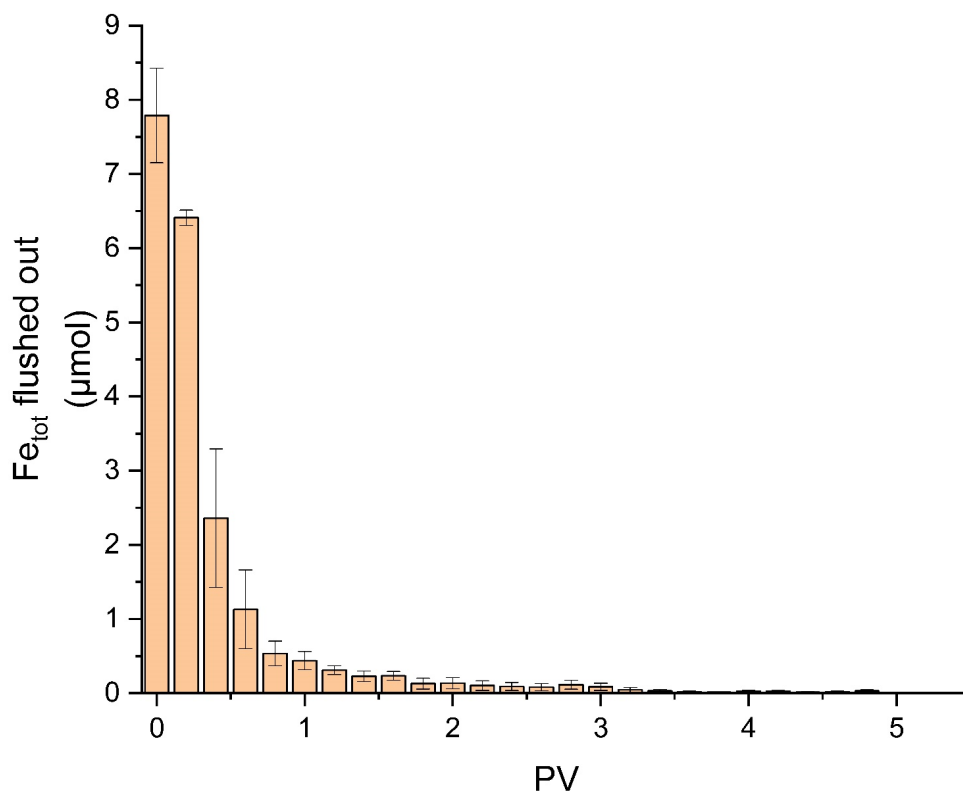
Figure 6-9   Loss in total Fe as a function of flushed Milli-Q pore volumes. The samples were manually collected and analyzed via ICP-OES.
The plotted data show the average values of 6 columns (3 columns run at 1 mL/min and 3 run at 3 mL/min). Prior to each Cr(VI) injection, the columns were pre-flushed with 5 PVs of Milli-Q water to remove aqueous Fe^{2+} present in the GR slurry that was mixed with the sand.

i   Effect of initial inlet Cr(VI) concentration

Normalized experimental breakthrough curves obtained for GR_{SO4} amended sand columns as a function of inlet Cr(VI) concentrations, $[Cr(VI)_0]$, are shown in Figure 6-10. By comparison to the tracer, it is clear that breakthrough of Cr(VI) was delayed in the presence of GR_{SO4} indicating that Cr(VI) was successfully immobilized by GR_{SO4}. Moreover, this delay in breakthrough became more pronounced with decreasing inlet Cr(VI) concentration, as shown by the breakthrough ($C/C_0 = 0.05$) and exhaustion ($C/C_0 = 0.9$) points, which increased from 1.5 to 11 PVs and from 2.5 to 19 PVs, respectively, for $[Cr(VI)_0]$ decreasing from 1 to 0.125 mM (Table 6-1). This is expected because the lower the $[Cr(VI)_0]$, the larger the water volume that can be treated by the GR_{SO4} present, whose mass was identical in all experiments. In terms of absolute amounts of Cr(VI) removed, this value substantially decreased with increasing $[Cr(VI)_0]$, from about 76.6 mg to 29.3 mg Cr(VI) per g of GR (Table 6-1). Moreover. along with the decreased Cr(VI) removal, the breakthrough curves became significantly steeper with

increasing [Cr(VI)$_0$]. Overall, these observations strongly indicate that GR$_{SO4}$ became more quickly exhausted at higher [Cr(VI)$_0$].
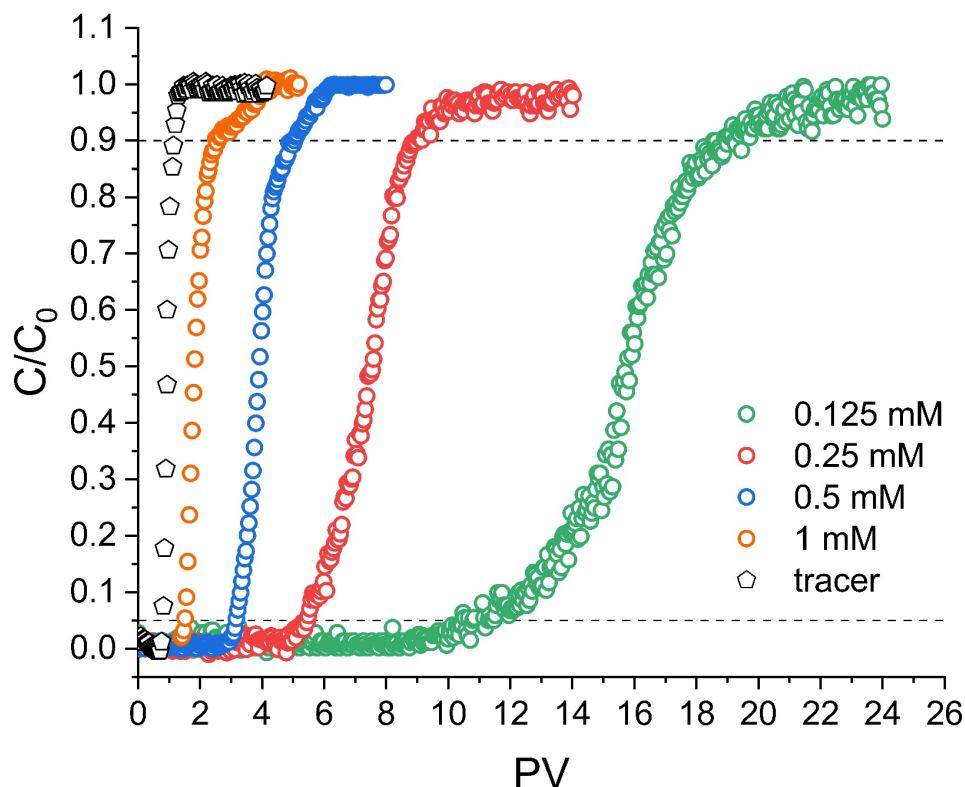
Figure 6-10   Cr(VI) breakthrough curves in GR$_{SO4}$ amended packed sand columns as function of different inlet Cr(VI) concentrations (C$_0$ = 0.125, 0.25, 0.5 and 1 mM; flow rate = 1 mL/min; pH 7.0). The tracer test was performed with 0.4 M NaNO$_3$. The dashed lines help to identify the breakthrough (*C/C$_0$* = 0.05) and the exhaustion (*C/C$_0$* = 0.9) points on each curve.

In terms of Cr(VI) removal efficiency relative to the added GR$_{SO4}$ reducing equivalents, the results of this study show that not all added GR$_{SO4}$ was oxidized in these reactions, and this was even more evident at higher [Cr(VI)$_0$] (Table 6-1). The removal efficiency decreased from about 85 % to 33 % with an increase in [Cr(VI)$_0$] from 0.125 to 1 mM. Such early GR$_{SO4}$ exhaustion was not observed in batch sand experiments performed at the 3 different Cr(VI) concentrations. The occurrence of early GR$_{SO4}$ exhaustion in columns can be explained by the constant Cr(VI) influx, which will keep reaction rates high on GR$_{SO4}$ particle surfaces, which in turn is more likely to induce the formation of passivating reaction rims. Such passivating rims were shown by Skovbjerg et al. (2006) and Williams and Scherer (2001) in GR batch experiments with high reduction rates. This assumption is also supported by the fact that GR$_{SO4}$ exhaustion occurs even faster if [Cr(VI)$_0$] is higher. Moreover, some GR$_{SO4}$ may not actually come in contact with the Cr(VI) solution, because of where the GR$_{SO4}$ particles are situated in the columns (for example near to dead-ends and/or in static flow areas); however, that effect should have been similar amongst the different [Cr(VI)$_0$] as the added GR$_{SO4}$ mass and the flow rate were constant.

Table 6-1 Amount of Cr(VI) immobilized within GR$_{SO4}$ amended sand columns (Cr(VI)$_q$, µmol), total Cr(VI) removal (mg/g) and Cr(VI) removal efficiency (%) calculated for different [Cr(VI)$_0$], flow rates and inlet solution pH.
Total Cr(VI) removal (mg/g) is the total amount of chromate immobilized (Cr(VI)$_q$, mg) per grams of GR$_{SO4}$ (9.1 mg). Cr(VI) removal efficiency (%) is calculated assuming that GR$_{SO4}$ amended columns have 46.7 µmol of reducing equivalents (= 46.7 µmol Fe(II)).
Breakthrough ($C/C_0 = 0.05$) and exhaustion ($C/C_0 = 0.9$) points are expressed in terms of PVs, for column experiments performed at different [Cr(VI)$_0$], flow rates and solution pHs.

[Cr(VI)$_0$] (mM)	[Cr(VI)$_0$] (mg/L)	pH	Q (mL/min)	q$_{imm}$ (µmol)	q$_{imm}$ (mg)	Cr(VI) removal (mg/g)	Cr(VI) removal efficiency (%)	Breakthrough point (PVs)	Exhaustion point (PVs)
		7	0.25	12.9	0.7	74.4	82.7	11	19
0.125	6.5	7	1	13.3	0.7	76.6	85.2	11	19
		7	3	11.8	0.6	68.0	75.6	13	18
		7	0.25	10.0±0.1	0.5±0.1	57.8±0.3	64.3±0.6	5	8
0.25	13	7	1	10.7±0.1	0.6±0.1	61.6±0.3	68.4±0.5	5	8
		7	3	10.3±0.3	0.5±0.3	59.2±1.8	65.9±2.9	5	8
		7	0.25	11.0±0.8	0.6±0.8	63.4±4.5	70.5±7.1	4	5
		4.5	1	13.5±0.3	0.7±0.3	77.7±1.6	86.4±2.6	4.5	6
0.5	26	7	1	10.1±0.1	0.5±0.1	58.2±0.5	64.8±0.8	3	5
		9.5	1	8.8±0.7	0.5±0.7	50.8±4.2	56.5±6.6	3	5
		7	3	8.7±0.7	0.5±0.7	50.1±3.7	55.7±5.9	3	5
		7	0.25	6.8±0.6	0.4±0.6	39.2±3.2	43.5±5.1	1.5	2.5
1	52	7	1	5.1±0.7	0.3±0.7	29.3±3.8	32.6±6.0	1.5	2.5
		7	3	3.4±0.1	0.2±0.1	19.6±0.5	21.8±0.7	1.5	2.5

ii Effect of flow rate

Normalized experimental breakthrough curves obtained for GR$_{SO4}$ amended sand columns as a function of flow rate, i.e., 0.25, 1 and 3 mL/min ($8.72 \cdot 10^{-3}$, $3.48 \cdot 10^{-2}$ and $10.5 \cdot 10^{-2}$ cm/s) for the different [Cr(VI)$_0$] are shown in Figure 6-11. Overall, the above discussed trends with increasing [Cr(VI)$_0$] do not greatly change with a change in flow rate: at all three tested flow rates, Cr(VI) removal (mg/g) and removal efficiencies (%) steadily decrease with increasing [Cr(VI)$_0$] (Table 6-1).
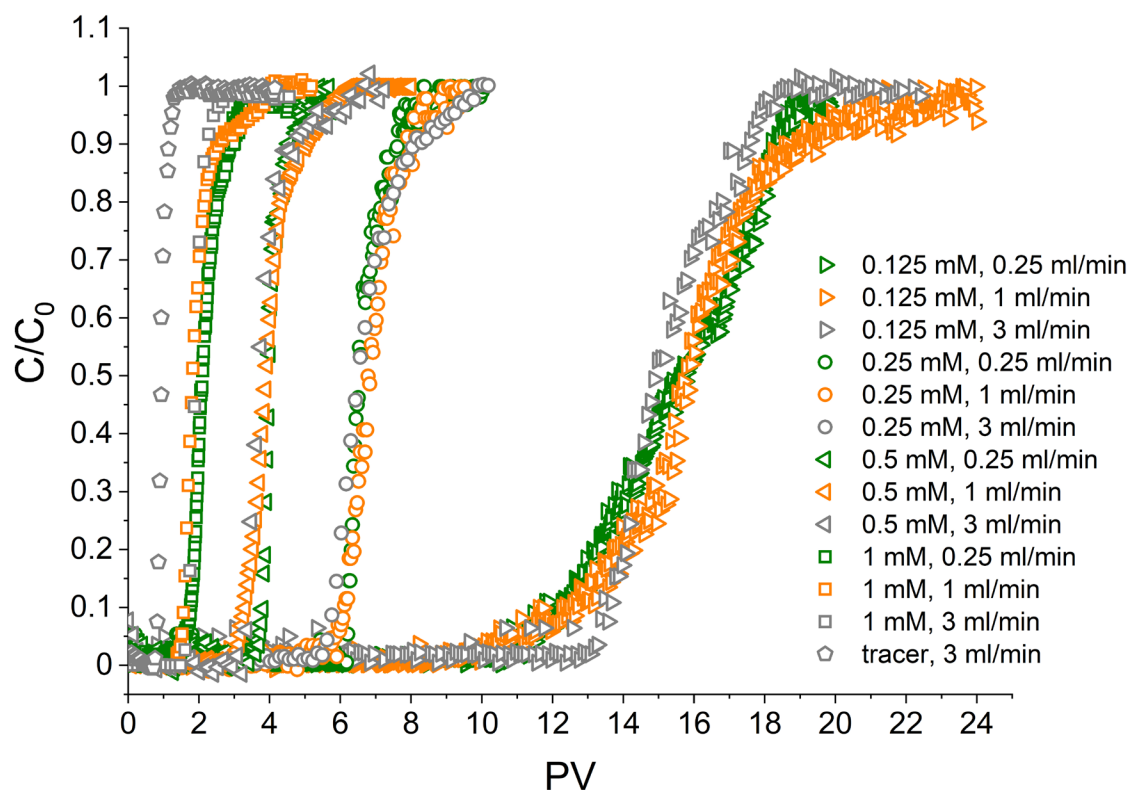
Figure 6-11 **Cr(VI) breakthrough curves in GR$_{SO4}$ amended packed sand columns at different flow rates (0.25, 1 and 3 mL/min) and inlet Cr(VI) concentrations (C$_0$ = 0.125, 0.25, 0.5 and 1 mM; pH 7.0).**
BTCs (*C/C$_0$* vs PV) for the tracer test at different flow rates are identical.

In terms of absolute values, it appears that these removal efficiencies are generally lower at higher flow rates, which is more clearly seen at higher [Cr(VI)$_0$] (i.e., 0.5 and 1 mM, Figure 6-112). This decrease in removal efficiency with increasing flow rate is explained by the proportional decrease in contact time between GR$_{SO4}$ particles and the Cr(VI) solution with increasing flow rate. Furthermore, with increasing flow rate, advection (i.e., flow through macropores) becomes more dominant, while flow close to pore surfaces decreases, and hence contact with immobilized GR$_{SO4}$ is further reduced. At the lower [Cr(VI)$_0$] (i.e., 0.125 and 0.25 mM), an increase in flow rate has less of an impact (Figure 6-11), because Cr(VI) reduction rates by GR are generally very high (as shown by batch sand experiments) and there seem to be sufficient GR$_{SO4}$ particles in the flow path to react with the Cr(VI) solution.
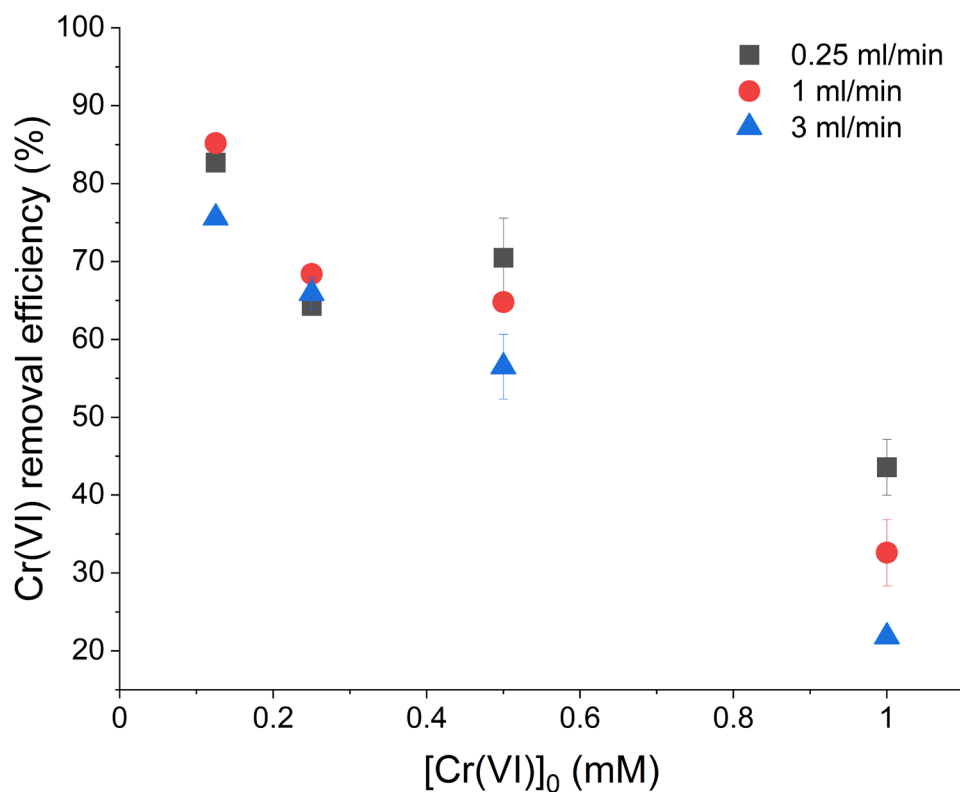
Figure 6-12   Calculated Cr(VI) removal efficiencies (%) in GR$_{SO4}$ amended packed sand columns at different flow rates (0.25, 1 and 3 mL/min) and inlet Cr(VI) concentrations (C$_0$ = 0.125, 0.25, 0.5 and 1 mM; pH 7.0).

iii   Effect of pH

Normalized experimental breakthrough curves obtained for GR$_{SO4}$ amended sand columns as a function of inlet solution pH (4.5, 7.0 and 9.5), where [Cr(VI)$_0$] and the flow rate were kept constant at 0.5 mM and 1 mL/min, respectively, are shown in Figure 6-13. Note that even in the pH 4.5 treatment, Cr(VI) was still the main dissolved Cr species as determined by solution analyses. The breakthrough curves at pH 7.0 and 9.5 are fairly similar, although calculated absolute Cr(VI) removal and removal efficiencies were a little lower at pH 9.5 compared to pH 7.0 (Table 6-1), but still within experimental error. In contrast, the breakthrough at pH 4.5 occurred substantially later (Figure 6-13), meaning a greater amount of Cr(VI) could be immobilized at this lower inlet pH (79.3 mg/g) compared to results at pH 7.0 and 9.5 (~ 58 mg/g, Table 6-1).
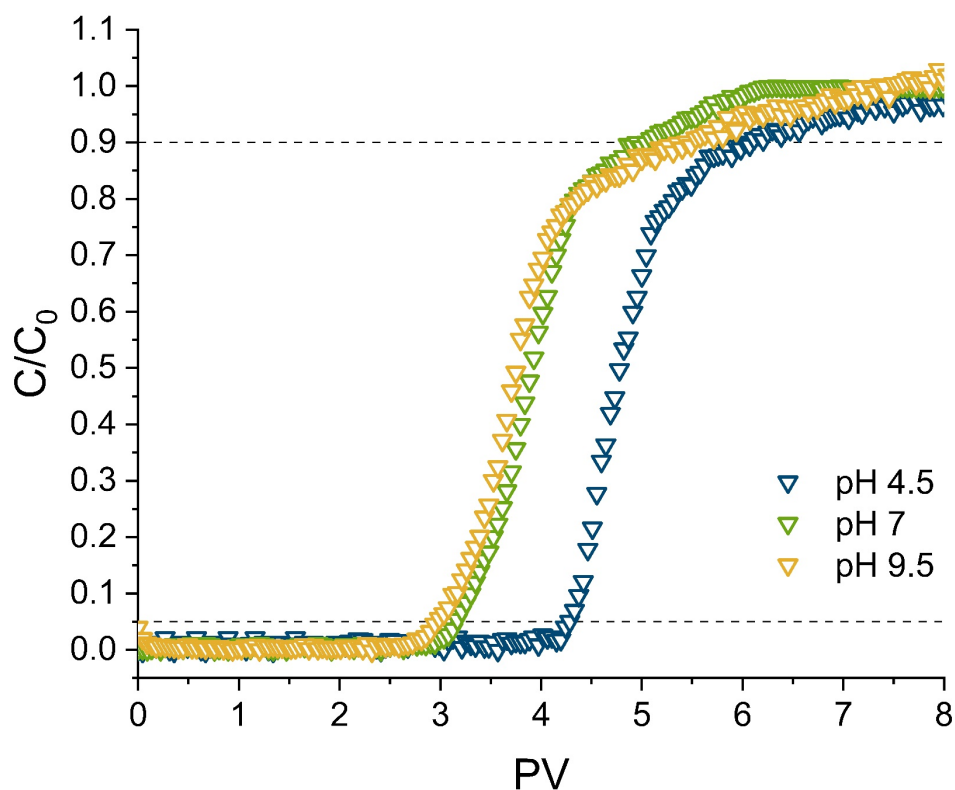
Figure 6-13 **Cr(VI) breakthrough curves in GR$_{SO4}$ amended packed sand columns as function of inlet solution pH: 4.5, 7.0 and 9.5 ([(Cr(VI)$_0$] = 0.5 mM, flow rate = 1 mL/min).**
The dashed lines help to identify the breakthrough (*C/C$_0$* = 0.05) and exhaustion (*C/C$_0$* = 0.9) points on each curve.

It is important to mention that GRs are fairly stable at pH between 6.5 and 10 (also depending on interlayer anion and geochemical conditions), while they will dissolve and/or transform to other phases at pH above or below this range (Génin et al., 1996; Génin et al., 1998). Thus, the enhanced Cr(VI) immobilization at acidic pH is likely triggered by GR dissolution, and subsequent release of aqueous Fe(II) that, in combination with the remaining Fe(II)$_s$, can readily react with the Cr(VI). The increased solubility of green rust and the dominance of aqueous Fe^{2+} over green rust under acidic conditions have been demonstrated in previous studies (Refait and Génin, 1993; Drissi et al., 1995; Génin et al., 1996; Génin et al., 2006). Furthermore, this reduction might be enhanced by the remaining GR$_{SO4}$, whose surface acts as catalyst (Skovbjerg et al., 2006). Indeed, under these acidic conditions, it is also less likely that passivation rims form on GR particles (Skovbjerg et al., 2006), thus the reaction can proceed for longer. For comparison, Williams and Scherer (2001) also observed an increase in Cr(VI) reduction rates with a decrease in pH from 9 to 5 in batch experiments, and argued that dissolution is likely responsible for this trend. It is worth noting that further processes such as (ad)sorption of Cr(VI) by GR oxidation products (e.g., goethite or ferrihydrite) might also be enhanced at acidic conditions and add to the observed immobilization, leading to a higher removal performance (Ajouyed et al., 2010). However, at acidic conditions the Cr(VI) removal is mainly attributable to the reductive precipitation of dissolved Cr(VI) by Fe(II) (Figure 6-6). Under all three tested pH conditions, reduction of Cr(VI) to

Cr(III) will therefore result in the formation of an insoluble Cr,Fe phase. Figure 6-14 shows the XRD patterns of reaction products of GR$_{SO4}$ being in contact with Cr(VI) solutions respectively at pH 4.5 and 7.0. Both spectra clearly exhibit the presence of GR$_{SO4}$ and goethite.
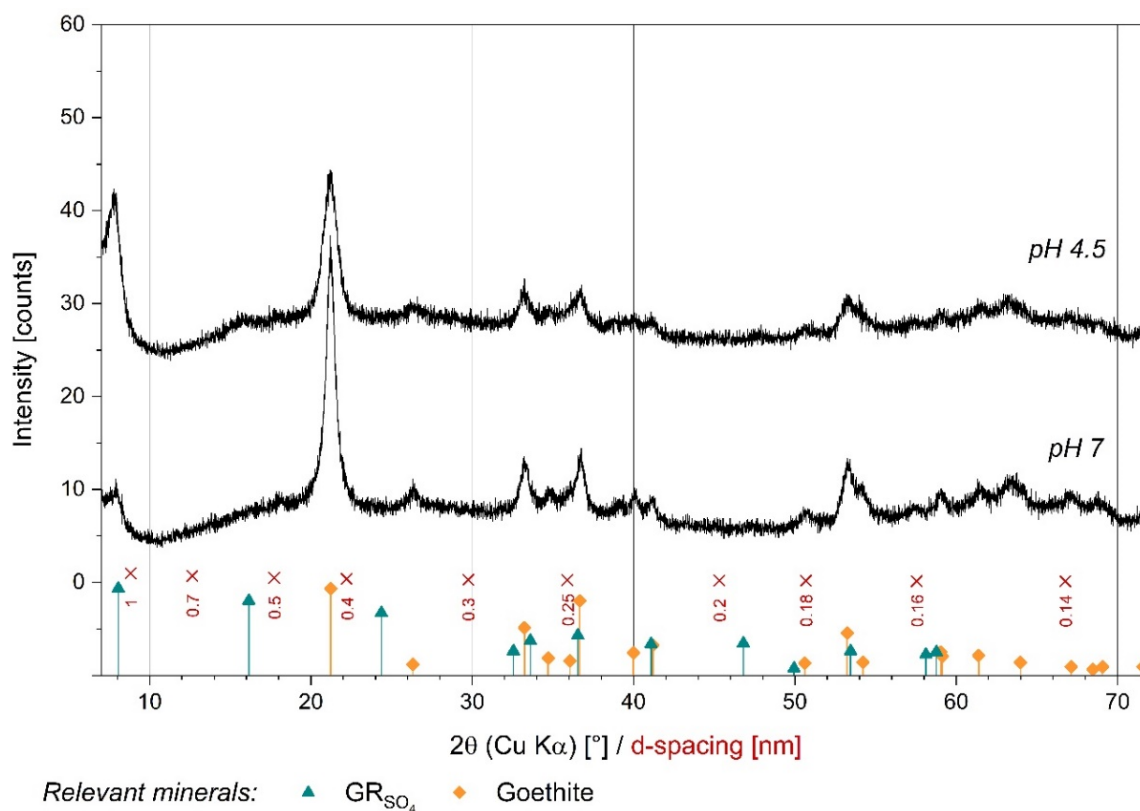
Figure 6-14   XRD patterns (Cu-Kα) of reaction products of GR$_{SO4}$ in buffered solutions at pH 4.5 and 7.0.

The ESEM images (Figure 6-15) of the same samples show that in both cases GR$_{SO4}$ particles kept their hexagonal shape. However, after reaction with Cr(VI) at pH 4.5, the edges of the crystals appeared irregular due to higher corrosion, which occurs at acidic conditions.
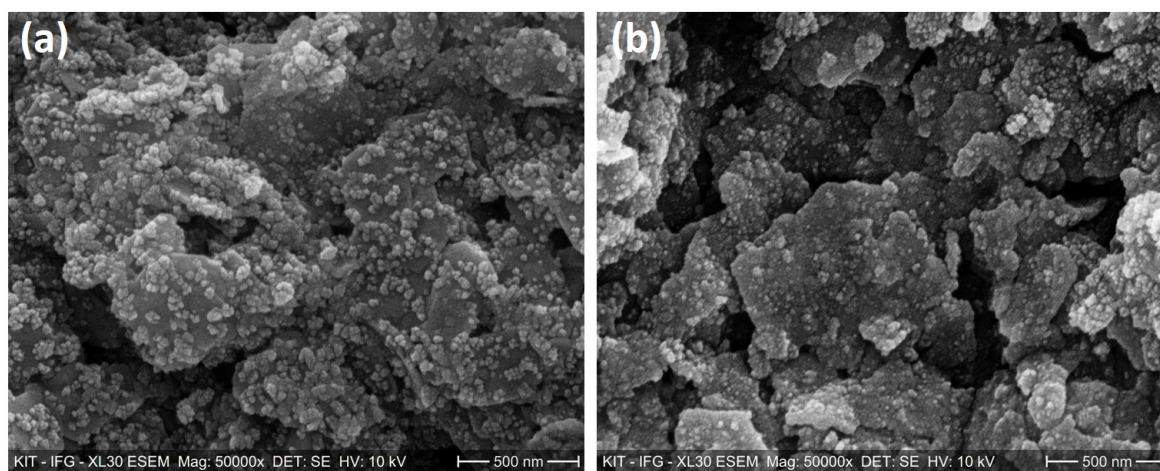
Figure 6-15   ESEM images of reaction products of GR$_{SO4}$ in buffered solutions at pH (a) 7.0 and (b) 4.5.

6.3.4 S-nZVI Batch and Column Studies

For comparison to GR$_{SO4}$, a representative set of batch and column experiments were performed with sulfidized nZVI (S-nZVI). Figure 6-16 shows that the removal of Cr(VI) by S-nZVI in batch sand experiments is significantly slower compared to GR$_{SO4}$, despite the 1.5x higher amount of reducing equivalents in S-nZVI reactions compared to GR$_{SO4}$.
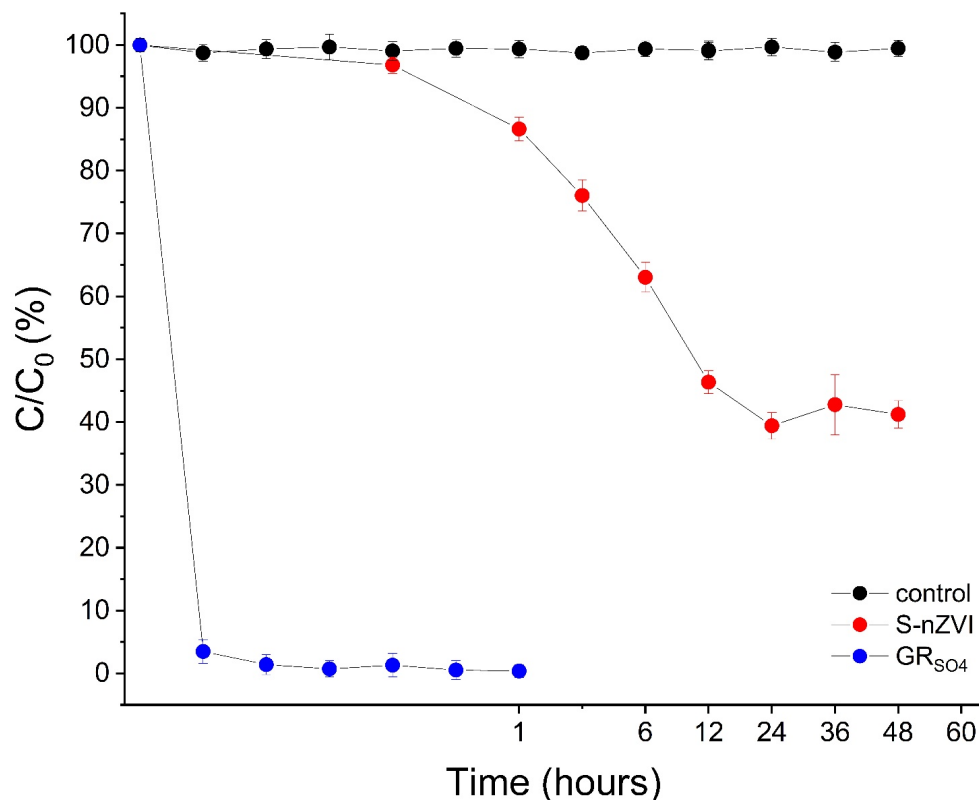
Figure 6-16 **Cr(VI) immobilization efficiency by S-nZVI and GR$_{SO4}$ (0.25 mM [Cr(VI)$_{in}$]). A control experiment with no added reducing agent is also shown. Each measurement represents one batch reaction (note that x-axis is not linear).**

Moreover, Cr(VI) removal by S-nZVI slows down considerably after 12 hours, and little change is observed thereafter, yielding a maximum Cr(VI) removal of ~ 60 % within 48 hours. In contrast, in GR$_{SO4}$ reactions nearly complete removal was observed within 30 minutes, indicating not only a higher removal efficiency but also higher reaction kinetics for GR$_{SO4}$ compared to S-nZVI. The lower reactivity of S-nZVI with Cr(VI) compared to GR$_{SO4}$ may be explained by S-nZVI particles forming larger aggregates due to magnetic attraction (Phenrat et al., 2007), thus available reactive surface area may be much lower than expected. Also, it is argued that Cr(VI) can be reduced on GR surfaces and in its interlayer, providing abundant reactive sites for reduction (Loyaux-Lawniczak et al., 2000; Loyaux-Lawniczak et al., 2001; Bond and Fendorf, 2003). Additionally, the observation that Cr(VI) removal was incomplete in S-nZVI batch reactions despite sufficient S-nZVI reducing equivalents, suggests that S-nZVI surfaces became passivated by oxidized Fe phases. This is supported by XRD analysis of solids after 24 h reaction between S-nZVI and Cr(VI) in sand-free batch reactors that show the characteristic

peaks of the initial S-nZVI phase, i.e., the Fe^0 core and the FeS shell (Figure 6-17), but also characteristic peaks of oxidized Fe (oxyhydr)oxide phases, including lepidocrocite (PDF# 44-1415) and magnetite (PDF# 19-0629). As for GR$_{SO4}$ experiments, some amorphous Cr,Fe phases may have also formed in S-nZVI reactions, but could not be identified with XRD here. These oxidized Fe phases have lower zero point of charge (lepidocrocite: 7.1 (Kim et al., 2008) and magnetite: 6.5 (He and Traina, 2005)) compared to goethite (which is the oxidation product in GR$_{SO4}$ reactions), thus Cr(VI) removal by adsorption is also less favored in S-nZVI reactions.
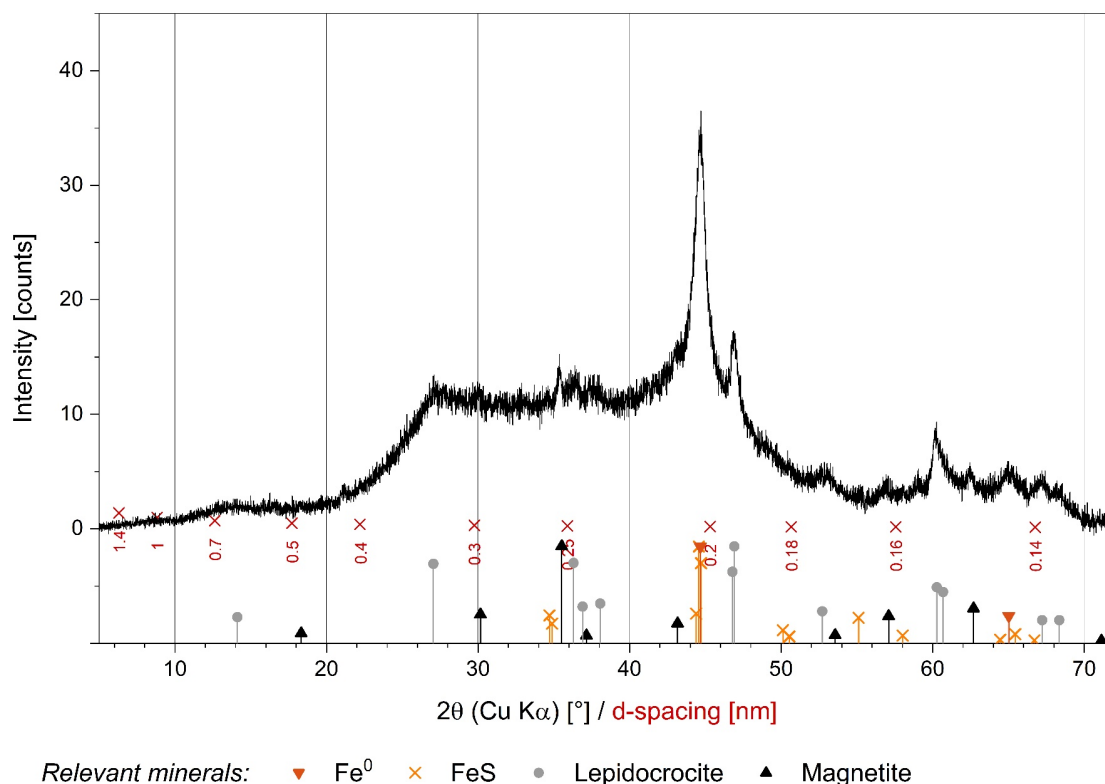
Figure 6-17   XRD patterns (Cu-Kα) of reaction products of S-nZVI in buffered solution at pH 7.0.

In terms of S-nZVI reduction performance in columns, Figure 6-18 shows the normalized experimental breakthrough curves obtained for S-nZVI amended sand columns (~ 38 μmol of Fe^0) as a function of flow rate, i.e., 0.25, 1 and 3 mL/min for [Cr(VI)$_0$] = 0.25 mM. For comparison, BTCs obtained in GR$_{SO4}$ amended sand columns at the same flow rates and [Cr(VI)$_0$] conditions are also shown.
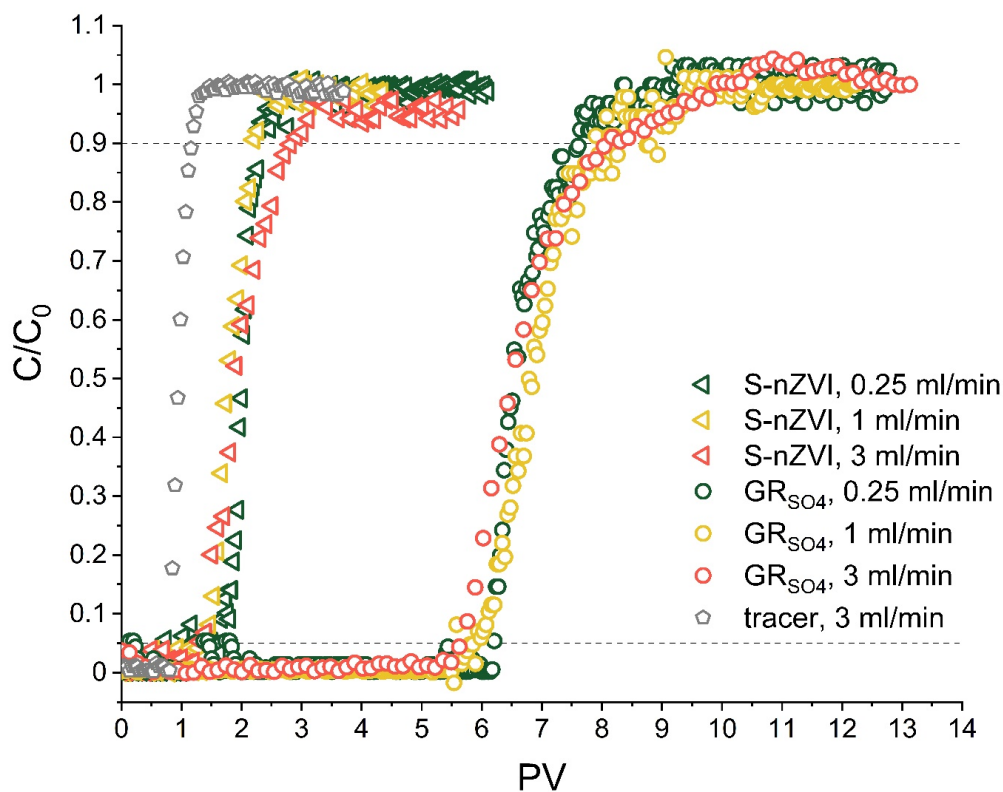
Figure 6-18 **Cr(VI) breakthrough curves in S-nZVI (triangles) and GR$_{SO4}$ (circles) amended sand columns as function of flow rates: 0.25, 1 and 3 mL/min ([(Cr(VI)$_0$] = 0.25 mM and pH 7.0). The black dotted lines mark the breakthrough (*C/C$_0$* = 0.05) and exhaustion (*C/C$_0$* = 0.9) points on each curve. BTCs (*C/C$_0$* vs *PV*) for the tracer test at different flow rates are identical.**

Similar to the GR$_{SO4}$ column results, flow rate had little effect on absolute Cr(VI) removal and removal efficiencies in S-nZVI columns, yielding 26.2, 20.7 and 22.1 mg/g and 3.5 %, 2.7 % and 2.9 % at 0.25, 1 and 3 mL/min, respectively, while lower pH conditions enhanced Cr(VI) removal (53.4 mg/g and 7.1 %) (Figure 6-19).
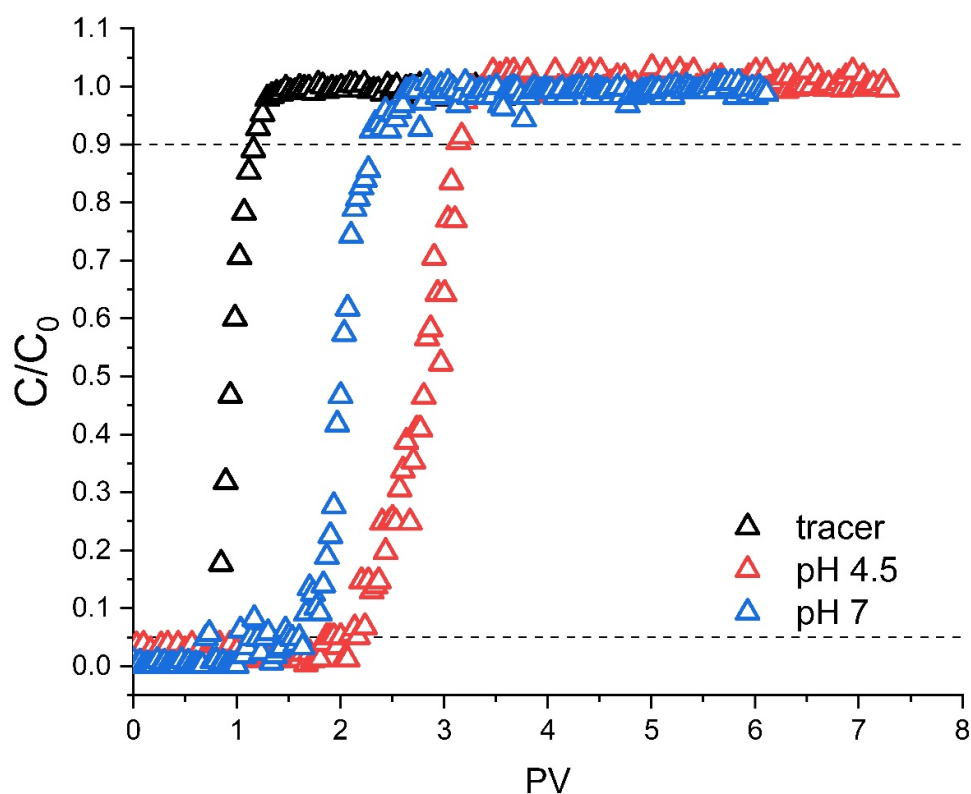
Figure 6-19 **Cr(VI) breakthrough curves in S-nZVI amended packed sand columns as function of inlet solution pH: 4.5 and 7.0, [(Cr(VI)$_0$] = 0.25 mM and flow rate = 0.25 mL/min.**
The dashed lines help to identify the breakthrough (C/C_0 = 0.05) and exhaustion (C/C_0 = 0.9) points on each curve.

The breakthrough (C/C_0 = 0.05) and exhaustion (C/C_0 = 0.9) points under those conditions are listed in Table 6-2.

Table 6-2 **Amount of Cr(VI) immobilized within S-nZVI amended sand columns (Cr(VI)$_q$, µmol), total Cr(VI) removal (mg/g) and Cr(VI) removal efficiency (%) calculated for Cr(VI)$_0$ of 0.25 mM (i.e., 13 mg/L), different flow rates and inlet solution pH.**
Cr(VI) removal (mg/g) is the total amount of chromate immobilized (Cr(VI)$_q$, mg) per grams of S-nZVI (2.6 mg). Cr(VI) removal efficiency (%) is calculated assuming that S-nZVI amended columns have 114 µmol (= 3x38 µmol Fe^0) of reducing equivalents. Breakthrough (C/C_0 = 0.05) and exhaustion (C/C_0 = 0.9) points expressed in terms of pore volumes (PVs) for S-nZVI sand column experiments performed at different [Cr(VI)$_0$], flow rates and solution pH values.

pH	Q (mL/min)	Cr(VI)$_q$ (µmol)	Cr(VI)$_q$ (mg)	Cr(VI) removal (mg/g)	Cr(VI) removal efficiency (%)	Breakthrough point (PVs)	Exhaustion point (PVs)
4.5	0.25	2.7±0.1	0.14	53.4±0.8	7.1±09	2.2	3.5
7	0.25	1.3±0.1	0.07	26.2±0.5	3.5±0.8	1.5	~2
7	1	1.0±0.1	0.05	20.7±0.3	2.7±0.5	1.5	~3
7	3	1.1±0.1	0.06	22.1±0.4	2.9±0.7	1.5	~3

These findings are in good agreement with Gong *et al.* (2017), who showed that immobilization of Cr(VI) by S-nZVI is strongly dependent on pH conditions, with higher performance at lower pH. Similar to GR_{SO4} observations, Cr(VI) removal in S-nZVI amended columns is significantly lower than

in batch sand experiments. However, the difference is much more pronounced in the S-nZVI system because of its much lower Cr(VI) reduction rate. This in turn suggests that a higher removal efficiency could potentially be achieved in the column, if the contact time is increased, i.e., flow rate is further decreased. However, surface passivation as observed in batch reactions is still a major concern in the application of S-nZVI, so it is doubtful that efficiencies would increase that much in the columns even if flow rates are considerably decreased.

6.4 Summary

This study demonstrated the high effectiveness of GR_{SO4} to immobilize mobile Cr(VI) inside porous quartz sand media. Batch sand studies confirmed similar fast reduction of Cr(VI) by GR_{SO4} as observed for batch studies in aqueous media (i.e., where no sand was added), with > 95 % Cr(VI) removed within only 10 minutes. Moreover, although incomplete removal was expected for conditions where there were insufficient reducing equivalents (i.e., Cr(VI) was in excess), the Cr(VI) removal resulted to be 15 % higher than the expected immobilization capacity based on reduction only. This may be due to additional Cr(VI) removal by Cr(VI) adsorption onto the newly formed goethite particles, which is favored at the neutral pH studied here (i.e., below goethite zero point of charge of 9.1).

In comparison, Cr(VI) removal efficiencies in sand columns under dynamic flow conditions were substantially lower than in batch studies, particularly at higher inlet Cr(VI) concentrations. This is likely explained by the constant influx of Cr(VI) solution, which keeps reaction rates high on GR particle surfaces likely promoting the formation of passivating rims on GR surfaces, as observed before in batch experiments with high initial Cr(VI) concentrations. Furthermore, lower Cr(VI) removal efficiencies were observed at higher flow rates and alkaline pH conditions (compared to acidic).

For comparison, similar batch and column studies were also performed with S-nZVI, an alternative reductant material. The results clearly showed that Cr(VI) reduction and immobilization by GR_{SO4} is substantially faster and yields 2.5 times higher efficiencies compared to S-nZVI, meaning GR_{SO4} performs substantially better under the tested flow conditions.

Overall, these results demonstrate the high potential for use of GR_{SO4} in Cr(VI) remediation applications. High immobilization yields that are considerable higher than what is observed for alternative reductants such as S-nZVI were observed also in presence of sand matrices, dynamic flow conditions and changing pH conditions. Moreover, the observed trends suggest that at much lower flow rates, Cr(VI) removal efficiencies by GR_{SO4} would likely be much higher. Thus, at flow rates closer to average groundwater flow (e.g., 6-220 cm/day), GR_{SO4} might achieve 100 % removal efficiency because of higher contact time with Cr(VI).

7 Transport Behavior of Green Rust Sulfate and Sulfidized Nano Zerovalent Iron in Sandy Porous Media

7.1 Introduction

In this chapter, the transport behavior of two promising iron-based reducing agents, sulfidized nanoscale zerovalent iron (S-nZVI) and sulfate green rust (GR_{SO4}), was investigated to evaluate their application potential for *in-situ* permeable reactive zones obtained via injection into the subsurface. For a successful injection strategy, it is important that the reactant material (usually suspended to form a slurry) spreads from the injection point, migrates through the porous matrix and reaches the contaminated zone. To date, there are no studies evaluating the transport behavior of GR_{SO4} in a sandy matrix, while the understanding of S-nZVI stability and its transport behavior in porous media is limited, which is made more challenging due to the different synthesis and sulfidation methods. Investigating the behavior of the two reactants in a representative porous medium as well as knowing their physicochemical characteristics (particle size, shape, morphology, etc.) will provide a better understanding of the mechanisms that regulate their mobility.

S-nZVI is a modified form of nZVI obtained by sulfidation treatment (Fan et al., 2016a). Although nZVI is frequently applied for *in-situ* field application, it reacts with water (i.e., anaerobic corrosion), dissolved oxygen and/or other redox-sensitive solutes commonly present in subsurface environments (e.g., nitrate) leading to loss in reactivity (Liu and Lowry, 2006; Lim and Zhu, 2008; Sarathy et al., 2008; Fan et al., 2016b). These interactions take place rapidly and cause the formation of an oxidized iron shell around the iron core (Fe^0), which is responsible for surface passivation (Sarathy et al., 2008; Fan et al., 2016b). Sulfidation treatment of nZVI using sodium dithionite or sodium sulfide is an emerging approach that is able to counterbalance some of these drawbacks (Han and Yan, 2016; Fan et al., 2017). Indeed, the formation of a thin FeS shell around Fe^0 is able to protect the iron core from anoxic corrosion and the rapid loss of reducing iron equivalents, while still enabling electron transfer from the Fe^0 core to the surface for effective reduction at FeS sites (Fan et al., 2013; Rajajayavel and Ghoshal, 2015). Moreover, the presence of the FeS layer improves the selectivity towards target contaminants (Fan et al., 2017). In many cases, reduction rates of key contaminants have shown to be higher for S-nZVI compared to non-sulfidized nZVI, for example for tetrachloroethylene (Rajajayavel and Ghoshal, 2015; Mangayayam et al., 2019a) and chromate (Li et al., 2018).

Although the FeS (e.g., mackinawite) shell is paramagnetic (Makovicky, 2006), S-nZVI is nevertheless ferromagnetic. Thus, S-nZVI particles tend to attract each other and aggregate. Surface modification, therefore, is needed to reduce attraction and aggregation between the particles. In this study, sodium carboxymethyl cellulose (CMC) was used as stabilizer to counteract the attractive magnetic forces between the iron particles (F. He et al., 2010; Kocur et al., 2014). CMC is an inexpensive, water soluble, anionic, and environmental-friendly polymer. The particle stabilization was carried out using two different approaches, called "pre-grafting" and "post-grafting" methods, following Cirtiu *et al*. (2011). In the former, the amount of CMC was added during the synthesis of nZVI and before sulfidation, while in the latter method the stabilization of the nanoparticles was performed after synthesis and sulfidation.

Additional to S-nZVI, GR$_{SO4}$ mobility has been tested using the same experimental set-up. GR$_{SO4}$ is easy to synthesize and has proven to be effective in degrading or adsorbing many contaminants such as As(V) (Perez et al., 2019), NO$_2^-$ (Hansen et al., 1994), Se(IV) and Se(VI) (Myneni et al., 2011; Börsig et al., 2018), nitroaromatic compounds (Boparai et al., 2010; Wu et al., 2013), or Cr(VI) (Loyaux-Lawniczak et al., 2000; Williams and Scherer, 2001; Bond and Fendorf, 2003; Skovbjerg et al., 2006; Thomas et al., 2018). In Chapter 6, GR$_{SO4}$ has shown to effectively reduce chromate also when mixed in a porous medium and under dynamic conditions.

The successful synthesis of the materials was verified by X-Ray diffraction (XRD) analysis; measurements of particle size and shape were performed via transmission electron microscopy (TEM), scanning electron microscopy (SEM) or environmental scanning electron microscopy (ESEM); electrophoretic mobility (EPM) measurements were performed to assess the electric surface charge of the particles. The mobility behavior of the reactants was evaluated via their injection in water saturated packed columns filled with fine quartz sand (d_c = 0.1-0.3 mm). Under these conditions, it was possible to simulate particle injection into natural aquifers. The impact of several tested operating parameters was evaluated by breakthrough curves (BTCs), and the particle distribution along the column was determined by means of retention profiles obtained via segmentation and acid digestion of the material of the columns.

In addition to conventional breakthrough curve analysis and retention profiles, magnetic resonance imaging (MRI) was performed during particle injection. MRI, which is based on nuclear magnetic resonance (NMR), is a promising non-invasive, *in-situ* technique mostly used in medical, biological and chemical sciences that recently has proven its suitability in contaminant hydrology and environmental research. So far, this technique has been used to quantitatively measure the concentration distributions of magnetic nanoparticles in coarse-grained sand systems (Ramanan et al., 2012), quartz and dolomite gravel (Lakshmanan et al., 2015a) and sandstone cores (Lakshmanan et al., 2015b); to assess colloid transport velocities and collision efficiencies in artificial porous media (Baumann and Werth, 2005) or to assess spatial distribution of magnetic particles within porous media during injection (Greiner et al., 1997; Werth et al., 2010; Cuny et al., 2015). In this study, the main goal of using MRI

was to visualize the magnetic nanoparticles within the column. By modelling the MRI data, it was possible to quantitatively assess the time-varying mobility of the nanoparticles, calculate the kinetics of the migration front and identify the presence of preferential transport paths along the flow direction within the column.

7.2 Experimental Section

All experiments, if not mentioned otherwise, were performed inside an anaerobic glovebox (Jacomex P[Box] Compact Glove Box, Dagneux, France) filled with an Ar atmosphere. All solutions were prepared using reagent grade chemicals and deionized, deoxygenated (by N$_2$ degassing) Milli-Q water (18.2 MΩ cm). GR$_{SO4}$ and S-nZVI were freshly synthesized prior to each experiment as described in Chapter 5.1.2.

7.2.1 Surface Modification of S-nZVI

In preparation for the experiments of this study, two compounds were selected as anionic stabilizers for S-nZVI: sodium carboxymethyl cellulose, CMC (also known as carboxymethyl cellulose sodium salt) and xanthan gum, XG. The chemical structures of the two stabilizers are shown in Figure A-6 and Figure A-7. CMC is a polysaccharide composed of fibrous tissues of plants and belongs to the class of anionic linear structured cellulose. It is a water soluble polymer, which can be used as a polyelectrolyte cellulose derivative (Peng et al., 2012). XG is a hydrophilic polysaccharide with high molecular weight (MW = 10^3 kDa), secreted by *Xanthomonas campestris* and produced by fermentation of carbohydrate (Quinten, 2011). CMC (MW = 250 kDa) and XG are commercially available as water-soluble dry powders. To prepare the polymer solutions (1-10 g/L), the powders were dissolved in Milli-Q water at 50 ºC and continuously stirred for 3 hours and then stored overnight at 4 ºC to ensure complete hydration of the powder (Wang et al., 2003). Nevertheless, undissolved residuals of XG were present in solution, which very likely would lead to negative effects during injection into the sandy porous matrix. For this reason, CMC was chosen as stabilizer agent for the experiments of this study. Prior to use, CMC solutions were purged with N$_2$.

S-nZVI was modified by CMC using two different approaches:

i. the post-grafting (or post-synthesis) method, which consisted of adding the CMC polymer after the S-nZVI synthesis. Specific amounts of S-nZVI were re-suspended in 50 mL serum bottles containing degassed polymer solutions of different concentrations (1-5 g/L). The resulting polymer-S-nZVI suspensions were then sealed with a butyl septum cap (Sigma-Aldrich) to prevent air oxidation, sonicated for 15 minutes to break agglomerates and shacked on an orbital shaker for 3 hours at 200 rpm (Figure 7-1b)

ii. the pre-grafting (or pre-synthesis) method, which consisted of adding the CMC polymer during nZVI synthesis (He et al., 2007). The stabilizer was added to the nZVI precursor solution as an

additional component, before the ionic iron precursor was reduced to Fe^0. Specifically, $FeCl_2$ was dissolved in water and mixed with an aqueous solution of the stabilizer to a final concentration of 0.5 % v/v. The following steps are the same as those for the S-nZVI synthesis described in Chapter 5.1.2 (Figure 7-1c).
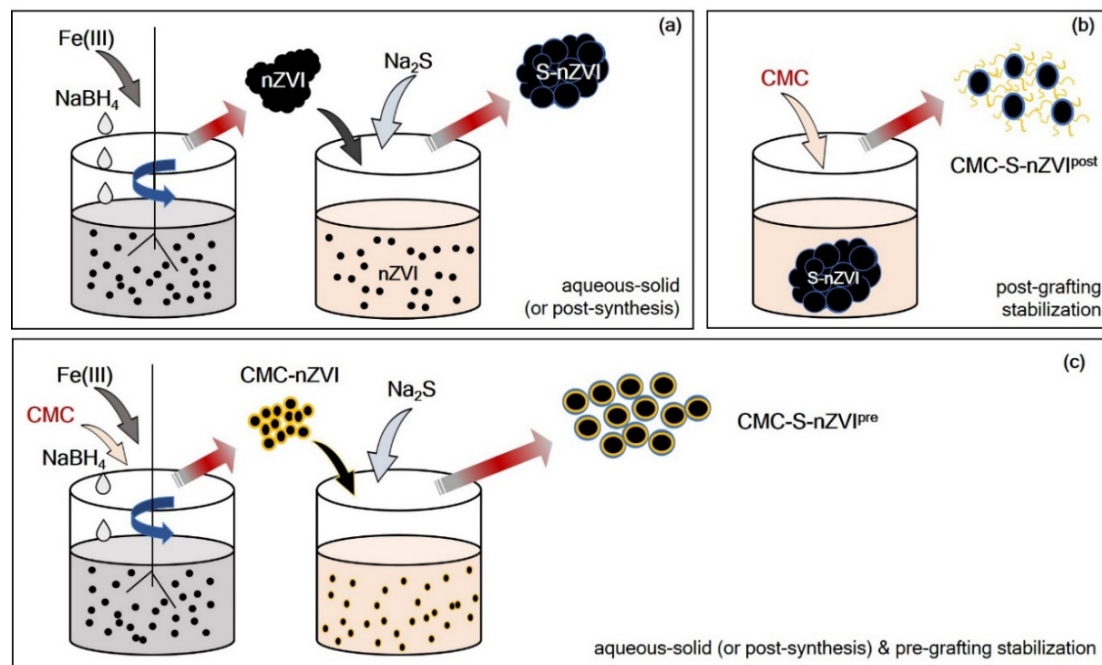
Figure 7-1   Schematic representation of the procedures used to synthesize bare and CMC-modified S-nZVI.
(a) bare S-nZVI by the post-synthesis sulfidation approach, (b) CMC-S-nZVI[post] with the post-grafting stabilization method and (c) CMC-S-nZVI[pre] with the pre-grafting stabilization method.

In this study, the following nomenclature has been used to differentiate between various types of sulfidized nanoscale zerovalent iron: S-nZVI that was not treated with CMC is called bare S-nZVI; CMC-pre-grafted S-nZVI is named as CMC-S-nZVI[pre], while CMC-post-grafted S-nZVI is denoted as CMC-S-nZVI[post]. Furthermore, in case of the CMC-treated-S-nZVI types, the prefixed numbers 1, 2.5 and 5 were used to refer to the respective concentration of the CMC solution in g/L (Table 7-1).

Table 7-1   Nomenclature used for various types of S-nZVI particles.

Treatment method	Polymer concentration (g/L)	Name
-	-	Bare S-nZVI
Pre-grafting	5	5-CMC-S-nZVI[pre]
Post-grafting	1	1-CMC-S-nZVI[post]
Post-grafting	2.5	2.5-CMC-S-nZVI[post]
Post-grafting	5	5-CMC-S-nZVI[post]

7.2.2 Particle Characterization

7.2.2.1 Structure, Size and Morphology

The successful synthesis of GR$_{SO4}$, S-nZVI and CMC-modified S-nZVI was verified via XRD. ESEM, SEM and TEM were used to acquire high resolution images of the synthesized particles. Detailed information about the analytical methods are described in Chapters 5.2.1, 5.2.2, 5.2.3 and 5.2.4.

7.2.2.2 ζ-Potential Measurements

The zeta potential, or ζ-potential, (mV) of bare S-nZVI, CMC-S-nZVI[pre] and CMC-S-nZVI[post] was measured via EPM for zeta potential measurement (Chapter 5.2.5). The suspensions were prepared shortly before the measurements, stored into tightly sealed 50 mL containers and sonicated for 5 minutes before the measurement. The pH electrode, the cell and apparatus were flushed with Milli-Q water prior to each measurement. To prevent oxidation of the particles, the suspensions were purged with a constant flow of Ar during the measurements. The measurements were made as a function of pH at room temperature and particle concentrations of 0.1 and 0.5 g/L were used. The pH was adjusted by adding 0.05 M HCl or 0.1 M NaOH.

7.2.3 Sedimentation Tests

The physical stability of bare S-nZVI, CMC-S-nZVI[pre] and CMC-S-nZVI[post] was qualitatively assessed by monitoring the particle settling process using time-resolved turbidity measurements (Chapter 5.2.6). The measurements were performed with a UV-Vis spectrophotometry inside an anoxic chamber at room temperature, similar to previous studies (He et al., 2007; Cirtiu et al., 2011). The absorbance (Abs) data were collected over a period of 1 h and in 10 s steps. Suspensions of 0.125 g/L were sonicated for 5 minutes prior to each measurement and analyzed in disposable and covered cuvettes (10 mm path length cuvette). The normalized absorbance values (*Abs/Abs$_0$*) give information about the colloidal stability of the S-nZVI suspension: the closer the value is to 1, the higher is the stability. The *Abs/Abs$_0$* values were used to calculate the settling velocity (v_s) and share rate (γ). In this context, the stability time (t$_{50}$ and t$_{90}$) are defined as the time required to reach 50 % and 90 % of the initial absorbance value. The corresponding average settling velocity (v_s) was obtained as follows (Gastone et al., 2014a):

$$\left(v_{s,50}\right) = \frac{x/2}{t_{50}} \qquad\qquad \textbf{Equation 7-1}$$

$$\left(v_{s,90}\right) = \frac{x/2}{t_{90}} \qquad\qquad \textbf{Equation 7-2}$$

where *x* is the height of the cuvette (45 mm).

The settling velocity of a single particle suspended in a Newtonian fluid is known to follow the Stokes law, while for a polymer concentration with a non-Newtonian rheological behavior, the viscosity (and consequently the settling velocity) depends on the shear rate experienced by the fluid close to the

particle (Gastone et al., 2014a). The shear rate (γ) of a spherical particle that settles at a velocity v_s can be estimated as follows (Gastone et al., 2014a):

$$\gamma = 2\,\frac{v_s}{d_{Stokes}} \qquad\qquad \textbf{Equation 7-3}$$

where d_{Stokes} corresponds to the sphere diameter. If the particle is not a sphere, d_{Stokes} is the diameter of a sphere with the same volume and density of the particle that sediments at the same velocity.

7.2.4 Transport Column Studies

In this work, water-saturated packed columns filled with quartz sand, as representative homogenous porous media, were used to assess the mobility behavior of S-nZVI and GR_{SO4}. The experiments were designed to reproduce conditions at the lab scale comparable to those of an *in-situ* injection. Therefore, experiments similar to the reactivity column tests (conducted and described in Chapter 6) were carried out. However, the resulting BTCs have a different meaning and give an insight into the particle transport behavior. In this context, the particle transport experiments were on-line monitored in order to continuously measure the amount of particles that cross the entire length of the column and reach the outlet. Therefore, the obtained normalized particle concentration (C/C_0) value as function of pore volumes (PVs) expresses the amount of eluted particles, while the rest represents the particles that are retained in small voids of dead-end pores of the matrix. Height and shape of the BTC provide information on the transport behavior of the injected particles within the porous medium and on the possible interaction mechanisms between the particles themselves (particle-particle) and between the particles and the porous media (particle-collector).

7.2.4.1 Experimental Set-Up for Breakthrough Analysis

The transport behavior of GR_{SO4} and different types of S-nZVI was evaluated by packed-bed column experiments (11 cm length and 1.4 cm inner diameter) under strictly anoxic conditions. The investigated operating parameters were particle concentration (0.1-1 g/L), stabilizer concentration (CMC 0-5 g/L), flow rate of the injection (0.5-2 mL/min) and grain size of the sand matrix (0.1-0.3 and 0.4-0.8 mm). Although there is no general agreement on the ideal particle concentration of the reactant suspension, the particle concentrations used for this study range between 0.1 and 1 g/L, whereby the lowest value is the typical concentration used in comparable transport studies and the highest value might be better suited for field application. Sand columns were wet-packed with 23 g of quartz sand and assembled in vertical position with flow from bottom to top to ensure homogeneous packing and avoid the formation of air bubbles. Transport experiments were conducted in horizontal manner, as these settings have shown to be more suitable for investigating particle transport compared to the vertical manner (Liu et al., 2019). Figure 7-2 shows the used experimental set-up. Non-reactive tracer tests (0.4 M $NaNO_3$) were performed to determine the values of porosity (n), pore water velocity (v) and longitudinal dispersion coefficients (D), as described in Chapter 6.2.2.3.
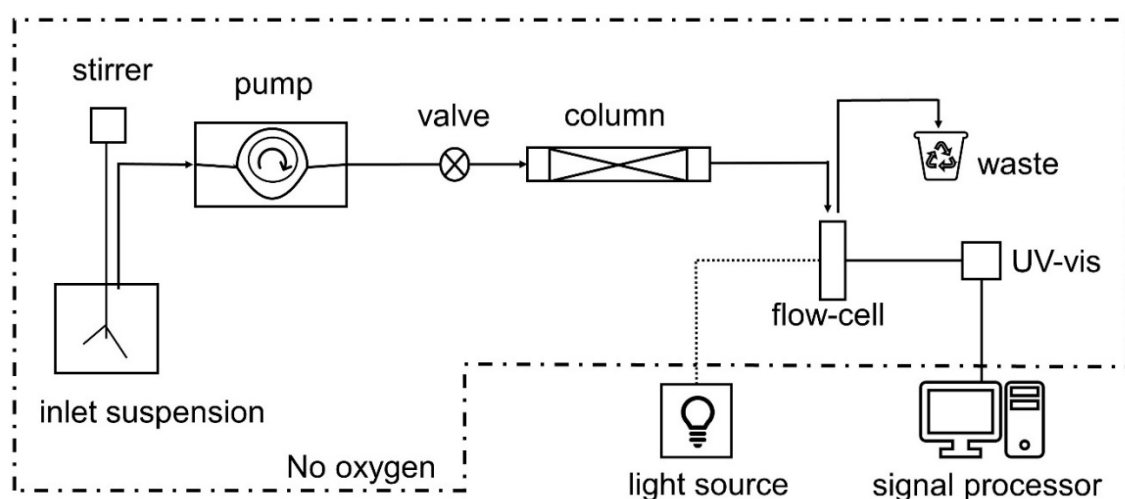
Figure 7-2 **Schematic experimental set-up used for measuring spectrophotometrically the breakthrough curves under strictly anoxic conditions.**
The solution absorbance was analyzed on-line using a flow through cell connected to an UV-Vis spectrophotometer.

The inlet suspension was pumped through the column using a peristaltic pump (Ismatec). During injection, the suspension was continuously stirred with a mechanical overhead stirrer to prevent settling of the particles. The effluent of the column was sent to a flow-through cell (2 mm path length, Hellma, Germany) connected to a spectrophotometer (Ocean Optics) for on-line turbidity measurements (further information are in Chapter 5.2.6). As absorbance and particle concentration have shown to be linearly correlated, BTCs were calculated by normalizing effluent particle (C) concentration with the inlet particle concentration (C_0). The calibration curves are shown in Figure 5-6.

Once packed, the columns were equilibrated by sequentially pumping 8 pore volumes (PVs) of degassed Milli-Q water, followed by 5 PVs of CMC solution with same polymer concentration used for the particle stabilization (in the case of CMC-modified S-nZVI). Then, 6 PVs of particle (GR$_{SO4}$, S-nZVI, CMC-S-nZVI^{pre} or CMC-S-nZVI^{post}) suspension were injected at the selected flow rate. Following the particle injection, a post-flush step was performed to monitor the potential elution of particles. The flow was never interrupted for the entire duration of the experiment, as this could have led to increased retention. The protocols used for each particle injection are listed in Table 7-2. All column experiments were performed in duplicate and conducted on different days, confirming reproducibility. The breakthrough curves were expressed as the average value of duplicate runs.

Table 7-2 **Protocols of transport experiments used for each particle suspension expressed in number of PVs of injected suspension/solution.**

Particle	Pre-flush (Milli-Q)	Pre-conditioning (CMC)	Particle injection	Post-flush (Milli-Q)	Post-flush (CMC)
GR$_{SO4}$	8	-	6	3	-
S-nZVI	8	-	6	3	-
CMC-S-nZVI	8	5	6	-	3

At the end of each transport experiment, the columns were dissected into 8 fragments (containing approximately 2.5 g of sand) to assess the spatial distribution of the retained iron along the column length. The column segments were oven-dried at 70 ºC over-night, then weighed and acid digested in aqua regia (mixture of HCl 35 % v/v and HNO_3 65 % v/v) so that the deposited iron particles were dissolved. The total concentration of iron was measured by ICP-OES at a wavelength of 259.94 nm.

7.2.4.2 Experimental Set-Up for Magnetic Resonance Imaging (MRI)

Selected column experiments were additionally monitored by MRI to visualize the column interior and to investigate the particle transport behavior and preferential pathways in more detail. To conduct the MRI experiments, the same self-made column apparatus was used as for the breakthrough curve analysis. The injected concentrations of particle suspensions were equal to those of the breakthrough analysis experiments (0.1 and 0.5 g/L). It is important to note that the column apparatus as well as the porous media used as filling material in MRI measurements must not contain any magnetic material (such as iron). Prior to each experiment, the column was wet-packed inside the glovebox and pre-conditioned with degassed Milli-Q water and CMC solution. The column was then vertically positioned at the center MR tomograph. Figure 7-3 shows the experimental set-up used for the acquisition of MR images.
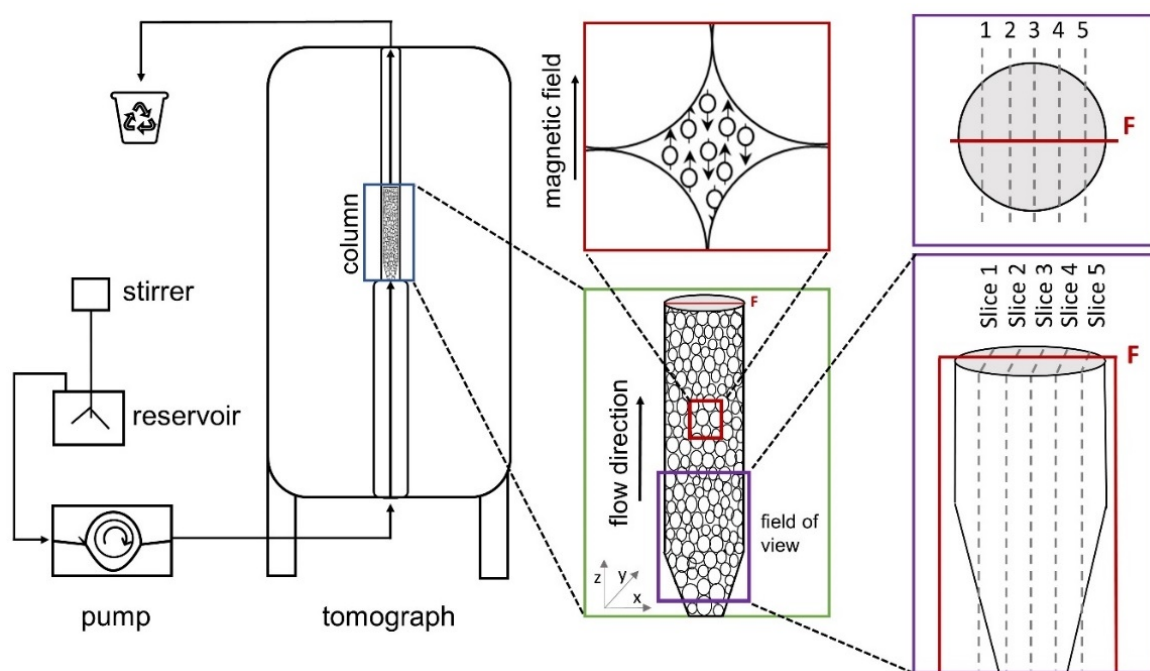
Figure 7-3   **Experimental set-up used for acquisition of MR column imaging during transport of iron nanoparticles in vertically positioned columns.**
The direction of the magnetic field, the flow direction and the field of view together with the position of the five sagittal slices (y-z plane) and the frontal (x-z) plane (F) are shown respectively in the red, green and violet rectangles.

During injection, the suspension was permanently stirred with an overhead stirrer and continuously pumped through the column using a peristaltic pump in up-flow mode to simulate saturated conditions.

MRI measurements were made for five sagittal slices of interest (slice 1, 2, 3, 4 and 5) of 2 mm thickness using the "rapid acquisition with relaxation enhancement" (RARE) method. The plane perpendicular to the sagittal slices was defined as the "frontal plane" (F). The field of view of the resulting images was 16 mm x 35 mm.

Measurements were performed at time intervals of 128 seconds. The intensity profile (I) of the signal for each of the five slices was normalized with the maximal intensity value (I_0) and studied as a function of the displacement (z) along the column direction (Figure 7-4). To determine the position of the particle front for each image, data points were fitted using the following Boltzmann function:

$$y(z) = \left\{ A \cdot \left[1 - \frac{1}{1+\exp[m \cdot (z-z_0)]} \right] + y_0 \right\}$$

Equation 7-4

where A is the amplitude of the function, y_0 represents an offset value, z_0 is the position of the inflection point of the curve and m describes the slope at the point z_0 (Figure 7-4). By modelling the data for each time interval, a more accurate description of MRI data was achieved. The calculated z_0 value was then subtracted from the entire length of the field of view (35 mm) to obtain the effective position of the particle front. The velocity at which the injected iron nanoparticles moved through the porous media was determined macroscopically by plotting the front position as function of time.

Model	Mono Boltzmann
Equation	$A*(1-(1/(1+\exp(m*(z-z_0)))))+y_0$
A	0.41554 ± 0.01183
Plot	I/I_0
z_0	31.67247 ± 0.15525
m	-0.37752 ± 0.01072
y_0	-0.08403 ± 0.01112
Reduced Chi-Sqr	$7.21085 \ 10^{-5}$
R-Square (COD)	0.99304
Adj. R-Square	0.99296
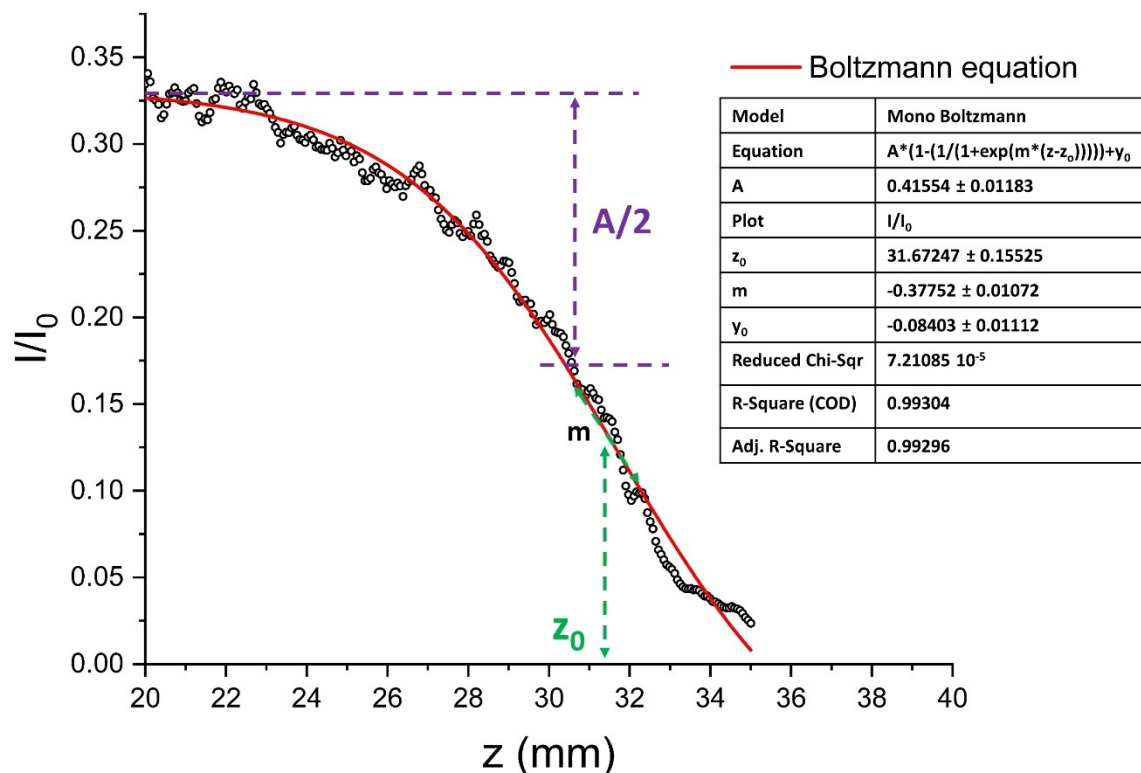
Figure 7-4   **Example of an MR intensity profile modelled using the Boltzmann equation.**
A is the amplitude of the function, y_0 is an offset value, z_0 is the position of the inflection point of the curve and m describes the slope at the point z_0.

7.3 Results and Discussions

7.3.1 Particle Characterization

The successful synthesis of GR$_{SO4}$, bare S-nZVI and 5-CMC-S-nZVI[post] was verified by XRD analysis; their respective XRD spectra are shown in Figure 6-3a, Figure 6-3b and Figure A-8. XRD spectra of S-nZVI and CMC-modified S-nZVI revealed the presence of Fe^0 and FeS peaks, and, as expected, did not show any indications for the presence of CMC. Figure 7-5 shows ESEM images of GR$_{SO4}$ particles, which consist of thin hexagonal plates with a size larger than 100 nm. This is in good agreement with the findings of Géhin *et al*. (2002), who also synthesized GR$_{SO4}$ with the co-precipitation method. TEM images of this referred study revealed regular hexagonal GR particles of different sizes varying from 300 to about 1000 nm and a thickness of between 30 and 80 nm.
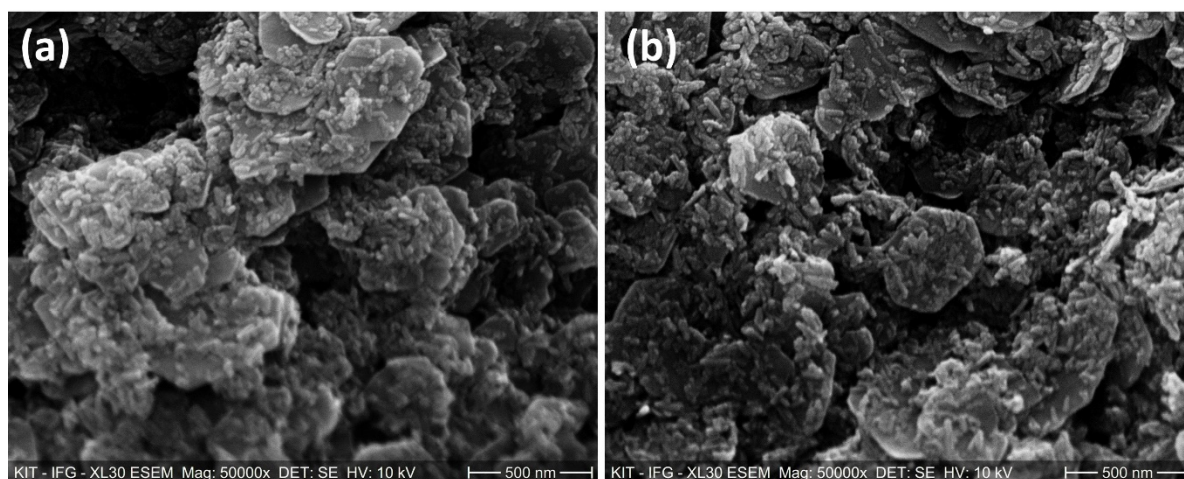
Figure 7-5   ESEM images (HV = 10 KV and Mag = 50 KX) of GR$_{SO4}$ crystals showing the hexagonal profile and particle sizes bigger than 100 nm.

SEM images of bare S-nZVI (a-c), CMC-S-nZVI[post] (d-f) and CMC-S-nZVI[pre] are shown in Figure 7-6. S-nZVI particles of all samples occurred mostly spherical and mainly in form of big agglomerates, which is in agreement with previous studies (Mangayayam et al., 2019b; Gong et al., 2020). The appearance of agglomerates in TEM or SEM images is very likely due to the sample preparation, which requires drying of the slurry and leads to higher magnetic attraction forces between nanoparticles (Cirtiu et al., 2011). Additional SEM images are shown in the Appendix from Figure A-9 to Figure A-18.

Bare S-nZVI

CMC-S-nZVIpost
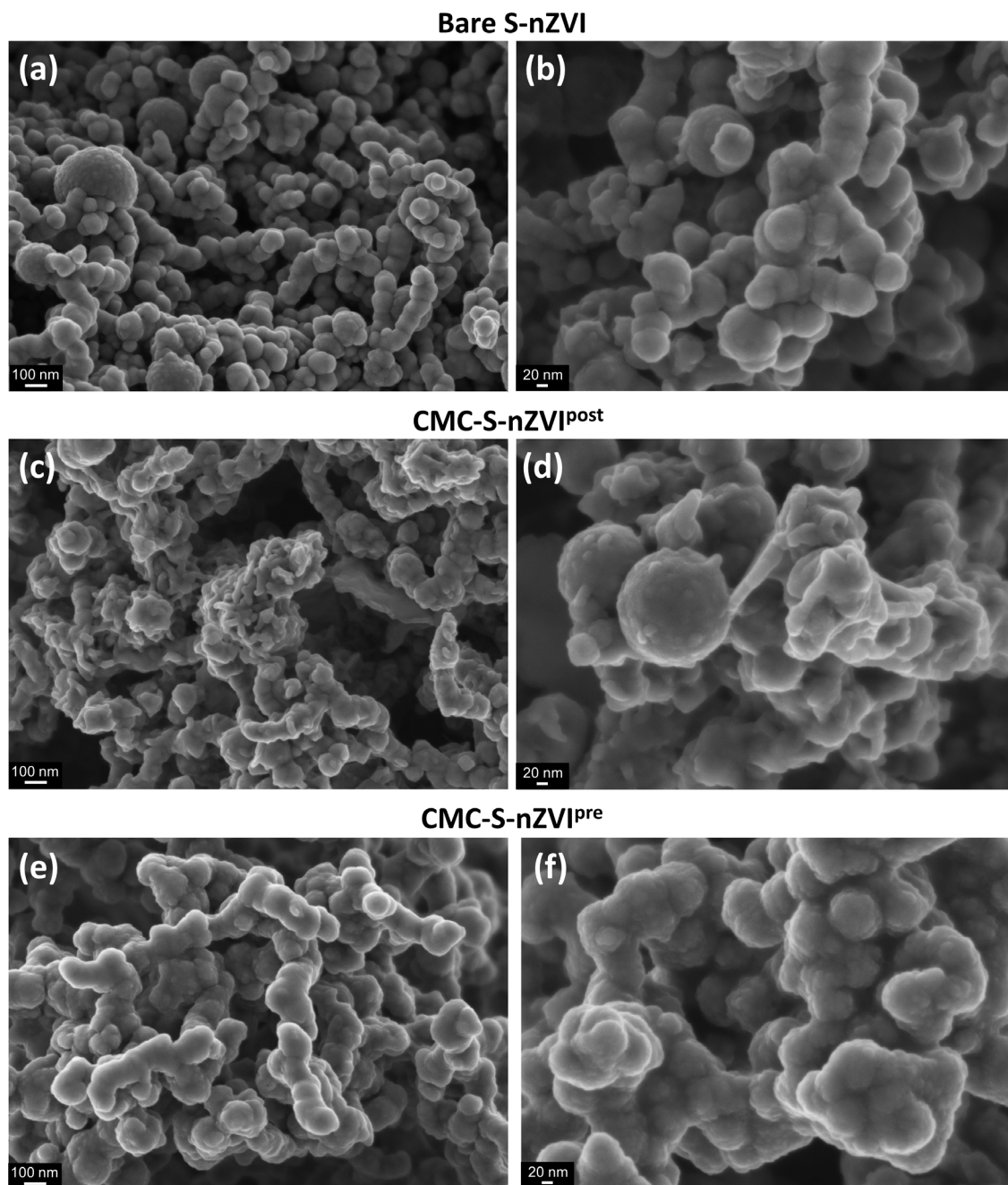
CMC-S-nZVIpre

Figure 7-6   **SEM images of (a-b) bare S-nZVI, (c-d) CMC-S-nZVIpost and (e-f) CMC-S-nZVIpre.**
EHT= 2.00 kV, Signal A = InLens, brightness = 49.8 %; aperture size = 20 µm, high
current = off with (a) WD = 1.6 mm, Mag = 50 KX, contrast 33.7 %; (b) WD = 2.5 mm,
Mag = 100 KX, contrast 32.4 %; (c) WD = 2.2 mm, Mag = 50 KX, contrast 32.3 %; (d)
WD = 2.2 mm, mag = 100 KX, contrast 32.3 %; (e) WD = 2.2 mm, Mag = 50 KX, contrast
32.4 %; (f) WD = 2.2 mm, mag = 100 KX, contrast 32.3 %.

The size, morphology, and spatial chemical composition of bare and CMC-modified S-nZVI were additionally characterized by TEM. Figure 7-7 shows the TEM images of bare S-nZVI (a-c), 5-CMC-S-nZVIpost (d-f) and 5-CMC-S-nZVIpre (g-i). Like for the SEM images, the TEM images exhibit S-nZVI particles organized in big aggregates with a chain-like structure due to the sample preparation.

Bare S-nZVI

CMC-S-nZVI^{post}
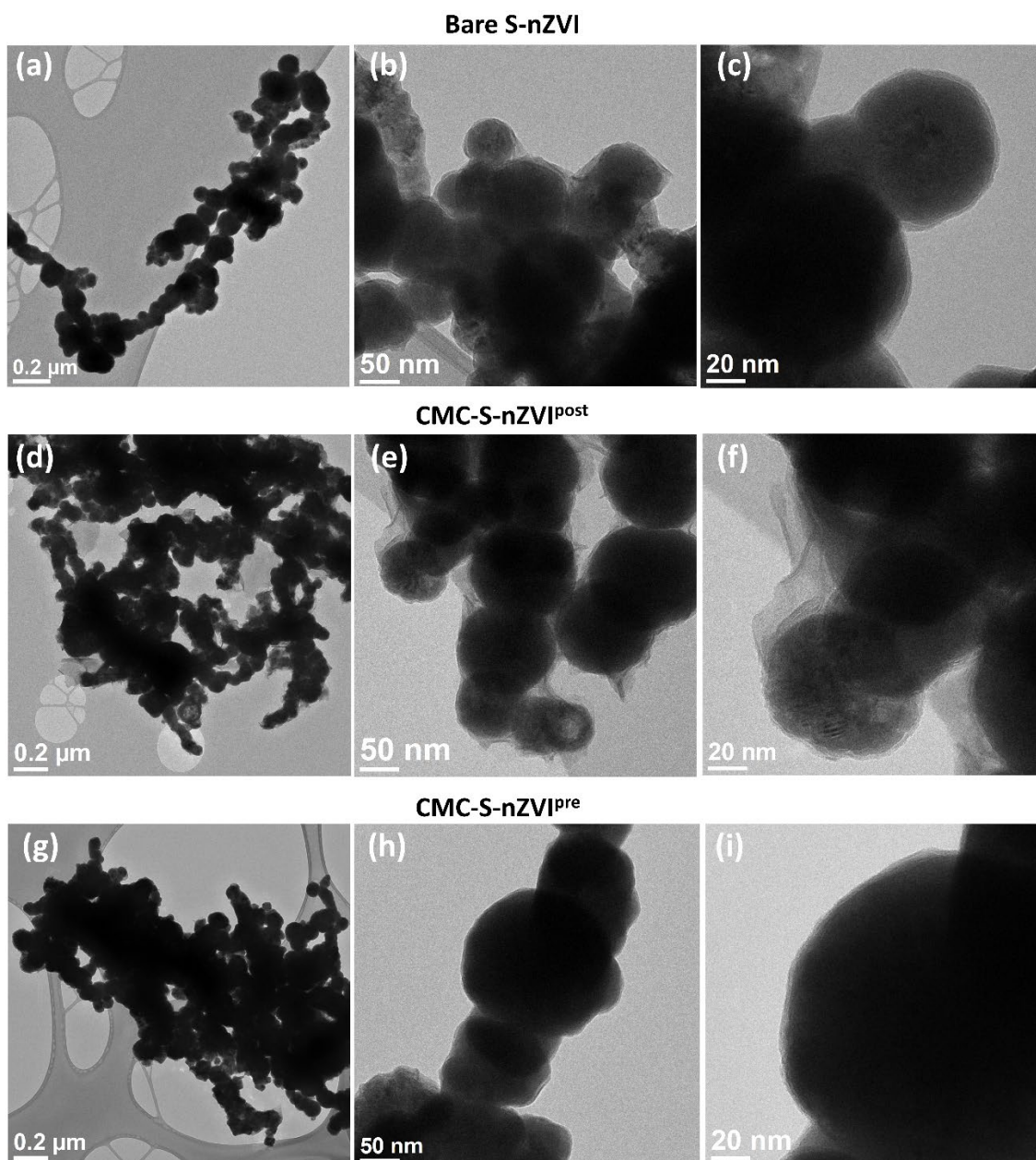
CMC-S-nZVI^{pre}

Figure 7-7 **TEM images of (a-c) bare S-nZVI, (d-f) CMC-S-nZVI^{post} and (g-i) CMC-S-nZVI^{pre}. (a-c) Mag = 22.5 KX, 105 KX and 260 KX; (d-f) Mag = 22.5 KX, 105 KX and 260 KX; (g-i) Mag = 18.5 KX, 105 KX and 260 KX.**

Particle size distribution analysis by TEM images was done on at least 250 nanoparticles of each S-nZVI type (Figure 7-8). The analysis revealed an average particle diameter of 95.5 ± 28.5 nm, 81.4 ± 24.4 nm and 110.5 ± 38.9 nm respectively for bare-S-nZVI, CMC-S-nZVI^{pre} and CMC-S-nZVI^{post}. It is important to note that the particle counting and size measurements were not affected by the chain-like arrangement, as they were performed manually. In some cases, the brightness/contrast/gamma of the TEM images was changed in order to distinguish the edges of the particles and to avoid that aggregated particles were considered as single particles. The results of the particle size distribution analysis indicate that bare S-nZVI and CMC-S-nZVI^{pre} are generally monodisperse, as the respective samples featured a unimodal distribution, while CMC-S-nZVI^{post} featured a more polydisperse particle population, as

suggested by the larger standard deviation. The results show that the pre-grafting method featured smaller S-nZVI particle sizes than bare S-nZVI. This was expected since the presence of a polymer usually results in the formation of smaller particles than without the presence of a polymer, as previously shown on Au and ZnO nanocrystals (Viswanatha and Sarma, 2007). On the other hand, the addition of CMC via the post-grafting method caused bigger particle sizes.
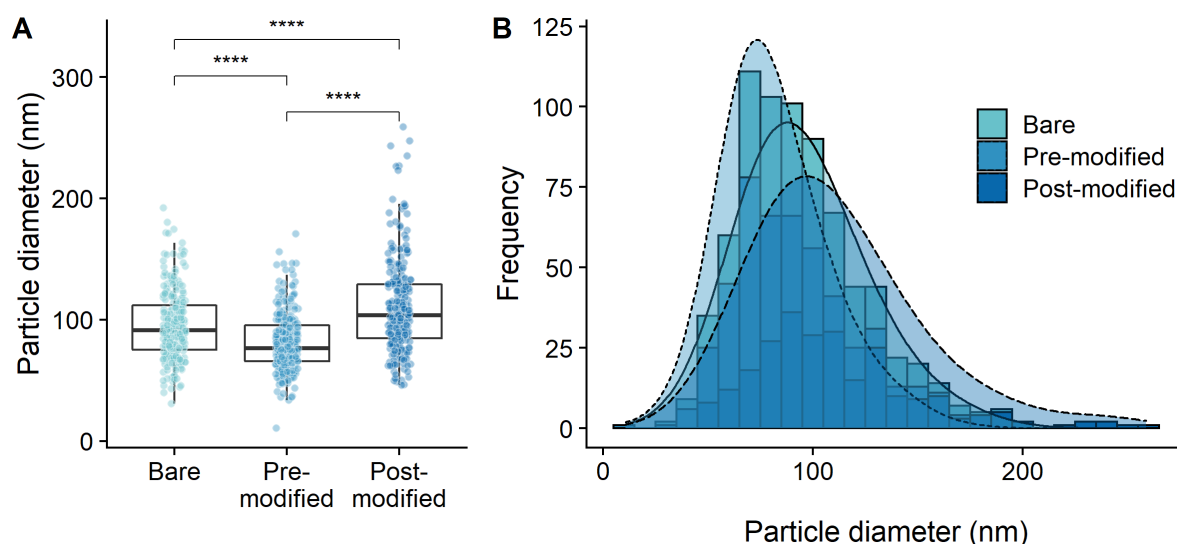
Figure 7-8 **Particle size distribution analysis by TEM images on bare and the two CMC-modified S-nZVI. A minimum of 250 particles were counted for each sample.**
(a) Box and whisker plots: the data points are plotted as circles, the 25th and 75th percentiles are bound by the boxes and the 10th and 90th percentiles are denoted by the whiskers. Single particle diameters can be summarized as: CMC-S-nZVIpre < bare S-nZVI < CMC-S-nZVIpost (** denotes p-value < 0.00001, Wilcoxon rank-sum test). (b) Distribution of the particle diameters of the three different S-nZVI particle types.**

STEM-EDX analyses (Table A-4) revealed that all synthesized S-nZVI types contained similar S/Fe ratios (Table A-5). EDX from blank areas (over a hole in the TEM grid) were also taken to show that the observed C signal intensities in the particles are real and not from adventitious C; there is also no detectable Fe, O and S signals (Figure A-19). In the TEM images, it is furthermore possible to observe the core-shell structure of the spherical S-nZVI particles, which consists of an electron dense iron core surrounded by a less electron dense FeS shell (Figure 7-9). The FeS shell of bare S-nZVI (Figure 7-9a) is around 5 nm thick and presents a sheet-like morphology with different crystal orientation and a d-spacing value of 5.2 ± 0.3 Å, which corresponds to the (001) lattice plane of mackinawite (Lennie et al., 1995). These findings are in agreement with previous studies (Mangayayam et al., 2019b). The FeS shell of CMC-S-nZVIpost was estimated to be > 6 nm thick and exhibits lattice fringes with d-spacing of 2.9 ± 0.3 Å (Figure 7-9b), which corresponds to the (101) lattice plane of mackinawite (Lennie et al., 1995). These findings suggest that via the post-grafting method, CMC was encapsulated into the FeS shell, which resulted in a slight increase in thickness. In case of CMC-S-nZVIpre, the FeS crystals curve around Fe^0 and exhibit a sheet-like morphology with better ordered FeS shells and about 5 nm thickness (Figure 7-9c). These findings indicate that the pre-grafting method affected the FeS structure.
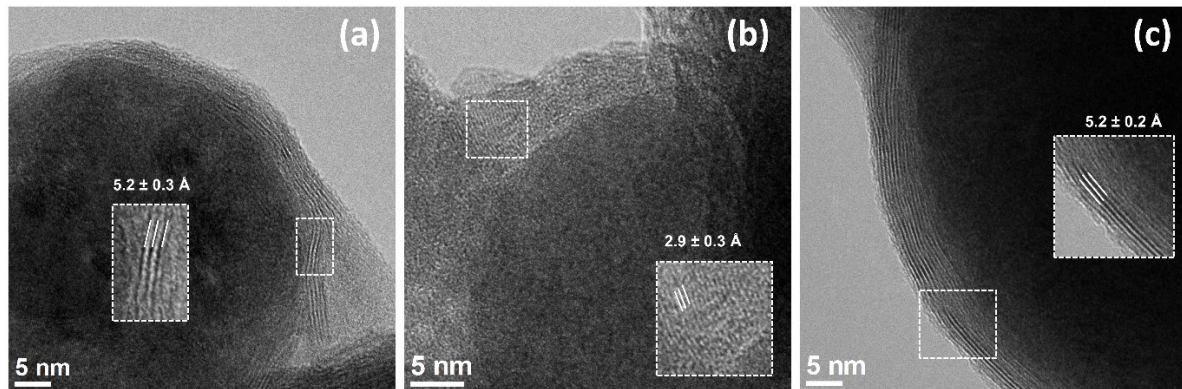
Figure 7-9   TEM images of the core-shell structure of (a) S-nZVI (Mag = 800 KX), (b) CMC-S-nZVI[post] (Mag = 1250 KX) and (c) CMC-S-nZVI[pre] (Mag = 800 KX).
The isolated areas in each picture show the FeS crystal orientation, which corresponds to lattice fringes with *d*-spacing of 5.2 ± 0.3 Å and 2.9 ± 0.3 Å consistent with (001) and (101) lattice plane, respectively.

7.3.2 Effect of CMC Modification on S-nZVI Colloidal Stability: Sedimentation Tests

Figure 7-10 shows the development of the normalized absorption (Abs/Abs_0) of bare S-nZVI, CMC-S-nZVI[pre] and CMC-S-nZVI[post] particle suspensions (0.125 g/L particle concentration) during the sedimentation tests. Normalized absorption values close to 1 indicate a high colloidal stability of the S-nZVI suspension. All tested S-nZVI suspensions treated with CMC were expected to behave like non-Newtonian fluids, since the CMC concentrations (1-5 g/L) used for the experiments exceeded the so-called overlap concentration (c^*), which was estimated by Lopez *et al.* (2014) to be equal to 0.07 g/L. As shown in Figure 7-10, the CMC-modified S-nZVI particles show a much higher colloidal stability compared to bare S-nZVI, which settles fastest. However, CMC-S-nZVI[pre] exhibits a significantly lower stability than the CMC-S-nZVI[post] samples. Specifically: (i) suspension stability of bare S-nZVI is very low, as rapid settling (t_{50}) occurred within approximately 4 min and complete settling (t_{sed}) in 22 min ($v_{s,50}$ of 5 mm/min), (ii) 5-CMC-S-nZVI[pre] reached complete settling in around 42 minutes ($v_{s,50}$ of 1.7 mm/min), (iii) none of the CMC-S-nZVI[post] suspensions achieved complete settling within 60 minutes of the experiment.
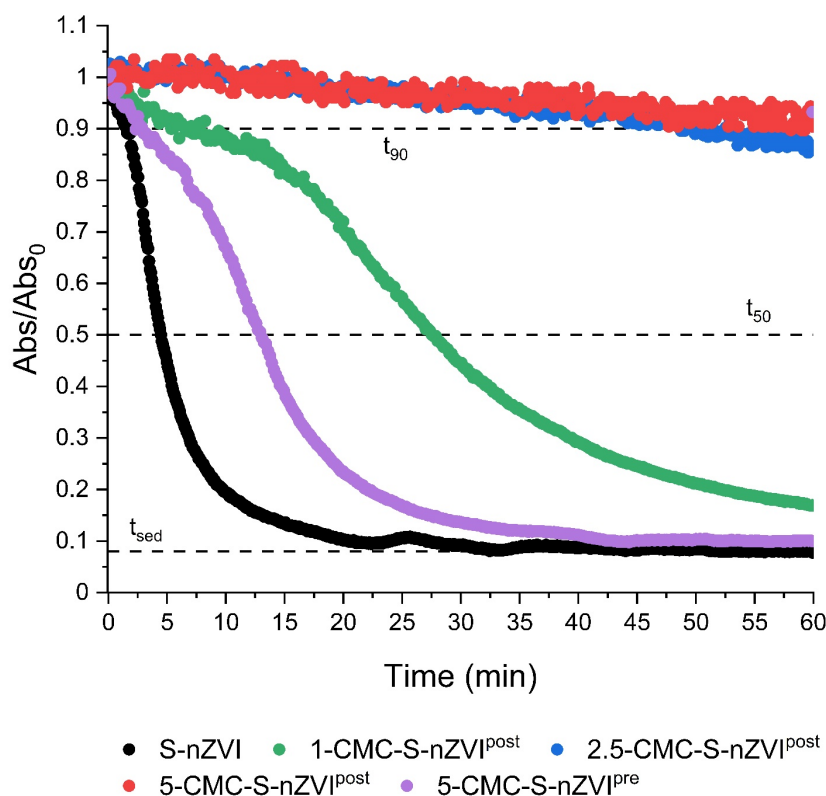
Figure 7-10   **Sedimentation curves for bare S-nZVI, 5-CMC-S-nZVI[pre], 1-CMC-S-nZVI[post], 2.5-CMC-S-nZVI[post] and 5-CMC-S-nZVI[post].**
Normalized absorption values close to 1 indicate a high colloidal stability of the S-nZVI suspension. The dotted lines indicate the sedimentation time (t_{sed}) and the time required to reach 50 % (t_{50}) and 90 % (t_{90}) of the initial absorbance value.

The settlement times, the calculated stability times (t_{50} and t_{90}), the settling velocities ($v_{s,50}$ and $v_{s,90}$) and the share rates (γ_{50} and γ_{90}) for the tested S-nZVI suspensions are listed in Table 7-3. d_{stokes} values correspond to d_p values estimated by measuring the single particle diameter on the TEM images (d_p bare S-nZVI = 95.5 nm, d_p CMC-S-nZVI[post] = 110.5 nm and d_p CMC-S-nZVI[pre] = 81.4 nm).

The decrease in absorbance over time is the result of the agglomeration and settlement of bigger and heavier particle aggregates. The faster the settlement, the lower the colloidal stability. The interaction between particles is one of the key factors that determines the stability of a suspension. Generally, colloidal stability is the result of the sum of the interparticle interaction forces involving magnetic, van der Waals, electrostatic and steric forces, where the former two forces lead to attraction between two particles, while the latter two forces counteract this attraction and are responsible for repulsion (Phenrat et al., 2008). In previous studies, it was shown that surface modification of non-sulfidized nZVI via the post-grafting method provides an adsorbed layer of modifier, which is responsible for steric repulsive forces that inhibit the aggregation of particles (Phenrat et al., 2008; Kim et al., 2009). The findings of this thesis show that a similar process occurred via the modification of sulfidized nZVI. The comparison of the sedimentation profiles for the both CMC-S-nZVI[post] samples shows that the suspension stability of post-grafted particles increased with increasing the CMC concentration from 1 to 5 g/L. Specifically,

after 60 minutes, the normalized absorption values are equal to 0.17, 0.86 and 0.93 for 1-CMC-S-nZVI^{post}, 2.5-CMC-S-nZVI^{post}, 5-CMC-S-nZVI^{post} respectively, confirming that the higher the CMC concentration, the higher the colloidal stability. The same trend can also be seen in the values for the sedimentation time t_{90} (Figure 7-11a) and the settling velocity $v_{s,90}$ (Figure 7-11b). This behavior can be explained by the fact that a lower polymer concentration lead to a thinner or irregular surface coverage of S-nZVI by CMC molecules, providing less steric repulsive forces.

Table 7-3 Stability times (t_{50}, t_{90}) and settling velocity (v_s) of bare S-nZVI (d_{Stokes} = 95.5 nm), 5-CMC-S-nZVI^{pre} (d_{Stokes} = 81.4 nm), 1-CMC-S-nZVI^{post}, 2.5-CMC-S-nZVI^{post}, 5-CMC-S-nZVI^{post} (d_{Stokes} = 110.5 nm).
$v_{s,50}$, γ_{50}, $v_{s,90}$ and γ_{90} were calculated with t_{50} and t_{90} defined as the time required to reach 50 % and 90 % of the initial absorbance.

Sample type	Complete settling (min)	t_{50} (min)	$v_{s,50}$ (mm/min)	γ_{50} (min^{-1})	t_{90} (min)	$v_{s,90}$ (mm/min)	γ_{90} (min^{-1})
S-nZVI	22	4.5	5	28.8	1.5	14.8	86.1
5-CMC-S-nZVI^{pre}	42	12.9	1.7	11.9	2.9	7.9	53.9
1-CMC-S-nZVI^{post}	> 60	27.5	0.8	4.1	8.2	2.7	13.8
2.5-CMC-S-nZVI^{post}	> 60	> 60	-	-	50	0.5	2.3
5-CMC-S-nZVI^{post}	> 60	> 60	-	-	~ 60	0.4	1.9

Compared to 5-CMC-S-nZVI^{post}, 5-CMC-S-nZVI^{pre} settled at least 20 times faster (Table 7-3), suggesting that the pre-grafting method is not as effective as the post-grafting counterpart in providing repulsive forces. As a fraction of CMC is adsorbed onto the S-nZVI surface in the post-grafting method, the fluid viscosity of the resulting suspension results to be lower due to a decrease in free polymer concentration, promoting injection into porous media. Cirtiu *et al.* (2011), who modified non-sulfidized nZVI particles and compared the efficiency of the two grafting methods, observed an opposite trend. They showed that colloidal stability of pre-grafted nZVI was around 1.3 higher than the post-grafted counterpart. The different outcomes indicate that, despite the very similar structure of nZVI and S-nZVI, the presence of FeS layers and hence a slightly different surface chemistry might be responsible for a different adsorption behavior of the polymer. Moreover, Cirtiu *et al.* (2011) post-modified nZVI by mixing the nanoparticles with a polymer solution (0.5 % v/v CMC) for 30 minutes, while the post-grafting method used in this study consisted of shaking the suspensions for 3 hours.
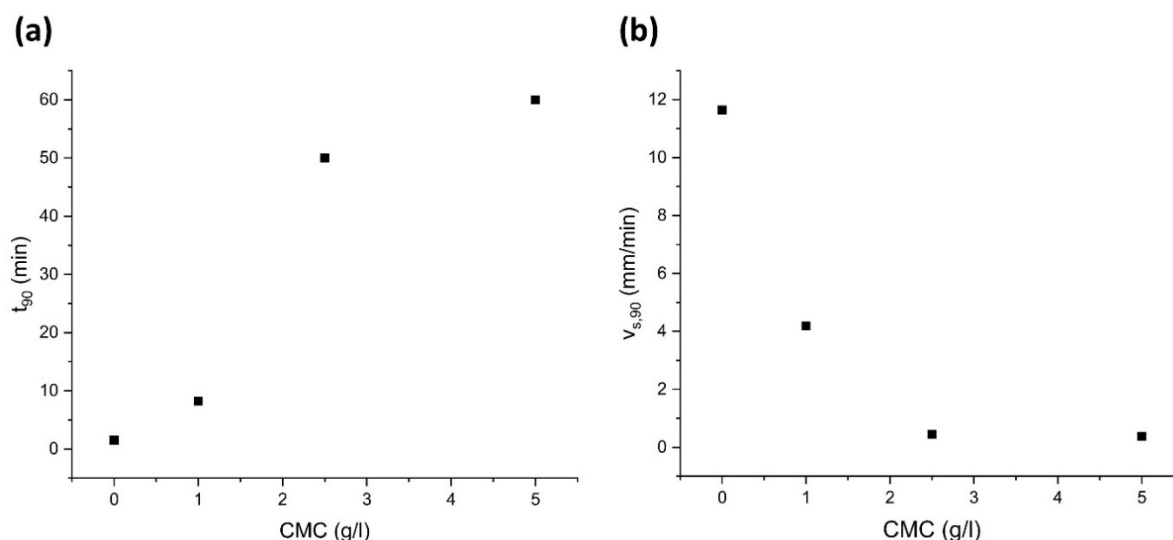
Figure 7-11 **Dependency of the (a) sedimentation time (t$_{90}$) and (b) settling velocity (v$_{s,90}$) on the CMC concentration for bare S-nZVI, 1-CMC-S-nZVI^{post}, 2.5-CMC-S-nZVI^{post} and 5-CMC-S-nZVI^{post}.**

Additionally, the influence of CMC modification on the sedimentation behavior of S-nZVI was also tested by visual observation and evaluation of the particle stability in suspension. Figure 7-12 shows a time series of photographs taken from sealed vials of undisturbed S-nZVI suspension that confirm the above described results.
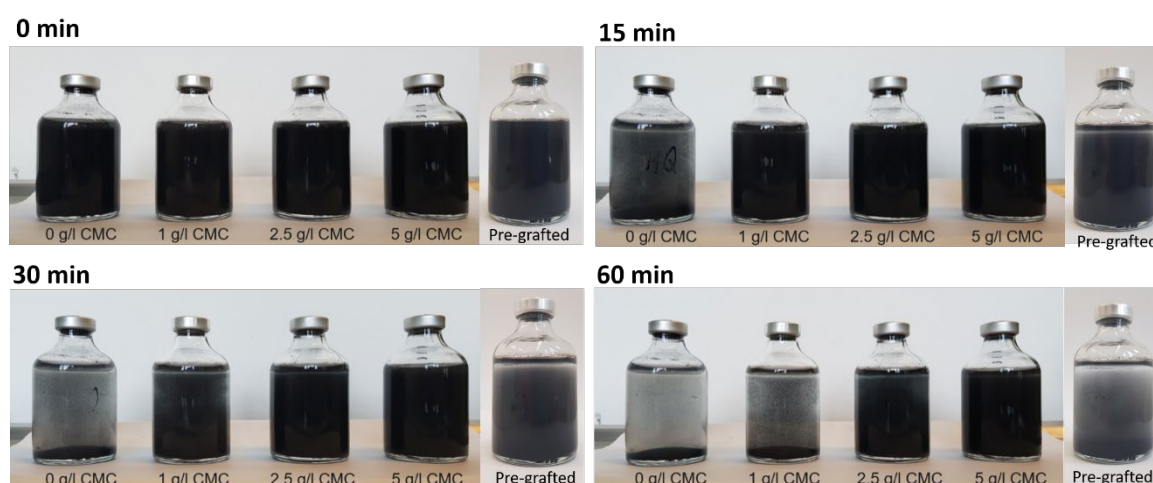
Figure 7-12 **Qualitatively visual evaluation of the sedimentation behavior of bare S-nZVI (no CMC), CMC-S-nZVI^{post} (1, 2.5 and 5 g/L CMC concentration) and CMC-S-nZVI^{pre}.**
The particle concentration used for each suspension is equal to 0.5 g/L. The photographs were taken at time 0, 15, 30 and 60 min.

7.3.3 Effect of CMC Modification on S-nZVI Surface Charge: ζ-Potential Measurements

ζ-potential values of bare S-nZVI, CMC-S-nZVI^{pre} and CMC-S-nZVI^{post} were obtained from EPM conducted by titration tests (pH 4-10) at room temperature (Table 7-4). The pH of the freshly prepared S-nZVI suspensions (bare and CMC-modified) was 8.7±0.7. Comparable ζ-potential values were

obtained at particle concentrations of 0.1 and 0.5 g/L, confirming that particle surface charge is not affected by the particle concentrations in suspension (Table 7-4).

Table 7-4 ζ-potential values (mV) of a pure CMC suspension without S-nZVI, bare S-nZVI (0 g/L CMC), 2.5-CMC-S-nZVI[post] and 5-CMC-S-nZVI[post] during titration tests.

Particles	Particle concentration (g/L)	CMC concentration (g/L)	pH	ζ-potential (mV)
-	-	1	7.3 ± 0.1	-59.8 ± 2.9
		2.5	7.3 ± 0.1	-62.5 ± 4.8
		5	7.6 ± 0.4	-52.9 ± 4.6
Bare S-nZVI	0.1	0	8.4 ± 0.3	-32.0 ± 9.9
			7.4 ± 0.2	9.2 ± 2.3
			7.3 ± 0.1	11.7 ± 3.8
			7.1 ± 0.1	16.4 ± 1.4
2.5-CMC-S-nZVI[post]	0.1	2.5	9.6 ± 0.1	-67.4 ± 2.0
			8.1 ± 0.1	-69.5 ± 2.1
			6.9 ± 0.1	-69.9 ± 1.7
			5.6 ± 0.2	-59.0 ± 1.7
			5.0 ± 0.1	-46.0 ± 1.3
			4.3 ± 0.1	-34.5 ± 1.4
5-CMC-S-nZVI[post]	0.1	5	9.7 ± 0.1	-97.5 ± 3.1
			9.5 ± 0.2	-92.1 ± 4.5
			8.8 ± 0.2	-88.7 ± 2.8
			8.3 ± 0.1	-85.3 ± 2.5
			7.0 ± 0.2	-82.5 ± 1.4
			4.3 ± 0.1	-52.6 ± 3.1
5-CMC-S-nZVI[post]	0.5	5	9.8 ± 0.1	-97.8 ± 6.3
			8.1 ± 0.2	-87.2 ± 5.8
			6.5 ± 0.2	-75.8 ± 10.7
			5.2 ± 0.1	-60.3 ± 4.1
5-CMC-S-nZVI[pre]	0.5	5	9.0 ± 0.1	39.7 ± 2.1
			8.2 ± 0.1	20.6 ± 2.1
			7.1 ± 0.2	-5.1 ± 4.4
			6.1 ± 0.1	-11.1 ± 2.6

A ζ-potential of -32.0 mV was measured for bare S-nZVI at a pH of 8.4. The titration to lower pH values resulted in a change to positive ζ-potential values with a point of zero charge (pzc) at around $pH_{pzc} = 7.6$ (Figure 7-13). CMC-S-nZVI[pre] showed the opposite trend with a positive ζ-potential value equal to 20.6 (mV) at pH of 8.2, while negative ζ-potentials were obtained via decreasing the pH ($pH_{pzc} = \sim7.2$). In contrast, CMC-S-nZVI[post] showed to carry negative charges over the entire tested pH range (pH between 4 and 10) with the absolute ζ-potential values also being much higher. The large negative values of CMC-S-nZVI[post] imply highly charged particles, which prevent aggregation between particles due to electric repulsion. These results explain the better physical stability of CMC-S-nZVI[post] compared to the pre-grafted counterpart and the non-modified S-nZVI, observed in the sedimentation studies (Figure 7-10 and Figure 7-11). Indeed, higher absolute ζ-potential values of below -30 mV or above +30 mV is considered to provide sufficient repulsive force to achieve better physical colloidal stability (Samimi et

al., 2019). On the other hand, the lower the ζ-potential, the higher the attraction forces (i.e., van der Waals) between particles, which are responsible for formation of chain-like aggregates and favor rapid gravitational sedimentation, leading to physical instability (Samimi et al., 2019).

These findings confirm that in the case of CMC-S-nZVI^{post}, the negatively charged CMC (average value of -58.1 mV at neutral pH conditions, Table 7-4), was successfully bonded onto the S-nZVI particles. Moreover, the absolute ζ-potential values decreased with decreasing CMC concentration from 5 to 2.5 g/L. This can be explained by the fact that, at lower CMC concentration, the polymer surface coverage was either partial, irregular or thinner than for higher concentration as the magnitude of "electrosteric" repulsion (combination of steric and electrostatic forces that counterbalance van der Walls and electromagnetic forces) between particles depends on the adsorbed polymer layer (Phenrat et al., 2008). Also these results are consistent with the colloidal stability results, which showed that the higher the polymer concentration, the higher the stability of S-nZVI in suspension.
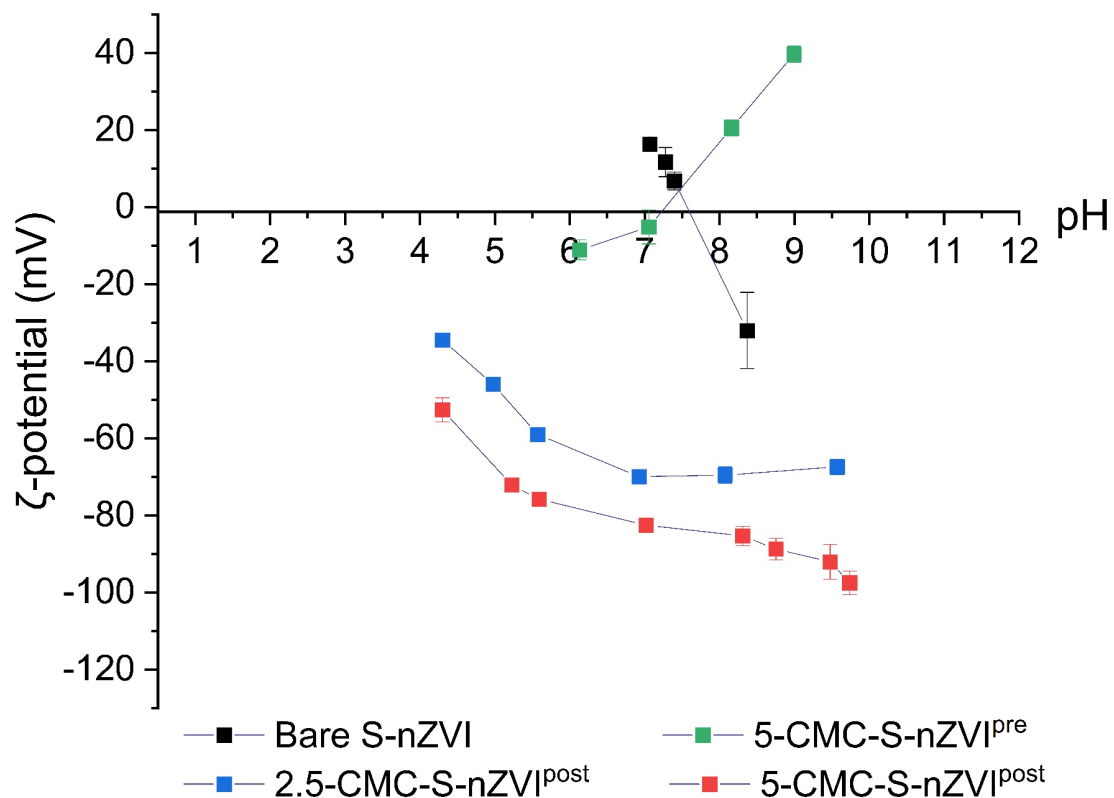
Figure 7-13 **ζ-potential dependency on CMC concentration and pH for bare S-nZVI (0 g/L CMC), 5-CMC-S-nZVI^{pre}, 2.5-CMC-S-nZVI^{post} and 5-CMC-S-nZVI^{post} during titration tests. Particle concentration of 0.1 g/L was used for bare S-nZVI and CMC-S-nZVI^{post}, and 0.5 g/L for CMC-S-nZVI^{pre}.**

Knowing the ζ-potential of the particles in suspension not only helps to understand the particle-particle interactions, but also allows to predict the interactions between the particles and a collector, thus also their behavior in porous media. Particle-particle and particle-collector interactions play a complementary role in the overall particle transport behavior in porous media. Since at typical natural

pH conditions (range of 4-9) quartz sand particles as well as silicate minerals are negatively charged (pH$_{pzc}$ = ~2.4) (Jada et al., 2006), at neutral conditions electrostatic forces between nanoparticles and the silica collector are expected to be attractive in the case of bare S-nZVI and lightly repulsive in the case of CMC-S-nZVI^{pre} (positively charged at pH > ~ 7.2). In the case of CMC-S-nZVI^{post}, the forces will be repulsive over the entire pH range as they constantly carry negative charges.

7.3.4 Transport Column Studies

7.3.4.1 Mobility of GR$_{SO4}$

Column experiments were performed to evaluate the transport behavior of GR$_{SO4}$ particles in porous media. Although low particle concentrations were used for injection (0.1 g/L), complete attachment of particles was observed shortly after the start of the injection in the first millimeters of the inlet point combined with negligible particle elution. This was a clear indication for the lack of mobility and complete attachment of the GR$_{SO4}$ particles onto the collector surface and/or their aggregation in the pore space. Moreover, further injection blocked the inlet port of the column, increasing the pressure until the flow was completely stopped.

The very low mobility of GR$_{SO4}$ particles through the voids of the porous medium can be ascribed to the crystal sizes and hexagonal shape of GR$_{SO4}$ (Figure 7-5). As it was shown by Guilbaud et al., (2013), the thickness of hexagonal plates of GR$_{SO4}$ is much smaller than the particle diameter, due to anisotropic crystal growth. With diameters varying between 300 and 1000 nm, the width of GR$_{SO4}$ crystals is typically 10 times bigger than their thickness (Géhin et al., 2002). Thus, the morphology of GR$_{SO4}$ particles differs very much from that of a spherical particle, which has an ideal mobility potential. Indeed, Liu et al., (2010) and Seymour et al., (2013) showed that non-spherical particles (e.g., rod-shaped with high aspect ratio or plate-like) easily aggregate and get entrapped within the pores, negatively affecting their transport. Therefore, crystal shape and crystal size are very likely responsible for straining phenomena (Chapter 3.4.2).

As shown by Guilbaud et al., 2013, the surface of sulfate green rust is positively charged at pH < 8.3, while quartz grains, like all silicate-based minerals, are typically negatively charged due to the deprotonation of silanol (Si-OH) surface groups (Jada et al., 2006; Bayat et al., 2015). Therefore, another factor that significantly reduces particle mobility is related to the opposite surface charges of GR$_{SO4}$ and quartz sand. Under these conditions, particle-collector interaction forces are strong, leading to attraction of particles on the collector surface. For this reason, neutral pH settings of subsurface environments provide unfavorable conditions for the mobility of GR$_{SO4}$ through a porous medium consisting of quartz and/or silicate minerals. However, at same environmental conditions immobilization of anions such as chromate is enhanced (as shown in Chapter 6) due to the positive surface charge of GR, which is the reason why GR$_{SO4}$ is still considered a promising material for

environmental *in-situ* applications. Figure 7-14 shows a schematic representation of the possible retention scenarios that can occur during GR$_{SO4}$ transport.

GR$_{SO4}$ mobility could be enhanced by decreasing the particle size. This can be achieved, for example, by substituting a part of the Fe(III) amount with divalent or trivalent cations during the synthesis procedure, which results in the formation of smaller GR crystals (Ruby et al., 2010). However, it is important to note that having smaller particles might not be enough to increase the mobility potential, as the particle surface charge plays an important role. Therefore, particle surface should also be modified in order to obtain negative surface charges and to create more favorable conditions for transport in subsurface environment. However, in this case the reactivity of GR$_{SO4}$ toward certain contaminants can no longer be guaranteed.
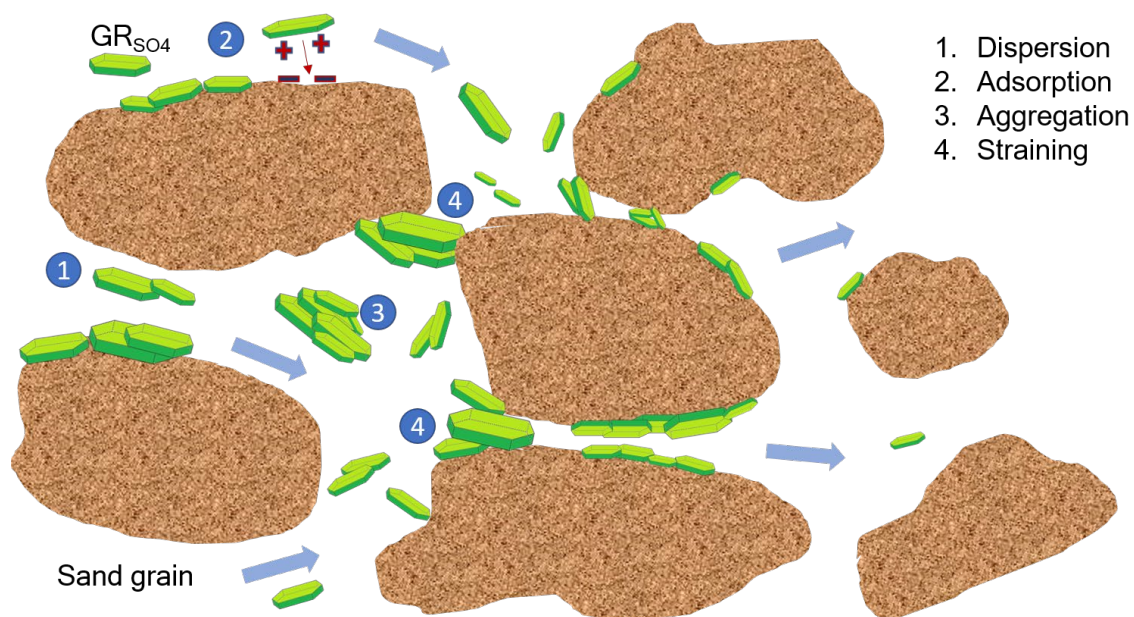
Figure 7-14   Schematic representation of transport and retention scenarios that might occur during GR$_{SO4}$ injection (modified after Liu et al. 2019).

7.3.4.2 Mobility of S-nZVI

i   Effects of CMC

Suspensions containing 0.5 g/L of bare S-nZVI, 5-CMC-S-nZVI^{pre}, 2.5-CMC-nZVI^{post} and 5-CMC-nZVI^{post} particles were injected within a sandy porous matrix at flow rates of 0.5, 1 and 2 mL/min. The prior tested NaNO$_3$ solution was eluted entirely after injection of 1 PV, exhibiting a conservative tracer-like behavior (Figure 7-15). This ensured homogeneous column packing, which will not interfere the particle mobility. The pore volume and the porosity of the column are equal to 7.5 mL and 44 %, while flow rates of 0.5, 1 and 2 mL/min resulted to be equal to pore water velocities of $1.73 \cdot 10^{-4}$, $3.48 \cdot 10^{-4}$ and $6.94 \cdot 10^{-4}$ m/s (i.e., 0.017, 0.035 and 0.070 cm/s), respectively. Injection of bare S-nZVI and 5-CMC-S-nZVI^{pre} resulted in negligible transport (with less than 1 % effluent particle concentration), with most of the particles deposited within the first few millimeters of the sand column,

while mobility of CMC-S-nZVI^{post} particles resulted to be significantly enhanced. Although the post-grafting method featured bigger particle sizes (~ 110.5 nm) compared to the bare (~ 95.5 nm) and the pre-grafted S-nZVI (~ 81.4 nm), CMC-S-ZVI^{post} has shown a significantly better transport behavior compared to the others. According to the DLVO theory, the decrease of particle size yields to higher chance of collision between particles and porous media, resulting to higher chance of attachment to the collector, thus, to higher retention. Furthermore, it is important to note that previous attempts of injecting CMC-S-nZVI particles in saturated packed columns without the pre-conditioning step with CMC have shown very low particle mobility. These findings reveal that CMC pre-conditioning of the sand matrix is a necessary step to ensure higher mobility through the pores of the sand matrix, as the CMC molecules provide a steric hindrance for the approach of the particles to the sand grains.
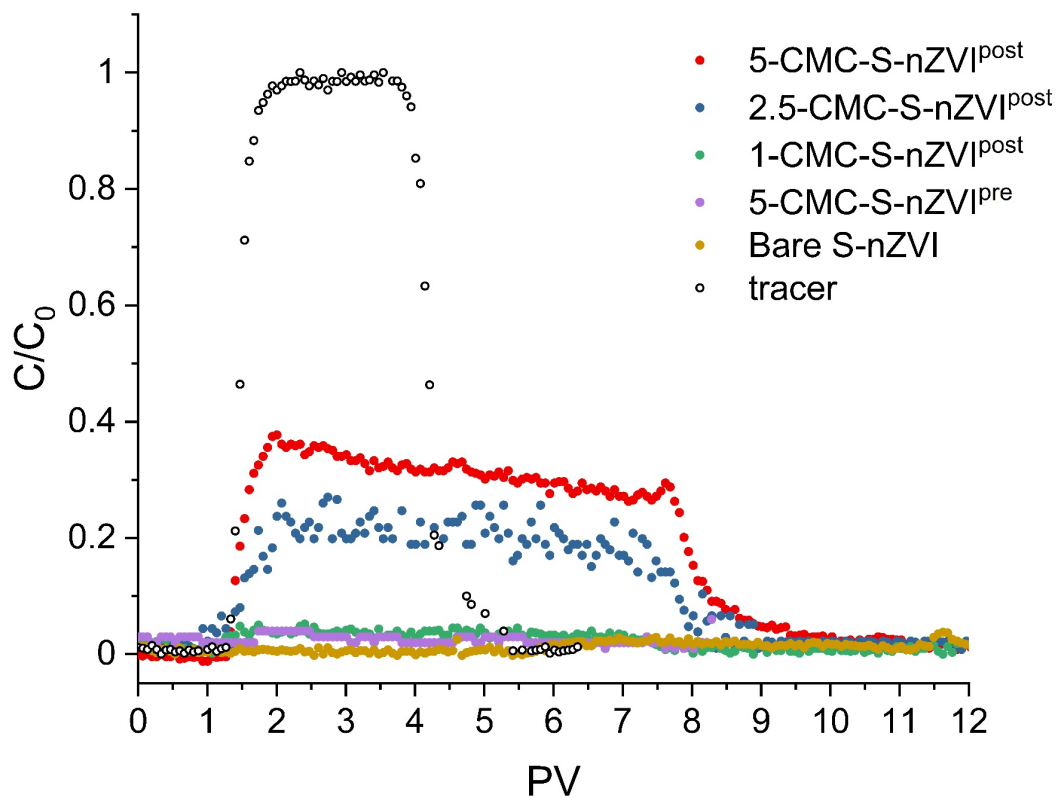
Figure 7-15 **Experimental BTCs obtained after injection of 0.5 g/L of bare S-nZVI, 5-CMC-S-nZVI^{pre},**
1-CMC-S-nZVI^{post}, 2.5-CMC-S-nZVI^{post} and 5-CMC-S-nZVI^{post} at 0.035 cm/s
BTC of the non-reactive tracer test is also shown.

The very low particle elution of bare S-nZVI and 5-CMC-S-nZVI^{pre}, which indicates their complete retention in the column, can furthermore be attributed to their rather low surface charge at neutral pH conditions and thus to the absence of electric repulsion forces that would prevent attachment/adsorption on the sand grains. Moreover, due to the strong interactions with the porous medium surfaces, the particles adhered irreversibly (i.e., no detachment) to the solid surface even after the post-flushing step of the system.

The BTCs of CMC-S-nZVI^{post} reveal a decrease from ~ 35 % to ~ 20 % and < 1 % when the CMC concentration was decreased from 5 to 2.5 and 1 g/L, respectively (Figure 7-15). The negligible particle elution of 1-CMC-S-nZVI^{post} indicated that in this case similar particle retention mechanisms occurred as described for bare S-nZVI and CMC-S-nZVI^{pre}. The higher the CMC/S-nZVI ratio, the higher the eluted particle concentrations, hence, the reduced the attachment capacity of the porous medium. This can be ascribed to the fact that the presence of higher amounts of CMC ensure a better polymer coverage, which helps to break up the aggregates that might form during particle synthesis. The improved transport behavior of CMC-S-nZVI^{post} compared to bare S-nZVI and CMC-S-nZVI^{pre} can be explained by the presence of the anionic CMC layer around the sulfidized particle, which provided a high negative surface charge and prevented particle aggregation. In addition, the adsorbed polymer layer around S-nZVI, together with the CMC molecules in the pre-flushed system, reduces the attractive forces between the S-nZVI particles and the quartz sand, resulting in higher particle quantities exiting the column.

Table 7-5 **Mass of Fe (mg) and percentage of Fe (%) retained within the column after CMC-post flushing, fragmentation and digestion of the solid material within the column. The injected Fe (mg) is obtained from the measured concentration of Fe (mg/L) in the injected slurry (6 PVs) containing various CMC concentrations. w$_{Fe}$ is the average Fe mass fraction in the column.**

Particle type	Fe concentration (g/L)	CMC concentration (g/L)	Injection velocity (mL/min)	Injected iron (mg)	Retained iron (mg)	Retained iron (%)	w$_{Fe}$ (mg/g)
CMC-S-nZVI^{post}	0.476	2.5	1	21.4	15.8	73.8	0.78
CMC-S-nZVI^{post}	0.778	5	0.5	35.0	28.0	80.0	1.49
CMC-S-nZVI^{post}	0.473	5	1	21.3	13.4	62.9	0.67
CMC-S-nZVI^{post}	0.227	5	2	10.2	2.37	23.3	0.12

The results from mass balance calculations shown in Table 7-5 indicate that the amount of iron retained in the column increased with decreasing CMC concentrations used to stabilize S-nZVI. Approximately 63 % and 74 % of the iron contained in the injected suspension of respectively 5-CMC-S-nZVI^{post} and 2.5-CMC-S-nZVI^{post} did not exit the packed column, proving that higher CMC concentrations enhance the mobility of S-nZVI within the column. This is supported by the retention profiles obtained after column dissection and acid digestions of the solid materials. These results provide information on the spatial distribution of iron (hence the injected iron-particles) within the column after post-flushing (Figure 7-16). Compared to the 2.5-CMC-S-nZVI^{post} profile, which shows that almost all irreversibly retained iron is located in the first centimeter of the column, 5-CMC-S-nZVI^{post} particles were more spread over the entire length of the column, proving that these particles were capable to move over longer distances. The small fraction of released particles during the post-flushing indicates that the majority of the particles are adsorbed/attached irreversibly on the collector surfaces and only a small amount of particles is carried away with the eluent flow. This can also be seen in the tail of the BTCs

at 8 PVs, suggesting that partial particle detachment from the grain surface has occurred (Raychoudhury et al., 2014).
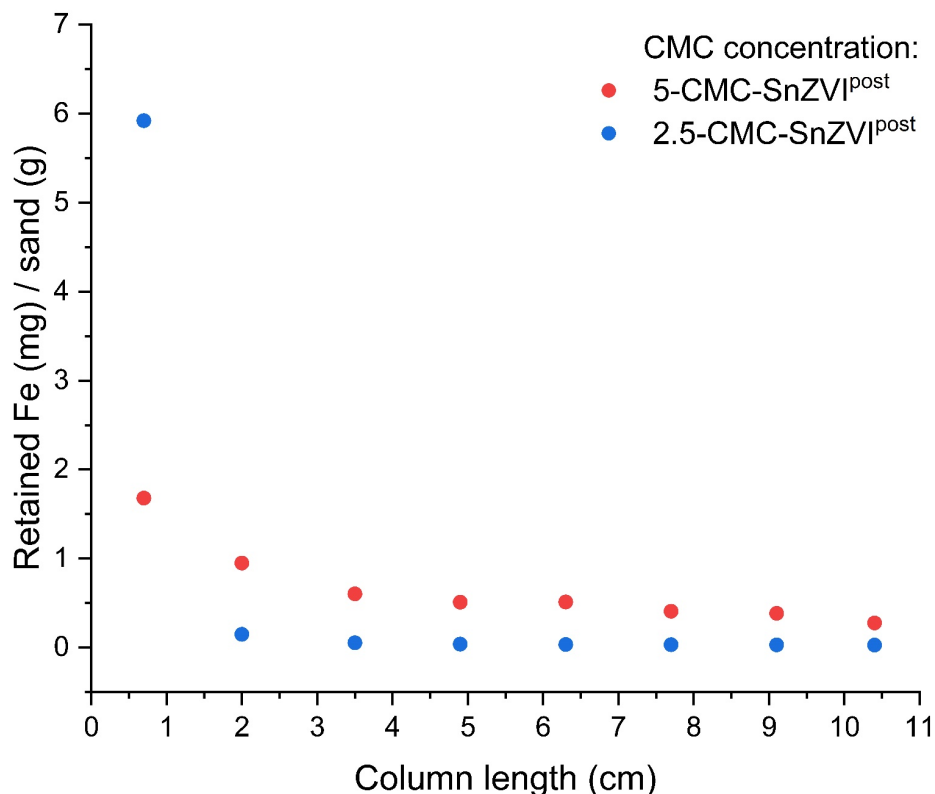
Figure 7-16 **Retention profiles of 5-CMC-S-nZVI[post] and 2.5-CMC-S-nZVI[post].**

In the case of 2.5-CMC-S-nZVI[post] and 5-CMC-S-nZVI[post], despite their higher mobility, the effluent concentrations decrease slowly but continuously over time. This descending plateau in the BTC plot can be ascribed to the increasing deposition rate of the iron particles with time, which is a typical behavior for ripening phenomena (Liu et al., 1995; Babakhani et al., 2017). Ripening occurs when particle-particle interactions are high and stronger than particle-collector interactions (Chapter 3.4.2). Once the attachment capacity of the porous medium is reached, the particles entering the voids subsequently are attached on the already adsorbed nanoparticles, which act as additional collector. This process leads to the formation of multi-layered accumulation on the grain surface (Liu et al., 2019). The enhanced mobility at higher CMC concentrations suggests that, despite ripening, higher CMC concentrations could further reduce attractive forces between the particles themselves and limit ripening effects. Therefore, a few attempts using 10 g/L of CMC were made. However, due to the too high viscosity of the respective suspension, the pressure inside the column reactor increased and caused the displacement of the quartz sand, forcing to stop the experiments.

Apart from ripening, formation of larger particle aggregates due to the collision with the sand surfaces could be another phenomenon that might further enhance particle deposition (Chen et al., 2011). Indeed, in a regime where the tendency to particle-particle attachment is dominant, straining phenomenon may

occur. However, it has been shown that straining is relevant for particle/collector diameter ratios (d_p/d_c) greater than 0.0017 (Bradford et al., 2002; Tufenkji et al., 2004; Bradford and Bettahar, 2006; Bradford et al., 2007). Since the d_p/d_c ratio in this study resulted to be equal to 0.0006, it is unlikely that straining is a relevant mechanism responsible for the retention of particles. Nevertheless, as shown in the SEM images (Figure 5-1 and Figure 5-2), the quartz sand used for this study consists of irregular quartz grains with rough surfaces, which could be responsible for sand-particle interactions and might trigger straining effects (Bradford et al., 2002; Tufenkji et al., 2004; Auset and Keller, 2006).

ii   Effects of inlet particle concentration

As the previous results showed, CMC-S-nZVI[post] has the highest mobility of tested S-nZVI particles and was therefore selected to investigate the influence of other parameters on the mobility in porous media. One of these tested parameters was the inlet particle concentration. The evaluation of BTCs obtained at a constant injection velocity of 0.035 cm/s revealed that the transport behavior of CMC-S-nZVI[post] is strongly dependent on the inlet particle concentration (Figure 7-17). The BTCs show that for the lowest particle concentration of 0.1 g/L, the maximum observed breakthrough is approximately 60 %, whereas an increase of the particle concentration to 0.5 g/L and 1 g/L caused a significant decrease of the maximum effluent concentration to 35 % or 20 %, respectively.

The higher mobility at lower particle concentration can be attributed to higher suspension stability. Indeed, at lower particle concentrations and thus higher CMC/S-nZVI ratios, the particles are better dispersed in suspension, and therefore tend less to aggregate. This leads to a higher transportability through the porous medium, whereas at lower CMC/S-nZVI ratios (higher particle concentration), the polymer surface coverage may be only incomplete and therefore insufficient to break up the pre-existing particle agglomerates or to avoid the formation of larger aggregates during dispersion through the pores. Moreover, higher nanoparticle concentrations increase the collision probability between the particles, which can favor the formation of aggregates (Raychoudhury et al., 2012).

Furthermore, the different shapes of the BTC plateaus suggest that different interaction and retention mechanisms occurred during injection due to the different amount of particles in contact with the collector and crossing the interconnected voids. As described in the previous section, the behavior at 0.5 g/L particle concentration resulting in a descending plateau of the respective BTC can be ascribed to the ripening phenomena, while the BTC for a particle concentration of 1 g/L displays an ascending plateau that is rather typical for blocking effects (Saiers et al., 1994; Babakhani et al., 2017). Indeed, at 1 g/L particle concentration there is a higher probability that the particles fill more quickly the available attachment sites of the collector (i.e., blocking), resulting in an enhanced mobility over time for the subsequently injected particles (Kasel et al., 2013; Iqbal et al., 2017). On the other hand, the lowest particle concentration exhibits a steady state plateau, which is an indication for favorable transport conditions.
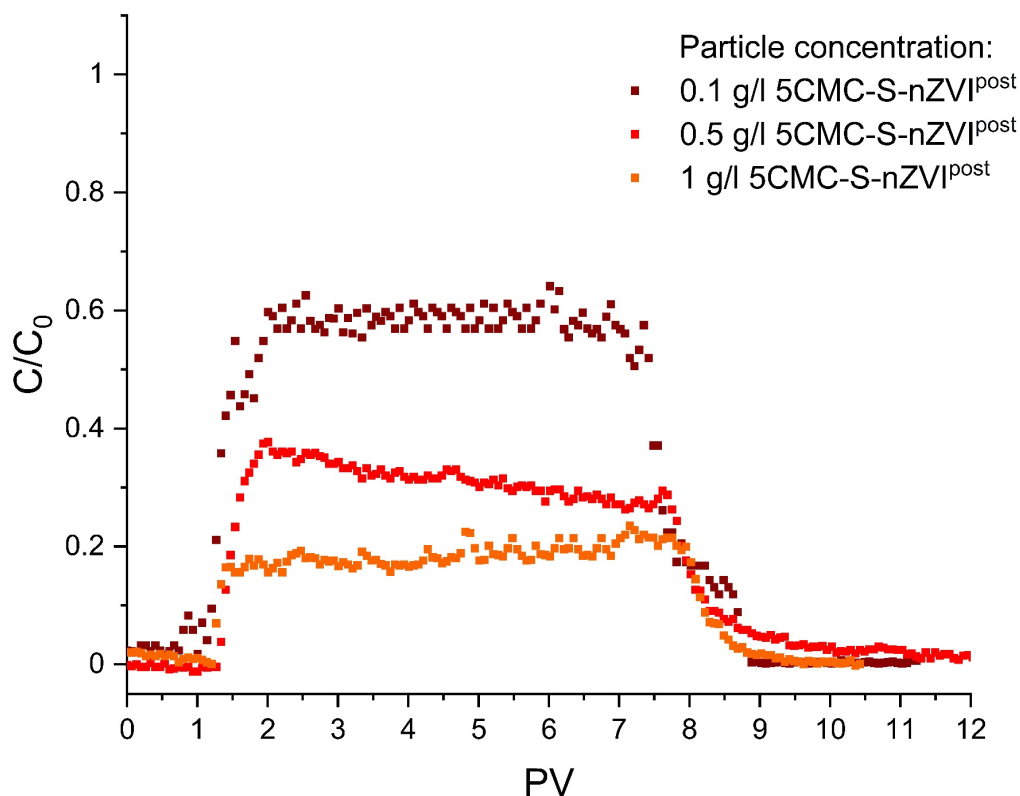
Figure 7-17   Experimental BTCs obtained after injection of 0.1, 0.5 and 1.0 g/L suspension of 5-CMC-S-nZVI[post] at 0.035 cm/s.

As shown by Hosseini and Tosco (2013) and Tosco and Sethi (2010), with increasing inlet particle concentration, ripening may lead to clogging of the porous media, as the higher amount of retained nanoparticles effectively decrease the pore size and block additional input of the nanoparticles. However, in the study on the assessment of the input particle concentration on the transport of S-nZVI nanoparticles from Gong et al. (2020), the authors reported the opposite trend (higher mobility at higher input particle concentration). They hypothesized that nanoparticles could occupy the available attachment sites, which limits the deposition of subsequent particles. Although they explained this behavior with the blocking effect, their BTCs showed no signs of blocking, which is most likely due to the low particle concentration used.

iii   Effects of pore water velocity

Figure 7-18 shows the BTCs obtained by injecting 5-CMC-S-nZVI[post] at flow velocities of 0.017, 0.035 and 0.070 cm/s. The slowest velocity gave a C/C_0 value of ~ 20 %, while at the fastest velocity a C/C_0 value of ~ 70 % was obtained. These results show that particle transport is dependent also on the injection velocity. Therefore, the transport of 5-CMC-S-nZVI[post] increases with increasing injection velocity and decreasing particle concentration. Transport could be favored by an increased shear force deriving from increased flow rates. Same trend has been shown in previous studies also for non-sulfidized nZVI (He et al., 2009; Raychoudhury et al., 2010).
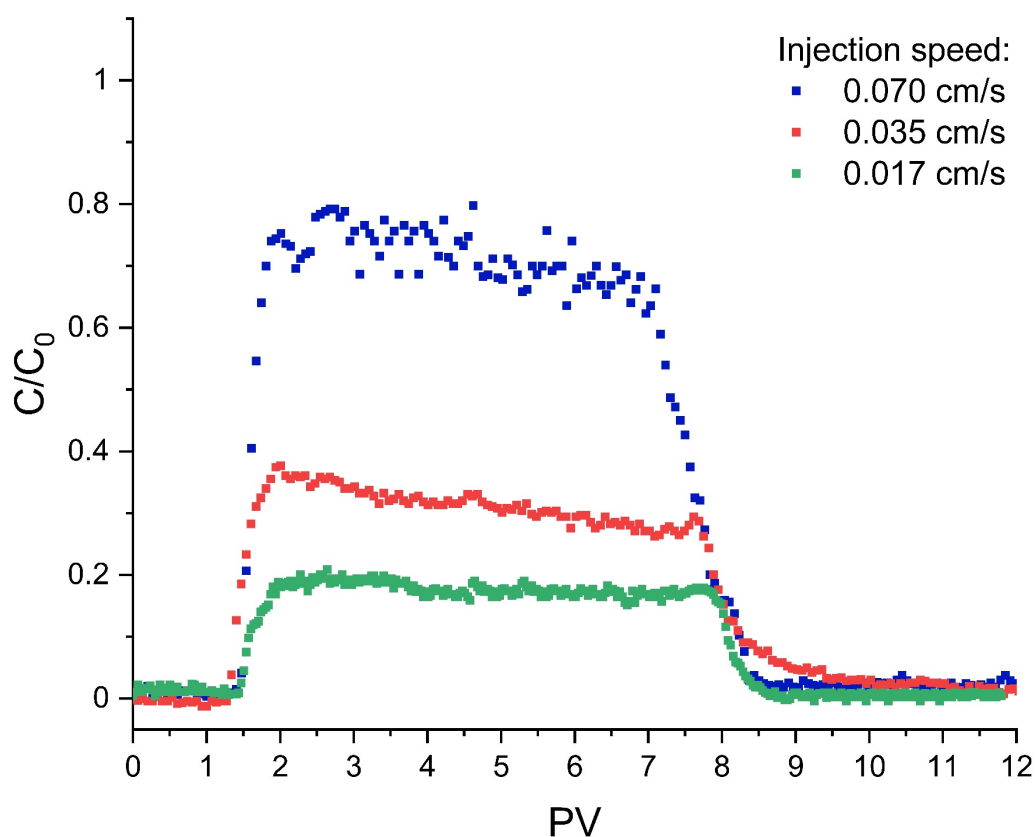
Figure 7-18 Experimental BTCs obtained after injection of 5-CMC-S-nZVI[post] at 0.017, 0.035 and 0.070 cm/s.

In addition, retention profiles obtained from the segmentation of columns after injection of the three particle concentrations at different injection velocities are shown in Figure A-20 and the respective mass balance values are listed in Table 7-5. The amount of iron that did not exit the packed column was approximately 80 % at the lowest velocity and approximately 23 % at the highest velocity. These profiles indicate that the quantity of retained iron, hence the retained S-nZVI particles, gradually decreased from the inlet to the outlet layer of the sand column. Although for all of the three scenarios, the highest amount of retained nanoparticles is located close to the inlet port, the different injection velocity are responsible for different particle distributions along the bed layers. This can be ascribed to the fact that at a higher injection velocity, nanoparticles move less through smaller pores, which can induce a stronger physical strain, but move preferentially through macropores, which act as preferential flow paths, allowing more particle eluting.

iv   Effect of sand particle diameter

Figure 7-19 shows the BTCs obtained by injecting a 0.25 g/L suspension of 5-CMC-S-nZVI[post] at a flow velocity of 0.070 cm/s in columns packed with quartz sand of particle diameters in the range of 0.1-0.3 mm or 0.4-0.8 mm. The normalized eluent concentrations demonstrate that the particle transport is enhanced in the coarser sand. This can be attributed to the smaller specific surface area of coarser quartz grains compared to finer sand, resulting in a lower amount of available attachment sites for the

injected nanoparticles (Mattison et al., 2011; Sharma et al., 2014). Moreover, the particle size of the medium significantly affects the occurring pore-size distribution and fluid velocities encountered by the particles, which might hinder the transport of nanoparticles through the porous media. Hence, the transport of CMC-S-nZVI[post] through quartz sand can increase as the grain size of the sand increases (Hou et al., 2017). These findings are in accordance with many previous studies that have shown that larger medium grain sizes lead to greater transport distances and less particle deposition in the porous media (Li et al., 2016; Hou et al., 2017). It is important to note that particle transport in natural aquifer sediments (e.g., soil and sediments) is generally lower than in homogenous quartz sand (Liu et al., 2019), due to wide range and variation of grain sizes, shapes, and surface roughness as well as the presence of organic material, bacteria or biofilms, which can enhance retention. Therefore, for a successful remediation approach, physical and geochemical conditions of the porous media must be carefully examined and taken into account.
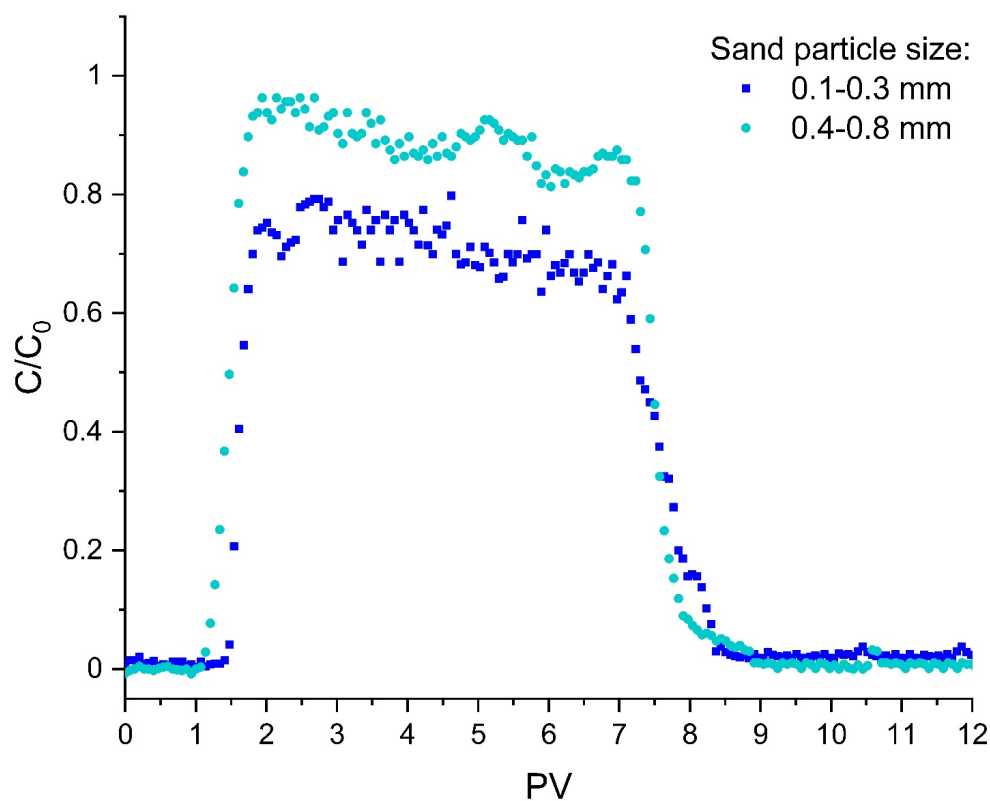
Figure 7-19   **Experimental BTCs of column transport tests of 5-CMC-S-nZVI[post] for sand grain diameters of 0.1-0.3 mm and 0.4-0.8 mm.**
Operating parameters: C_0 = 0.25 g/L, velocity = 0.070 cm/s.

7.3.5 Column Imaging

MR tomography and MR imaging were performed for on-line monitoring the spatial particles distribution during their injection. 5-CMC-S-nZVI[post] was chosen as target particle as it showed to have a higher mobility compared to the other tested S-nZVI types. Figure 7-20 shows eight selected MRI images along the sagittal (*y-z*) plane in the middle position (slice 3) of the column, during injection of

0.1 g/L 5-CMC-S-nZVI^{post} suspension at 0.035 cm/s in up-flow mode (schematic representation of the column and of the *x-z* and *y-z* planes are presented in Figure A-21).
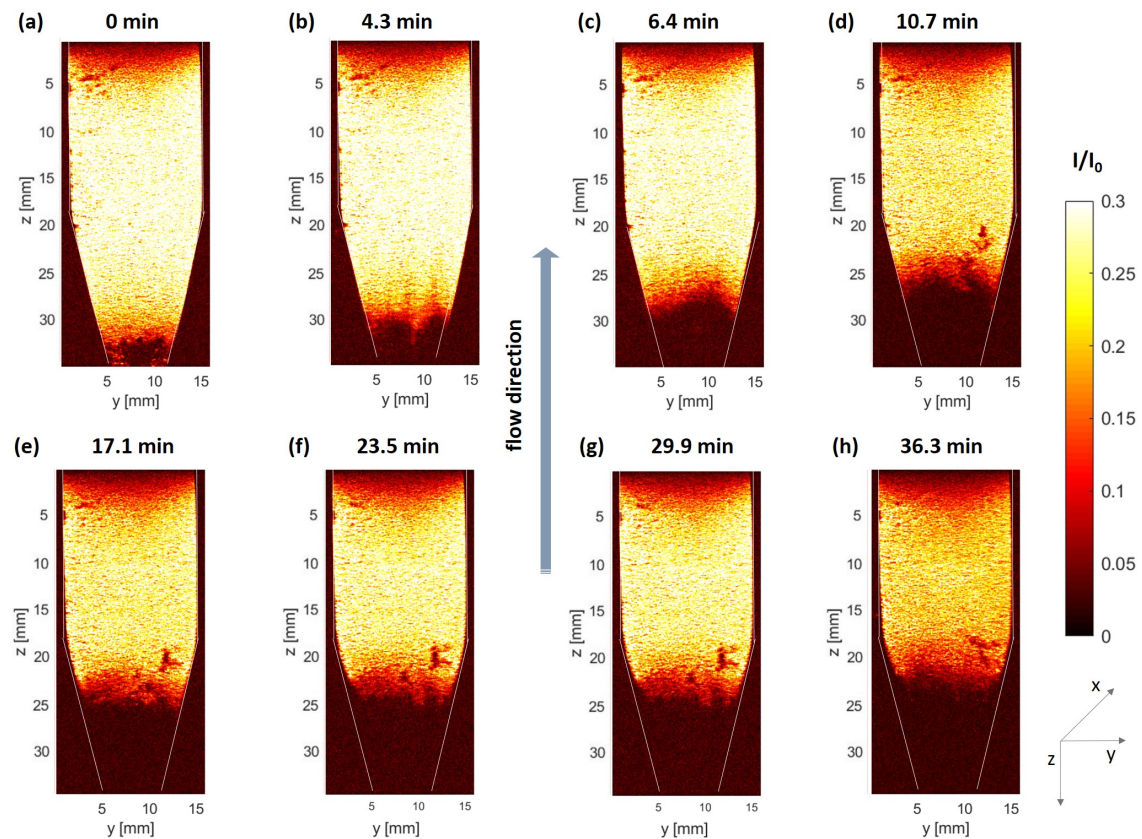
Figure 7-20 **MR images along the sagittal (y-z) plane in the central position (slice 3) during injection of 0.1 g/L 5-CMC-S-nZVI^{post} suspension at 0.035 cm/s.**
Eight selected time intervals are shown (a-h). The color range (0-0.3) corresponds to the normalized signal intensity (*I/I₀*). Due to their magnetic behavior, S-nZVI particles are shown in dark red to black, while the sand matrix is shown in bright colors. The column edges are marked with white lines for easier recognition. Note that the darker upper area is due to inhomogeneity of the signal intensity and not to the presence of iron nanoparticles.

The field of view is equal to 560 mm^2 and shows the lower part of the column near the injection point, which is filled with a small layer ($\sim$ 3 mm) of coarser sand to ensure homogeneous flow. In the MR image, the iron nanoparticles, which move through the void spaces of the porous matrix, can be recognized by the dark spots/areas (less intense signal) as they reduce the MRI signal. Thus, the transport of the particles is shown by the upward enlargement of the darker areas into the column. Figure 7-20a shows the reference image of the column after the pre-conditioning with CMC and shortly before the particle injection, confirming that the column was packed homogeneously and maintained its homogeneity after the polymer solution had passed through. It is important to note that the darker area at the top ($\sim$ 5 mm) of each image, including the reference image, is most likely due to the inhomogeneity of both the B_0 and radio frequency field B_1 that characterize the upper part of the field of view, and not to the presence of nanoparticles. As injection proceeded, the particles moved through the porous medium (Figure 7-20b-h). The enlargement of the darker area near the inlet point of the

column is the result of the migration of the injected particles. The fact that a certain portion of nanoparticles can cross the column and eventually reach the eluent is demonstrated by the presence of dark spots along the entire column. These observations are consistent with the breakthrough analysis (Chapter 7.3.4). While a certain amount of nanoparticles can pass through the column, a large part is irreversibly retained between the sand grains.

7.3.5.1 Retained and Eluted Particles: Behavior and Kinetics of Migration Front

To better understand the flow path of the iron nanoparticles and identify any asymmetric particles distributions, which might occur during injection, MRI measurements were made for five sagittal slices (in z-direction) of interest (slice from 1 to 5) using the "rapid acquisition with relaxation enhancement" (RARE) method (further information are in Chapter 5.2.8). Images were processed with a self-written MATLAB script and the obtained one dimensional normalized intensity profiles (I/I_0) were modelled using the Boltzmann equation (Equation 7-4). Figure 7-21a demonstrates that the MR data obtained from the middle position of the column (slice 3) match well with the Boltzmann fit, giving an average goodness-of-fit value (R^2) of 0.99. Same calculations and model fits were made for the other four slices, providing similar goodness-of-fit values (modelled curves in Figure A-22 and Figure A-23).
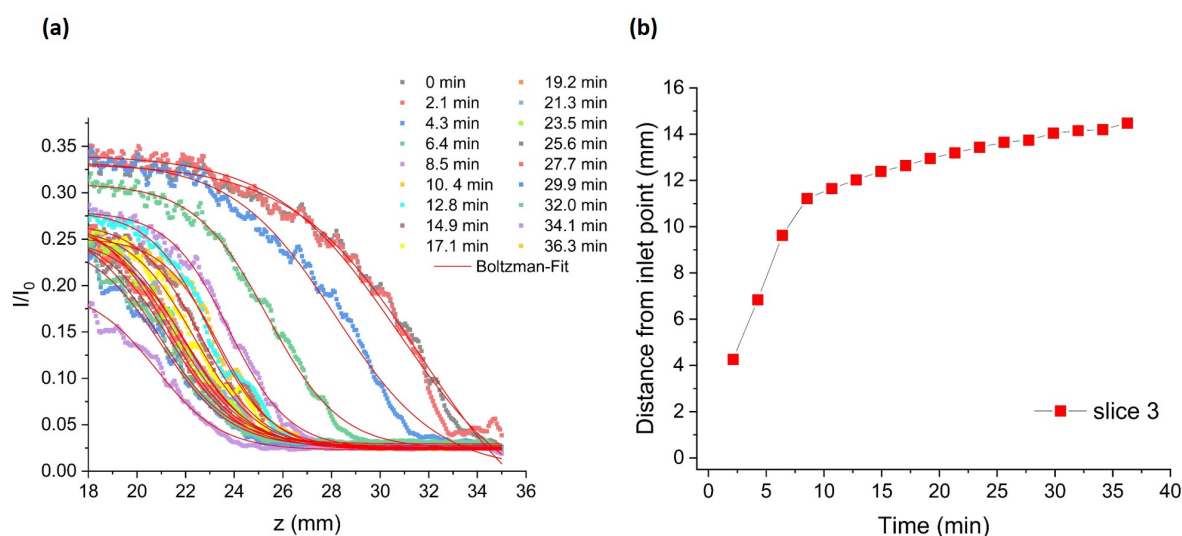
Figure 7-21   **MRI data obtained (intensity profiles and kinetics plot) at slice 3 during injection of CMC-S-nZVI[post] inside a sandy porous medium.**
(a) Normalized intensity profiles (dots) and modelled data (red lines) used to calculate the position of the inflection point of the curve (z_0); (b) kinetics plot of the distance of the migration front the inlet point.

The modelled data were used to calculate the z_i-values, which represent the distance (mm) that the nanoparticle migration front has travelled from the inlet point at each time interval, and then plotted as function of time. The time-distance plot gives information on the kinetics of the injected particles within the column at each singular slice (Figure 7-21b). The kinetics of the injected particles indicates that during the injection of 1 PV slurry, which took approximately 8.5 minutes, the front moved faster than during the rest of the injection time (from 10.7 to 36.3 min). This is also confirmed by the trend of

m-values (i.e., slope of the curve at each z_0 point) obtained with the Boltzmann equation fits (Table A-7). This trend was observed also for the other four slices, and was therefore studied together with the breakthrough curve (BTC) of the analogue experiment (Chapter 7.3.4), which was monitored via spectrophotometric analysis (Figure 7-17). Figure 7-22a shows the section of the BTC corresponding to the injection of 5-CMC-S-nZVI^{post} that has been monitored via MRI measurements (the MR data do not cover the pre- and post-flush of the column with CMC). Figure 7-22b, on the other hand, shows the kinetics of the particle migration within the column obtained at all five slices by means of MRI. The comparison of the two graphs showed that:

- the time at which the breakthrough curve reached the plateau (8.5 min) corresponds to the time at which the kinetics of particle migration shows a change in trend;
- during the injection of 1 PV, C/C_0 increased rapidly over time, while the migration front moved with a high velocity;
- after approximately 1 PV, C/C_0 reached a plateau meaning that the column reached the equilibrium state, while the particle front significantly reduced its velocity without stopping its migration through the porous medium.

(a)

(b)
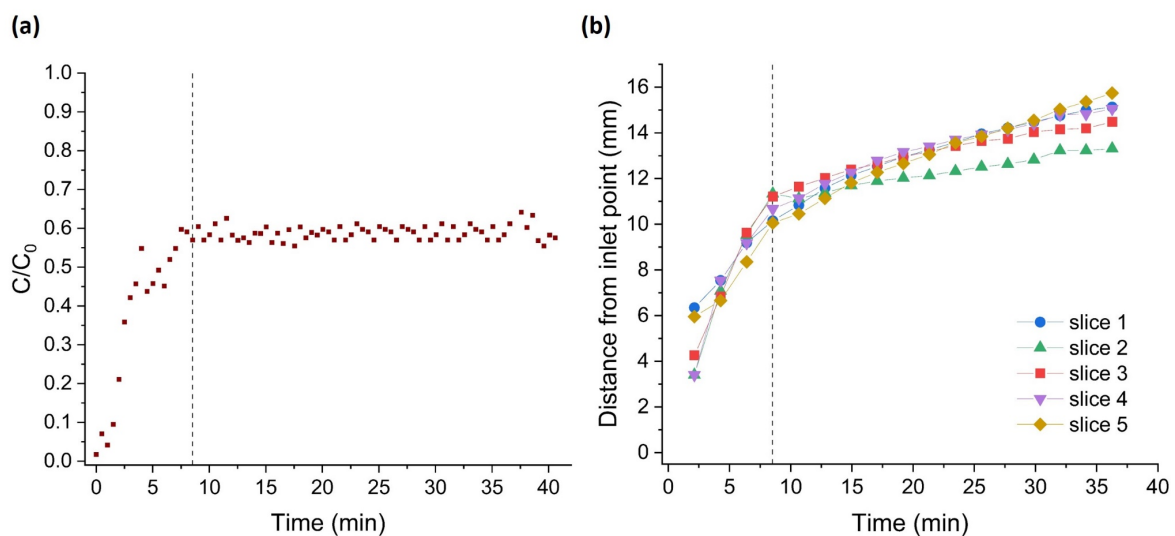
Figure 7-22 **BTC and kinetics of the migration front obtained injecting 0.1 g/L of 5-CMC-S-nZVI^{post} at 0.035 cm/s.**
(a) BTC corresponding to the injection of the particles obtained by means of spectrophotometric analysis; b) kinetics of the migration front of the particles within the column obtained via MRI measurements at five different slices.

For the first time, MRI has been used in combination with BTCs analysis to better understand the particles behavior during injection. Their comparison together with the parameters obtained from modelling (x_0, x_i and m) gave key information on the mobility of the particles through the porous medium as well as the migration of the retained particles within the column. An ascending or descending plateau, which corresponds to different particles behavior (e.g., blocking, straining or ripening) due to varying particle concentrations (Chapter 7.3.4) might result in different kinetic trends of the migration

front of the retained particles (Babakhani et al., 2017). An additional injection of the same slurry with a higher particle concentration of 0.5 g/L was monitored by MRI, however due to the too high particle concentration, the image contrast was not good enough and it was not possible to process the data.

7.3.5.2 Reconstruction of Migration Front and Preferential Paths

Figure 7-23a shows how the MR images of the five column slices looked like after 36.3 min of particle injection. The entire particle front was reconstructed along the frontal (F) plane (z-x plane) by combining the calculated distances from the inlet point, obtained for the five slices at each time interval (Figure 7-23b). The upward spreading of the front within the column is indicated by the green lines, which represent the front of the retained particles at different points in time. As it can be seen, the lines become narrower over time. Furthermore, the irregular shape of the front lines suggests that preferential flow paths formed during injection. Shortly after the injection had started, the migration front presented a convex profile, indicating that a preferential flow due to the shape of the column occurred in the central position, near the inlet port of the column.
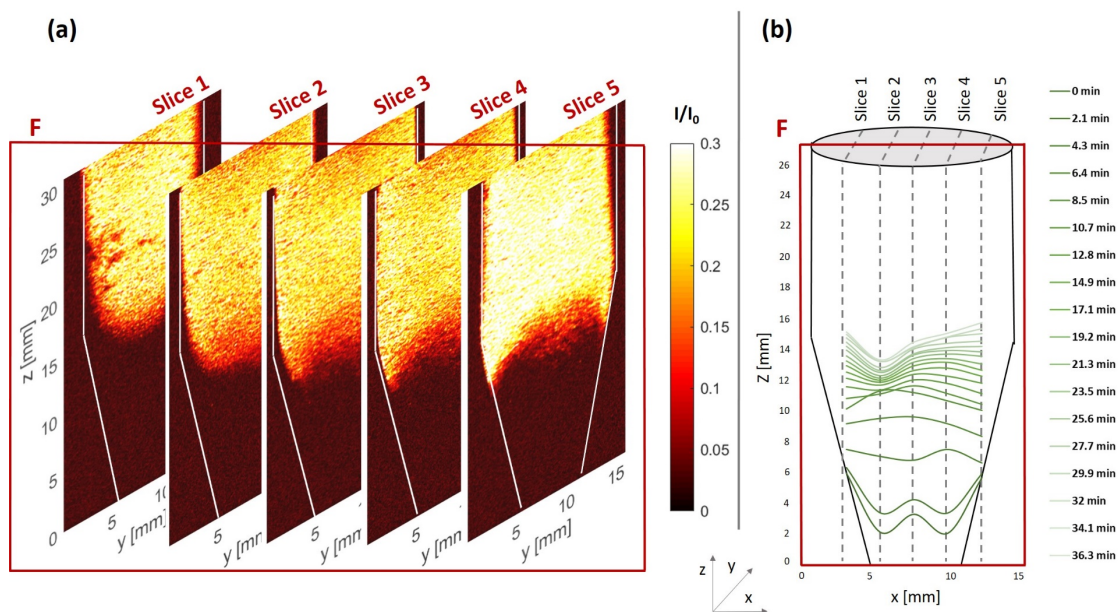
Figure 7-23 **(a) MR images along the five slices (y-z plane) after 36.3 min of 5-CMC-S-nZVI[post] injection. (b) Reconstruction of the migration front of the injected particles along the frontal plane F (x-z plane) at each time interval (0-36.3 min).**
The color range (0-0.3) of the MR images corresponds to the normalized signal intensity (I/I$_0$). The reconstruction of the migration front was made by combining the calculated distances from the inlet point of the five slices.

After a distance of around 6-8 mm, the convex portion became less pronounced and slightly moved to the right. This deformation is the result of the different flow velocities at the five different slices. Indeed, as Figure 7-24 clearly shows, slice 2, 3 and 4 exhibit steeper curves on a short time scale than slice 1 and 5. Thus, on a short time scale, the particle front moved faster in the inner regions of the column (Figure 7-24a). Conversely, the opposite trend can be observed on a long time scale (Figure 7-24b). The respective velocity of the front is reported in Table 7-6.
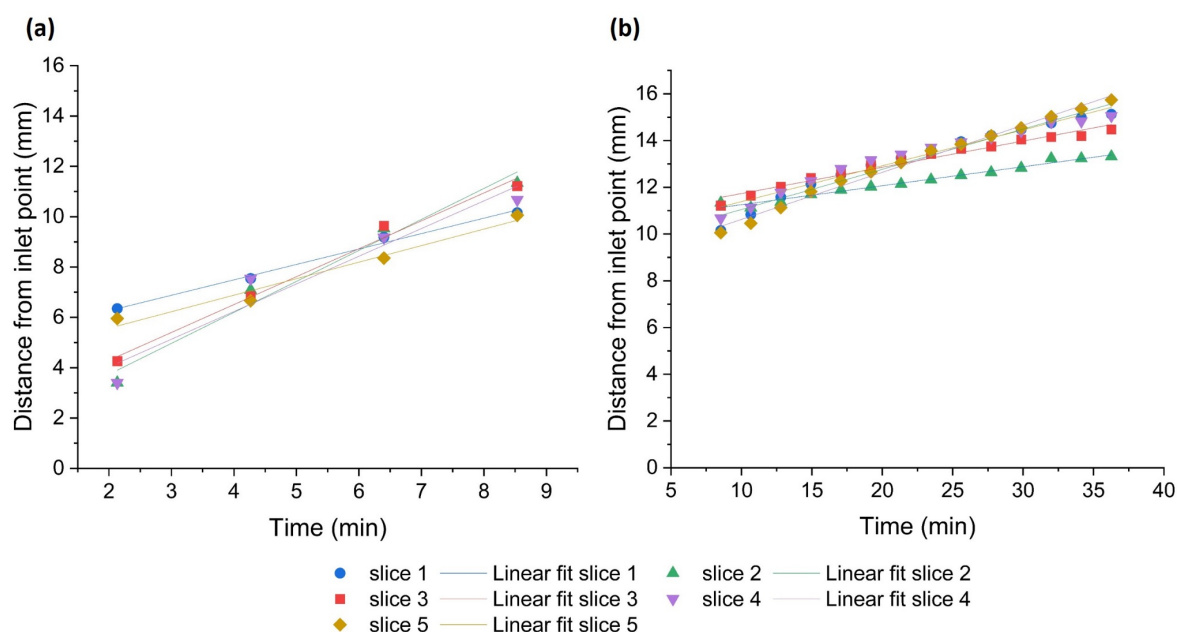
Figure 7-24 **Kinetics of the migration of the particle front between (a) 2 and 8.5 min and (b) 8.5 and 36.2 min after injection.**
In both time intervals, the data points can be represented quite well by a linear fit.

In general, these results support the results from the BTC analyses, showing that some of the particles travelled for a certain distance in the column before being retained within the sand grains, while the particles eluted from the column moved homogeneously through the voids.

Table 7-6 **Values of flow velocity of the particle front (mm/min) during injection.**
The values velocity$_{2-8.5}$ and velocity$_{8.5-36.2}$ correspond to the velocity in the time interval from 2 to 8.5 min and from 8.5 to 36.2 min.

Slice number	Velocity$_{2-8.5}$ (mm/min)	R^2	Velocity$_{8.5-36.2}$ (mm/min)	R^2
Slice 1	0.61	0.99	0.16	0.97
Slice 2	1.23	0.97	0.08	0.99
Slice 3	1.11	0.98	0.11	0.97
Slice 4	1.10	0.93	0.14	0.96
Slice 5	0.66	0.97	0.20	0.99

7.4 Summary

This study demonstrated the increased mobility of S-nZVI by modification with CMC, whereby a CMC treatment after S-nZVI synthesis (post-grafting method) led to significantly better results than the pre-grafting counterpart method (CMC treatment before the S-nZVI synthesis). Furthermore, the results of this study showed the inability of GR_{SO4} to migrate through a porous medium consisting of fine quartz sand. The very low transport potential of GR_{SO4} was mainly attributed to its hexagonal shape and larger crystal size, which are not compatible with the size and shape of the voids of the tested porous medium. On the other hand, SEM and TEM measurements revealed that all synthesized S-nZVI types

investigated in this study are spherical with a core-shell structure. The average diameter of bare S-nZVI (95.5 ± 28.5 nm) decreased in case of CMC modification by the pre-grafting method (81.4 ± 24.4 nm) and increased by the post-grafting method (110.5 ± 38.9 nm). Overall, the nanoparticle diameters can be summarized as: CMC-S-nZVI^{pre} < bare S-nZVI < CMC-S-nZVI^{post}. For the CMC-modified S-nZVI particles, the presence of carbon was detected by STEM-EDX analysis, confirming the successful shell modification of S-nZVI by CMC in case of both methods. The electrophoretic mobility measurements revealed small absolute zeta potential values (< ±40 mV) at near-neutral pH values for bare S-nZVI and CMC-S-nZVI^{pre}, which cause higher attractive forces (e.g., van der Waals) between particles and, on the other hand, higher zeta potential values (> -70 mV) at near-neutral pH values for CMC-S-nZVI^{post}, which provide enough electrostatic repulsive forces to keep the particles in suspension for a longer time. The findings of the sedimentation tests together with the surface charge analysis indicated that the most effective approach to increase the colloidal stability of S-nZVI particles by providing negative electric surface charges is the post-grafting CMC modification method. An increased colloidal stability of the nanoparticles is then also reflected in an enhanced mobility. Evaluation of BTCs obtained via injecting CMC-S-nZVI^{post} under various conditions proved that the higher the CMC concentration used to stabilize S-nZVI, the lower the amount of retained particles in the column. Moreover, the mobility of the particles is enhanced in case of lower inlet nanoparticle concentrations, higher injection speeds or coarser grain sizes of the porous medium. The results of the tests of the different operating parameters indicate that choosing the optimal combination of operating parameters can contribute to achieve the remedial goal.

Lastly, the application of the magnetic resonance imaging (MRI) technology allowed the quantitative assessment of the kinetics of the particle front and the presence of asymmetric particle flow paths during the injection of the most stable and mobile S-nZVI type. Moreover, by modelling the obtained MR data, it was possible to reconstruct the position and shape of the particle front at specific time intervals. This study illustrates the applicability of the tested MRI approach in environmental research for the spatial characterization of the transport behaviors of any magnetic nanoparticles inside a non-magnetic porous media (e.g., quartz sand system).

8 Concluding Remarks and Outlook

To achieve the ambitious goal of decontaminating hundreds of thousands of polluted sites in Europe (Pérez and Rodríguez Eugenio, 2018), there is a strong demand for the development of more-efficient and cost-effective remediation techniques. Despite the extensive use of *ex-situ* technologies around the world, there is now a clear trend to strengthen the use of *in-situ* techniques. In this context, *in-situ* remediation strategies such as permeable reactive zones have gained increasing attention as they allow faster and less disruptive clean-up and are also more environmentally friendly compared to *ex-situ* approaches (Gu et al., 1999; Puls et al., 1999; Gavaskar et al., 2005). Additionally, by using *in-situ* applications, contaminated areas can often be treated without interfering with existing infrastructures. However, the design of an *in-situ* reactive zone, which can be obtained via the construction of barriers (PRBs) containing reactive materials or injection wells, requires careful consideration of the physical and chemical characteristics of the chosen reactive material. It is of fundamental importance that a remediation technique must be able to meet the intended clean-up goals without losing its reactivity in the long term. This depends on the general reactivity of the selected material against the target contaminant. Another important consideration is how the reactivity is affected by the way the reactant is introduced into the subsurface, injected or mixed with the aquifer material.

This study aimed to investigate and characterize two promising reactants, sulfate green rust (GR_{SO4}) and the sulfidized form of nano zerovalent iron (S-nZVI). GR_{SO4} has been extensively investigated for its redox reactivity and easy synthesis procedure, while S-nZVI is an emerging nanomaterial, which has recently proven its high reactivity and longevity compared to its non-sulfidized form (nZVI). The first goal of this thesis was to assess the immobilization behavior of the two reactants against hexavalent chromium, Cr(VI), in a porous sandy media. Cr(VI) is a major toxic pollutant posing a great threat to humans, flora and fauna. The exact knowledge of the main factors that influence the Cr(VI) removal processes under dynamic conditions, as they occur in PRB systems, is of great importance for the field applications of the tested reactants.

The second goal of the thesis was to examine the suitability of GR_{SO4} and S-nZVI in creating reactive zones in the subsurface via direct injection. In this context, it is crucial that the reactant material, which is mostly in suspension, spreads from the injection point, migrates through the porous aquifer matrix and reaches the contaminated zone. Therefore, a series of particle characterization techniques were employed in combination with stability tests and transport column experiments. The findings of this work highlight how characteristics of the particlea such as size, shape and surface charge strongly influence the mobility behavior of the both tested reactants through a porous medium.

8.1 Major Findings on the Reactivity of GR$_{SO4}$ and S-nZVI against Cr(VI)

The objectives of the first study (Chapter 6) were to investigate how the sand matrix influences the immobilization capacity of GR$_{SO4}$ and S-nZVI against Cr(VI) as well as how the immobilization processes are affected by parameters such as pH conditions, flow rate and Cr(VI) concentrations.

To meet these goals, batch experiments containing sand as matrix material were performed and combined with laboratory continuous packed bed columns studies, where each reactant was exposed to dynamic flow conditions and steady Cr(VI) concentrations. With these settings, the interactions of chromate anions with the sand grain surfaces were also considered. Moreover, it was possible to assess the effectiveness of GR or S-nZVI in immobilizing Cr(VI) as it would occur in the case of a PRB system, as well as to determine the main parameters that enhance or hinder the immobilization process.

The results from the sand batch studies showed high Cr(VI) immobilization rate by GR$_{SO4}$ in presence of sand, with > 95 % Cr(VI) removed within only 10 minutes, matching well with the removal rates observed in previous sand-free batch experiments (Eary and Rai, 1988; Thomas et al., 2018). These results indicate that the sand matrix behaves as inert material, and hence, does not interfere the immobilization processes. Moreover, the higher Cr(VI) removal observed in the case of a Cr(VI) excess (compared to the amount of Fe equivalents) suggests that in addition to reduction, Cr(VI) can also be sorbed on the newly formed Fe(III)-phases under neutral pH conditions. The results of the analogue batch studies carried out with S-nZVI clearly showed the substantial higher and faster Cr(VI) immobilization by GR$_{SO4}$, although in S-nZVI is available a higher amount of Fe equivalents.

In this study, an on-line spectrophotometric method was developed to determine the Cr(VI) concentration in water samples produced by the column experiments, which allowed quick analysis of the samples in their original state, without the use of a complexing agent. Once the validity and reliability of this method was established by comparing the results with those obtained by the standard 1,5-diphenylcarbazide colorimetric method (EPA Method 7196A), it was decided to modify the experimental set-up of the column experiments and to use the new analysis method for on-line Cr(VI) measurements. With the method without complexing agent, it was not only possible to monitor the development of Cr(VI) concentration on-line during the reaction, but also to perform faster and more accurate Cr(VI) measurements with a much higher temporal resolution. With this method it was also possible to monitor potential pH changes during the experiment.

The results of the reactivity column tests, prepared by mixing a defined amount of quartz sand with the reactive material, clearly showed that GR$_{SO4}$ performs substantially faster and better in immobilizing Cr(VI) than S-nZVI. However, for both materials, substantially lower Cr(VI) removal efficiencies were observed compared to those obtained in batch studies. This is explained by the fact that in column

systems, as for PRBs, a constant influx of Cr(VI) solution occurs, which keeps reaction rates high, promoting quicker passivation of the reactants. Furthermore, higher Cr(VI) removal efficiencies were observed at lower flow rates and at acidic conditions, giving insights into the optimal hydro-geochemical conditions for potential field applications. These outcomes highlight the importance of testing the effectiveness and behavior of reactive materials in column set-ups, where phenomena can be observed that otherwise would not be seen in batch studies.

8.2 Major Findings on the Transport Behavior of GR_{SO4} and S-nZVI in Porous Media

The aim of the study on the transport behavior (Chapter 7) of S-nZVI and GR_{SO4} was to investigate whether these materials are suitable for injection-based *in-situ* technologies. Column experiments were performed and their outcomes showed the high potential of S-nZVI, if properly modified, for injection purposes in porous media,. By contrast, GR_{SO4} showed negligible mobility in the transport column experiments with sand as matrix.

Sedimentation tests and surface charge analysis on bare S-nZVI revealed the need for a surface modification to improve particle stability and transport efficiency. Therefore, sodium carboxymethyl cellulose (CMC), which is an anionic, inexpensive and environmental-friendly substance, has been selected as particle stabilizer and added to S-nZVI using two different approaches: pre-grafting and post-grafting methods. In case of the pre-grafting method, CMC was added during S-nZVI synthesis (CMC-S-nZVI[pre]), whereas for the post-grafting, CMC was added afterwards (CMC-S-nZVI[post]). It was observed that the presence of CMC via pre-grafting featured smaller S-nZVI particles than in the absence of CMC, while the post-grafting method provided larger average particle sizes. Overall, single particle diameters can be summarized as follows: CMC-S-nZVI[pre] < bare S-nZVI < CMC-S-nZVI[post].

Apart from forming larger particles, the post-grafting method has proven to be more effective in providing repulsive electrosteric (combination of steric and electrostatic) forces than the pre-grafting method. This advantageous behavior was ascribed to the fact that CMC is more efficient as stabilizer when adsorbed as coating around the FeS layer rather than when CMC is present inside the S-nZVI structure. Moreover, at the same particle concentration, it was shown that the higher the CMC concentration used for post-grafting, the higher the colloidal stability due to a more uniform and homogeneous surface coverage.

The low colloidal stability of the bare S-nZVI and the CMC-S-nZVI[pre] particles has resulted in a highly limited mobility in quartz-packed columns. In contrast, CMC-S-nZVI[post] particles are much more mobile. Based on these findings, various column sets were performed via injecting CMC-S-nZVI[post] to evaluate the impact of different parameters like CMC concentration, S-nZVI particle concentration, injection velocity and particle size of the matrix. The data from breakthrough curves (BTCs) indicated

that the preconditioning of the column with CMC is necessary to ensure better transport behavior, as the polymer molecules provide a steric hindrance for the S-nZVI particles to approach the sand grains. Furthermore, under these conditions, all tested operating parameters had a strong influence on the transport behavior of the CMC-S-nZVI^{post} particles and their retention mechanisms. The outcomes can be summarized as follows:

- the higher the CMC concentration used to stabilize S-nZVI, the lower the amount of retained S-nZVI particles within the column and the higher their mobility. However, at 0.5 g/L particle concentration, which is a realistic concentration for field applications, ripening effects might have occurred as the main retention mechanism;

- higher S-nZVI particle concentrations were characterized by lower mobility and higher retention, controlled by blocking effects within the porous medium;

- higher injection velocity and coarser porous media enhanced particle transport behavior.

Breakthrough curves together with the retention profiles provided information on the transport behavior of the tested particles as well as on the possible retention mechanisms responsible for the reduced mobility. Moreover, these results can serve as a basis for building a numerical model that can be used to predict the particle behavior in different geochemical conditions not only at lab scale but also for field scale applications. Additionally, a column experiment monitored with magnetic resonance imaging (MRI) technique provided key information on the particle transport and distribution along the column, which complemented the BTC results. In this study, MRI was successfully employed to assess the kinetics of the injection front of the injected particles and to detect the presence of any asymmetric particle paths. Moreover, by modelling the MRI results and integrating them accordingly, it was possible to reconstruct the shape and position of the particle front at each time interval during injection. This study illustrates the suitability of the MRI approach in environmental research to spatially resolve the transport behaviors of any magnetic nanoparticle, not only S-nZVI, inside fine-grained non-magnetic media.

The negligible mobility of GR$_{SO4}$ was mainly attributed to the size and shape as well as to the positive surface charge of the GR crystals. The tested GR$_{SO4}$ particles, which were produced via the co-precipitation method, exhibited thin hexagonal plates that differed too much from generally more mobile spherical particles. Transport experiments with GR showed the impossibility for these particles to move through the interconnected voids of the sandy porous medium. The first starting point for enhancing GR mobility would be the synthesis of particles with smaller crystal sizes. However, it is important to note that smaller particles might not be sufficient to increase the mobility potential, as the particle surface charge plays also an important role. Therefore, particle surfaces should also be modified in order to obtain a negative surface charge and create more favorable conditions for transport in subsurface environments.

8.3 Outlook - Implications for Field Applications

For a successful *in-situ* remediation technology, it is essential that the selected reactant can achieve the remediation target value of the occurring harmful compound(s) without losing reactivity or longevity due to interaction with the surrounding environment. However, in addition to the reactivity effectiveness, another key factor in evaluating a reactant is how it can be introduced into the subsurface. This is decisive not only in terms of operational aspects (i.e., feasibility, infrastructural conditions, costs, etc.) but also with regard to the specific transport behavior of a certain reactant, defining which permeable reactive zone techniques are applicable and which are not.

As shown in this laboratory studies of a simulated PRB system, the high removal efficiency of GR_{SO4} against Cr(VI), as selected target contaminant, represents an important notch to its use as *in-situ* reactant and furthermore stimulates the research in the field of other GR types (GR_{CO3} and GR_{Cl}), which have proven to be reactive with other contaminants. Moreover, in addition to the application of GR as engineered reactant, it is worth emphasizing its remedial potential as naturally occurring mineral phase, which might contribute to the immobilization of contaminants in polluted subsurface environments. Although with a much lower efficiency and under favorable conditions, S-nZVI is also generally able to immobilize Cr(VI) in the presence of sand and under dynamic flow conditions. Moreover, both reactants can be employed also for remediation of other inorganic and organic compounds. Given that each contaminated site has its own characteristics depending on the hydrogeological and geochemical properties of the contaminated subsurface (i.e., type of pollutants, sand, gravel or unconsolidated sediments, presence of organic matter/biology, permeability, anoxic vs anoxic), remediation techniques based on S-nZVI may be suitable for sites where GR is not applicable and vice versa. Therefore, these materials certainly warrant further study on how to apply them at larger scale.

Overall, this study demonstrated that GR is generally better suited for *in-situ* applications against oxyanion contaminations than S-nZVI. However, due to its highly restricted mobility, without further modifications, GR might be limited to PRB applications based on the construction of barriers (continuous walls or funnel-and-gate technologies), where the reactive material is introduced into the subsurface after previous excavation. In case of S-nZVI, on the other hand, there is a high potential that it can be used not only in PRBs but, if properly modified, also in case of injection-based *in-situ* technologies.

References

Abdel-Samad H. and Watson P. R. (1997) An XPS study of the adsorption of chromate on goethite (α-FeOOH). *Appl. Surf. Sci.* **108**, 371–377.

Abdelmoula, M.Trolard F., Bourrié G. and Génin J.-M. R. (1998) Evidence for the Fe(II)-Fe(III) green rust "Fougerite" mineral occurrence in a hydromorphic soil and its transformation with depth. *Hyperfine Interact.* **112**, 235–238.

Ahmed I. A. M., Benning L. G., Kakonyi G., Sumoondur A. D., Terrill N. J. and Shaw S. (2010) Formation of green rust sulfate: A combined in situ time-resolved X-ray scattering and electrochemical study. *Langmuir* **26**, 6593–6603.

Aissa R., Francois M., Ruby C., Fauth F., Medjahdi G., Abdelmoula M. and Génin J.-M. (2006) Formation and crystallographical structure of hydroxysulphate and hydroxycarbonate green rusts synthetised by coprecipitation. *J. Phys. Chem. Solids* **67**, 1016–1019.

Ajouyed O., Hurel C., Ammari M., Allal L. Ben and Marmier N. (2010) Sorption of Cr(VI) onto natural iron and aluminum (oxy)hydroxides: Effects of pH, ionic strength and initial concentration. *J. Hazard. Mater.* **174**, 616–622.

Aksu Z. and Gönen F. (2004) Biosorption of phenol by immobilized activated sludge in a continuous packed bed: Prediction of breakthrough curves. *Process Biochem.* **39**, 599–613.

Aksu Z., Gönen F. and Demircan Z. (2002) Biosorption of chromium(VI) ions by Mowital®B30H resin immobilized activated sludge in a packed bed: Comparison with granular activated carbon. *Process Biochem.* **38**, 175–186.

Alowitz M. J. and Scherer M. M. (2002) Kinetics of nitrate, nitrite, and Cr(VI) reduction by iron metal. *Environ. Sci. Technol.* **36**, 299–306.

Andersson K. I., Eriksson M. and Norgren M. (2012) Lignin removal by adsorption to fly ash in wastewater generated by mechanical pulping. *Ind. Eng. Chem. Res.* **51**, 3444–3451.

Astrup T., Stipp S. L. S. and Christensen T. H. (2000) Immobilization of chromate from coal fly ash leachate using an attenuating barrier containing zero-valent iron. *Environ. Sci. Technol.* **34**, 4163–4168.

ATSDR (2020) Agency for Toxic Substances and Disease Registry (ATSDR)'s Substance Priority List. *Subst. Prior. List*. Available at: https://www.atsdr.cdc.gov/spl/index.html#2019spl [Accessed December 6, 2020].

Audi G., Bersillon O., Blachot J. and Wapstra A. H. (2003) The NUBASE evaluation of nuclear and decay properties. *Nucl. Phys. A* **729**, 3–128.

Auset M. and Keller A. A. (2004) Pore-scale processes that control dispersion of colloids in saturated porous media. *Water Resour. Res.* **40**, 1–11.

Auset M. and Keller A. A. (2006) Pore-scale visualization of colloid straining and filtration in saturated porous media using micromodels. *Water Resour. Res.* **42**, 1–9.

Ayala-Luis K. B., Koch C. B. and Hansen H. C. B. (2010) One-pot synthesis and characterization of FeII-FeIII hydroxide (green rust) intercalated with C9-C14 linear alkyl carboxylates. *Appl. Clay Sci.* **50**, 512–519.

Babakhani P., Bridge J., Doong R. an and Phenrat T. (2017) Continuum-based models and concepts for the transport of nanoparticles in saturated porous media: A state-of-the-science review. *Adv. Colloid Interface Sci.* **246**, 75–104.

Banzhaf S. and Hebig K. H. (2016) Use of column experiments to investigate the fate of organic micropollutants - A review. *Hydrol. Earth Syst. Sci.* **20**, 3719–3737.

Baral A. and Engelken R. D. (2002) Chromium-based regulations and greening in metal finishing industries in the USA. *Environ. Sci. Policy* **5**, 121–133.

Baumann T. and Werth C. J. (2005) Visualization of colloid transport through heterogeneous porous media using magnetic resonance imaging. *Colloids Surfaces A Physicochem. Eng. Asp.* **265**, 2–10.

Bayat A. E., Junin R., Shamshirband S. and Tong Chong W. (2015) Transport and retention of engineered Al2 O3, TiO2, and SiO2 nanoparticles through various sedimentary rocks. *Sci. Rep.* **5**, 1–12.

References

Bearcock J. M., Perkins W. T., Dinelli E. and Wade S. C. (2006) Fe(II)/Fe(III) 'green rust' developed within ochreous coal mine drainage sediment in South Wales, UK. *Mineral. Mag.* **70**, 731–741.

Bernal J. D., Dasgupta D. R. and Mackay A. L. (1959) The oxides and hydroxides of iron and their structural inter-relationships. *Clay Miner.* **4**, 15–30.

Bhattacharya A. K., Naiya T. K., Mandal S. N. and Das S. K. (2008) Adsorption, kinetics and equilibrium studies on removal of Cr(VI) from aqueous solutions using different low-cost adsorbents. *Chem. Eng. J.* **137**, 529–541.

Bi X., Zhang H. and Dou L. (2014) Layered double hydroxide-based nanocarriers for drug delivery. *Pharmaceutics* **6**, 298–332.

Birke V. and Burmeier H. (2014) Permeable Reactive Barriers in Europe. In *Permeable Reactive Barriers - Sustainable Groundwater Remediation* (eds. R. Naidu and V. Birke). CRC Press, Boca Raton, FL, Chapter 13. pp. 276–308.

Birke V., Burmeier H., Jefferis S., Gaboriau H., Touzé S. and Chartier R. (2006) Permeable reactive barriers (PRBs) in Europe: potentials and expectations. *Proceedings of the Fifth International Conference - Remediation of Chlorinated and Recalcitrant Compounds*, Monterey, CA.

Birke V., Burmeier H. and Rosenau D. (2002) PRB technologies in Germany: Recent progress and new developments. *Fresenius Environ. Bull. - Conference: Symposium on Environmental Chemistry and Buitechnology*, 521–528.

Blowes D. W., Ptacek C. J. and Jambor J. L. (1997) In-situ remediation of Cr(VI)-contaminated groundwater using permeable reactive walls: Laboratory studies. *Environ. Sci. Technol.* **31**, 3348–3357.

Blümich B. (2000) *NMR Imaging of Materials*. ed. Clarendon Press, Oxford University Press, Oxford. 542 pages.

Bocher F., Géhin A., Ruby C., Ghanbaja J., Abdelmoula M. and Génin J. M. R. (2004) Coprecipitation of Fe(II-III) hydroxycarbonate green rust stabilised by phosphate adsorption. *Solid State Sci.* **6**, 117–124.

Bond D. L. and Fendorf S. (2003) Kinetics and structural constraints of chromate reduction by green rusts. *Environ. Sci. Technol.* **37**, 2750–2757.

Boparai H. K., Comfort S. D., Satapanajaru T., Szecsody J. E., Grossl P. R. and Shea P. J. (2010) Abiotic transformation of high explosives by freshly precipitated iron minerals in aqueous FeII solutions. *Chemosphere* **79**, 865–872.

Börsig N., Scheinost A. C., Shaw S., Schild D. and Neumann T. (2018) Retention and multiphase transformation of selenium oxyanions during the formation of magnetite: Via iron(II) hydroxide and green rust. *Dalt. Trans.* **47**, 11002–11015.

Bourdoiseau J. A., Sabot R., Jeannin M., Termemil F. and Refait P. (2012) Determination of standard Gibbs free energy of formation of green rusts and its application to the Fe(II-III) hydroxy-oxalate. *Colloids Surfaces A Physicochem. Eng. Asp.* **410**, 72–80.

Bradford S. A. and Bettahar M. (2006) Concentration dependent transport of colloids in saturated porous media. *J. Contam. Hydrol.* **82**, 99–117.

Bradford S. A., Morales V. L., Zhang W., Harvey R. W., Packman A. I., Mohanram A. and Welty C. (2013) Transport and fate of microbial pathogens in agricultural settings. *Crit. Rev. Environ. Sci. Technol.* **43**, 775–893.

Bradford S. A., Simunek J., Bettahar M., Van Genuchten M. T. and Yates S. R. (2003) Modeling colloid attachment, straining, and exclusion in saturated porous media. *Environ. Sci. Technol.* **37**, 2242–2250.

Bradford S. A. and Torkzaban S. (2008) Colloid transport and retention in unsaturated porous media: A review of interface-, collector-, and pore-scale processes and models. *Vadose Zo. J.* **7**, 667–681.

Bradford S. A., Torkzaban S. and Walker S. L. (2007) Coupling of physical and chemical mechanisms of colloid straining in saturated porous media. *Water Res.* **41**, 3012–3024.

Bradford S. A., Yates S. R., Bettahar M. and Simunek J. (2002) Physical factors affecting the transport and fate of colloids in saturated porous media. *Water Resour. Res.* **38**, 1–12.

Brown H. S., Bishop D. R. and Rowan C. A. (1984) The role of skin absorption as a route of exposure for volatile organic compounds (VOCs) in drinking water. *Am. J. Public Health* **74**, 479–484.

Buerge I. J. and Hug S. J. (1999) Influence of mineral surfaces on chromium(VI) reduction by iron(II). *Environ. Sci. Technol.* **33**, 4285–4291.

References

Buerge I. J. and Hug S. J. (1997) Kinetics and pH dependence of chromium(VI) reduction by iron(II). *Environ. Sci. Technol.* **31**, 1426–1432.

Calace N., Di Muro A., Nardi E., Petronio B. M. and Pietroletti M. (2002) Adsorption isotherms for describing heavy-metal retention in paper mill sludges. *Ind. Eng. Chem. Res.* **41**, 5491–5497.

Callaghan P. T. (1993) *Principles of Nuclear Magnetic Resonance Microscopy*. ed. Clarendon Press, Oxford University Press, Oxford. 492 pages.

Chakravarti A. K., Chowdhury S. B. and Mukherjee D. C. (1995) Liquid membrane multiple emulsion process of chromium(VI) separation from waste waters. *Colloids Surfaces A Physicochem. Eng. Asp.* **103**, 59–71.

Chen G., Liu X. and Su C. (2011) Transport and retention of TiO2 rutile nanoparticles in saturated porous media under low-ionic-strength conditions: Measurements and mechanisms. *Langmuir* **27**, 5393–5402.

Chowdhury A. I. A., Krol M. M., Kocur C. M., Boparai H. K., Weber K. P., Sleep B. E. and O'Carroll D. M. (2015) nZVI injection into variably saturated soils: Field and modeling study. *J. Contam. Hydrol.* **183**, 16–28.

Christiansen B. C., Balic-Zunic T., Dideriksen K. and Stipp S. L. S. (2009a) Identification of green rust in groundwater. *Environ. Sci. Technol.* **43**, 3436–3441.

Christiansen B. C., Balic-Zunic T., Petit P. O., Frandsen C., Mørup S., Geckeis H., Katerinopoulou A. and Stipp S. L. S. (2009b) Composition and structure of an iron-bearing, layered double hydroxide (LDH) - Green rust sodium sulphate. *Geochim. Cosmochim. Acta* **73**, 3579–3592.

Cirtiu C. M., Raychoudhury T., Ghoshal S. and Moores A. (2011) Systematic comparison of the size, surface characteristics and colloidal stability of zero valent iron nanoparticles pre- and post-grafted with common polymers. *Colloids Surfaces A Physicochem. Eng. Asp.* **390**, 95–104.

Cornelis G., Hund-Rinke K., Kuhlbusch T., Van Den Brink N. and Nickel C. (2014) Fate and bioavailability of engineered nanoparticles in soils: A review. *Crit. Rev. Environ. Sci. Technol.* **44**, 2720–2764.

Cornell R. M. and Schwertmann U. (2003) Crystal structure. In *The Iron Oxides: Structure, Properties, Reactions, Occurrence and Uses* Second Completely Revised and Extended Edition, Wiley-VCH, Weinheim, Chapter 2. pp. 9–38.

Crane R. A. and Scott T. B. (2012) Nanoscale zero-valent iron: Future prospects for an emerging water treatment technology. *J. Hazard. Mater.* **211**–**212**, 112–125.

Cuny L., Herrling M. P., Guthausen G., Horn H. and Delay M. (2015) Magnetic resonance imaging reveals detailed spatial and temporal distribution of iron-based nanoparticles transported through water-saturated porous media. *J. Contam. Hydrol.* **182**, 51–62.

Daughton C. G. (2004) PPCPs in the environment: Future research - Beginning with the end always in mind. In *Pharmaceuticals in the Environment* (ed. K. Kümmerer). Second Ed., Springer, Berlin Heidelberg, Part V. pp. 463–495.

Deng S. and Bai R. (2004) Removal of trivalent and hexavalent chromium with aminated polyacrylonitrile fibers: Performance and mechanisms. *Water Res.* **38**, 2424–2432.

Derjaguin B. and Landau L. (1941) Theory of the stability of strongly charged lyophobic sols and of the adhesion of strongly charged particles in solutions of electrolytes. *Prog. Surf. Sci.* **14**, 633–663.

Digiacomo F., Tobler D. J., Held T. and Neumann T. (2020) Immobilization of Cr (VI) by sulphate green rust and sulphidized nanoscale zerovalent iron in sand media: Batch and column studies. *Geochem. Trans.* **21**, 1–12.

Dong H., Zeng G., Zhang C., Liang J., Ahmad K., Xu P., He X. and Lai M. (2015) Interaction between Cu2+ and different types of surface-modified nanoscale zero-valent iron during their transport in porous media. *J. Environ. Sci. (China)* **32**, 180–188.

Doty C. B. and Travis C. C. (1991) The effectiveness of groundwater pumping as a restoration technology. *ORNL/TM-11866*, Washington, DC.

Drissi S. H., Refait P., Abdelmoula M. and Génin J. M. R. (1995) The preparation and thermodynamic properties of Fe(II)Fe(III) hydroxide-carbonate (green rust 1); Pourbaix diagram of iron in carbonate-containing aqueous media. *Corros. Sci.* **37**, 2025–2041.

Drits V. A. and Bookin A. S. (2001) Crystal structure and X-Ray identification of Layered Double Hydroxides. In *Layered Double Hydroxides: Present and Future* (ed. V. Rives). Fifth Ed., Nova Science Publishers Inc., New York, Chapter 2. pp. 41–100.

References

Eary L. E. and Rai D. (1988) Chromate removal from aqueous wastes by reduction with ferrous ion. *Environ. Sci. Technol.* **22**, 972–977.

Eary L. E. and Rai D. (1989) Kinetics of chromate reduction by ferrous ions derived from hematite and biotite at 25 degrees C. *Am. J. Sci.* **289**, 180–213.

ECHA (2010) Annex XVII to REACH - Conditions of restriction (European Chemicals Agency). , Helsinki, FI.

Eisele T. C. and Gabby K. L. (2014) Review of reductive leaching of iron by anaerobic bacteria. *Miner. Process. Extr. Metall. Rev.* **35**, 75–105.

Elsner M., Schwarzenbach R. P. and Haderlein S. B. (2004) Reactivity of Fe(II)-bearing minerals toward reductive transformation of organic contaminants. *Environ. Sci. Technol.* **38**, 799–807.

Erbs M., Hansen H. C. B. and Olsen C. E. (1999) Reductive dechlorination of carbon tetrachloride using iron(II) iron(III) hydroxide sulfate (green rust). *Environ. Sci. Technol.* **33**, 307–311.

Ertani A., Mietto A., Borin M. and Nardi S. (2017) Chromium in agricultural soils and crops: A review. *Water. Air. Soil Pollut.* **228**, 1–12.

European Commission - JRC (2014) Progress in the management of contaminated sites in Europe. *EUR/26376 EN*, Joint Research Centre.

Faisal A. A. H., Sulaymon A. H. and Khaliefa Q. M. (2018) A review of permeable reactive barrier as passive sustainable technology for groundwater remediation. *Int. J. Environ. Sci. Technol.* **15**, 1123–1138.

Fan D., Anitori R. P., Tebo B. M., Tratnyek P. G., Pacheco J. S. L., Kukkadapu R. K., Engelhard M. H., Bowden M. E., Kovarik L. and Arey B. W. (2013) Reductive sequestration of pertechnetate (99TcO4-) by nano zerovalent iron (nZVI) transformed by abiotic sulfide. *Environ. Sci. Technol.* **47**, 5302–5310.

Fan D., Lan Y., Tratnyek P. G., Johnson R. L., Filip J., O'Carroll D. M., Nunez Garcia A. and Agrawal A. (2017) Sulfidation of iron-based materials: A review of processes and implications for water treatment and remediation. *Environ. Sci. Technol.* **51**, 13070–13085.

Fan D., O'Brien Johnson G., Tratnyek P. G. and Johnson R. L. (2016a) Sulfidation of nano zerovalent iron (nZVI) for improved selectivity during in-situ chemical reduction (ISCR). *Environ. Sci. Technol.* **50**, 9558–9565.

Fan D., O'Carroll D. M., Elliott D. W., Xiong Z., Tratnyek P. G., Johnson R. L. and Nunez Garcia A. (2016b) Selectivity of nano zerovalent iron in in situ chemical reduction: Challenges and improvements. *Remediation* **26**, 27–40.

Fawcett E. (1988) Spin-density-wave antiferromagnetism in chromium. *Rev. Mod. Phys.* **60**, 209–283.

Feitknecht W. and Keller G. (1950) Uber die dunkelgrunen Hydroxyverbindungen des Eisensl. *Zeitschrift für Anorg. und Allg. Chemie* **262**, 61–68.

Fendorf S. E. and Li G. (1996) Kinetics of chromate reduction by ferrous iron. *Environ. Sci. Technol.* **30**, 1614–1617.

Fendorf S. E. and Zasoski R. J. (1992) Chromium(III) oxidation by Δ-manganese oxide (MnO2). 1. Characterization. *Environ. Sci. Technol.* **26**, 79–85.

FisherScientific (2020) Chemical structure of sodium carboxymethyl cellulose (CMC). *Fish. Sci. Prod. Website*. Available at: https://www.fishersci.com/shop/products/pyruvic-acid-100gr/50493623 [Accessed December 6, 2020].

Fournier-Salaün M. C. and Salaün P. (2007) Quantitative determination of hexavalent chromium in aqueous solutions by UV-Vis spectrophotometer. *Cent. Eur. J. Chem.* **5**, 1084–1093.

Franco D. V., Da Silva L. M. and Jardim W. F. (2009) Reduction of hexavalent chromium in soil and ground water using zero-valent iron under batch and semi-batch conditions. *Water. Air. Soil Pollut.* **197**, 49–60.

Fruchter J. (2002) In situ treatment of chromium-contaminated groundwater. *Environ. Sci. Technol.* **36**.

Fruchter J. S., Cole C. R., Williams M. D., Vermeul V. R., Amonette J. E., Szecsody J. E., Istok J. D. and Humphrey M. D. (2000) Creation of a subsurface permeable Treatment zone for aqueous chromate contamination using in situ redox manipulation. *Spring Gr. Water Mon. Remed.* **20**, 66–77.

Gad C. S. (1989) Acute and chronic systemic chromium toxicity. *Sci. Total Environ.* **86**, 149–157.

Gastone F., Tosco T. and Sethi R. (2014a) Green stabilization of microscale iron particles using guar gum: Bulk rheology, sedimentation rate and enzymatic degradation. *J. Colloid Interface Sci.* **421**, 33–43.

Gastone F., Tosco T. and Sethi R. (2014b) Guar gum solutions for improved delivery of iron particles in porous

References

media (Part 1): Porous medium rheology and guar gum-induced clogging. *J. Contam. Hydrol.* **166**, 23–33.

Gavaskar A. R. (1999) Design and construction techniques for permeable reactive barriers. *J. Hazard. Mater.* **68**, 41–71.

Gavaskar A., Yoon W. S., Sminchak J., Sass B., Gupta N., Hicks J. and Lal V. (2005) Long term performance assessment of a permeable reactive barrier at former naval air station moffett field. *CR 05-006-ENV*, Naval Facilities Engineering Command, Port Hueneme.

Géhin A., Ruby C., Abdelmoula M., Benali O., Ghanbaja J., Refait P. and Génin J. M. R. (2002) Synthesis of Fe(II-III) hydroxysulphate green rust by coprecipitation. *Solid State Sci.* **4**, 61–66.

Génin J. M. R., Bourrié G., Trolard F., Abdelmoula M., Jaffrezic A., Refait P., Maitre V., Humbert B. and Herbillon A. (1998) Thermodynamic equilibria in aqueous suspensions of synthetic and natural Fe(II)-Fe(III) green rusts: Occurrences of the mineral in hydromorphic soils. *Environ. Sci. Technol.* **32**, 1058–1068.

Génin J. M. R., Olowe A. A., Refait P. and Simon L. (1996) On the stoichiometry and pourbaix diagram of Fe(II)-Fe(III) hydroxy-sulphate or sulphate-containing green rust 2: An electrochemical and mössbauer spectroscopy study. *Corros. Sci.* **38**, 1751–1762.

Génin J. M. R., Refait P., Bourrié G., Abdelmoula M. and Trolard F. (2001) Structure and stability of the Fe(II)-Fe(III) green rust "fougerite" mineral and its potential for reducing pollutants in soil solutions. *Appl. Geochemistry* **16**, 559–570.

Génin J. M. R., Ruby C., Géhin A. and Refait P. (2006) Synthesis of green rusts by oxidation of Fe(OH)2, their products of oxidation and reduction of ferric oxyhydroxides; Eh-pH Pourbaix diagrams. *Comptes Rendus - Geosci.* **338**, 433–446.

Gerth J., Dankwarth F. and Förstner U. (2001) Natural Attenuation of Inorganic Pollutants — a Critical View. *Treat. Contam. Soil*, 603–614.

Geurts J. J. M., Sarneel J. M., Willers B. J. C., Roelofs J. G. M., Verhoeven J. T. A. and Lamers L. P. M. (2009) Interacting effects of sulphate pollution, sulphide toxicity and eutrophication on vegetation development in fens: A mesocosm experiment. *Environ. Pollut.* **157**, 2072–2081.

Gheju M. (2011) Hexavalent chromium reduction with zero-valent iron (ZVI) in aquatic systems. *Water Air Soil Pollut.* **222**, 103–148.

Gillham R. W. and O'Hannesin S. F. (1994) Enhanced degradation of halogenated haliphatics by zero-valent iron. *Ground Water* **32**, 958–967.

Gong L., Shasha S., Neng L., Wenqiang X., Ziwei Y., Gao B., O'Carroll D. M. and Feng H. (2020) Sulfidation enhances stability and mobility of carboxymethyl cellulose stabilized nanoscale zero-valent iron in saturated porous media. *Sci. Total Environ.* **718**, 137427.

Gong Y., Gai L., Tang J., Fu J., Wang Q. and Zeng E. Y. (2017) Reduction of Cr(VI) in simulated groundwater by FeS-coated iron magnetic nanoparticles. *Sci. Total Environ.* **595**, 743–751.

Gong Y., Tang J. and Zhao D. (2016) Application of iron sulfide particles for groundwater and soil remediation: A review. *Water Res.* **89**, 309–320.

Gould J. P. (1982) The kinetics of hexavalent chromium reduction by metallic iron. *Water Res.* **16**, 871–877.

Greiner A., Schreiber W., Brix G. and Kinzelbach W. (1997) Magnetic resonance imaging of paramagnetic tracers in porous media: Quantification of flow and transport parameters. *Water Resour. Res.* **33**, 1461–1473.

Grossl P. R., Eick M., Sparks D. L., Goldberg S. and Ainsworth C. C. (1997) Arsenate and chromate retention mechanisms on goethite. 2. Kinetic evaluation using a pressure-jump relaxation technique. *Environ. Sci. Technol.* **31**, 321–326.

Gu B., Phelps T. J., Liang L., Dickey M. J., Roh Y., Kinsall B. L., Palumbo A. V. and Jacobs G. K. (1999) Biogeochemical dynamics in zero-valent iron columns: Implications for permeable reactive barriers. *Environ. Sci. Technol.* **33**, 2170–2177.

Gu Y., Wang B., He F., Bradley M. J. and Tratnyek P. G. (2017) Mechanochemically sulfidated microscale zero valent iron: Pathways, kinetics, mechanism, and efficiency of trichloroethylene dechlorination. *Environ. Sci. Technol.* **51**, 12653–12662.

Guilbaud R., White M. L. and Poulton S. W. (2013) Surface charge and growth of sulphate and carbonate green rust in aqueous media. *Geochim. Cosmochim. Acta* **108**, 141–153.

References

Gupta V. K., Agarwal S. and Saleh T. A. (2011) Chromium removal by combining the magnetic properties of iron oxide with adsorption properties of carbon nanotubes. *Water Res.* **45**, 2207–2212.

Gupta V. K., Srivastava S. K. and Mohan D. (1997) Equilibrium uptake, sorption dynamics, process optimization, and column operations for the removal and recovery of malachite green from wastewater using activated carbon and activated slag. *Ind. Eng. Chem. Res.* **36**, 2207–2218.

Gupta V. K., Tyagi I., Agarwal S., Singh R., Chaudhary M., Harit A. and Kushwaha S. (2016) Column operation studies for the removal of dyes and phenols using a low cost adsorbent. *Glob. J. Environ. Sci. Manag.* **2**, 1–10.

Han I., Schlautman M. A. and Batchelor B. (2006) Removal of hexavalent chromium from groundwater by granular activated carbon. *Water Environ. Res.* **72**, 29–39.

Han Y. S., Hyun S. P., Jeong H. Y. and Hayes K. F. (2012) Kinetic study of cis-dichloroethylene (cis-DCE) and vinyl chloride (VC) dechlorination using green rusts formed under varying conditions. *Water Res.* **46**, 6339–6350.

Han Y. and Yan W. (2016) Reductive dechlorination of trichloroethene by zero-valent iron nanoparticles: reactivity enhancement through sulfidation treatment. *Environ. Sci. Technol.* **50**, 12992–13001.

Hansen H. C. B., Borggaard O. K. and Sørensen J. (1994) Evaluation of the free energy of formation of Fe(II)-Fe(III) hydroxide-sulphate (green rust) and its reduction of nitrite. *Geochim. Cosmochim. Acta* **58**, 2599–2608.

Hansen H. C. B., Guldberg S., Erbs M. and Bender Koch C. (2001) Kinetics of nitrate reduction by green rusts - effects of interlayer anion and Fe(II):Fe(III) ratio. *Appl. Clay Sci.* **18**, 81–91.

Hasan M. A., Selim Y. T. and Mohamed K. M. (2009) Removal of chromium from aqueous waste solution using liquid emulsion membrane. *J. Hazard. Mater.* **168**, 1537–1541.

He F., Zhang M., Qian T. and Zhao D. (2009) Transport of carboxymethyl cellulose stabilized iron nanoparticles in porous media: Column experiments and modeling. *J. Colloid Interface Sci.* **334**, 96–102.

He F. and Zhao D. (2007) Manipulating the size and dispersibility of zerovalent iron nanoparticles by use of carboxymethyl cellulose stabilizers. *Environ. Sci. Technol.* **41**, 6216–6221.

He F., Zhao D., Liu J. and Roberts C. B. (2007) Stabilization of Fe-Pd nanoparticles with sodium carboxymethyl cellulose for enhanced transport and dechlorination of trichloroethylene in soil and groundwater. *Ind. Eng. Chem. Res.* **46**, 29–34.

He F., Zhao D. and Paul C. (2010) Field assessment of carboxymethyl cellulose stabilized iron nanoparticles for in situ destruction of chlorinated solvents in source zones. *Water Res.* **44**, 2360–2370.

He Y. T. and Traina S. J. (2005) Cr(VI) reduction and immobilization by magnetite under alkaline pH conditions: The role of passivation. *Environ. Sci. Technol.* **39**, 4499–4504.

He Y. T., Wilson J. T. and Wilkin R. T. (2010) Impact of iron sulfide transformation on trichloroethylene degradation. *Geochim. Cosmochim. Acta* **74**, 2025–2039.

Heiserman D. L. (1992) *Exploring Chemical Elements and their Compounds.*, McGraw-Hill Companies, 376 pages.

Henderson A. D. and Demond A. H. (2007) Long-term performance of zero-valent iron permeable reactive barriers: A critical review. *Environ. Eng. Sci.* **24**, 401–423.

Higgins M. R. and Olson T. M. (2009) Life-cycle case study comparison of permeable reactive barrier versus pump-and-treat remediation. *Environ. Sci. Technol.* **43**, 9432–9438.

Hosseini S. M. and Tosco T. (2013) Transport and retention of high concentrated nano-Fe/Cu particles through highly flow-rated packed sand column. *Water Res.* **47**, 326–338.

Hou J., Zhang M., Wang P., Wang C., Miao L., Xu Y., You G., Lv B., Yang Y. and Liu Z. (2017) Transport and long-term release behavior of polymer-coated silver nanoparticles in saturated quartz sand: The impacts of input concentration, grain size and flow rate. *Water Res.* **127**, 86–95.

Hu Z., Zhao J., Gao H., Nourafkan E. and Wen D. (2017) Transport and deposition of carbon nanoparticles in saturated porous media. *Energies* **10**, 1–17.

Iqbal M., Lyon B. A., Ureña-Benavides E. E., Moaseri E., Fei Y., McFadden C., Javier K. J., Ellison C. J., Pennell K. D. and Johnston K. P. (2017) High temperature stability and low adsorption of sub-100 nm magnetite nanoparticles grafted with sulfonated copolymers on Berea sandstone in high salinity brine. *Colloids*

References

Surfaces A Physicochem. Eng. Asp. **520**, 257–267.

Istok J. D., Amonette J. E., Cole C. R., Fruchter J. S., D.; H. M., Szecsody J. E., Teel S. S., Vermeul V. R., Williams M. D. and Yabusaki S. B. (1999) In situ redox manipulation by dithionite injection: Intermediate-scale laboratory experiments. *Ground Water* **37**, 884–889.

ITRC (2008) In situ bioremediation of chlorinated ethene: DNAPL source zones - Technical/Regulatory guidance (The interstate technology and regulatory council: Bioremediation of DNAPLs Team). , Washington, DC.

ITRC (2011) Permeable reactive barrier: Technology update - Technical/Regulatory guidance (The Interstate Technology and Regulatory Council PRB: Technology Update Team). , Washington, DC.

ITRC (2005) Permeable Reactive Barriers : Lessons Learned/New Directions - Technical/Regulatory guidelines (The Interstate Technology and Regulatory Council Permeable: Reactive Barriers Team). , Washington, DC.

Izbicki J. A., Wright M. T., Seymour W. A., McCleskey R. B., Fram M. S., Belitz K. and Esser B. K. (2015) Cr(VI) occurrence and geochemistry in water from public-supply wells in California. *Appl. Geochemistry* **63**, 203–217.

Jada A., Ait Akbour R. and Douch J. (2006) Surface charge and adsorption from water onto quartz sand of humic acid. *Chemosphere* **64**, 1287–1295.

Jan A. T., Azam M., Siddiqui K., Ali A., Choi I. and Haq Q. M. R. (2015) Heavy metals and human health: Mechanistic insight into toxicity and counter defense system of antioxidants. *Int. J. Mol. Sci.* **16**, 29592–29630.

Jeong H. Y., Anantharaman K., Hyun S. P., Son M. and Hayes K. F. (2013) pH impact on reductive dechlorination of cis-dichloroethylene by Fe precipitates: An X-ray absorption spectroscopy study. *Water Res.* **47**, 6639–6649.

Jeong H. Y. and Hayes K. F. (2003) Impact of transition metals on reductive dechlorination rate of hexachloroethane by mackinawite. *Environ. Sci. Technol.* **37**, 4650–4655.

JGW (2008) Magnesiochromite, Wakamatsu mine, Japan. *Mindat.org*. Available at: https://www.mindat.org/photo-155305.html [Accessed December 6, 2020].

Johnson C. A., Freyer G., Fabisch M., Caraballo M. A., Küsel K. and Hochella M. F. (2014) Observations and assessment of iron oxide and green rust nanoparticles in metal-polluted mine drainage within a steep redox gradient. *Environ. Chem.* **11**, 377–391.

Johnson R. L., Nurmi J. T., O'Brien Johnson G. S., Fan D., O'Brien Johnson R. L., Shi Z., Salter-Blanc A. J., Tratnyek P. G. and Lowry G. V. (2013) Field-scale transport and transformation of carboxymethylcellulose-stabilized nano zero-valent iron. *Environ. Sci. Technol.* **47**, 1573–1580.

Jönsson J. and Sherman D. M. (2008) Sorption of As(III) and As(V) to siderite, green rust (fougerite) and magnetite: Implications for arsenic release in anoxic groundwaters. *Chem. Geol.* **255**, 173–181.

Jorand F. P. A., Sergent A. S., Remy P. P., Bihannic I., Ghanbaja J., Lartiges B., Hanna K. and Zegeye A. (2013) Contribution of anionic vs. neutral polymers to the formation of green rust 1 from γ-FeOOH bioreduction. *Geomicrobiol. J.* **30**, 600–615.

Jung C., Heo J., Han J., Her N., Lee S. J., Oh J., Ryu J. and Yoon Y. (2013) Hexavalent chromium removal by various adsorbents: Powdered activated carbon, chitosan, and single/multi-walled carbon nanotubes. *Sep. Purif. Technol.* **106**, 63–71.

Kamolpornwijit W., Liang L., West O. R., Moline G. R. and Sullivan A. B. (2003) Preferential flow path development and its influence on long-term PRB performance: Column study. *J. Contam. Hydrol.* **66**, 161–178.

Karn B., Kuiken T. and Otto M. (2009) Nanotechnology and in situ remediation: A review of the benefits and potential risks. *Environ. Health Perspect.* **117**, 1823–1831.

Kasel D., Bradford S. A., Šimůnek J., Heggen M., Vereecken H. and Klumpp E. (2013) Transport and retention of multi-walled carbon nanotubes in saturated porous media: Effects of input concentration and grain size. *Water Res.* **47**, 933–944.

Kate Bronstein (2005) Permeable reactive barriers for inorganic and radionuclide. *U.S. Environ. Prot. Agency*, 1–62.

Khan A. I. and O'Hare D. (2002) Intercalation chemistry of layered double hydroxides: Recent developments and

References

applications. *J. Mater. Chem.* **12**, 3191–3198.

Kim E. J., Kim J. H., Azad A. M. and Chang Y. S. (2011) Facile synthesis and characterization of Fe/FeS nanoparticles for environmental applications. *ACS Appl. Mater. Interfaces* **3**, 1457–1462.

Kim H.-J., Phenrat T., Tilton R. D. and Lowry G. V. (2009) Fe0 nanoparticles remain mobile in porous media after aging due to slow desorption of polymeric surface modifiers. *Environ. Sci. Technol.* **43**, 3824–3830.

Kim J., Nielsen U. G. and Grey C. P. (2008) Local environments and lithium adsorption on the iron oxyhydroxides lepidocrocite (γ-FeOOH) and goethite (α-FeOOH): A 2H and 7Li solid-state MAS NMR study. *J. Am. Chem. Soc.* **130**, 1285–1295.

Kirpichtchikova T. A., Manceau A., Spadini L., Panfili F., Marcus M. A. and Jacquet T. (2006) Speciation and solubility of heavy metals in contaminated soil using X-ray microfluorescence, EXAFS spectroscopy, chemical extraction, and thermodynamic modeling. *Geochim. Cosmochim. Acta* **70**, 2163–2190.

Klausen J., Vikesland P. J., Kohn T., Burris D. R., Ball W. P. and Roberts A. L. (2003) Longevity of granular iron in groundwater treatment processes: Solution composition effects on reduction of organohalides and nitroaromatic compounds. *Environ. Sci. Technol.* **37**, 1208–1218.

Kleber R. J. and Helz G. R. (1992) Indirect photoreduction of aqueous chromium(VI). *Environ. Sci. Technol.* **26**, 307–312.

Ko C. H. and Elimelech M. (2000) The "shadow effect" in colloid transport and deposition dynamics in granular porous media: Measurements and mechanisms. *Environ. Sci. Technol.* **34**, 3681–3689.

Kocur C. M., Chowdhury A. I., Sakulchaicharoen N., Boparai H. K., Weber K. P., Sharma P., Krol M. M., Austrins L., Peace C., Sleep B. E. and O'Carroll D. M. (2014) Characterization of nZVI mobility in a field scale test. *Environ. Sci. Technol.* **48**, 2862–2869.

Kocur C. M., O'Carroll D. M. and Sleep B. E. (2013) Impact of nZVI stability on mobility in porous media. *J. Contam. Hydrol.* **145**, 17–25.

Kukkadapu R. K., Zachara J. M., Fredrickson J. K. and Kennedy D. W. (2004) Biotransformation of two-line silica-ferrihydrite by a dissimilatory Fe(III)-reducing bacterium: Formation of carbonate green rust in the presence of phosphate. *Geochim. Cosmochim. Acta* **68**, 2799–2814.

Kuppusamy S., Thavamani P., Megharaj Mallavarapu, Kadiyala V. and Ravi N. (2016) In-situ remediation approaches for the management of contaminated sites: a comprehensive overview. In *Reviews of environmental contamination and toxicology* (ed. Pim De Voogt). Springer, Summerfield, N Carolina. pp. 1–115.

Lai K. C. K. and Lo I. M. C. (2008) Removal of chromium(VI) by acid-washed zero-valent iron under various groundwater geochemistry conditions. *Environ. Sci. Technol.* **42**, 1238–1244.

Lakshmanan S., Holmes W. M., Sloan W. T. and Phoenix V. R. (2015a) Characterization of nanoparticle transport through quartz and dolomite gravels by magnetic resonance imaging. *Int. J. Environ. Sci. Technol.* **12**, 3373–3384.

Lakshmanan S., Holmes W. M., Sloan W. T. and Phoenix V. R. (2015b) Nanoparticle transport in saturated porous medium using magnetic resonance imaging. *Chem. Eng. J.* **266**, 156–162.

Latta D., Boyanov M., Kemner K., O'Loughlin E. and Scherer M. (2015) Reaction of Uranium(VI) with green rusts: Effect of interlayer anion. *Curr. Inorg. Chem.* **5**, 156–168.

Lee W. and Batchelor B. (2002) Abiotic reductive dechlorination of chlorinated ethylenes by iron-bearing soil minerals. 2. Green rust. *Environ. Sci. Technol.* **36**, 5348–5354.

Lee W. and Batchelor B. (2003) Reductive capacity of natural reductants. *Environ. Sci. Technol.* **37**, 535–541.

Legrand L., Abdelmoula M., Géhin A., Chaussé A. and Génin J. M. R. (2001) Electrochemical formation of a new Fe(II)-Fe(III) hydroxy-carbonate green rust: Characterization and morphology. *Electrochim. Acta* **46**, 1815–1822.

Legrand L., El Figuigui A., Mercier F. and Chausse A. (2004) Reduction of aqueous chromate by Fe(II)/Fe(III) carbonate green rust: Kinetic and mechanistic studies. *Environ. Sci. Technol.* **38**, 4587–4595.

Lennie A. R., Redfern S. A. T., Schofield P. F. and Vaughan D. J. (1995) Synthesis and Rietveld crystal structure refinement of mackinawite, tetragonal FeS. *Mineral. Mag.* **59**, 677–683.

Lenntech (2020) Chromium in water. *Elem. water*. Available at: https://www.lenntech.com/periodic/water/chromium/chromium-and-water.htm#:~:text=Rivers contain

References

approximately 1 ppb,the River Elbe in 1988.&text=In natural waters trivalent chromium is most abundant. [Accessed December 6, 2020].

Li J., Rajajayavel S. R. C. and Ghoshal S. (2016) Transport of carboxymethyl cellulose-coated zerovalent iron nanoparticles in a sand tank: Effects of sand grain size, nanoparticle concentration and injection velocity. *Chemosphere* **150**, 8–16.

Li J., Zhang X., Liu M., Pan B., Zhang W., Shi Z. and Guan X. (2018) Enhanced reactivity and electron selectivity of sulfidated zerovalent iron toward chromate under aerobic conditions. *Environ. Sci. Technol.* **52**, 2988–2997.

Li L., Benson C. H. and Lawson E. M. (2005) Impact of fouling on the long-term hydraulic behaviour of permeable reactive barriers. *Ground Water* **43**, 582–596.

Li L., Benson C. H. and Lawson E. M. (2006) Modeling porosity reductions caused by mineral fouling in continuous-wall permeable reactive barriers. *J. Contam. Hydrol.* **83**, 89–121.

Liang X. and Butler E. C. (2010) Effects of natural organic matter model compounds on the transformation of carbon tetrachloride by chloride green rust. *Water Res.* **44**, 2125–2132.

Liang X., Paul Philp R. and Butler E. C. (2009) Kinetic and isotope analyses of tetrachloroethylene and trichloroethylene degradation by model Fe(II)-bearing minerals. *Chemosphere* **75**, 63–69.

Liang Y., Bradford S. A., Simunek J., Vereecken H. and Klumpp E. (2013) Sensitivity of the transport and retention of stabilized silver nanoparticles to physicochemical factors. *Water Res.* **47**, 2572–2582.

Lim T. T. and Zhu B. W. (2008) Effects of anions on the kinetics and reactivity of nanoscale Pd/Fe in trichlorobenzene dechlorination. *Chemosphere* **73**, 1471–1477.

Liu D., Johnson P. R. and Elimelech M. (1995) Colloid deposition dynamics in flow through porous media: Role of electrolyte concentration. *Environ. Sci. Technol.* **29**, 2963–2973.

Liu G., Zhong H., Ahmad Z., Yang X. and Huo L. (2019) Transport of engineered nanoparticles in porous media and its enhancement for remediation of contaminated groundwater. *Crit. Rev. Environ. Sci. Technol.* **50**, 2301–2378.

Liu Q., Lazouskaya V., He Q. and Jin Y. (2010) Effect of particle shape on colloid retention and release in saturated porous media. *J. Environ. Qual.* **39**, 500–508.

Liu Y. and Lowry G. V. (2006) Effect of particle age (Fe0 content) and solution pH on NZVI reactivity: H2 evolution and TCE dechlorination. *Environ. Sci. Technol.* **40**, 6085–6090.

Liu Y., Majetich S. A., Tilton R. D., Sholl D. S. and Lowry G. V. (2005) TCE dechlorination rates, pathways, and efficiency of nanoscale iron particles with different properties. *Environ. Sci. Technol.* **39**, 1338–1345.

Lopez C. G., Rogers S. E., Colby R. H., Graham P. and Cabral J. T. (2014) Structure of sodium carboxymethyl cellulose aqueous solutions: A SANS and rheology study. *J. Polym. Sci. Part B Polym. Phys.* **53**, 492–501.

Loyaux-Lawniczak S., Lecomte P. and Ehrhardt J. J. (2001) Behavior of hexavalent chromium in a polluted groundwater: Redox processes and immobilization in soils. *Environ. Sci. Technol.* **35**, 1350–1357.

Loyaux-Lawniczak S., Refait P., Ehrhardt J. J., Lecomte P. and Génin J. M. R. (2000) Trapping of Cr by formation of ferrihydrite during the reduction of chromate ions by Fe(II)-Fe(III) hydroxysalt green rusts. *Environ. Sci. Technol.* **34**, 438–443.

Lunk H.-J. (2015) Discovery, properties and applications of chromium and its compounds. *ChemTexts* **1**, 1–17.

MacDonald J. A. (2000) Evaluating natural attenuation for groundwater cleanup. *Environ. Sci. Technol.* **34**, 346–353.

Makovicky E. (2006) Crystal structures of sulfides and other chalcogenides. *Rev. Mineral. Geochemistry* **61**, 7–125.

Malone D. R. (2004) In situ immobilization of hexavalent chromium in groundwater with ferrous iron: A case study. In *Proceedings of the Fourth International Conference on Remediation of Chlorinated and Recalcitrant Compounds* ARCADIS, Inc., Raleigh, NC.

Mangayayam M. C., Dideriksen K. and Tobler D. J. (2018) Can or cannot green rust reduce chlorinated ethenes? *Energy Procedia* **146**, 173–178.

Mangayayam M., Dideriksen K., Ceccato M. and Tobler D. J. (2019a) The structure of sulfidized zero valent iron by one-pot synthesis: Impact on contaminant selectivity and long-term performance. *Environ. Sci. Technol.* **53**, 4389–4396.

References

Mangayayam M., Perez J. P. H., Dideriksen K., Freeman H. M., Bovet N., Benning L. G. and Tobler D. J. (2019b) Structural transformation of sulfidized zerovalent iron and its impact on long-term reactivity. *Environ. Sci. Nano* **6**, 3422–3430.

Manning B. A., Kiser J. R., Kwon H. and Kanel S. R. (2007) Spectroscopic investigation of Cr(III)- and Cr(VI)-treated nanoscale zerovalent iron. *Environ. Sci. Technol.* **41**, 586–592.

Mao X., Barry D. A., Li L., Stagnitti F., Allinson G. and Turoczy N. (2004) Modelling the fate of chromated copper arsenate in a sandy soil. *Water. Air. Soil Pollut.* **156**, 357–377.

Mateo-Sagasta J., Zadeh S. M. and Turral H. (2017) Water pollution from agriculture: A global review - Executive summary. *CGIAR*, FAO and IWMI.

Matheson L. J. (1994) Abiotic and biotic reductive dehalogenation of halogenated methanes. *PhD Thesis*.

Mattison N. T., O'Carroll D. M., Kerry Rowe R. and Petersen E. J. (2011) Impact of porous media grain size on the transport of multi-walled carbon nanotubes. *Environ. Sci. Technol.* **45**, 9765–9775.

May R. and Li Y. (2013) The effects of particle size on the deposition of fluorescent nanoparticles in porous media: Direct observation using laser scanning cytometry. *Colloids Surfaces A Physicochem. Eng. Asp.* **418**, 84–91.

Mayer K. U., Frind E. O. and Blowes D. W. (2002) Multicomponent reactive transport modeling in variably saturated porous media using a generalized formulation for kinetically controlled reactions. *Water Resour. Res.* **38**, 1–21.

McMurtry D. C. and Elton R. O. (1985) New approach to in situ treatment of contaminated groundwater. *Environ. Prog.* **4**, 168–170.

Mehmani Y. and Balhoff T. M. (2015) Eulerian network modeling of longitudinal. *Water Resour. Res.* **51**, 8586–8606.

Meija J., Coplen T. B., Berglund M., Brand W. A., De Bièvre P., Gröning M., Holden N. E., Irrgeher J., Loss R. D., Walczyk T. and Prohaska T. (2016) Atomic weights of the elements 2013 (IUPAC Technical Report). *Pure Appl. Chem.* **88**, 265–291.

Metal-Aid (2016) Groundwater remediation scheme. *Metail-Aid Proj. Website*. Available at: http://metal-aid.eu/ [Accessed December 6, 2020].

Mitra P., Banerjee P., Chakrabarti S., Sarkar D. and Bhattacharjee S. (2010) Solar photo reduction of hexavalent chromium in wastewater with zinc oxide semiconductor catalyst. In *International Conference on Environment 2010 (ICENV 2010)*

Morrison S. (2003) Performance evaluation of a permeable reactive barrier using reaction products as tracers. *Environ. Sci. Technol.* **37**, 2302–2309.

Morrison S. J., Metzler D. R. and Carpenter C. E. (2001) Uranium precipitation in a permeable reactive barrier by progressive irreversible dissolution of zerovalent iron. *Environ. Sci. Technol.* **35**, 385–390.

Morse J. W. and Arakaki T. (1993) Adsorption and coprecipitation of divalent metals with mackinawite (FeS). *Geochim. Cosmochim. Acta* **57**, 3635–3640.

Mueller N. C., Braun J., Bruns J., Černík M., Rissing P., Rickerby D. and Nowack B. (2012) Application of nanoscale zero valent iron (NZVI) for groundwater remediation in Europe. *Environ. Sci. Pollut. Res.* **19**, 550–558.

Mugo R. K. and Orians K. J. (1993) Seagoing method for the determination of Chromium(III) and total chromium in sea water by electron-capture detection gas chromatography. *Anal. Chim. Acta* **271**, 1–9.

Mulligan C. N. and Gibbs B. F. (2001) Remediation technologies for metal-contaminated soils and groundwater: an evaluation. *Eng. Geol.* **60**, 193–207.

Myneni S. C. B., Tokunaga T. K. and Brown Jr. G. E. (2011) Abiotic selenium redox transformations in presence of Fe (II, III) oxides. *Science* **278**, 1106–1109.

Nag S., Mondal A., Mishra U., Bar N. and Das S. K. (2016) Removal of chromium(VI) from aqueous solutions using rubber leaf powder: batch and column studies. *Desalin. Water Treat.* **57**, 16927–16942.

Naidu R., Bekele D. N. and Birke V. (2014) Permeable reactive barriers: Cost-effective and sustainable remediation of groundwater. In *Permeable Reactive Barriers - Sustainable Groundwater Remediation* (eds. R. Birke and V. Naidu). CRC Press, Boca Raton, FL, Chapter 1. pp. 1–24.

National Research Council (1994a) Characterizing sites for ground water cleanup. In *Alternatives for Ground*

References

Water Cleanup National Academy Press, Washington, DC, Chapter 5. pp. 193–212.

National Research Council (1994b) Complexity of the contaminated subsurface. In *Alternatives for Ground Water Cleanup* National Academy Press, Washington, DC, Chapter 2. pp. 35–79.

National Research Council (1994c) The ground water cleanup controversy. In *Alternatives for Ground Water Cleanup* National Academy Press, Washington, DC, Chapter 1. pp. 19–35.

O'Carroll D. M., Liu X., Mattison N. T. and Petersen E. J. (2013a) Impact of diameter on carbon nanotube transport in sand. *J. Colloid Interface Sci.* **390**, 96–104.

O'Carroll D. M., Sleep B., Krol M., Boparai H. and Kocur C. (2013b) Nanoscale zero valent iron and bimetallic particles for contaminated site remediation. *Adv. Water Resour.* **51**, 104–122.

O'Hannesin S. F. and Gillham R. W. (1998) Long-term performance of an in situ "iron wall" for remediation of VOCs. *Ground Water* **36**, 164–170.

O'Loughlin E. J., Kemner K. M. and Burris D. R. (2003) Effects of Ag(I), Au(III), and Cu(II) on the reductive dechlorination of carbon tetrachloride by green rust. *Environ. Sci. Technol.* **37**, 2905–2912.

O'Loughlin E. J., Larese-Casanova P., Scherer M. and Cook R. (2007) Green rust formation from the bioreduction of γ-FeOOH (lepidocrocite): Comparison of several Shewanella species. *Geomicrobiol. J.* **24**, 211–230.

Ona-Nguema G., Abdelmoula M., Jorand F., Benali O., Géhin A., Block J. C. and Génin J. M. R. (2002) Iron(II,III) hydroxycarbonate green rust formation and stabilization from lepidocrocite bioreduction. *Environ. Sci. Technol.* **36**, 16–20.

Oze C., Fendorf S., Bird D. K. and Coleman R. G. (2004) Chromium geochemistry of serpentine soils. *Int. Geol. Rev.* **46**, 97–126.

Pagilla K. R. and Canter L. W. (1999) Laboratory studies on remediation of chromium contaminated sites. *J. Environ. Eng.* **125**, 243–248.

Pal A., He Y., Jekel M., Reinhard M. and Gin K. Y. H. (2014) Emerging contaminants of public health significance as water quality indicator compounds in the urban water cycle. *Environ. Int.* **71**, 46–62.

Pantke C., Obst M., Benzerara K., Morin G., Ona-Nguema G., Dippon U. and Kappler A. (2012) Green rust formation during Fe(II) oxidation by the nitrate-reducing acidovorax sp. strain BoFeN1. *Environ. Sci. Technol.* **46**, 1439–1446.

Pawlisz A. V., Kent R. A., Schneider U. A. and Jefferson C. (1997) Canadian water quality guidelines for chromium. *Environ. Toxicol. Water Qual.* **12**, 123–184.

Pelley A. J. and Tufenkji N. (2008) Effect of particle size and natural organic matter on the migration of nano- and microscale latex particles in saturated porous media. *J. Colloid Interface Sci.* **321**, 74–83.

Peng H., Ma G., Ying W., Wang A., Huang H. and Lei Z. (2012) In situ synthesis of polyaniline/sodium carboxymethyl cellulose nanorods for high-performance redox supercapacitors. *J. Power Sources* **211**, 40–45.

Pérez A. P. and Rodríguez Eugenio N. (2018) Status of local soil contamination in Europe - Revision of the indicator "Progress in the management contaminated sites in Europe". *EUR 29124 EN*, JRC Technical Reports.

Perez J. P. H., Freeman H. M., Schuessler J. A. and Benning L. G. (2019) The interfacial reactivity of arsenic species with green rust sulfate (GRSO4). *Sci. Total Environ.* **648**, 1161–1170.

Petersen S. W., Thompson K. M. and Tonkin M. J. (2009) *Results from recent science and technology investigations targeting chromium in the 100D Area, Hanford Site, Washington, USA.*,

Peterson M. L., Brown G. E. and Parks G. A. (1996) Direct XAFS evidence for heterogeneous redox reaction at the aqueous chromium/magnetite interface. *Colloids Surfaces A Physicochem. Eng. Asp.* **107**, 77–88.

Peterson M. L., White A. F., Brown G. E. and Parks G. A. (1997) Surface passivation of magnetite by reaction with aqueous Cr(VI): XAFS and TEM results. *Environ. Sci. Technol.* **31**, 1573–1576.

Pettine M., D'Ottone L., Campanella L., Millero F. J. and Passino R. (1998) The reduction of chromium(VI) by iron(II) in aqueous solutions. *Geochim. Cosmochim. Acta* **62**, 1509–1519.

Phenrat T., Kim H. J., Fagerlund F., Illangasekare T. and Lowry G. V. (2010) Empirical correlations to estimate agglomerate size and deposition during injection of a polyelectrolyte-modified Fe0 nanoparticle at high particle concentration in saturated sand. *J. Contam. Hydrol.* **118**, 152–164.

References

Phenrat T., Kim H. J., Fagerlund F., Illangasekare T., Tilton R. D. and Lowry G. V. (2009a) Particle size distribution, concentration, and magnetic attraction affect transport of polymer-modified Fe0 nanoparticles in sand columns. *Environ. Sci. Technol.* **43**, 5079–5085.

Phenrat T., Liu Y., Tilton R. D. and Lowry G. V. (2009b) Adsorbed polyelectrolyte coatings decrease Fe0 nanoparticle reactivity with TCE in water: Conceptual model and mechanisms. *Environ. Sci. Technol.* **43**, 1507–1514.

Phenrat T., Saleh N., Sirk K., Kim H. J., Tilton R. D. and Lowry G. V. (2008) Stabilization of aqueous nanoscale zerovalent iron dispersions by anionic polyelectrolytes: adsorbed anionic polyelectrolyte layer properties and their effect on aggregation and sedimentation. *J. Nanoparticle Res.* **10**, 795–814.

Phenrat T., Saleh N., Sirk K., Tilton R. D. and Lowry G. V. (2007) Aggregation and sedimentation of aqueous nanoscale zerovalent iron dispersions. *Environ. Sci. Technol.* **41**, 284–290.

Phillips D. H. (2009) Permeable reactive barriers: A sustainable technology for cleaning contaminated groundwater in developing countries. *Desalination* **248**, 352–359.

Phillips D. H., Nooten T. Van, Bastiaens L., Russell M. I., Dickson K., Plant S., Ahad J. M. E., Newton T., Elliot T. and Kalin R. M. (2010) Ten year performance evaluation of a field-scale zero-valent iron permeable reactive barrier installed to remediate trichloroethene contaminated groundwater. *Environ. Sci. Technol.* **44**, 3861–3869.

Porubcan A. A. and Xu S. (2011) Colloid straining within saturated heterogeneous porous media. *Water Res.* **45**, 1796–1806.

Postma D. and Appelo C. A. J. (2000) Reduction of Mn-oxides by ferrous iron in a flow system: Column experiment and reactive transport modeling. *Geochim. Cosmochim. Acta* **64**, 1237–1247.

Poston T. M., Hanf R. W., Dirkes R. L. and Morasch L. F. (2002) *Hanford Site Environmental Report for Calendar Year 2001*., Pacific Northwest National Laborarory: Richland, Washington.

Powell R. M., Puls R. W., Hightower S. K. and Sabatini D. A. (1995) Coupled Iron Corrosion and Chromate Reduction: Mechanisms for Subsurface Remediation. *Environ. Sci. Technol.* **29**, 1913–1922.

Pratt A. R., Blowes D. W. and Ptacek C. J. (1997) Products of chromate reduction on proposed subsurface remediation material. *Environ. Sci. Technol.* **31**, 2492–2498.

PubChem (2020) Compound summary - Chromium. *Natl. Libr. Med.* Available at: https://pubchem.ncbi.nlm.nih.gov/compound/Chromium [Accessed December 6, 2020].

Puls R. W., Paul C. J. and Powell R. M. (1999) The application of in situ permeable reactive (zero-valent iron) barrier technology for the remediation of chromate-contaminated groundwater: A field test. *Appl. Geochemistry* **14**, 989–1000.

Quinten T. (2011) Evaluation of injection molding as a pharmaceutical production technology for sustained-release matrix tablets. *PhD Thesis*.

Rahman T., George J. and Shipley H. J. (2013) Transport of aluminum oxide nanoparticles in saturated sand: Effects of ionic strength, flow rate, and nanoparticle concentration. *Sci. Total Environ.* **463**–**464**, 565–571.

Rai D., Eary L. E. and Zachara J. M. (1989) Environmental chemistry of chromium. *Sci. Total Environ.* **86**, 15–23.

Rai D., Sass B. M. and Moore D. A. (1987) Chromium(III) hydrolysis constants and solubility of Chromium(III) hydroxide. *Inorg. Chem.* **26**, 345–349.

Rajajayavel S. R. C. and Ghoshal S. (2015) Enhanced reductive dechlorination of trichloroethylene by sulfidated nanoscale zerovalent iron. *Water Res.* **78**, 144–153.

Ramanan B., Holmes W. M., Sloan W. T. and Phoenix V. R. (2012) Investigation of nanoparticle transport inside coarse-grained geological media using magnetic resonance imaging. *Environ. Sci. Technol.* **46**, 360–366.

Randall S. R., Sherman D. M. and Ragnarsdottir K. V. (2001) Sorption of As(V) on green rust (Fe4(II)Fe2(III)(OH)12SO4 · 3H2O) and lepidocrocite (γ-FeOOH): Surface complexes from EXAFS spectroscopy. *Geochim. Cosmochim. Acta* **65**, 1015–1023.

Raychoudhury T., Naja G. and Ghoshal S. (2010) Assessment of transport of two polyelectrolyte-stabilized zero-valent iron nanoparticles in porous media. *J. Contam. Hydrol.* **118**, 143–151.

Raychoudhury T., Tufenkji N. and Ghoshal S. (2012) Aggregation and deposition kinetics of carboxymethyl cellulose-modified zero-valent iron nanoparticles in porous media. *Water Res.* **46**, 1735–1744.

References

Raychoudhury T., Tufenkji N. and Ghoshal S. (2014) Straining of polyelectrolyte-stabilized nanoscale zero valent iron particles during transport through granular porous media. *Water Res.* **50**, 80–89.

Refait P., Abdelmoula M., Trolard F., Génin J.-M. R., Ehrhardt J. J. and Bourrié G. (2001) Mössbauer and XAS study of a green rust mineral; the partial substitution of Fe2+ by Mg2+. *Am. Mineral.* **86**, 731–739.

Refait P., Géhin A., Abdelmoula M. and Génin J. M. R. (2003) Coprecipitation thermodynamics of Iron(II-III) hydroxysulphate green rust from Fe(II) and Fe(III) salts. *Corros. Sci.* **45**, 659–676.

Refait P. H., Abdelmoula M. and G.M.R. G. (1998) Mechanisms of formation and structure of green rust one in aqueous corrosion of iron in the presence of chloride ions. *Corros. Sci.* **40**, 1547–1560.

Refait P. H. and Génin J. M. R. (1993) The oxidation of ferrous hydroxide in chloride-containing aqueous media and Pourbaix diagrams of green rust one. *Corros. Sci.* **34**, 797–819.

Refait P., Simon L. and Génin J. M. R. (2000) Reduction of SeO42- anions and anoxic formation of iron(II)-iron(III) hydroxy-selenate green rust. *Environ. Sci. Technol.* **34**, 819–825.

Rennert T., Eusterhues K., De Andrade V. and Totsche K. U. (2012) Iron species in soils on a mofette site studied by Fe K-edge X-ray absorption near-edge spectroscopy. *Chem. Geol.* **332**–**333**, 116–123.

Reynolds G. W., Hoff J. T. and Gillham R. W. (1990) Sampling bias caused by materials used to monitor halocarbons in groundwater. *Environ. Sci. Technol.* **24**, 135–142.

Richard A A. (1997) Chromium as an essential nutrient for humans. *Regul. Toxicol. Pharmacol.* **26**, S35–S41.

Roberts A. L., Totten L. A., Arnold W. A., Burris D. R. and Campbell T. J. (1996) Reductive elimination of chlorinated ethylenes by zero-valent metals. *Environ. Sci. Technol.* **30**, 2654–2659.

Roh Y., Lee S. Y. and Elless M. P. (2000) Characterization of corrosion products in the permeable reactive barriers. *Environ. Geol.* **40**, 184–194.

Ruby C., Abdelmoula M., Aissa R., Medjahdi G., Brunelli M. and François M. (2008) Aluminium substitution in Iron(II-III)-layered double hydroxides: Formation and cationic order. *J. Solid State Chem.* **181**, 2285–2291.

Ruby C., Aïssa R., Géhin A., Cortot J., Abdelmoula M. and Génin J. M. (2006a) Green rusts synthesis by coprecipitation of FeII-FeIII ions and mass-balance diagram. *Comptes Rendus - Geosci.* **338**, 420–432.

Ruby C., Géhin A., Abdelmoula M., Génin J. M. R. and Jolivet J. P. (2003) Coprecipitation of Fe(II) and Fe(III) cations in sulphated aqueous medium and formation of hydroxysulphate green rust. *Solid State Sci.* **5**, 1055–1062.

Ruby C., Upadhyay C., Géhin A., Ona-Nguema G. and Génin J. M. R. (2006b) In situ redox flexibility of FeII-III oxyhydroxycarbonate green rust and fougerite. *Environ. Sci. Technol.* **40**, 4696–4702.

Ruby C., Usman M., Naille S., Hanna K., Carteret C., Mullet M., François M. and Abdelmoula M. (2010) Synthesis and transformation of iron-based layered double hydroxides. *Appl. Clay Sci.* **48**, 195–202.

Rudnick R. L. (2010) Earth's Continental Crust. In *Encyclopedia of Geochemistry* (ed. Springer International Publishing AG). part of Springer Nature 2018. pp. 392–417.

Saberinasr A., Rezaei M., Nakhaei M. and Hosseini S. M. (2016) Transport of CMC-stabilized nZVI in saturated sand column: The effect of particle concentration and soil grain size. *Water. Air. Soil Pollut.* **227**.

Saiers J. E., Hornberger G. M. and Liang L. (1994) First- and second-order kinetics approaches for modeling the transport of colloidal particles in porous media. *Subsurf. Hydrol.* **30**, 2499–2506.

Sakulchaicharoen N., O'Carroll D. M. and Herrera J. E. (2010) Enhanced stability and dechlorination activity of pre-synthesis stabilized nanoscale FePd particles. *J. Contam. Hydrol.* **118**, 117–127.

Saleh N. and Kim H. (2008) Ionic strength and composition affect the mobility of surface-modified Fe0 nanoparticles in water saturated sand columns. *Environ. Sci. Technol.*, 3349–3355.

Samimi S., Maghsoudnia N., Eftekhari R. B. and Dorkoosh F. (2019) Lipid-based nanoparticles for drug delivery systems. In *Characterization and Biology of Nanomaterials for Drug Delivery* (eds. S. S. Mohapatra, S. Ranjan, N. Dasgupta, R. K. Mishra, and S. Thomas). Micro and Nano Technologies. First Ed., Elsevier, Chapter 3. pp. 47–76.

Samsonov G. V. (1968) Mechanical properties of the elements. In *Handbook of the Physicochemical Properties of the Elements* (ed. G. V. Samsonov). Springer, Boston, MA., Chapter 6. pp. 387–446.

Santana Rodríguez J. J., Santana Hernández F. J. and González González J. E. (2002) XRD and SEM studies of the layer of corrosion products for carbon steel in various different environments in the province of Las

Palmas (The Canary Islands, Spain). *Corros. Sci.* **44**, 2425–2438.

Sarathy V., Tratnyek P. G., Nurmi J. T., Baer D. R., Amonette J. E., Chun C. L., Penn R. L. and Reardon E. J. (2008) Aging of iron nanoparticles in aqueous solution: effects on structure and reactivity. *J. Phys. Chem. C* **112**, 2286–2293.

Schad H., Haist-Gulde B., Klein R., Maier D., Maier M. and Schulze B. (2000) Funnel- and-gate at the former manufactured gas plant site in Karlsruhe: sorption test results, hydraulic and technical design, construction. In *Contaminated Soil 2000* Leipzig, Germany. pp. 2: 951-959.

Sedlak D. L. and Chan P. G. (1997) Reduction of hexavalent chromium by ferrous iron. *Geochim. Cosmochim. Acta* **61**, 2185–2192.

Sedman R. M., Beaumont J., McDonald T. A., Reynolds S., Krowech G. and Howd R. (2006) Review of the evidence regarding the carcinogenicity of hexavalent chromium in drinking water. *J. Environ. Sci. Heal. - Part C Environ. Carcinog. Ecotoxicol. Rev.* **24**, 155–182.

Seymour M. B., Chen G., Su C. and Li Y. (2013) Transport and retention of colloids in porous media: Does shape really matter? *Environ. Sci. Technol.* **47**, 8391–8398.

Sharma D. C. and Forster C. F. (1994) The treatment of chromium wastewaters using the sorptive potential of leaf mould. *Bioresour. Technol.* **49**, 31–40.

Sharma P., Bao D. and Fagerlund F. (2014) Deposition and mobilization of functionalized multiwall carbon nanotubes in saturated porous media: effect of grain size, flow velocity and solution chemistry. *Environ. Earth Sci.* **72**, 3025–3035.

Sharma S. and Bhattacharya A. (2017) Drinking water contamination and treatment techniques. *Appl. Water Sci.* **7**, 1043–1067.

Shen Y. S., Wang S. L., Tzou Y. M., Yan Y. Y. and Kuan W. H. (2012) Removal of hexavalent Cr by coconut coir and derived chars - The effect of surface functionality. *Bioresour. Technol.* **104**, 165–172.

Silva B., Figueiredo H., Quintelas C., Neves I. C. and Tavares T. (2008) Zeolites as supports for the biorecovery of hexavalent and trivalent chromium. *Microporous Mesoporous Mater.* **116**, 555–560.

Simon L., François M., Refait P., Renaudin G., Lelaurain M. and Génin J. M. R. (2003) Structure of the Fe(II-III) layered double hydroxysulphate green rust two from Rietveld analysis. *Solid State Sci.* **5**, 327–334.

Sirinawin W., Turner D. R. and Westerlund S. (2000) Chromium(VI) distributions in the Arctic and the Atlantic Oceans and a reassessment of the oceanic Cr cycle. *Mar. Chem.* **71**, 265–282.

Skovbjerg L. L., Stipp S. L. S., Utsunomiya S. and Ewing R. C. (2006) The mechanisms of reduction of hexavalent chromium by green rust sodium sulphate: Formation of Cr-goethite. *Geochim. Cosmochim. Acta* **70**, 3582–3592.

Smith J. W. N., Boshoff G. and Bone B. D. (2003) Good practice guidance on permeable reactive barriers for remediating polluted groundwater, and a review of their use in the UK. *L. Contam. Reclam.* **11**, 411–418.

Southard R. J., Li X., Eisen E. A. and Pinkerton K. E. (2014) Silica, crystalline. In *Encyclopedia of Toxicology* (ed. P. Wexler). Third Edition, Academic Press, Oxford. pp. 266–269.

Starr R. C. and Cherry J. A. (1994) In situ remediation of contaminated ground water: the funnel-and-gate system. *Groundwater* **32**, 465–476.

Tadesse I., Isoaho S. A., Green F. B. and Puhakka J. A. (2006) Lime enhanced chromium removal in advanced integrated wastewater pond system. *Bioresour. Technol.* **97**, 529–534.

Taylor S. R. (1964) Abundance of chemical elements in the continental crust: a new table. *Geochim. Cosmochim. Acta* **28**, 1273–1285.

Thiruvenkatachari R., Vigneswaran S. and Naidu R. (2008) Permeable reactive barrier for groundwater remediation. *J. Ind. Eng. Chem.* **14**, 145–156.

Thomas A., Eiche E., Göttlicher J., Steininger R., Benning, Liane G., Freeman H. M., Dideriksen K. and Neumann T. (2018) Products of hexavalent chromium reduction by green rust sodium sulfate and associated reaction mechanisms. *Soil Syst.* **2**, 58.

Thomas A. O., Drury D. M., Norris G., O´Hannesin S. F. and Vogan J. L. (1995) The In-Situ Treatment of Trichloroethene-Contaminated Groundwater Using a Reactive Barrier — Results of Laboratory Feasibility Studies and Preliminary Design Considerations. *Van Den Brink W.J., Bosman R., Arendt F. Contam. Soil '95. Soil Environ.* **5**, 1083–1091.

References

Tiraferri A., Chen K. L., Sethi R. and Elimelech M. (2008) Reduced aggregation and sedimentation of zero-valent iron nanoparticles in the presence of guar gum. *J. Colloid Interface Sci.* **324**, 71–79.

Tiraferri A. and Sethi R. (2009) Enhanced transport of zerovalent iron nanoparticles in saturated porous media by guar gum. *J. Nanoparticle Res.* **11**, 635–645.

Tobiszewski M. and Namieśnik J. (2012) Abiotic degradation of chlorinated ethanes and ethenes in water. *Environ. Sci. Pollut. Res.* **19**, 1994–2006.

Tosco T., Petrangeli Papini M., Cruz Viggi C. and Sethi R. (2014) Nanoscale zerovalent iron particles for groundwater remediation: A review. *J. Clean. Prod.* **77**, 10–21.

Tosco T. and Sethi R. (2010) Transport of non-newtonian suspensions of highly concentrated micro- and nanoscale iron particles in porous media: A modeling approach. *Environ. Sci. Technol.* **44**, 9062–9068.

Tratnyek P. G. and Johnson R. L. (2006) Nanotechnologies for environmental cleanup. *Nano Today* **1**, 44–48.

Travis C. C. and Doty C. B. (1990) Can contaminated aquifers at Superfund sites be remediated? *Environ. Sci. Technol.* **24**, 1464–1466.

Trolard F., Bourrié G., Abdelmoula M., Refait P. and Feder F. (2007) Fougerite, a new mineral of the pyroaurite-iowaite group: Description and crystal structure. *Clays Clay Miner.* **55**, 323–334.

Trolard F., Génin J. M. R., Abdelmoula M., Bourrié G., Humbert B. and Herbillon A. (1997) Identification of a green rust mineral in a reductomorphic soil by Mössbauer and Raman spectroscopies. *Geochim. Cosmochim. Acta* **61**, 1107–1111.

Tufenkji N. and Elimelech M. (2004) Deviation from the classical colloid filtration theory in the presence of repulsive DLVO interactions. *Langmuir* **20**, 10818–10828.

Tufenkji N., Miller G. F., Ryan J. N., Harvey R. W. and Elimelech M. (2004) Transport of Cryptosporidium oocysts in porous media: Role of straining and physicochemical filtration. *Environ. Sci. Technol.* **38**, 5932–5938.

US EPA (2008a) A systematic approach for evaluation of capture zones at pump and treat systems - Final project report. *EPA/600/R-08/003*, US Environmental Protection Agency, Cincinnati, OH.

US EPA (1999a) An in situ permeable reactive barrier for the treatment of hexavalent chromium and trichloroethylene in ground water: Volume 1. Design and installation. *EPA/600/R-99/095a*, US Environmental Protection Agency, Cincinnati, OH.

US EPA (1990) Basic of pump-and-treat ground-water remediation technology. *EPA/600/8-90/003*, US Environmental Protection Agency, Herndon, VA.

US EPA (2001) Cost analyses for selected groundwater cleanup projects: Pump and treat systems and permeable reactive arriers. *EPA/542/R-00/013*, US Environmental Protection Agency, Washington, DC.

US EPA (2018) Critical source area identification and BMP selection: Supplement to watershed planning handbook. *EPA 841/K-18/001*, US Environmental Protection Agency, Washington, DC.

US EPA (2002a) Economic analysis of the implementation of permeable reactive barriers for remediation of contaminated ground water. *EPA/600/R-02/034*, US Environmental Protection Agency, Cincinnati, OH.

US EPA (1989a) Evaluation of ground-water extraction remedies - Volume 1: Summary Report. *EPA/540/2-89/054*, US Environmental Protection Agency, Washington, DC.

US EPA (1989b) Evaluation of ground-water extraction remedies - Volume 2: Case studies. *EPA/540/2-89/054b*, US Environmental Protection Agency, Washington, DC.

US EPA (1989c) Evaluation of ground-water extraction remedies - Volume 3: General site data base reports. *EPA/540/2-89/054c*, US Environmental Protection Agency, Washington, DC.

US EPA (1999b) Field applications of in-situ remediation technologies: Permeable reactive barriers. *EPA/542/R-99/002*, US Environmental Protection Agency, Washington, DC.

US EPA (2002b) Field applications of in situ remediation technologies: Permeable reactive barriers. *EPA/542/R-1/122*, US Environmental Protection Agency, Washington, DC.

US EPA (2008b) Green remediation: incorporating sustainable environmental practices into remediation of contaminated sites. *EPA/542/R-08/002*, US Environmental Protection Agency, Cincinnati, OH.

US EPA (1997) Ground water issue design guidelines for conventional pump-and-treat systems. *EPA/540/S-97/504*, US Environmental Protection Agency, Washington, DC.

References

US EPA (1999c) Groundwater cleanup: Overview of operating experience at 28 sites. *EPA/542/R-99/006*, US Environmental Protection Agency, Washington, DC.

US EPA (2006) Inorganic contaminant accumulation in potable water distribution systems. *EPA/68/C-02/042*, US Environmental Protection Agency, Washington, DC.

US EPA (1994) Methods for monitoring pump-and-treat performance. *EPA/600/R-94/123*, US Environmental Protection Agency, Washington, DC.

US EPA (1998) Permeable reactive barrier technologies for contaminant remediation. *EPA/600/R-98/125*, US Environmental Protection Agency, Washington DC.

US EPA (1996) Pump-and-treat ground-water remediation: A guide for decision makers and practitioners. *EPA/625/R-95/005*, US Environmental Protection Agency, Washington DC.

US EPA (2020) Superfund: National Priorities List (NPL). *Superfund*. Available at: https://www.epa.gov/superfund/superfund-national-priorities-list-npl [Accessed June 10, 2020].

US Geological Survey (2020) Mineral commodity summaries 2020. *USGS*, US Geological Survey, Reston, VA.

Usman M., Byrne J. M., Chaudhary A., Orsetti S., Hanna K., Ruby C., Kappler A. and Haderlein S. B. (2018) Magnetite and green rust: Synthesis, properties, and environmental applications of mixed-valent iron minerals. *Chem. Rev.* **118**, 3251–3304.

Vermeul V. R., Szecsody J. E., Fritz B. G., Williams M. D., Moore R. C. and Fruchter J. S. (2014) An injectable apatite permeable reactive barrier for in situ 90Sr immobilization. *Groundw. Monit. Remediat.* **34**, 28–41.

Veselská V., Fajgar R., Číhalová S., Bolanz R. M., Göttlicher J., Steininger R., Siddique J. A. and Komárek M. (2016) Chromate adsorption on selected soil minerals: Surface complexation modeling coupled with spectroscopic investigation. *J. Hazard. Mater.* **318**, 433–442.

Viswanatha R. and Sarma D. D. (2007) Growth of nanocrystals in solution. In *Nanomaterials Chemistry* John Wiley & Sons, Ltd. pp. 139–170.

Voudrias E. A. (2001) Pump-and-treat remediation of groundwater contaminated by hazardous waste: Can it really be achieved? *Glob. NEST Int. J.* **3**, 1–10.

Wang C. B. and Zhang W. X. (1997) Synthesizing nanoscale iron particles for rapid and complete dechlorination of TCE and PCBs. *Environ. Sci. Technol.* **31**, 2154–2156.

Wang C., Bobba A. D., Attinti R., Shen C., Lazouskaya V., Wang L. P. and Jin Y. (2012) Retention and transport of silica nanoparticles in saturated porous media: Effect of concentration and particle size. *Environ. Sci. Technol.* **46**, 7151–7158.

Wang M., Gao B. and Tang D. (2016) Review of key factors controlling engineered nanoparticle transport in porous media. *J. Hazard. Mater.* **318**, 233–246.

Wang Q., Ellis P. R. and Ross-Murphy S. B. (2003) Dissolution kinetics of guar gum powders - II. Effects of concentration and molecular weight. *Carbohydr. Polym.* **53**, 75–83.

Wang Q., Qian H., Yang Y., Zhang Z., Naman C. and Xu X. (2010) Reduction of hexavalent chromium by carboxymethyl cellulose-stabilized zero-valent iron nanoparticles. *J. Contam. Hydrol.* **114**, 35–42.

Wang Y., Kim J. H., Baek J. B., Miller G. W. and Pennell K. D. (2012) Transport behavior of functionalized multi-wall carbon nanotubes in water-saturated quartz sand as a function of tube length. *Water Res.* **46**, 4521–4531.

Wang Y., Morin G., Ona-Nguema G., Juillot F., Guyot F., Calas G. and Brown G. E. (2010) Evidence for different surface speciation of arsenite and arsenate on green rust: An EXAFS and XANES study. *Environ. Sci. Technol.* **44**, 109–115.

Weijden C. H. and Middelburg J. J. (1989) Hydrogeochemistry of the river Rhine: Long term and seasonal variability, elemental budgets, base levels a n d pollution. *Water Res.* **23**, 1247–1266.

Weinrich (2014) Chromite - Mtoroshanga, Makonde District, Mashonaland West, Zimbabwe. *Weinrich Miner. Inc.* Available at: https://en.wikipedia.org/wiki/Chromite#/media/File:Chromite.jpg [Accessed December 6, 2020].

Werth C. J., Zhang C., Brusseau M. L., Oostrom M. and Baumann T. (2010) A review of non-invasive imaging methods and applications in contaminant hydrogeology research. *J. Contam. Hydrol.* **113**, 1–24.

Wharton M. J., Atkins B., Charnock J. M., Livens F. R., Pattrick R. A. D. and Collison D. (2000) An X-ray absorption spectroscopy study of the coprecipitation of Tc and Re with mackinawite (FeS). *Appl.*

Geochemistry **15**, 347–354.

Wilbur S., Abadin H., Fay M., Yu D., Tencza B., Sciences H., Ingerman L., Klotzbach J. and Shelly J. (2012) Health effects. In *Toxicological profile for chromium* U.S. Dept. of Health and Human Services, Public Health Service, Agency for Toxic Substances and Disease Registry, Atlanta, Georgia. pp. 49–215.

Wilkin R. T., Acree S. D., Ross R. R., Puls R. W., Lee T. R. and Woods L. L. (2014) Fifteen-year assessment of a permeable reactive barrier for treatment of chromate and trichloroethylene in groundwater. *Sci. Total Environ.* **468**–**469**, 186–194.

Wilkin R. T., Puls R. W. and Sewell G. W. (2003) Long-Term Performance of Permeable Reactive Barriers Using Zero-Valent Iron: Geochemical and Microbiological Effects. *Ground Water* **41**, 493–503.

Williams A. G. B. and Scherer M. M. (2001) Kinetics of Cr(VI) reduction by carbonate green rust. *Environ. Sci. Technol.* **35**, 3488–3494.

Wu Y., Geng L., Wang X., Chen R., Wei Y. and Wu D. (2013) Reductive transformation of p-nitrophenol by Fe(II) species: The effect of anionic media. *J. Hazard. Mater.* **263**, 556–561.

Wuana R. A. and Okieimen F. E. (2011) Heavy metals in contaminated soils: A review of sources, chemistry, risks and best available strategies for remediation. *ISRN Ecol.* **2011**, 1–20.

Xenidis A., Moirou A. and Paspaliaris I. (2002) Reactive Materials and Attenuation Processes for Permeable Reactive Barriers. *Miner. Wealth* **123**, 35–49.

Xu S., Liao Q. and Saiers J. E. (2008) Straining of nonspherical colloids in saturated porous media. *Environ. Sci. Technol.* **42**, 771–778.

Yabusaki S., Cabtrell K., Sass B. and Steefel C. (2001) Multicomponent reactive transport in an in situ zero-valent iron cell. *Environ. Sci. Technol.* **35**, 1493–1503.

Yao X., Deng S., Wu R., Hong S., Wang B., Huang J., Wang Y. and Yu G. (2016) Highly efficient removal of hexavalent chromium from electroplating wastewater using aminated wheat straw. *RSC Adv.* **6**, 8797–8805.

Yin W., Wu J., Huang W. and Wei C. (2015) Enhanced nitrobenzene removal and column longevity by coupled abiotic and biotic processes in zero-valent iron column. *Chem. Eng. J.* **259**, 417–423.

Zachara J. M., Ainsworth C. C., Brown G. E., Catalano J. G., McKinley J. P., Qafoku O., Smith S. C., Szecsody J. E., Traina S. J. and Warner J. A. (2004) Chromium speciation and mobility in a high level nuclear waste vadose zone plume. *Geochim. Cosmochim. Acta* **68**, 13–30.

Zachara J. M., Girvin D. C., Schmidt R. L. and Resch C. T. (1987) Chromate adsorption on amorphous iron oxyhydroxide in the presence of major groundwater ions. *Environ. Sci. Technol.* **21**, 589–594.

Zakari S., Liu H., Tong L., Wang Y. and Liu J. (2016) Transport of bisphenol-A in sandy aquifer sediment: Column experiment. *Chemosphere* **144**, 1807–1814.

Zegeye A., Bonneville S., Benning L. G., Sturm A., Fowle D. A., Jones C. A., Canfield D. E., Ruby C., MacLean L. C., Nomosatryo S., Crowe S. A. and Poulton S. W. (2012) Green rust formation controls nutrient availability in a ferruginous water column. *Geology* **40**, 599–602.

Zhang W. X. (2003) Nanoscale iron particles for environmental remediation: An overview. *J. Nanoparticle Res.* **5**, 323–332.

Zhong H., Liu G., Jiang Y., Yang J., Liu Y. and Yang X. (2017) Transport of bacteria in porous media and its enhancement by surfactants for bioaugmentation : A review. *Biotechnol. Adv.* **35**, 490–504.

Zhou X. A. and Korenaga T. (1993) A Process monitoring/controlling system for the treatment of wastewater containing Chromium (VI). **27**, 1049–1054.

Appendix

A.1 Background Information

A.1.1 Permeable Reactive Barriers in Germany

Table A-1 Overview of permeable reactive barriers installations present in Germany as March 2002 (Birke et al., 2002).

| Startup	Site	Contaminants	Status	Construction	Reactor	Total costs
May 1998	Edenkoben, industrial plant, supplier for car manufacturers	cVOCs (cis-DCE, 1,1,1-TCA, TCE, PCE)	Pilot-scale	F&G, length 30 m, depth ~ 15 m, 1 gate	Granular ZVI. 2 chambers, vertical flow (up and down)	350,000 €
February 2001			Full-scale	F&G, length 440 m, depth ~ 15 m, 6 gates		1,750,000 €
June 1998	Rheine, former dry cleaner´s	cVOCs (PCE, TCE, cis-DCE)	Pilot-scale	CRB, overlapping boreholes (diameter 0.9 m) in row, length 22.5 m, depth 6 m	2 iron types: Granular ZVI and "iron sponge" in separated sections	170,000 €
October 1998	Tübingen, former industrial site	cVOCs (TCE, cis-DCE, MCE)	Full-scale	F&G, length 200 m, depth 10 m, 3 gates	ZVI, boreholes, horizontal flow	Not available
October 1999	Bitterfeld, chemical industry	Chlorobenzenes, CHC, phenols	Pilot-scale, R&D only	5 shafts equipped with steel reacotrs, depth 24 m	FAC, ZVI, nutrients etc…	6,000,000 €
January 2000	Reichenbach an der Fils, metal-processing industry	cVOCs, (PCE, TCE, cis-DCE)	Full-scale	CRB, non-overlapping boreholes in 2 rowes, length 20 m, depth 7 m	AC specially conditioned	200,000 €
January 2001	Karlsruhe, former gas works plant	PAHs, VC	Full-scale	F&G, length 240 m, depth ~ 17 m, 8 gates	GAC	4,000,000 €
August 2001	Denkendorf, trading estate	cVOCs, (PCE, TCE, TCA, cis-DCE, VC)	Full-scale	D&G, 1 gate (shaft, depth 6 m), drainage: length ~ 90 m	AC	Not available
September 2001	Bernau, former dry cleaner´s (abandoned military site)	cVOCs (TCE), very high concentrations in 2 aquifers	Pilot-scale, mainly R&D for potential scale-up	Special F&G design capturing 2 contaminated aquifers, closed funnel, partly operated actively	Granular ZVI, microbiology and/or palladium planned	1,500,000 €
September 2002	Denkendorf, trading state	Mainly VC	Small pilot-scale, treatability/feasibility	Column installed inside the shaft using a bypass	Pd on zeolits, hydrogen	120,000 €
January 2002	Oberursel, industry	cVOCs	Full scale	F&G, length 175 , depth 4-17 m, 1 gate	Granular ZVI	Not available

A.1.2   Eh-pH Diagrams
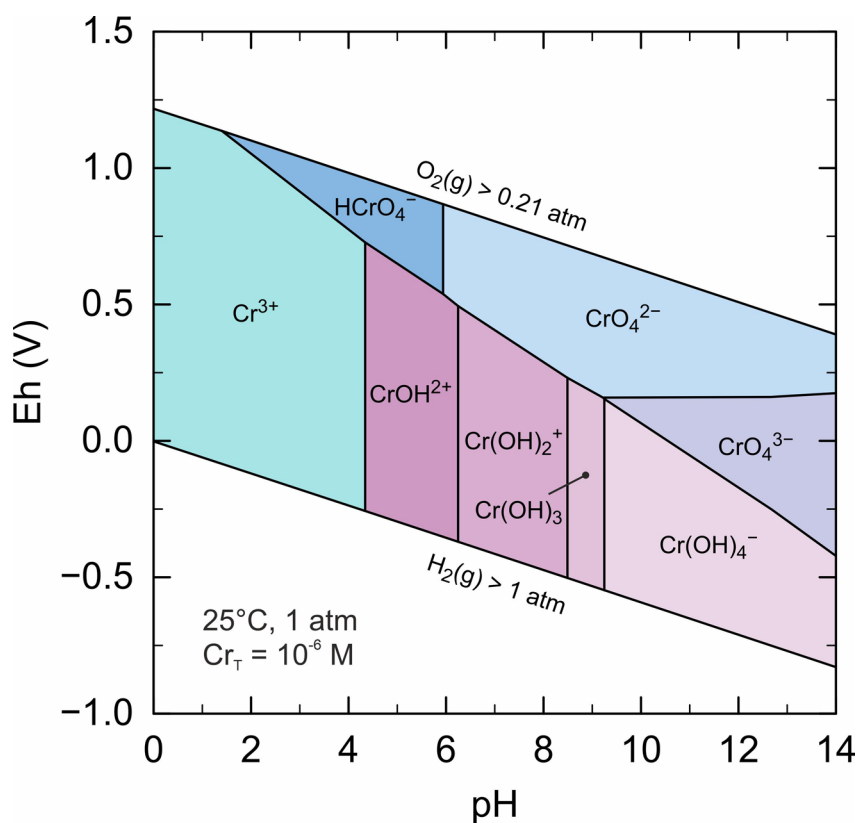
Figure A-1   **Eh-pH diagram for the system Cr-H$_2$O at 25°C and 1 atm; Cr$_{total}$: 10^{-6} M.**
Diagrams were calculated with PHREEQC (USGS) using the Lawrence Livermore National Laboratory *(LLNL)* database.
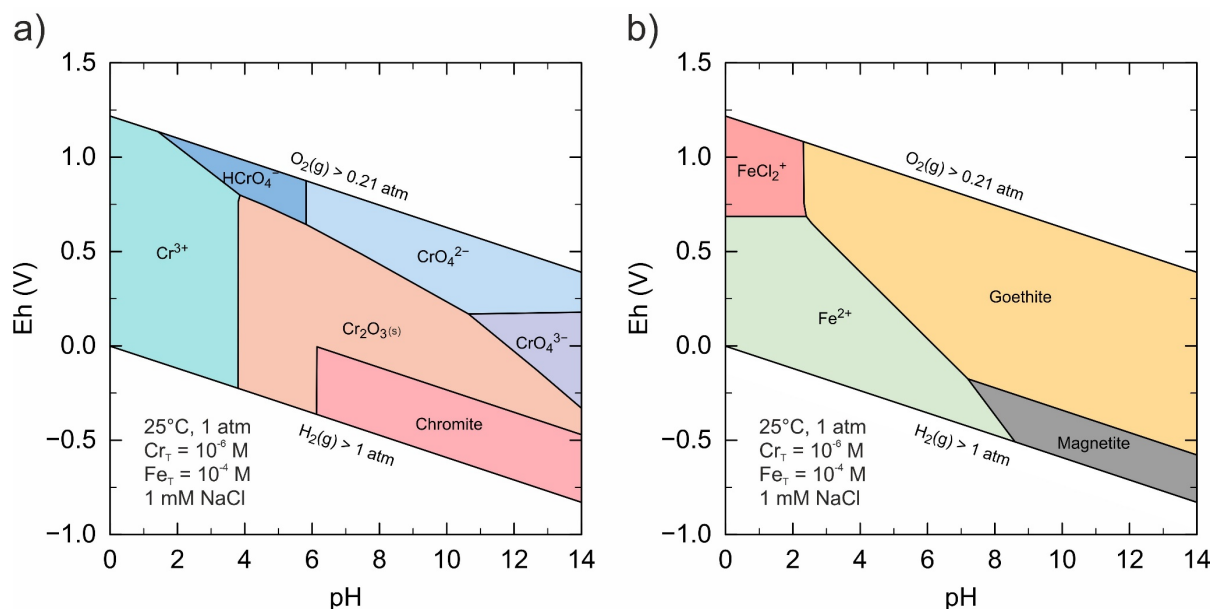

Figure A-2   **Eh-pH diagram for (a) chromium and for (b) for iron. The Pourbaix diagrams of the Fe-Cr-H$_2$O system at 25°C and 1 atm were obtained taking into account different solid Fe-Cr phases and iron (hydr)oxides.**
These phases are: Cr$_2$O$_3$, chromite [FeCr$_2$O$_4$], magnetite [Fe$_3$O$_4$] and goethite [α-FeOOH]; Fe$_T$: 10^{-4} mol/L; Cr$_T$: 10^{-6} M.

A.2 Materials and Methods

A.2.1 Quartz Sand

Table A- 2   Characteristics of silica.

Chemical composition	SiO_2
Molecular weight	60.09 g/mol
Density	2.66 g/cm^3
Boling point	> 2230 ºC
Melting point	> 1610 ºC

Table A- 3   Specification of the quartz sands used for the experiments, provided by the manufacturers (Chemsolute®, Th. Geyer and Carl Roth Germany). * Sea sand purified by acid and calcined.

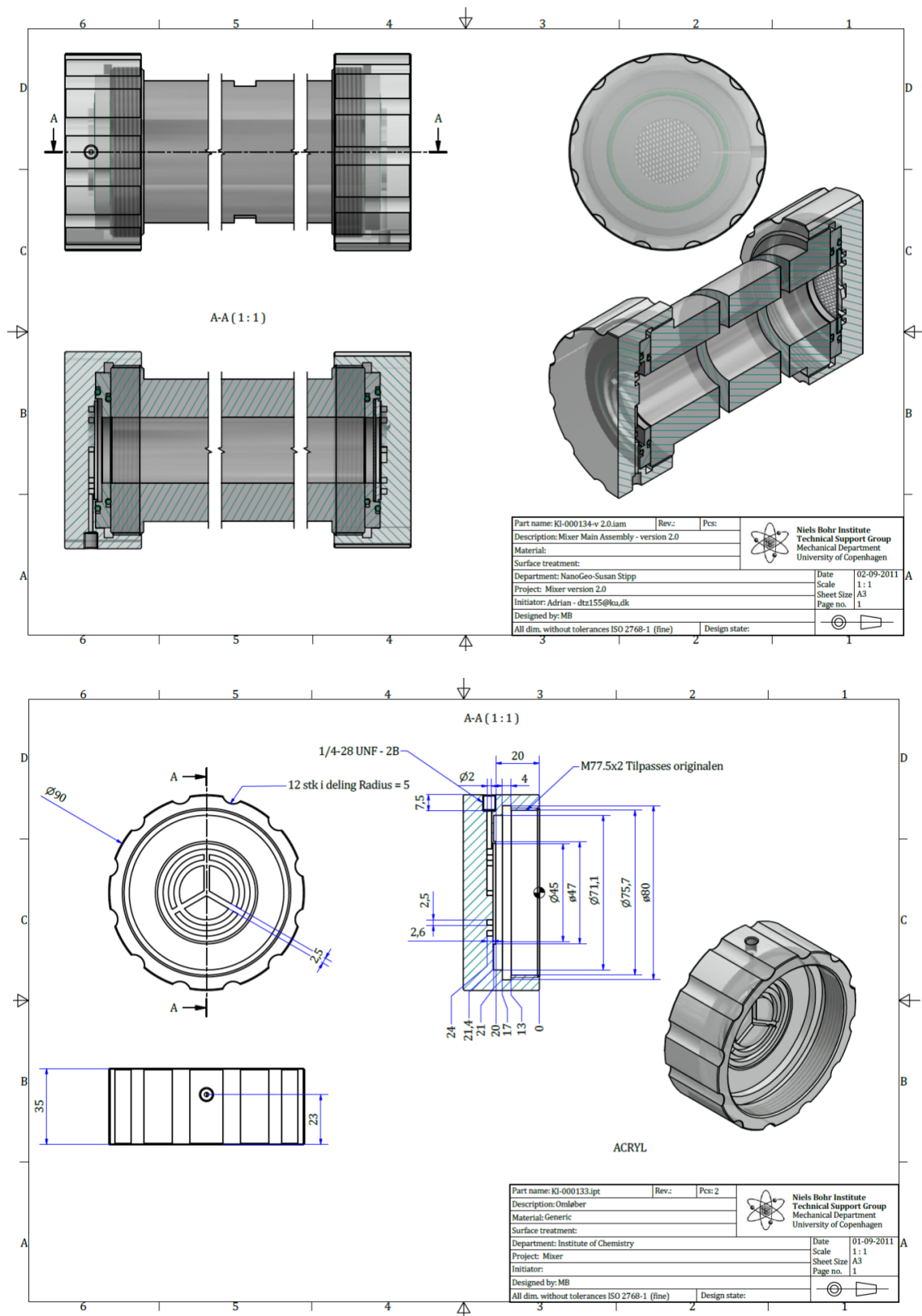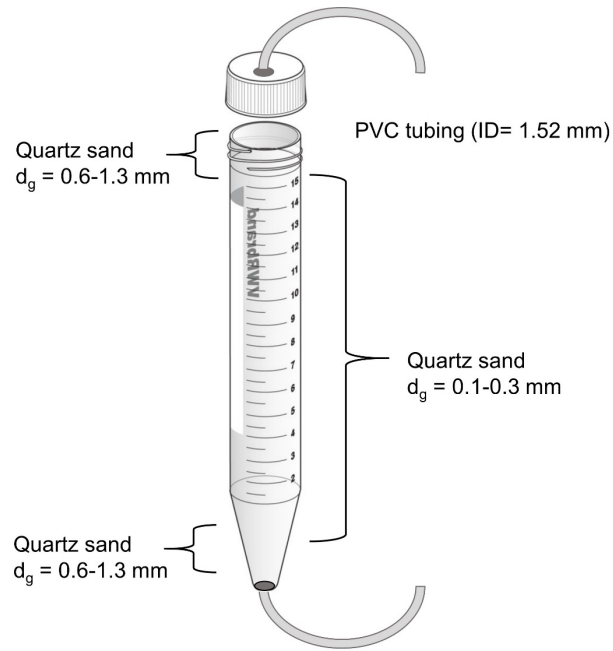| Manufacturer	Chemsolute®	Carl Roth
Grain size distribution	0.1-0.3 mm	0.6-1.3 mm
SiO_2	~ 100 %	~ 98.0 %
Fe_2O_3	-	~ 0.02 %
Al_2O_3	-	~ 1.1 %
TiO_2	-	~ 0.04 %
Acid-soluble iron (Fe)	max 0.01 % *	-
Loss on ignition	max 0.05 %	-
Acid soluble substances	max 0.15 %	-
Chloride (Cl)	max 0.005 %	-

A.2.2   Column Reactors

Figure A-3   Prototype of the column reactor manufactured by the workshop of University of Copenhagen.

Figure A-4 **Column reactor (diameter of 1.4 cm and length of 11 cm) used for the reactivity and transport column experiments.**
It was obtained from conical centrifuge tubes superclear (VWR, 15 ml) made of polypropylene (PP).
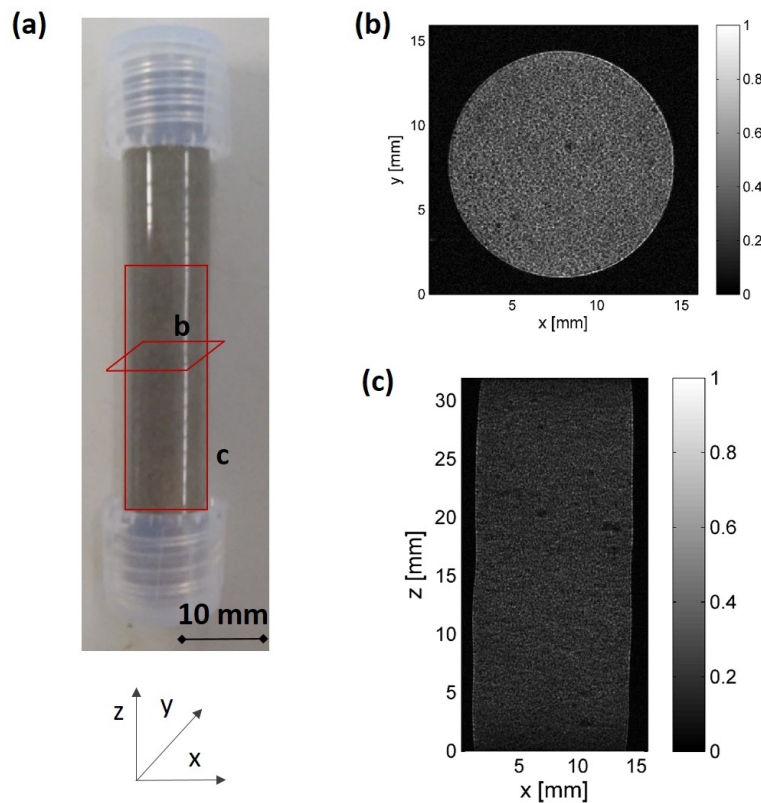
Figure A-5 **(a) Column packed with the wet-packing method and scanned with MRT and MR image of the column (b) along the axial plane (*x-y*) and (c) along the sagittal plane (*x-z*).**

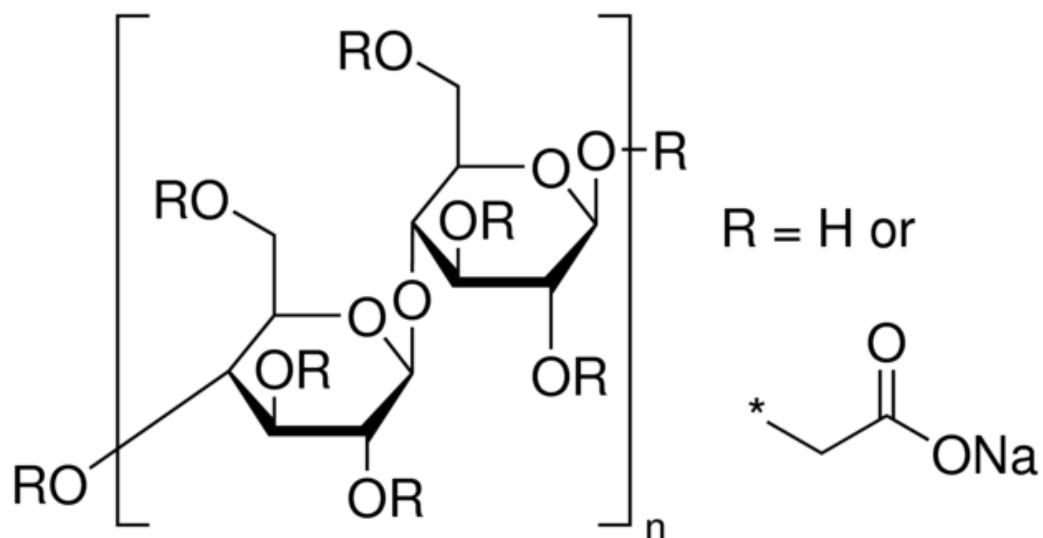## A.2.3 Sodium Carboxymethyl Cellulose and Xanthan Gum

Figure A-6 Chemical structure of sodium carboxymethyl cellulose (CMC) (FisherScientific, 2020).
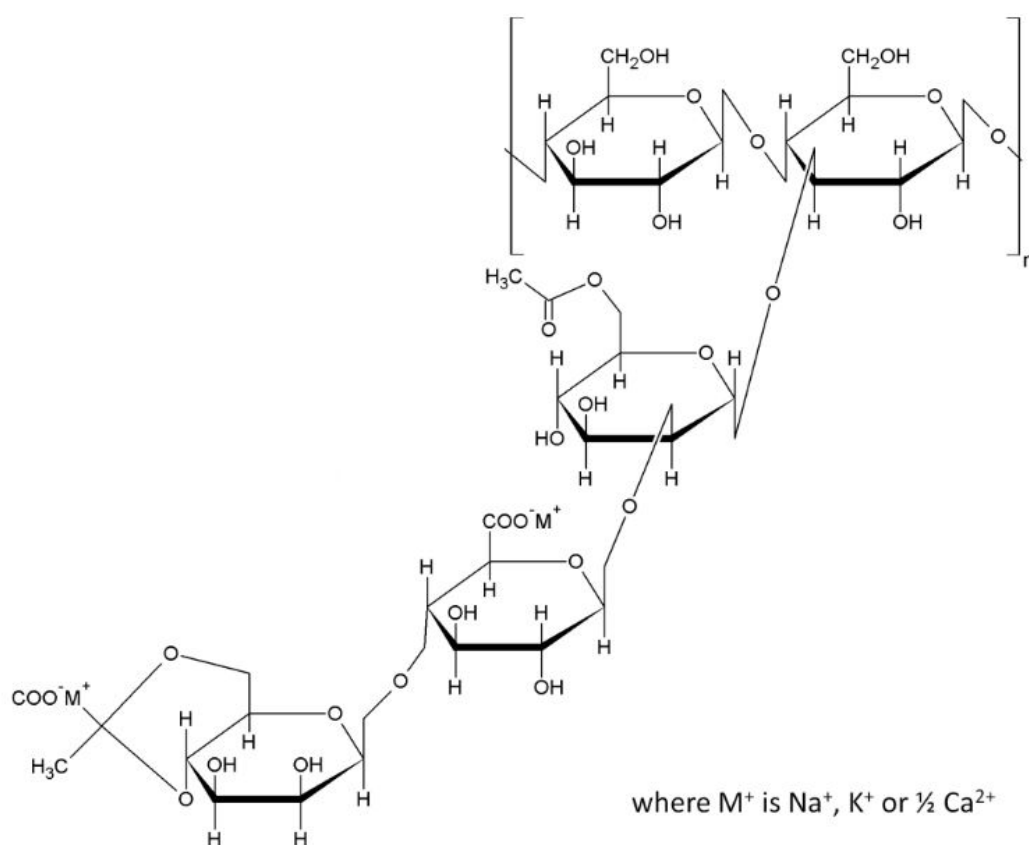

Figure A-7 Chemical structure of xanthan gum (Quinten, 2011).

A.3 Results and Data

A.3.1 Solid Characterization
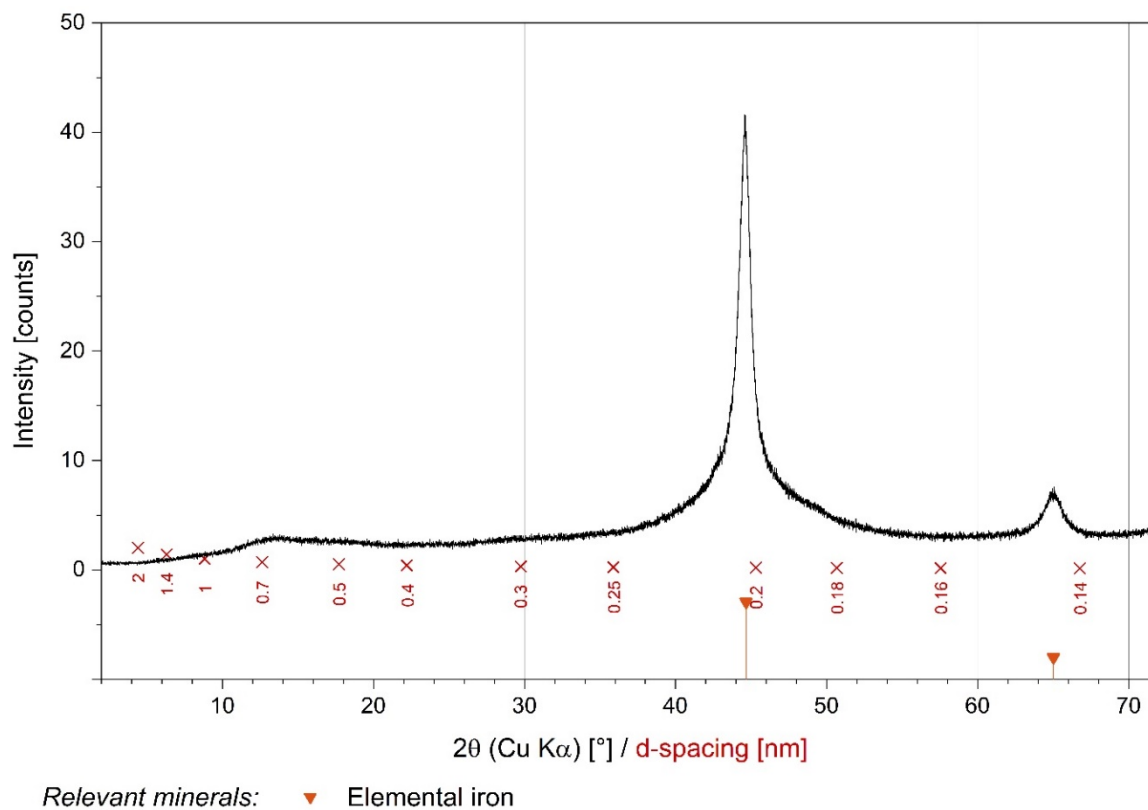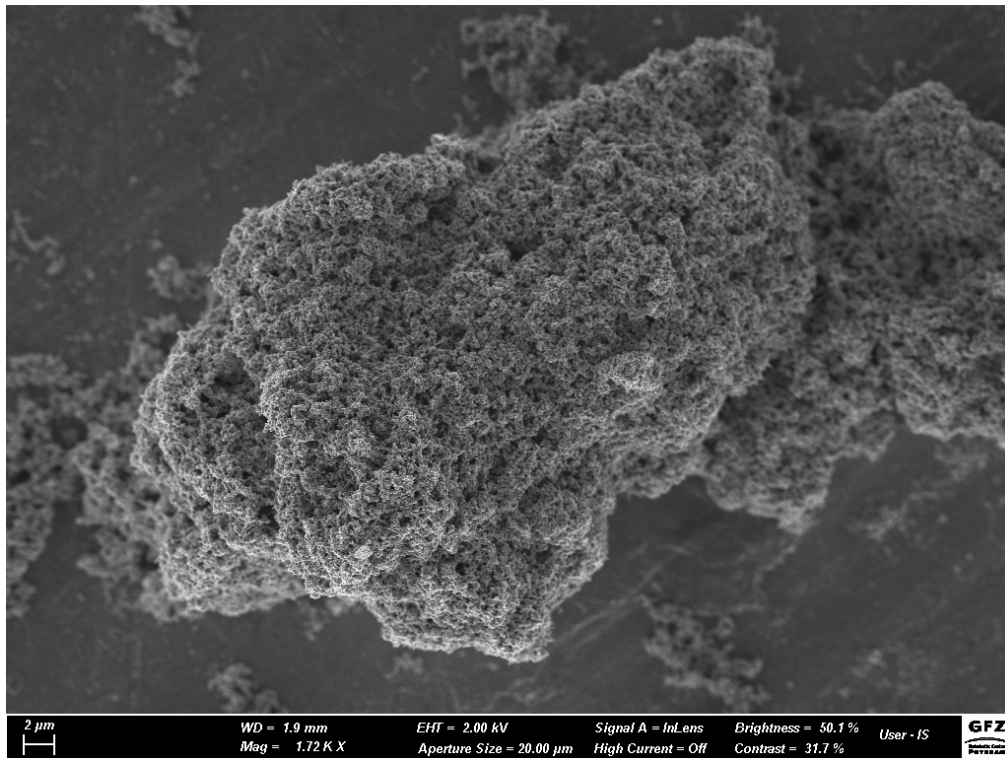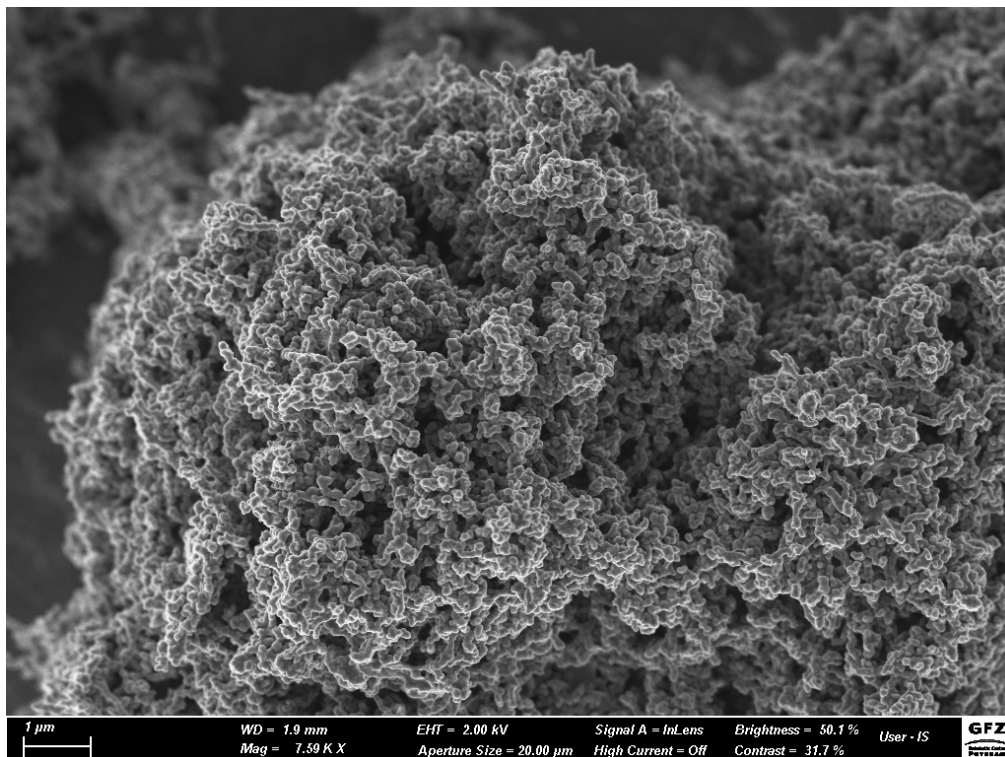
A.3.1.1 XRD analysis on 5-CMC-S-nZVI[post]

Relevant minerals: ▼ Elemental iron

Figure A-8   XRD pattern (Cu-Kα) of 5-CMC-S-nZVI[post] (Fe[0]: PDF# 06-0696 and FeS: PDF# 89-6268).

A.3.1.2   SEM Analysis on Bare S-nZVI, 5-CMC-S-nZVI[post] and 5-CMC-S-nZVI[pre]

Figure A-9   **SEM images of bare S-nZVI with Mag = 1.72 KX.**
WD = 1.9 mm, , EHT= 2.00 kV, contrast 31.7 %, brightness = 50.1 %, signal A = InLens, aperture size = 20 µm, high current = off.

Figure A-10   **SEM images of bare S-nZVI with Mag = 7.59 KX.**
WD = 1.9 mm, EHT= 2.00 kV, contrast 31.7 %, brightness = 50.1 %, signal A = InLens, aperture size = 20 µm, high current = off.
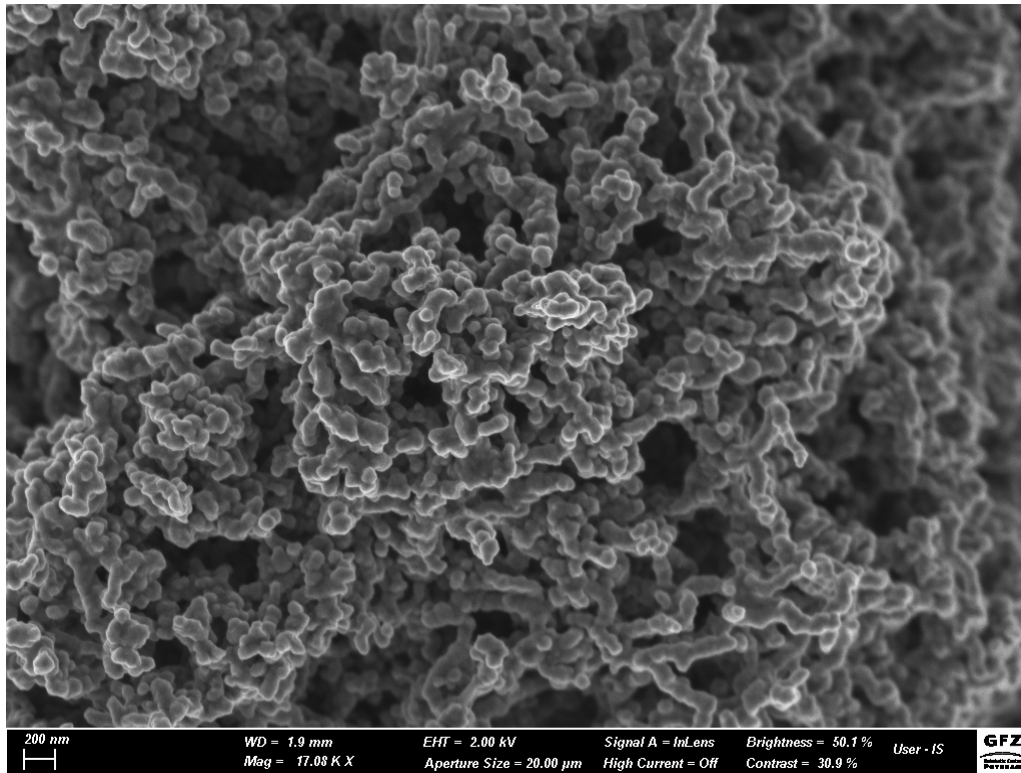
Figure A-11 SEM images of bare S-nZVI with Mag = 17.08 KX.
WD = 1.9 mm, EHT= 2.00 kV, contrast 30.9 %, brightness = 50.1 %, signal A = InLens,
aperture size = 20 µm, high current = off.

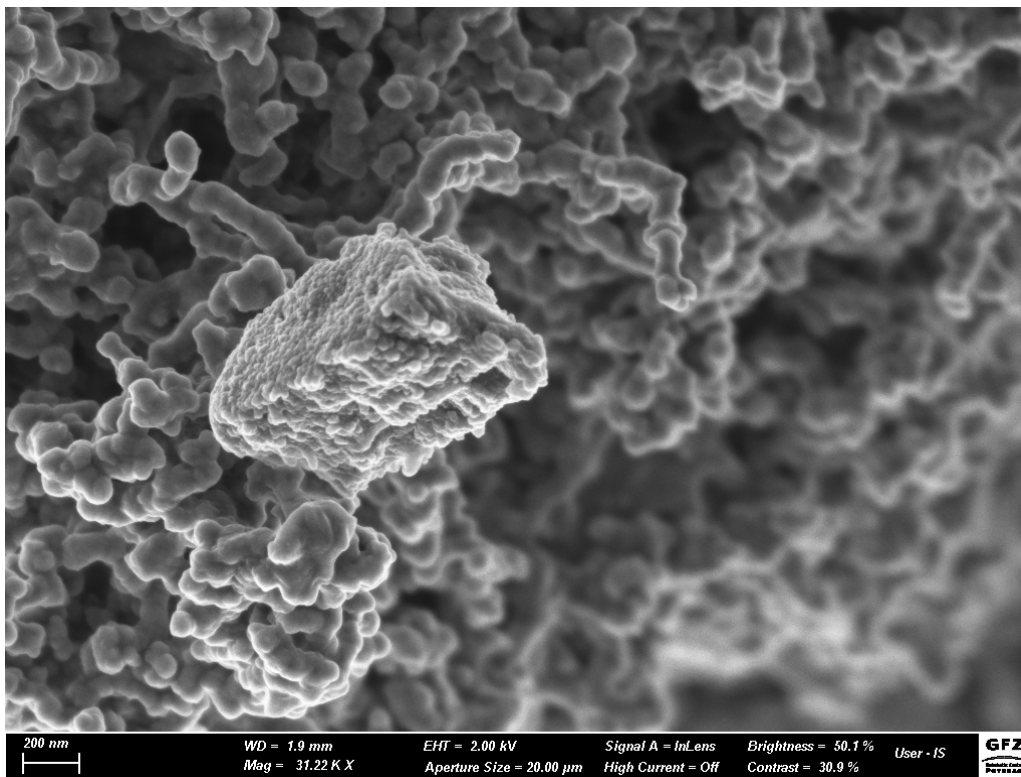**Figure A-12 SEM images of bare S-nZVI with Mag = 31.22 KX.**
WD = 1.9 mm, EHT= 2.00 kV, contrast 30.9 %, brightness = 50.1 %, signal A = InLens,
aperture size = 20 µm, high current = off.

Figure A-13   SEM images of 5-CMC-S-nZVI^{post} with Mag = 5.00 KX.
WD = 10.2 mm, EHT= 15.00 kV, contrast 30.5 %, brightness = 49.8 %, signal A = SE2,
aperture size = 60 µm, high current = on.

Figure A-14   SEM images of 5-CMC-S-nZVI^{post} with Mag = 10.00 KX.
WD = 2.2 mm, EHT= 2.00 kV, contrast 32.3 %, brightness = 49.9 %, signal A = InLens,
aperture size = 20 µm, high current = off.

Figure A-15   SEM images of 5-CMC-S-nZVI^post with Mag = 30.00 KX.
WD = 2.2 mm, EHT= 2.00 kV, contrast 32.3 %, brightness = 50.1 %, signal A = InLens, aperture size = 20 µm, high current = off.
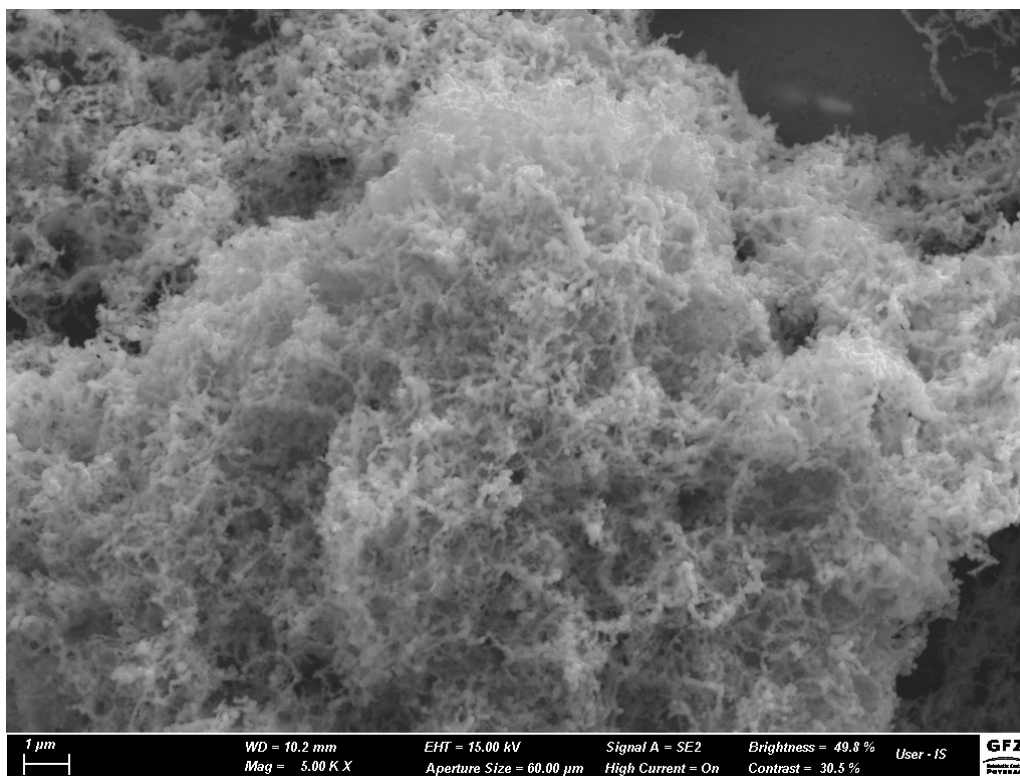

Figure A-16   SEM images of 5-CMC-S-nZVI^pre with Mag = 5.05 KX.
WD = 10.1 mm, EHT= 15.00 kV, contrast 32.3 %, brightness = 49.1 %, signal A = SE2, aperture size = 60 µm, high current = off.
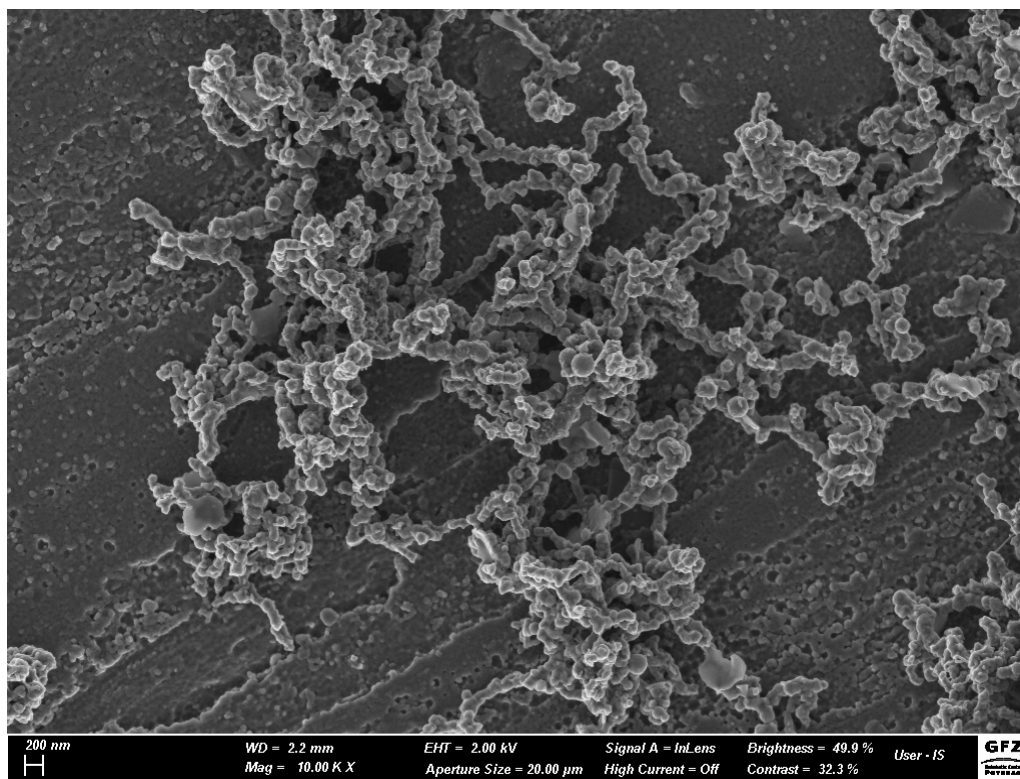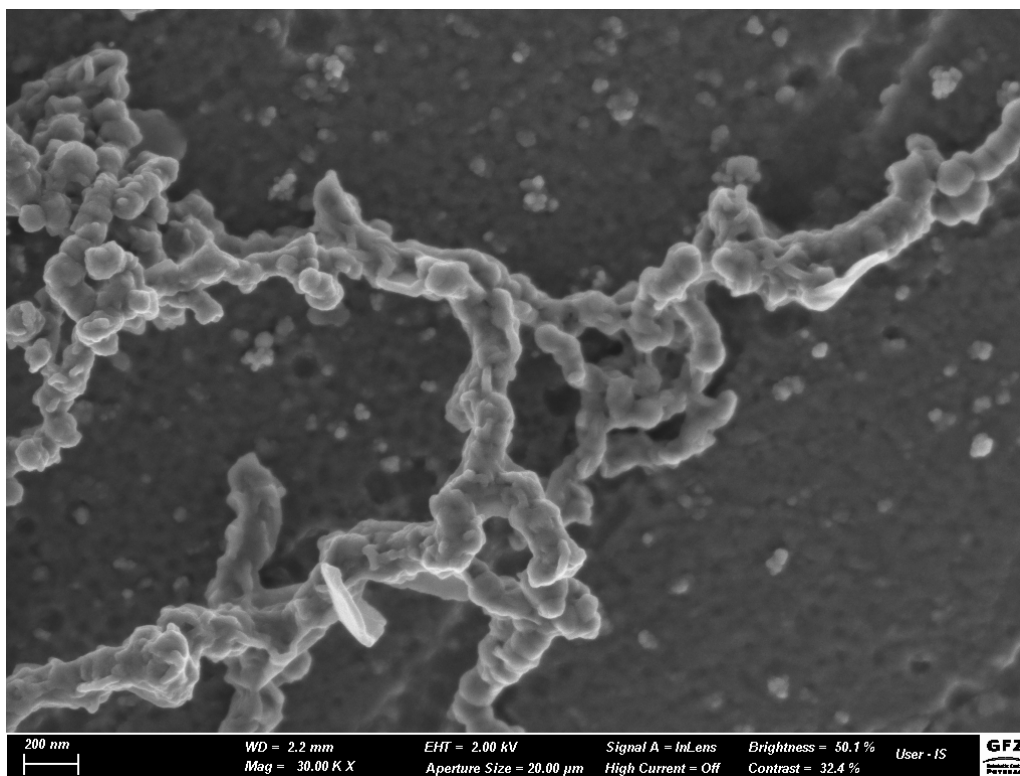
Figure A-17   SEM images of 5-CMC-S-nZVI^{pre} with Mag = 10.00 KX.
WD = 2.2 mm, EHT= 2.00 kV, contrast 32.3 %, brightness = 49.9 %, signal A = InLens,
aperture size = 20 μm, high current = off.

Figure A-18   SEM images of 5-CMC-S-nZVI^{pre} with Mag = 25.00 KX.
WD = 2.2 mm, EHT= 2.00 kV, contrast 32.3 %, brightness = 49.9 %, signal A = InLens,
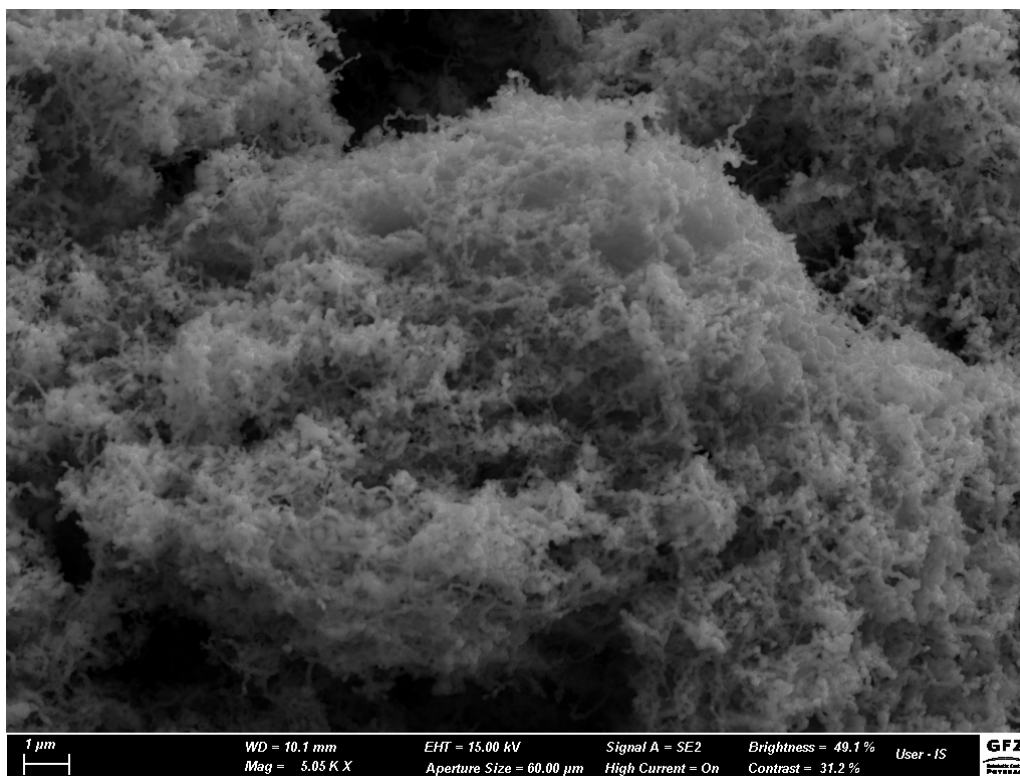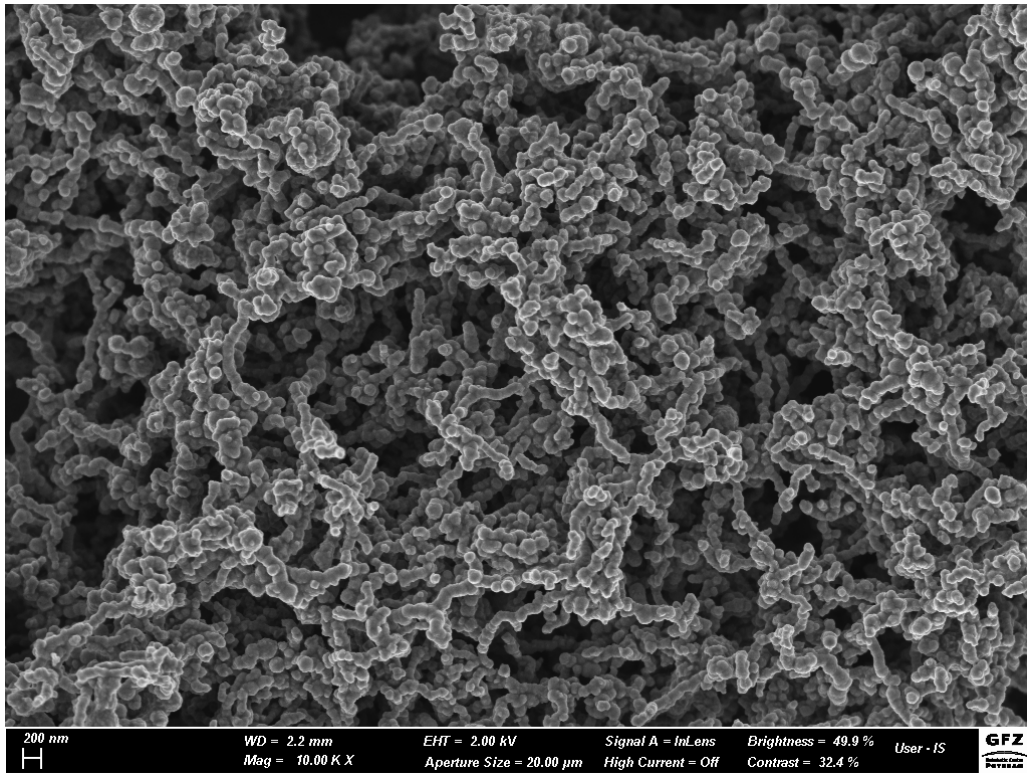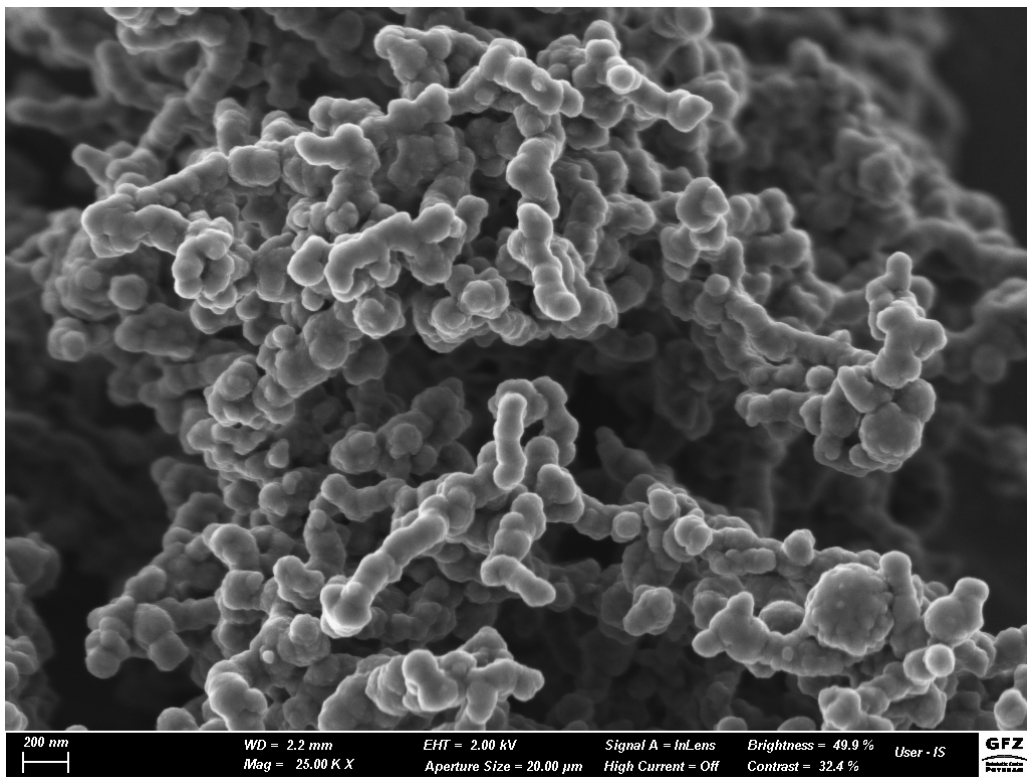**aperture size = 20 μm, high current = off.**

A.3.1.3 STEM-EDX

Table A-4 STEM-EDX elemental quantification of C, O, S and Fe contents (atomic %) and elemental/atomic ratios (i.e., O/Fe, S/Fe and C/Fe) in bare S-nZVI, CMC-S-nZVI[post] and CMC-S-nZVI[pre]. The LOD of C is 0.1 atomic %.

Sample	ROI	Area	C	O	S	Fe	O/Fe	S/Fe	C/Fe
	1a	1	4.5	27.7	3. 9	60.6	0.46	0.06	0.07
		2	2.8	14.1	1.4	77.5	0.18	0.02	0.04
		1	< 0.1	1.0	1.2	93.3	0.01	0.01	< 0.01
	1b	2	8.8	29.6	1.9	57.3	0.52	0.03	0.15
		3	13.4	3.6	0.5	79.0	0.04	0.01	0.17
		4	28.5	8.9	1.0	58.7	0.15	0.02	0.49
	4	1	6.9	9.7	2.2	77.2	0.13	0.03	0.09
		2	11.7	11.1	1.8	71.5	0.15	0.03	0.16
Bare S-nZVI	5	1	6.9	16.3	1.2	71.8	0.23	0.02	0.10
		2	30.0	12.0	0.9	54.3	0.22	0.02	0.55
	6	1	4.9	20.1	2.3	69.3	0.29	0.03	0.07
		2	15.6	14.7	1.2	65.5	0.22	0.02	0.24
		1	< 0.1	15.4	2.0	78.4	0.20	0.02	< 0.01
	7	2	1.1	11.9	2.1	80.1	0.15	0.03	0.01
		3	< 0.1	16.6	2.7	76.8	0.22	0.04	< 0.01
		1	< 0.1	16.9	2.3	77.1	0.22	0.03	< 0.01
	8	2	2.9	9.8	2.2	81.5	0.12	0.03	0.04
		3	10.3	10.0	1.4	73.9	0.14	0.02	0.14
		1	3.2	10.5	2.3	79.3	0.13	0.03	0.04
	2	2	17.6	10.1	2.5	65.8	0.15	0.04	0.27
CMC-S-nZVI[post]		3	18.2	10.5	1.9	64.8	0.16	0.03	0.28
		4	19.3	11.3	1.9	63.2	0.18	0.03	0.31
	3	1	9.1	15.2	1.8	69.5	0.22	0.03	0.13
	5	1	15.1	11.2	2.1	64.7	0.17	0.03	0.23
		1	7.6	18.1	9.4	60.8	0.30	0.15	0.13
	1	2	3.7	10.3	5.4	76.0	0.14	0.07	0.05
		3	1.6	4.6	3.0	84.6	0.05	0.04	0.02
		4	14.3	10.1	3.54	66.8	0.15	0.05	0.21
		1	0.7	2.4	2.6	88.8	0.03	0.03	0.01
	4	2	1.6	3.2	1.6	86.7	0.04	0.02	0.02
		3	1.9	2.6	0.9	88.2	0.03	0.01	0.02
		1	5.7	18.3	2.6	68.7	0.27	0.04	0.08
		2	1.8	13.9	1.9	76.8	0.18	0.03	0.02
CMC-S-nZVI[pre]	5	3	5.2	7.4	4.2	78.6	0.09	0.05	0.07
		4	8.0	7.5	3.2	76.9	0.10	0.04	0.10
		5	17.9	3.7	0.5	73.5	0.05	0.01	0.24
		6	11.4	17.0	1.5	65.6	0.26	0.02	0.17
	6	1	5.5	7.8	1.6	80.4	0.10	0.02	0.07
		2	< 0.1	4.5	1.7	87.6	0.05	0.02	< 0.01
		1	< 0.1	3.5	0.5	90.4	0.04	< 0.01	< 0.01
		2	5.8	13.7	5.7	69.8	0.20	0.08	0.08
	7	3	5.5	9.8	3.5	75.6	0.13	0.05	0.07
		4	9.9	5.1	1.3	78.7	0.06	0.02	0.13
		5	5.6	8.8	1.5	79.1	0.11	0.02	0.07

Table A-5   **O/Fe, S/Fe and C/Fe ratios calculated with the average values from Table A-4 in bare S-nZVI, CMC-S-nZVI^{post} and CMC-S-nZVI^{pre} samples.**

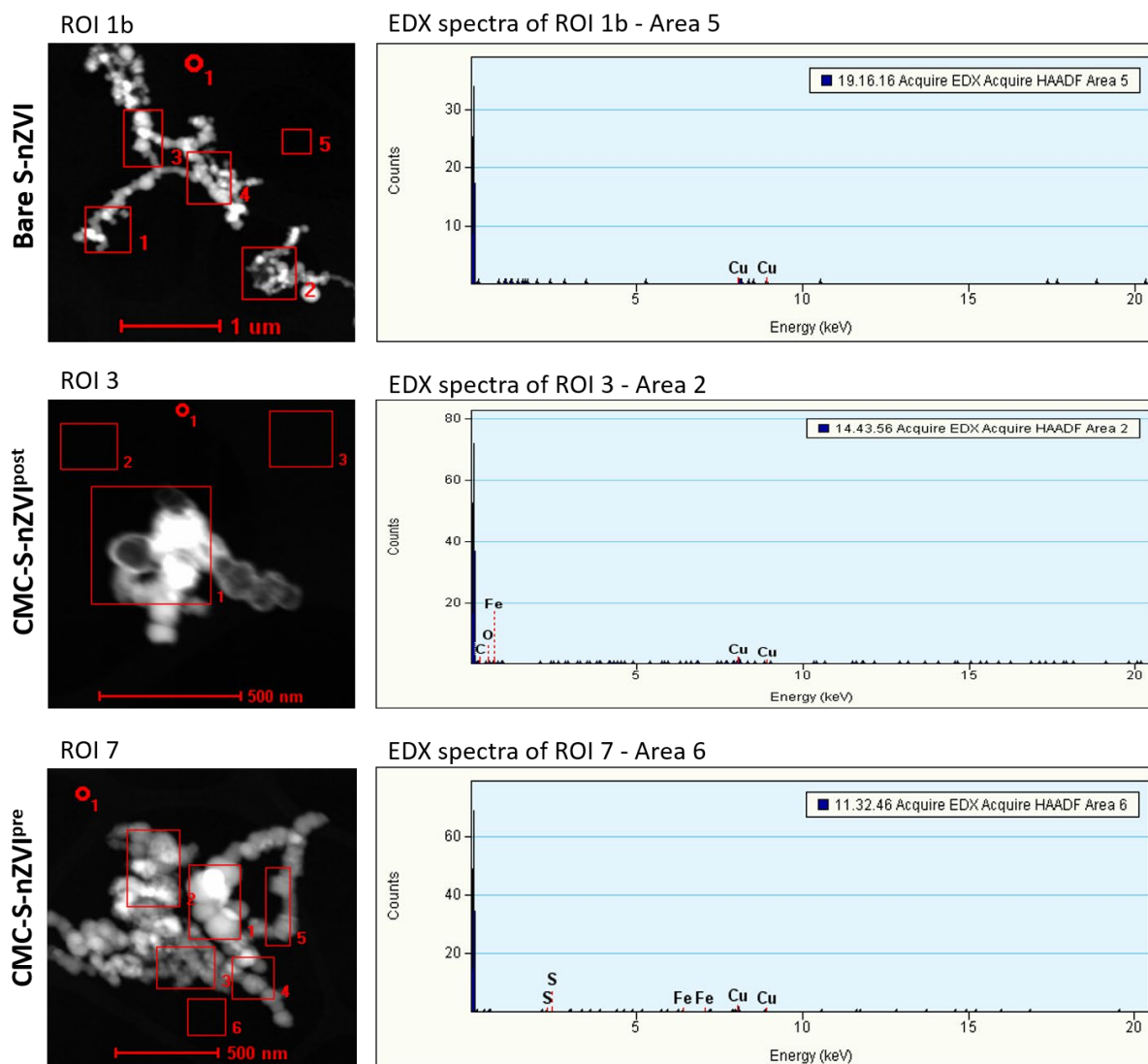| Sample	O/Fe	S/Fe	C/Fe
Bare S-nZVI	0.20 ± 0.12	0.02 ± 0.01	0.17 ± 0.16
CMC-S-nZVI^{post}	0.17 ± 0.03	0.03 ± 0.01	0.21 ± 0.10
CMC-S-nZVI^{pre}	0.12 ± 0.08	0.04 ± 0.03	0.09 ± 0.07

Figure A-19   **EDX measures made in blank areas (over a hole in the TEM grid) of selected S-nZVI samples.**
EDX acquired in Area 5 in ROI 1b of bare S-nZVI; Area 2 of ROI 3 of CMC-S-nZVI^{post} and Area 6 of ROI 7 of CMC-S-nZVI^{pre} show that there is no detectable C, Fe, O and S signals.
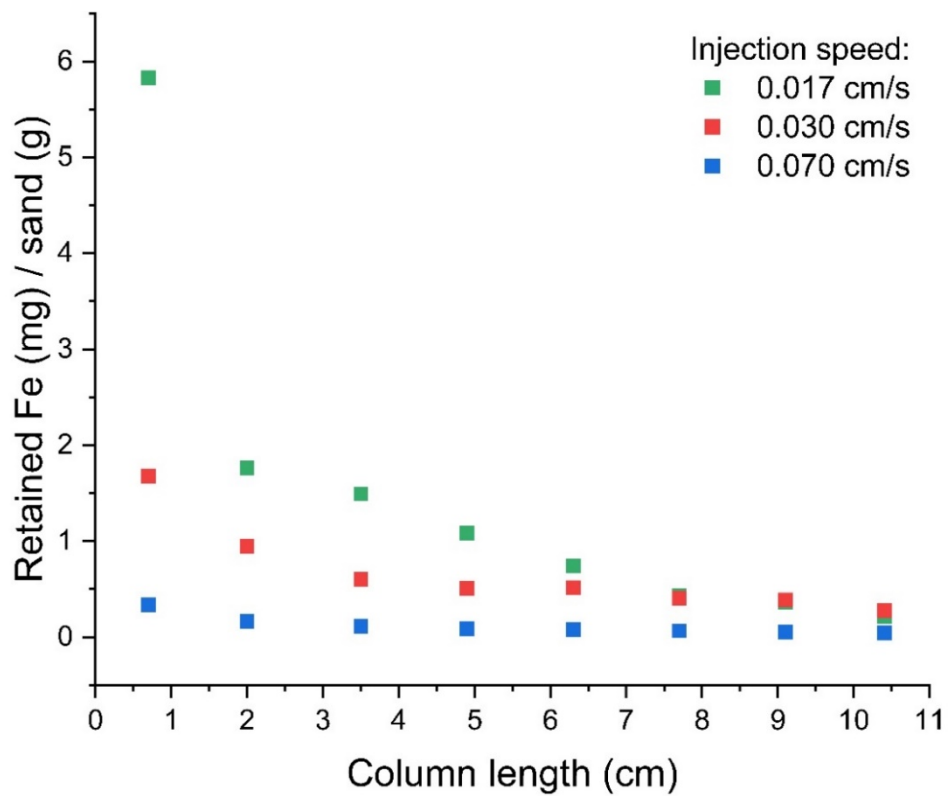
A.3.2 Retention Profile

Figure A-20 Retention profiles obtained after injection of 5-CMC-S-nZVIpost at 0.017, 0.035 and 0.070 cm/s and with inlet particle concentration (C0) of 0.8, 0.5 and 0.25 g/L.

A.3.3 Magnetic Resonance Imaging

A.3.3.1 Measurement Parameters and Set-Up

Table A-6 **Parameters for MRI measurements.**

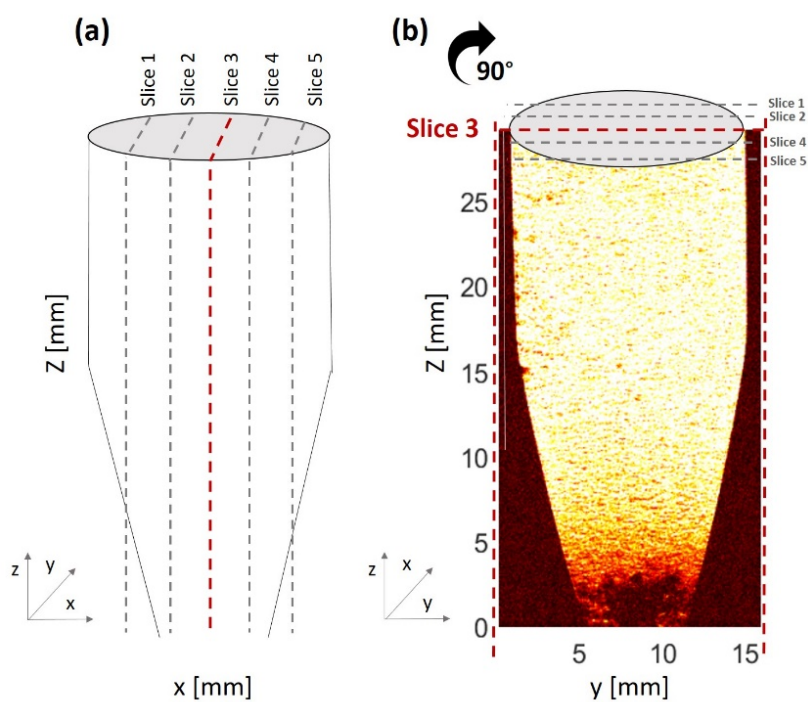| Bruker Avance 200 SWB HD III	
Parameter	Method RARE
Matrix (z/x)	520 x 256 px
Echo time	8 ms
Repetition time	2 s
Rare factor	8
Number of averages	2
Measurement time	128 s
Field of view (x/z)	16 mm x 35 mm
Spatial resolution in x-z plane	0.067 mm/px
Slice thickness	2 mm
Slice(s)	5 sagittal (y-z plane)

Figure A-21 **Schematic representation of the column along (a) the frontal (x-z) plane and (b) MR image along the sagittal (y-z) plane in the middle position (slice 3).**

A.3.3.2 Boltzmann Fits

(a)

(b)

(c)

(d)
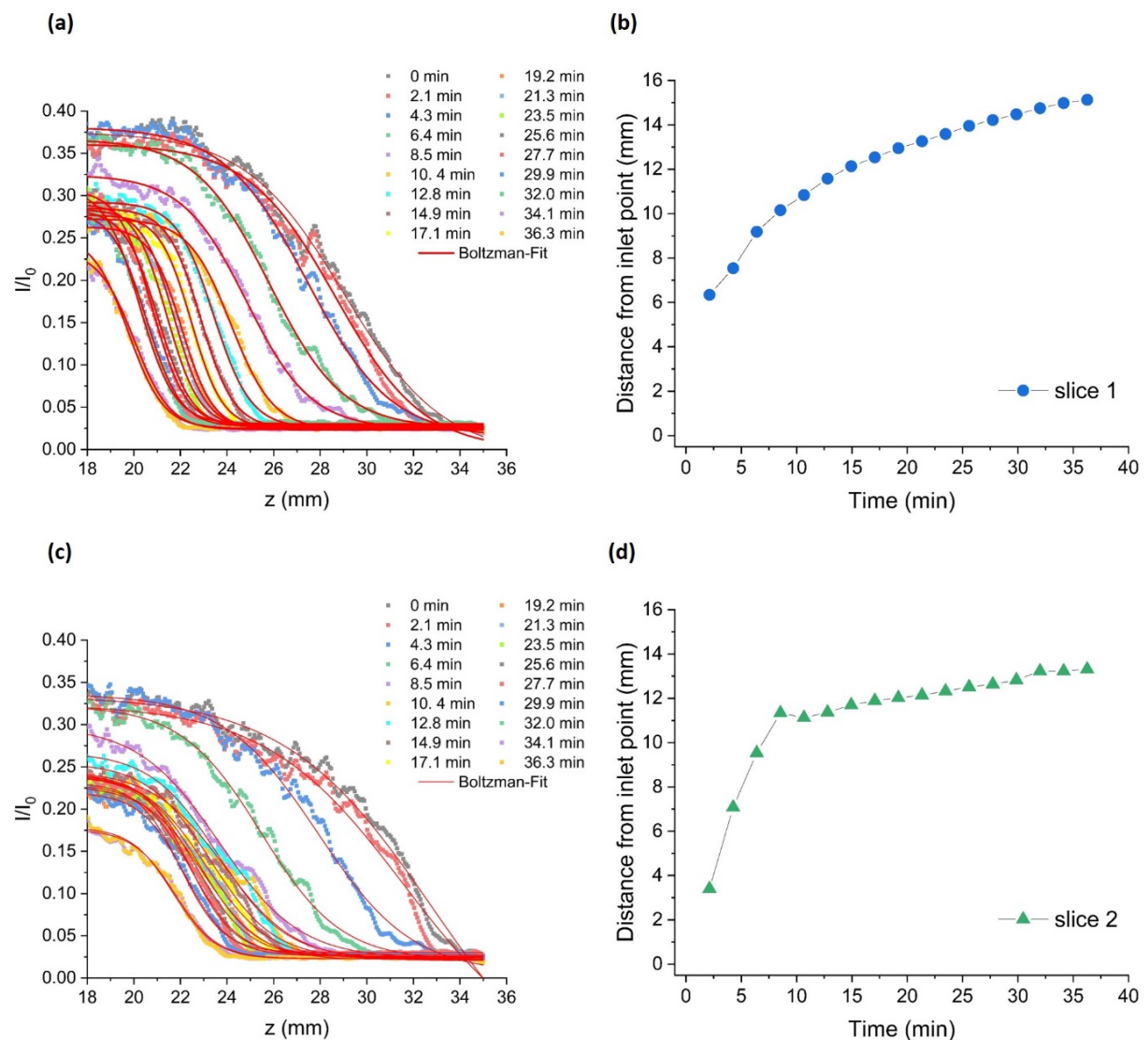
Figure A-22 MRI data obtained at slice 1 (a, b) and 2 (c, d) during injection of CMC-S-nZVI[post] inside a sandy porous medium.
(left) Normalized intensity profiles (dots) and modelled data (red lines) used to calculate the position of the inflection point of the curve (z_0); (right) kinetics plots of the distance of the migration front from the inlet point.

(e)

(f)

(g)

(h)

(i)

(l)
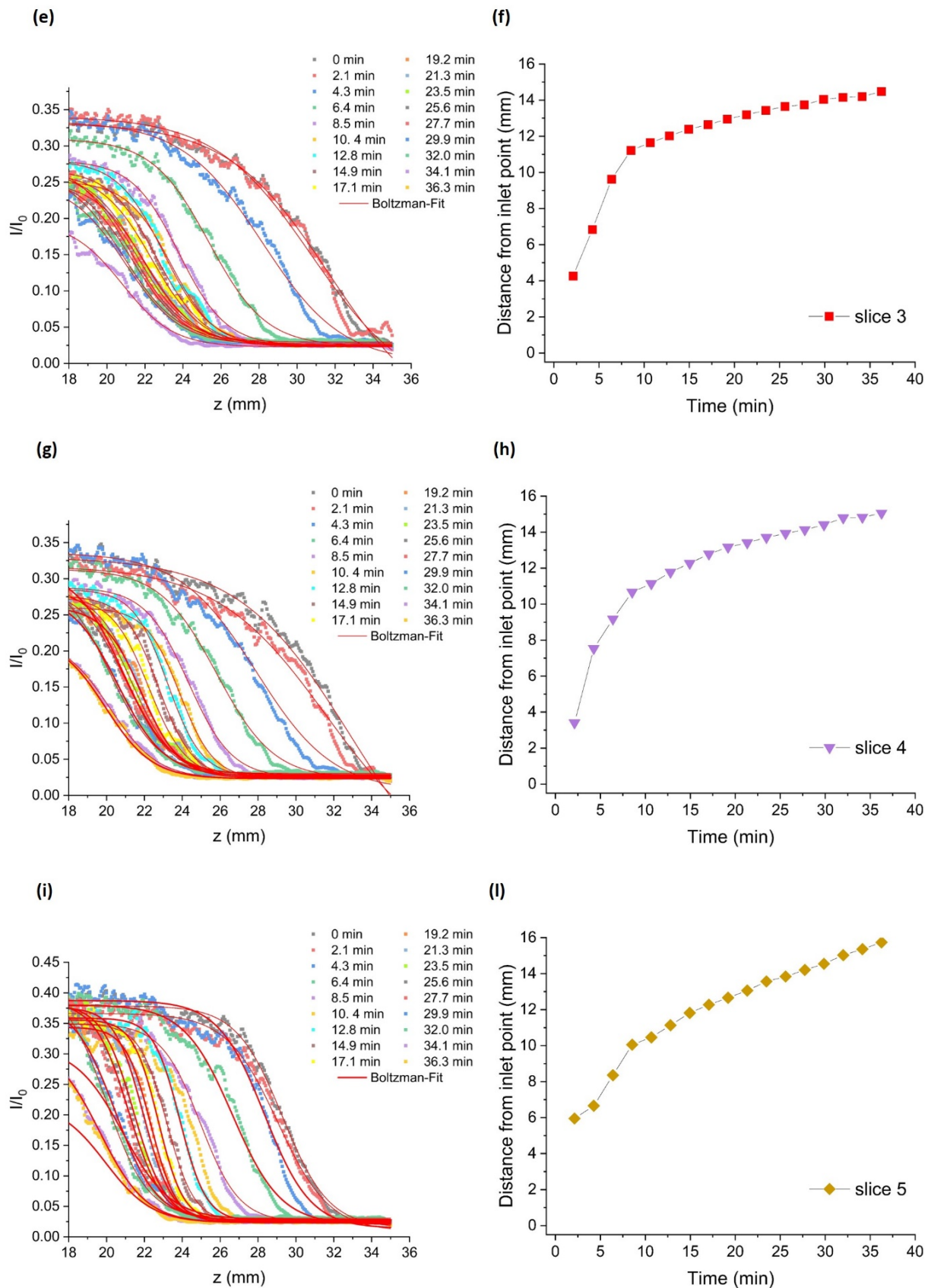
Figure A-23 MRI data obtained at slice 3 (e, f), 4 (g, h) and 5 (l, l) during injection of CMC-S-nZVI[post] inside a sandy porous medium.
(left) Normalized intensity profiles (dots) and modelled data (red lines) used to calculate the position of the inflection point of the curve (z_0); (right) kinetics plots of the distance of the migration front from the inlet point.

Table A-7 *m*-values (slope of the curve at each z_0 point) and z_i-values (distance from the inlet point) calculated from the curves modelled with the Boltzmann equation obtained at each sagittal slice (sl. from 1 to 5).

Time (min)	z_i (sl. 1)	m (sl. 1)	z_i (sl. 2)	m (sl. 2)	z_i (sl. 3)	m (sl. 3)	z_i (sl. 4)	m (sl. 4)	z_i (sl. 5)	m (sl. 5)
0.0	6.286	-0.530	3.024	-0.346	3.328	-0.393	3.128	-0.360	5.705	-0.692
2.1	6.349	-0.532	3.403	-0.336	4.263	-0.384	3.403	-0.344	5.955	-0.735
4.3	7.543	-0.559	7.086	-0.495	6.843	-0.475	7.538	-0.519	6.661	-0.819
6.4	9.187	-0.631	9.535	-0.583	9.631	-0.670	9.177	-0.664	8.357	-0.783
8.5	10.156	-0.723	11.340	-0.573	11.217	-0.807	10.673	-0.868	10.057	-0.979
10.7	10.837	-1.099	11.128	-0.654	11.646	-0.862	11.138	-1.110	10.462	-1.383
12.8	11.581	-1.257	11.373	-0.688	12.026	-0.821	11.780	-1.101	11.133	-1.438
14.9	12.137	-1.397	11.701	-0.736	12.396	-0.795	12.267	-1.103	11.819	-1.382
17.1	12.538	-1.481	11.893	-0.753	12.646	-0.754	12.786	-1.021	12.275	-1.502
19.2	12.952	-1.477	12.027	-0.808	12.950	-0.735	13.163	-0.989	12.662	-1.483
21.3	13.263	-1.472	12.141	-0.847	13.192	-0.728	13.409	-0.933	13.060	-1.318
23.5	13.588	-1.428	12.324	-0.882	13.432	-0.709	13.707	-0.881	13.567	-1.181
25.6	13.957	-1.378	12.515	-0.963	13.649	-0.715	13.933	-0.831	13.843	-1.111
27.7	14.2187	-1.388	12.637	-1.028	13.746	-0.698	14.138	-0.793	14.206	-0.978
29.9	14.477	-1.353	12.830	-1.043	14.045	-0.692	14.408	-0.806	14.547	-0.909
32.0	14.755	-1.330	13.232	-1.097	14.155	-0.686	14.796	-0.783	15.029	-0.896
34.1	14.987	-1.305	13.232	-1.102	14.197	-0.742	14.828	-0.794	15.358	-0.814
6.3	15.130	-1.306	13.315	-1.110	14.481	-0.723	15.056	-0.808	15.739	-0.772